Fortschritt-Berichte VDI

VDI

Reihe 3

Verfahrenstechnik

Dipl.-Ing. Matthias Johannink,
Köln

Nr. 949

Model-based and Experimental Analysis of Transient Electrodialysis Processes

Berichte aus der
Aachener Verfahrenstechnik - Prozesstechnik

RWTH Aachen University

Model-based and Experimental Analysis of Transient Electrodialysis Processes

Von der Fakultät für Maschinenwesen der Rheinisch-Westfälischen Technischen Hochschule Aachen zur Erlangung des akademischen Grades eines Doktors der Ingenieurwissenschaften genehmigte Dissertation

vorgelegt von

Matthias Johannink

Berichter: Universitätsprofessor Dr.-Ing. Wolfgang Marquardt
Universitätsprofessor Dr.-Ing. Mathias Wessling

Tag der mündlichen Prüfung: 26.11.2015

Fortschritt-Berichte VDI

Reihe 3

Verfahrenstechnik

Dipl.-Ing. Matthias Johannink,
Köln

Nr. 949

Model-based and Experimental Analysis of Transient Electrodialysis Processes

Berichte aus der
Aachener Verfahrenstechnik - Prozesstechnik

RWTH Aachen University

Johannink, Matthias
Model-based and Experimental Analysis of Transient Electrodialysis Processes
Fortschr.-Ber. VDI Reihe 3 Nr. 949. Düsseldorf: VDI Verlag 2016.
190 Seiten, 61 Bilder, 25 Tabellen.
ISBN 978-3-18-394903-8, ISSN 0178-9503,
€ 67,00/VDI-Mitgliederpreis € 60,30.

Keywords: Electrodialysis – Transient processes – Modelling – Ionic mass transport – Partial differential-algebraic equations – Index analysis – Model-based and experimental analysis – High performance computing

This thesis is concerned with the integration of a model-based and experimental analysis for the systematic investigation of transient electrodialysis (ED) processes. In this context a mechanistic process model for transient ED systems is developed which is based on a rigorous dynamic description of the underlying ionic transport processes. Important requirements for a systematic model development are elaborated in a systematic manner. This includes the development of a new method for the characterization of partial differential-algebraic equations and an experimental sensitivity analysis of a transient electrodialysis system. The findings can easily be generalized to related electrochemical processes such as fuel cells or batteries. By this means this work provides important results for scientist and engineers in the fields of mechanistic modeling, electro-membrane processes and electrochemical systems.

Bibliographische Information der Deutschen Bibliothek
Die Deutsche Bibliothek verzeichnet diese Publikation in der Deutschen Nationalbibliographie; detaillierte bibliographische Daten sind im Internet unter http://dnb.ddb.de abrufbar.

Bibliographic information published by the Deutsche Bibliothek
(German National Library)
The Deutsche Bibliothek lists this publication in the Deutsche Nationalbibliographie (German National Bibliography); detailed bibliographic data is available via Internet at http://dnb.ddb.de.

D82 (Diss. RWTH Aachen University, 2015)

Als Manuskript gedruckt. Printed in Germany.
ISSN 0178-9503
ISBN 978-3-18-394903-8

Vorwort

Diese Arbeit entstand im Rahmen meiner Tätigkeit als wissenschaftlicher Mitarbeiter der Aachener Verfahrenstechnik - Prozesstechnik an der RWTH Aachen. Sie wurde in Teilen durch die Max-Buchner-Stiftung und vom Bundesministerium für Bildung und Forschung (BMBF) im Rahmen der HPC Softwareinitiative im Projekt *HISEEM* gefördert. Elemente dieser Arbeit wurden vorab veröffentlicht in Johannink et al. (2010, 2015, 2011, 2016b,c).

Mein erster und besonderer Dank gilt meinem Doktorvater Prof. Dr.-Ing. Wolfgang Marquardt. Seine engagierte Unterstützung, die zahlosen Anregungen und seine stete Begeisterung waren wichtige Vorraussetzungen für das Gelingen dieser Arbeit. Des Weiteren möchte ich Prof. Dr.-Ing. M. Wessling für die Übernahme des Mitberichts, Prof. R. A. Sauer, Ph.D. für die Übernahme des Beisitzes und Prof. Dr. rer. nat. A. Schuppert für die Übernahme des Vorsitzes der Prüfungskomission danken.

Für die gute fachliche Zusammenarbeit im Projekt *HISEEM* möchte ich Prof. Dr.-Ing. Sabine Roller und Harald Klimnach meinen Dank aussprechen. Ein besonderes Dankeschön geht hier an Jens Zudrop und Kanan Masilamani für die ausgezeichnete kollegiale Zusammenarbeit, die mir fachlich sehr geholfen und mir stets viel Freude bereitet hat.

Für die gute Zusammenarbeit und die stets nette Atmosphäre möchte ich allen Mitarbeitern der Aachener Verfahrenstechnik - Prozesstechnik danken. Stellvertretend für alle möchte ich Manuel Dahmen, Juan Villeda, Fady Assassa und Mirko Skiborowski für den intensiven Austausch zu fachlichen und nicht-fachlichen Themen und die vielen gemeinsam verbrachten Stunden danken. Ein besonderer Dank gilt Adel Mhamdi für die lange und intensive Zusammenarbeit.

Eine große Hilfe waren die studentischen Hilfskräfte, die mit großem Engagement meine Forschungsarbeiten unterstützen. Für die lange Zusammenarbeit möchte ich hier Johannes Brenner, Robert Pack, Lukas Mertens, Marc-Alexander Drosner, Florian Tran, Thomas Berners und Christian Tomala besonders danken.

Den größten und schwer in Worte zu fassenden Dank möchte ich meinen Eltern und meiner Frau Judith aussprechen. Ohne eure enorme Unterstützung und eure unendliche Geduld wäre das Gelingen dieser Arbeit nicht möglich gewesen.

Köln, im März 2015 *Matthias Johannink*

für Judith und meine Eltern

Contents

Nomenclature IX

Kurzfassung 1

1 Introduction 4

1.1 Fundamentals of electrodialysis processes 4

1.1.1 Ion exchange membranes 6

1.1.2 Spacer-filled flow channels 6

1.1.3 Secondary transport effects 7

1.2 Ionic mass transport and process performance 8

1.2.1 Module and spacer design 8

1.2.2 Transient electrodialysis processes 9

1.3 Modeling ionic mass transport and electrodialysis processes 10

1.3.1 Investigation of spacers by CFD methods 10

1.3.2 Modeling of ion exchange membranes 11

1.3.3 Electrodialysis process modeling 11

1.3.4 Modeling ionic mass-transport in a homogenous phase 13

1.4 Conclusions and scope of this work 14

2 Experimental analysis of electrodialysis process dynamics 17

2.1 Experimental set-up and methods 17

2.1.1 Experimental set-up 17

2.1.2 Batch desalination experiments 19

2.1.3 Current-voltage experiments 19

2.1.4 Degrees of freedom, measurements and performance measures 19

2.2 Scope of the experimental study 20

2.3 Current-voltage behavior 22

2.4 Sensitivities with respect to operational and design parameters 25

2.4.1 Applied current 25

2.4.2 Volumetric flow rate 28

2.4.3 Comparison of different spacers 28

2.4.4 Discussion 30

2.5 Operation with transient applied currents 31

2.6 ED with pulsed current . . . 33
2.6.1 Desalination of $NaCl$ solution using a pulsed applied current . . . 33
2.6.2 Desalination of $NaCl - Na_2SO_4$ solution using a pulsed applied current . . . 37
2.6.3 Discussion . . . 37
2.7 Conclusions . . . 40

3 Index analysis and reduction of PDAE systems 42
3.1 Introduction . . . 42
3.2 Index concepts for DAE and PDAE systems . . . 46
3.2.1 Index concepts for DAE systems . . . 46
3.2.2 Index concepts for PDAE systems . . . 49
3.2.3 Comparison of the index concepts for PDAE systems . . . 53
3.3 Index analysis and reduction for semi-explicit PDAE systems . . . 54
3.3.1 Differential index . . . 54
3.3.2 Index analysis . . . 55
3.3.3 Generalization of the index reduction algorithm . . . 56
3.3.4 Systematic procedure for the index analysis and reduction . . . 58
3.4 Index analysis and reduction in the modeling work flow . . . 60
3.4.1 Physical interpretation of the reformulated model . . . 60
3.4.2 Identification of consistent initial and boundary conditions . . . 61
3.5 Conclusions . . . 64

4 Modeling of ionic transport in electrolytes 66
4.1 Modeling equations and theoretical framework . . . 66
4.1.1 Species balance equations and definition of the reference velocity . . . 67
4.1.2 Constitutive equations . . . 68
4.1.3 Momentum balance equation and hydrodynamics . . . 72
4.1.4 Complete mathematical models . . . 73
4.2 Index analysis and reduction . . . 74
4.2.1 Index with respect to time . . . 75
4.2.2 Index with respect to the spatial coordinates . . . 76
4.2.3 Reformulated low index model . . . 77
4.3 Reduced system and consistent initial and boundary conditions . . . 79
4.3.1 Reformulation into a reduced system of PDE . . . 79
4.3.2 Initial and boundary conditions . . . 81
4.4 Conclusions . . . 82

5 A dynamic process model of an electrodialysis plant 84
5.1 Hierarchical model structure and model components . . . 84
5.1.1 General modeling assumptions . . . 85
5.1.2 Spacer-filled flow channels and ion exchange membranes . . . 86

5.1.3 Electrodes and plant periphery . . . 89
5.1.4 Interface models and coupling of model components . . . 90
5.2 Problem specification and implementation . . . 92
5.2.1 Degrees of freedom and model parameters . . . 92
5.2.2 Implementation . . . 93
5.3 Model-based analysis of dynamic transport effects . . . 94
5.3.1 Dynamics in pulsed-current electrodialysis . . . 94
5.3.2 Discrimination of transport resistances . . . 97
5.3.3 Competitive transport in pulsed current experiments . . . 100
5.3.4 Discussion . . . 101
5.4 Comparison with experimental data . . . 102
5.4.1 Current-voltage experiments . . . 102
5.4.2 Batch desalination experiments . . . 105
5.5 Conclusions . . . 108

6 Spacer geometry and process performance **111**
6.1 Towards an integrated description of hydrodynamics and ionic mass transport . . . 111
6.2 Methods . . . 113
6.2.1 Pressure drop experiments . . . 113
6.2.2 Geometric modeling of the spacer and simulation scenario . . . 114
6.2.3 Software and implementation . . . 115
6.2.4 Semi-empirical modeling of pressure drop in spacer-filled channels . . . 116
6.2.5 Work flow for model identification . . . 117
6.2.6 Parameter estimation, identifiability analysis and design of experiments . . . 118
6.3 Simulation results and validation . . . 121
6.3.1 Velocity profiles . . . 121
6.3.2 Pressure drop profiles . . . 122
6.3.3 Comparison with experimental data . . . 122
6.4 Identification of friction-factor models for varying design parameters . . . 123
6.4.1 Non-woven spacers . . . 123
6.4.2 Woven spacer . . . 126
6.4.3 Predictive capabilities of the identified pressure drop models . . . 130
6.5 Summary and Discussion . . . 131

7 Concluding remarks **134**
7.1 Summary . . . 134
7.2 Outlook . . . 136

Appendices **139**

A Geometrical properties and reproducibility of the experiments **140**
A.1 Geometric properties of the lab-scale ED plant 140
A.2 Repeatability and measurement error 140
A.2.1 Pulsed current 141
A.2.2 Mixture experiments 143
A.2.3 Current-voltage experiments 143
A.3 Overview current-voltage experiments 143
A.4 Desalination experiments 145

B Physico-chemical property models for electrolytes **148**
B.1 Conversion of different reference velocities 148
B.2 Conversion of activity coefficients 148
B.3 Multi-component density model 149
B.4 Maxwell-Stefan diffusion coefficients for aqueous electrolyte solutions 150
B.4.1 MS coefficients of ion-ion pairs 151
B.4.2 MS coefficients of ion-water pairs 152
B.5 Model parameters 152

C Results of pressure drop model identification **154**
C.1 Geometric parameters of the spacer geometries in the basis data set 154
C.2 Parameter estimates for the final friction coefficient model for the non-woven and woven spacer 155
C.3 Model candidates for the identification of a generalized pressure drop model 156

Bibliography **161**

Nomenclature

Abbreviations

AEM	cation exchange membrane
CEM	anion exchange membrane
CFD	computational fluid dynamics
DAE	differential-algebraic equations
DOE	design of experiments
DOF	degrees of freedom
ED	electrodialysis
IEM	ion exchange membrane
LBM	Lattice Boltzmann method
MOL	method of lines
ODE	ordinary differential equations
PDAE	partial differential-algebraic equations
PDE	partial differential equations

Greek Symbols

Symbol	**Description**	**Units**
η	overpotential of the electrode reactions	V
Γ	matrix of basis vectors of the nullspace	
γ_k	concentration based activity coefficient of species k	-
Γ_{kj}	thermodynamic factor	-
κ	electric conductivity	$\Omega\, m$
μ_k^0	standard potential of species k	$\frac{J}{mol}$
μ_k	chemical potential of species k	$\frac{J}{mol}$
ν	kinematic viscosity	$Pa\, s$
ν_d	differential index	

ν_p	perturbation index	
$\nu_{d,j}$	differential index with respect to ζ_j	
Ω	coefficient matrix defined by Eqs. (4.112), (4.113), (4.115) and (4.116)	
ω	states of PDAE system)	
ω_k	mass fraction of species k	-
Ψ_k	total flux density of species k	$\frac{mol}{m^2\,s}$
ρ^e	electric charge density	$\frac{C}{m}$
ζ	vector of independent variables	
α	flow attack angle	$^\circ$
β	angle between filaments	$^\circ$
$\Delta\theta_k$	confidence intervals	-
ρ	density	$\frac{kg}{m^3}$
σ	standard deviation of measurements	-
ζ^{MUSUBI}	friction coefficient predicted by MUSUBI	-
ζ^{sp}	friction coefficient of the spacer	-
ϕ	electric potential	V
δ	boundary layer thickness	m

Roman Symbols

Symbol	Description	Units
AIC_i	Akaike criterion	-
A	Debye-Hueckel constant	$\sqrt{\frac{kg}{mol}}$
$\mathbf{B}$	matrix defined in Eq. 4.26	
$\mathbf{c}$	concentration vector	$\frac{mol}{m^3}$
c_f	correction factor	-
c_k	molar density of species k	$\frac{mol}{m^3}$
c_T	total molar concentration	$\frac{mol}{m^3}$
C_{kj}	binary Bromley interaction parameter	$\frac{mol}{kg}$
d^{st}	depth of the stack	m
d_f	filament diameter	m
d_g	characteristic diameter	m

D_{kl}	Maxwell-Stefan diffusion coefficient	$\frac{m^2}{s}$
$\mathbf{E}$	electric field	$\frac{V}{m}$
$\mathbf{F}$	Fischer information matrix	-
F	Faraday constant	$\frac{As}{mol}$
$\bar{\mathbf{G}}$	Jacobian matrix	-
$\mathbf{H}$	Hessian matrix	-
$\mathbf{i}$	electric current density	$\frac{A}{m^2}$
I	electric current	A
IS	ionic strength	$\frac{mol}{m^3}$
$\mathbf{J}$	flux density tensor	$\frac{mol}{m^2\,s}$
$\mathbf{J}_k$	molar diffusive flux density of species k	$\frac{mol}{m^2 s}$
K_j	equilibrium constant of reaction j	$\frac{mol}{m^3\,s}$
l_m	orthogonal distance of filaments	m
l_{ch}	channel length	m
M_k	molar weight of species k	$\frac{kg}{mol}$
n^{sp}, m^{sp}	model parameters in the friction coefficient model	-
$\hat{\mathbf{p}}^k$	empirical model parameters	-
$\mathbf{p}$	parameter vector	
p	total pressure	Pa
$p_{tp,i}$	averaged total pressure at tracking plane i	Pa
Q	volumetric flow rate	$\frac{m^3}{s}$
r_j^0	normalized reactions rate of reaction j	$\frac{mol}{m^3\,s}$
r_k^V	volumetric reaction flux density of species k	$\frac{mol}{m^3\,s}$
R^{circ}	resistance of the electric circuit	Ω
R^{ERS}	resistance of the electrolyte rinsing solution	Ω
Re	Reynolds number	-
$RSSCV$	averaged root mean square error	-
R	molar gas constant	$\frac{J}{kgK}$
Sc	Schmidt number	-
Sh	Sherwood number	-
t	time	s

T	temperature	K
$\mathbf{u}$	vector of system inputs	
$\mathbf{u}^k$	geometric design parameters	-
U	electric potential difference at the electrodes	V
U^{cell}	potential drop from the transport in the ED cell	V
U^{er}	potential drop from the electrode reactions	V
V	volume in the storage tanks	m^3
$\mathbf{v}$	reference velocity	$\frac{m}{s}$
$\mathbf{v}^{bar}$	barycentric reference velocity	$\frac{m}{s}$
$\mathbf{v}^{va}$	volume-averaged reference velocity	$\frac{m}{s}$
$\mathbf{v}_k$	absolute velocity of species k	$\frac{m}{s}$
$\tilde{V}_k$	infinite dilution partial molar volume of species k	$\frac{m^3}{mol}$
V^E	excess volume of the mixture	$\frac{m^3}{mol}$
v_{ch}	mean velocity	$\frac{m}{s}$
$\mathbf{w}$	differential states in pseudo-DAE (3.21), (3.22)	
w_k^{bar}	weighting factor for the barycentric velocity	$\frac{kg}{mol}$
w_k^{va}	weighting factor for the volume-averaged velocity	$\frac{m^3}{mol}$
w_k	weighting factor of species k	
w_{ch}	channel widths	m
$w_{i,c}$	Akaike weights w.r.t. model c	-
$\mathbf{x}$	spatial coordinates	m
$\mathbf{y}_1$	first group of algebraic states in pseudo-DAE (3.21), (3.22)	
$\mathbf{y}_2$	second group of algebraic states in pseudo-DAE (3.21), (3.22)	
$\mathbf{z}$	state vector	
z_k	specific charge number of species k	-

Kurzfassung

Die Elektrodialyse (ED) wird in industriellen Anwendungen als Trennprozess zur Entsalzung von Brack- und Meerwasser sowie zur Isolation von Säuren und Metallen eingesetzt (Huang et al., 2007, Valero and Arbós, 2010). Hierbei werden Ionenaustauschermembranen (IEM) und ein von Arbeitselektroden induziertes elektrisches Feld eingesetzt, um einen ladungsselektiven Transport ionischer Spezies zu ermöglichen. Die Intensität dieser lokalen Transportprozesse ionischer Spezies in einem elektrischen Feld bestimmt maßgeblich den spezifischen Energieverbrauch und damit das ökonomische Potential des Prozesses (Strathmann, 2004).

Obwohl der ED-Prozess bereits seit Jahrzehnten industriell genutzt wird, sind wichtige Mechanismen der zugrundeliegenden Transportprozesse noch weitestgehend unverstanden (Nikonenko et al., 2010, Strathmann, 2010). Dadurch ist nur sehr begrenzt grundlegendes Wissen zum Prozessverhalten verfügbar, insbesondere wenn der Prozess zur Behandlung komplexer Elektrolytlösungen, wie z.B. Meerwasser, eingesetzt wird. Zudem fehlt eine geeignete Wissensbasis für einen systematischen konzeptionellen Entwurf von ED-Prozessen, insbesondere in neuen Anwendungsbereichen.

Die bestehenden Limitationen im Hinblick auf das Verständnis der zugrunde liegenden Mechanismen sind besonders ausgeprägt, wenn das dynamische Verhalten in transient betriebenen ED-Prozessen betrachtet wird. Der transiente Betrieb von ED-Prozessen wird als viel versprechende Option zur Steigerung der Effizienz von ED-Prozessen angesehen (Malek et al., 2013, Strathmann, 2010). Das diesbezügliche Potential ist jedoch noch weitestgehend unklar, da der Einfluss dynamischer Phänomene auf die Intensität des Stofftransports weitestgehend unverstanden ist.

Das stark begrenzte Prozessverständnis ist zum einen auf die starke Kopplung der verschiedenen dem Prozess zugrunde liegenden Mechanismen zurückzuführen. Hierdurch kann es nur in einer systematischen umfassenden Analyse unter Berücksichtigung aller wesentlichen Phänomene und Wechselwirkungen gelingen, tiefgreifendes Prozessverständnis aufzubauen. Zum anderen sind Elektrodialysesysteme üblicherweise durch eine sehr kompakte Bauform charakterisiert. Diese stellt eine bedeutende Herausforderung für eine experimentelle Analyse der zugrunde liegenden Mechanismen dar.

Die Identifikation detaillierter mechanistischer Modelle für Elektrodialyseprozesse kann einen wesentlichen Beitrag zu einem tieferen Verständnis der zugrunde liegenden Transportprozesse und des Prozessverhaltens leisten (Kuppinger et al., 1995). Zielgerichtete Simulationsstudien und Sensitivitätsanalysen ermöglichen die Analyse wichtiger Zusammenhänge zwischen zugrunde liegenden lokalen Phänomenen und dem integralen Prozessverhalten. Darüber hinaus können die identifizierten Modelle als Basis für optimierungsbasierte Ansätze zum Entwurf und zur Steuerung

von Elektrodialyseprozessen genutzt werden.

Bislang verfolgte Ansätze zur Modellierung von ED-Prozessen sind überwiegend durch stark vereinfachende Annahmen gekennzeichnet. So werden in der Regel quasi-stationäre Verhältnisse vorausgesetzt und die Beschreibung von Transportprozessen auf eine örtliche Koordinate beschränkt (Kraaijeveld et al., 1995, Visser, 2001). Insbesondere die Beschränkung auf quasi-stationäre Verhältnisse macht diese Modelle ungeeignet zur Beschreibung transienter Elektrodialyseprozesse. Ein umfassendes Prozessmodell, welches über eine rigorose dynamische Beschreibung der zugrunde liegenden Transportprozesse insbesondere das dynamische Prozessverhalten akkurat beschreiben kann, ist nicht verfügbar.

In dieser Arbeit wird ein integrierter modellbasierter und experimenteller Ansatz verfolgt, um einen Zugang zu einem tiefgreifenden Verständnis der zugrunde liegenden Transportprozesse in transienten ED-Prozessen zu eröffnen. Ein wesentliches Ergebnis ist hierbei die Entwicklung eines mechanistischen Prozessmodells für transiente ED-Systeme. Hierbei wird die bisherige Einschränkung auf pseudo-stationäres Verhalten durch die Ausarbeitung einer adäquaten dynamischen Beschreibung der zugrunde liegenden Transportprozesse überwunden. Darüber hinaus wird die eindimensionale Beschreibung der Transportprozesse durch das Zugrundelegen einer mehrdimensionalen Beschreibung des Stofftransports verallgemeinert. Damit wird es erstmalig möglich, transiente Elektrodialyseprozesse mit einem dynamischen mechanistischen Prozessmodell zu beschreiben.

Um der Komplexität des Prozesses und der zugrunde liegenden Phänomene Rechnung zu tragen, werden wesentliche Voraussetzungen für die Entwicklung des generalisierten Prozessmodells systematisch erarbeitet. Hierbei werden zunächst in einer experimentellen Analyse mit einer transient betriebenen Elektrodialyseanlage die wesentlichen Merkmale des dynamischen Prozessverhaltens ermittelt. Dabei werden erstmalig auch die Sensitivitäten des dynamischen Prozessverhaltens im Hinblick auf wesentliche Steuer- und Auslegungsgrößen des Prozesses systematisch analysiert.

Eine weitere zentrale Voraussetzung für eine erfolgreiche Modellentwicklung ist eine verlässliche mathematische Charakterisierung sämtlicher Modellteile und des finalen generalisierten Prozessmodells. Eine besondere Rolle nehmen hierbei die verwendeten Stofftransportmodelle ein, da sie im Wesentlichen die Komplexität des Gesamtmodells bestimmen. Hierbei ist zu berücksichtigen, dass die Charakterisierung der in bisherigen Arbeiten verwendeten stark vereinfachten Stofftransportmodelle aufgrund ihrer einfachen Struktur keine besondere Herausforderung darstellt. Der Charakterisierung der in dieser Arbeit zugrunde gelegten detaillierten Stofftransportmodelle in Form von Systemen partieller differential-algebraischer Gleichungen (PDAE) muss jedoch besondere Beachtung geschenkt werden (Martinson and Barton, 2001a, Neumann and Pantelides, 2008). Vor diesem Hintergrund besteht ein wesentlicher Beitrag in der Entwicklung einer neuen Methode zur Charakterisierung und Reformulierung allgemeiner PDAE Systeme. Die Grundlage bildet dabei das Konzept der Analyse und Reduktion der differentiellen Indices von PDAE Systemen.

Die neue Methode zur Charakterisierung und Reformulierung von PDAE Systemen bildet die Grundlage für die Entwicklung detaillierter Modelle zur dynamischen Beschreibung der lokalen Stofftransportprozesse. Das Ziel ist hierbei, Modelle zu erhalten, die zum einen durch einen

hohen Detaillierungsgrad charakterisiert sind und sich zum anderen durch einen strukturellen Aufbau auszeichnen, der für allgemeine numerische Verfahren geeignet ist. Hierdurch können die Stofftransportmodelle effizient für die Entwicklung des generalisierten Prozessmodells genutzt werden.

Ein Schwerpunkt der Entwicklung des finalen generalisierten Prozessmodells ist die Integration verschiedener Teilmodelle in einer geeigneten hierarchischen Modellstruktur. Eine wichtige Maßgabe ist hierbei, dass verschiedene Prozesskonfigurationen effizient abgebildet werden können. Dies ermöglicht im Rahmen dieser Arbeit einen ersten Vergleich mit Daten aus unterschiedlichen Experimenten. Hierbei kann gezeigt werden, dass das entwickelte Modell insbesondere das transiente Betriebsverhalten qualitativ gut abbilden kann. Eine systematische Analyse der Modellprädiktion für unterschiedliche Betriebsmoden zeigt zudem, dass das Modell wichtige Zusammenhänge zwischen integralem Prozessverhalten und zugrunde liegenden Transportprozessen aufzeigen kann.

Abschließend werden die im Prozessmodell zugrunde gelegten Transportmodelle vor dem Hintergrund einer weiteren Erhöhung des Detaillierungsgrades betrachtet. Hierbei wird das Ziel verfolgt, langfristig die rigorose Beschreibung des Stofftransports mit einer detaillierten dreidimensionalen Beschreibung der Hydrodynamik zu koppeln. Dafür wird derzeit in einem interdisziplinären Forschungsvorhaben ein effizientes Softwaretool zur numerischen Behandlung der hochgradig detaillierten Modelle auf Höchstleistungsrechnern entwickelt. Weit vorangeschritten ist hierbei die Entwicklung eines Tools zur numerischen Strömungssimulation auf der Basis des Lattice-Boltzmann-Ansatzes. Dies ermöglicht insbesondere eine Betrachtung der Einflüsse geometrischer Auslegungsgrößen auf die Prozesseffizienz. Die quantitativen Beziehungen zwischen Kenngrößen der Prozesseffizienz und der Vielzahl von Auslegungsgrößen können effizient in einfachen algebraischen Modellen abgebildet werden. Für die Identifikation solcher Modelle aus den detaillierten Simulationsergebnissen wird im Rahmen dieser Arbeit ein systematischer Arbeitsprozess entwickelt. Dieser auf optimierungsbasierten Methoden beruhende Ansatz wird am Beispiel der Identifikation algebraischer Druckverlustmodelle aus detaillierten Simulationsergebnissen demonstriert.

Mit dem hier verfolgten integrierten Ansatz einer modellbasierten und experimentellen Analyse wird ein wesentlicher Beitrag zu einem besseren Verständnis transient betriebener Elektrodialyseprozesse geleistet. Insbesondere das entwickelte dynamische Prozessmodell auf der Basis detaillierter mehrdimensionaler Transportmodelle ermöglicht es, das experimentell gemessene integrale transiente Prozessverhalten systematisch zu analysieren. Durch den Einsatz vorwiegend rigoroser Modelle und universeller Paradigmen der Modellbildung sind die Ergebnisse dieser Arbeit in einem weiten Rahmen übertragbar auf ähnliche elektrochemische Prozesse wie Brennstoffzellen oder Batterien. Darüber hinaus sind die entwickelten Methoden zur Analyse und Reformulierung von PDAE-Systemen sowie zur effizienten Identifikation algebraischer Modelle aus detaillierten Simulationsergebnissen auch außerhalb des Anwendungsfeldes von Elektromenbranverfahren nutzbar.

1 Introduction

This thesis is concerned with the integration of a model-based and experimental analysis for the systematic investigation of transport phenomena in transient electrodialysis (ED) processes. In this context this work addresses the development of detailed mechanistic models, the analysis of the dynamic process behavior in transient experiments, as well as the efficient integration of model-based and experimental techniques. As these fields are rather broad, this chapter is devoted to thoroughly introducing the scope of this thesis on the basis of a sound introduction of important fundamentals and existing limitations in the distinct fields. First, the fundamentals of ED and the underlying principles are introduced in Section 1.1. On this basis the dependence of process performance on ionic transport phenomena occurring in ED systems is discussed in Section 1.2. In Section 1.3 existing modeling approaches are reviewed in the context of current limitations of process insight specifically concerning the transient process behavior of ED processes. Based on this review and the identified shortcomings the scope of this work is presented in Section 1.4.

1.1 Fundamentals of electrodialysis processes

Electrodialysis (ED) is an electro-membrane process applied in large-scale industrial applications for the desalination of saline water (Valero and Arbós, 2010), the concentration of organic or anorganic acids (Baltazar et al., 1992, Huang et al., 2007) and the demineralization of food products (Strathmann, 2010). Here, ED allows the separation of salts, acids and their corresponding dissociated ionic species from a typically aqueous solvent. This separation is achieved in competing processes as multi-effect distillation or reversed osmosis by a removal of a nearly pure stream of solvent from the electrolyte solution. In contrast to this, the separation in ED is a result of a charge-specific transport of ionic species.

The transport of ionic species is induced in ED systems by a couple of working electrodes applying an electric potential gradient. This gradient constitutes a driving force for the transport of anions towards the positively charged anode and cations towards the negatively charged cathode, respectively. A locally charge-selective transport of ions is realized by exploiting the selective properties of ion-exchange membranes (IEM). These IEM are configured either as cation exchange membranes (CEM) or anion exchange membranes (AEM) allowing for a charge-selective transport for cations and anions, respectively.

By arranging AEM and CEM membranes in an alternating manner between the anode and the cathode as shown in Fig. 1.1, the concentration and dilution of ions occurs in neighboring flow channels. The neighboring concentrate and diluate flow channels and the corresponding

membrane pair constitutes the smallest functional unit in the ED system, which is referred to as electrodialytic cell. In industrial applications up to 200 cells and a single couple of working electrodes are integrated in a compact module (Strathmann, 2004).

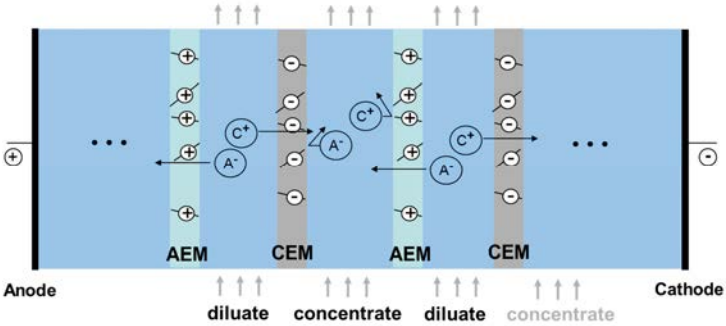

Figure 1.1: Schematic principle of the electrodialysis process for the concentration of a salt AC by a charge selective transport of cations C^+ and anions A^-.

ED processes are operated either in stationary or batch mode. In stationary mode the ED module is supplied with feed electrolyte of constant concentration yielding a corresponding constant product concentration in the concentrate and diluate streams. The structure of an ED process operated in batch mode is sketched in Fig. 1.2. Here, the processed electrolyte solution is initially fed to storage tanks of the concentrate and diluate cycle. From the storage tanks the electrolyte solution is pumped through the electrodialysis module, where the ion concentration in the concentrate cycle increases while it decreases in the diluate cycle in a transient manner. When leaving the module, the solutions are recycled to the corresponding storage tanks until the desired product quality, i.e., a specific diluate or concentrate concentration, is obtained.

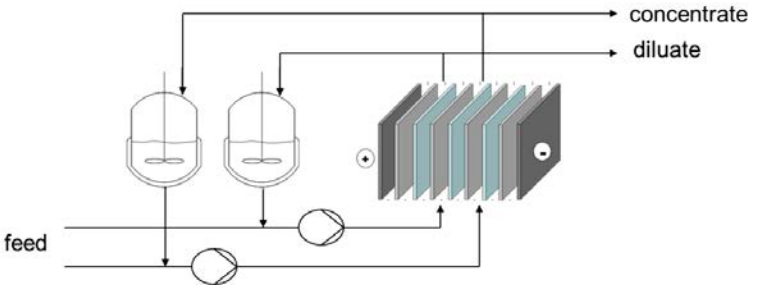

Figure 1.2: Scheme of a typical ED batch process.

The performance of industrial ED plants is governed by the intensity of the underlying transport processes occurring in the membrane module. Here, the transport is to be considered in both the

electrolyte solution in the flow channels and the polymeric material of the IEM. The characteristics of transport phenomena in these process components are introduced in Sections 1.1.1 and 1.1.2. In addition, transport phenomena are to be considered arising at the interface of electrolyte and membrane. An introduction to these secondary transport effects is given in Section 1.1.3.

1.1.1 Ion exchange membranes

The charge-selective transport properties of polymeric IEM result from charged functional groups incorporated in the membrane material. An IEM with positively or negatively charged functional groups excludes cations or anions by electrostatic effects, respectively. Accordingly, the transport of the excluded ions (referred to as co-ions) through the membrane is hindered and the transport of electric current is dominated by ions with an opposite charge (referred to as counter-ions). The degree of co-ion exclusion governs the perm-selectivity of the IEM, which is an important integral membrane property. A second membrane property having a large influence on the total process performance is its electric resistance. It characterizes the voltage drop associated with the charge transport through the membrane. Both properties strongly depend on the meso- and microscopic morphology of the membrane material (Sata, 2004).

The morphology of macroscopically homogenous IEM is characterized by the material properties of the functionalized polymeric material. In most commercially available IEM a perfluorinated unpolar polymer is used as a matrix in which acidic or caustic functional groups are incorporated (Goering et al., 1998). Due to the hydrophilic properties of the functional groups and the hydrophobic properties of the polymer matrix, a heterogenous nanostructured morphology is obtained. This structure consists of an amorphous polymer phase with micro-crystalline inclusions formed by highly crosslinked unpolar polymer chains. In the amorphous regions the functional groups are arranged in the form of clusters with a diameter of $2-4$ nm connected by nano-channels with a diameter of about 1 nm (Freger et al., 1999). Within the network of clusters and nano-channels ions and uncharged solvents are transported across the membrane.

The identification of the transport mechanisms in IEM has been in the focus of recent research. However, the mechanisms are far from being understood. A major difficulty in the experimental investigation of integral membrane properties is to distinguish the phenomena occurring in the membrane from those occurring in the adjacent electrolyte solution (Długołęcki et al., 2010). Galama et al. (2014) emphasize the strong dependence of both the membrane resistance and selectivity on the concentration of the external electrolyte solution. In multi-salt systems this concentration dependence is even more pronounced as competing counter-ions are transported trough the IEM (Martí-Calatayud et al., 2014).

1.1.2 Spacer-filled flow channels

The flow channels between the IEM are commonly filled by structural components called spacers. Spacers commonly used in industrial applications are characterized by a planar net-like structure assembled from polymeric filaments. These filaments are typically arranged in a woven or non-

woven manner as shown in Figure 1.3. The main functionality of the spacers is the separation of adjacent membranes. However, the spacer geometry also governs the local hydrodynamic conditions in the flow channels. By this means the spacer also strongly affects (i) the pressure-drop in the perfusing electrolyte, (ii) the shear stress rate at the membrane surfaces and (iii) the local mass transport intensity.

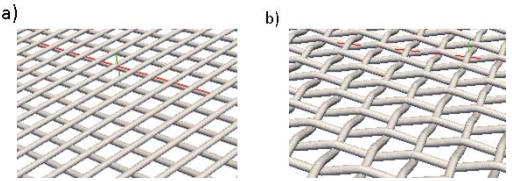

Figure 1.3: Commonly used a) non-woven and b) woven spacer geometries.

In ED the pressure-drop is directly proportional to the energy demand of the pumps (Strathmann, 2004), which contributes to the operational costs of the process (Melin and Rautenbach, 2004). The wall shear stress rate at the membrane surface has an important influence on the formation of scaling and fouling. Fouling is understood as the attachment of macro-molecules, particles or biofilms at the membrane surface (Fritzmann, 2012). Scaling denotes the formation of solid salt deposits at the membrane surface if the solubility of the solution is (locally) exceeded. Both fouling and scaling affect the transport trough the membranes and the pressure drop in the flow channels. By this means, both phenomena strongly influence the overall process efficiency.

The local mass transport intensity is affected by hydrodynamic conditions giving rise to the formation of steady or turbulent vortices. These vortices induce a lateral mixing enhancing the local mass transfer intensity by reducing concentration polarization effects (Fimbres-Weihs and Wiley, 2007, Koutsou et al., 2004). Concentration polarization denotes the local enrichment or depletion of solutes adjacent to the membranes. A local enrichment arises in the concentrate flow channels adjacent to the membrane surfaces as a consequence of the species fluxes entering through the IEM. In an analogous manner, depletion of ionic species occurs close to the membrane surfaces in the diluate channels as a consequence of the species fluxes leaving the channel.

1.1.3 Secondary transport effects

The transport phenomena in the IEM and flow channels are commonly investigated in specific scenarios aiming at the isolated analysis of a specific effect. However, the reliable experimental assessment of a single effect in the membrane-electrolyte system is difficult and recent findings emphasize the strong interaction of the phenomena in the different phases. One specific form of these interactions are secondary transport mechanisms.

Secondary transport mechanisms arise in the form of gravitational convection, coriolis effects and electroconvection (Balster et al., 2007) at the membrane-electrolyte interphase. Rubinstein and Zaltzman (2000) have shown that electroconvection is likely to induce stable vortices in the

vicinity of the membrane surfaces if a certain current density is exceeded. The formation and size of these electroconvective vortices strongly depends on both the structure of the membrane surface and the total flow of ions through the membranes (Nikonenko et al., 2010). The fact that secondary transport effects can have a significant effect on the transport in the membrane-electrolyte system has been shown by Urtenov et al. (2013) and van Pham et al. (2012).

However, the interaction of these phenomena with the primary transport mechanisms – convection, diffusion and migration – dominating the transport in the membrane phase and the bulk solution of the flow channels is little understood (Nikonenko et al., 2010). In addition, the occurrence of secondary transport mechanisms complicates the commonly aspired assignment of transport resistances to the IEM, flow channels and the membrane-electrolyte interphases (Dlugolecki, 2009).

1.2 Ionic mass transport and process performance

The intensification of the local ionic mass transport by revising the geometry of the spacers is an important aspect for the improvement of the process performance in ED applications and has thus been addressed in numerous model-based and experimental studies. A brief overview of studies in this field is given in Section 1.2.1. Next to the local hydrodynamic conditions, concentration polarization, fouling and scaling depends on the net transport of solutes or particles towards the membranes. These fluxes are governed by the main driving force of the process, which is the current or potential difference applied to the working electrodes. Hence, the operational mode of the working electrodes provides an additional possibility for the reduction of these undesired effects. In this context, the transient operation of ED processes offers a promising option to improve process performance (cf. Section 1.2.2).

1.2.1 Module and spacer design

Significant effort has been directed at investigating the effect of module and spacer design on concentration polarization and fouling (e.g., Da Costa et al. (1994), Fárková (1991), Sonin and Isaacson (1974)). The focus of these studies has been on the complex hydrodynamics in spacer-filled flow channels as well as on the local mass transport intensities. The quantitative effect of important design parameters on the design objectives, i.e., on pressure drop, shear-stress pattern and mass-transport efficiency, has been investigated by various authors (Chaumeil and Crapper, 2013, Koutsou et al., 2007, Li et al., 2002, Shakaib et al., 2009).

All studies emphasize the strong sensitivity of the design objectives with respect to the design parameters. Most of them vary one parameter and fix all the others to nominal values to identify trends between design parameters and objectives. However, in such an approach the resulting insight is limited to a small section of the multi-dimensional space spanned by the design parameters. The systematic evaluation of the large space spanned by the design parameters can be considered as a major challenge in spacer design.

1.2.2 Transient electrodialysis processes

A first important process operated in a transient mode is the ED reversal (EDR) process. EDR is characterized by a periodic reversal of the polarity of the working electrodes. The resulting inversion of the ionic species fluxes in the membrane-electrolyte system results in a (partial) removal of both concentration polarization and fouling layers (Valero and Arbós, 2010). To reduce the loss of product resulting from the inversion of the species fluxes, the transition in the polarity is synchronized with an inversion of the hydraulic concentrate and diluate streams entering and leaving the flow channels. Especially for the prevention of both colloidal fouling and scaling, EDR has become the state of the art technique in ED water desalination systems (Strathmann, 2010).

A second process concept characterized by a transient operational mode is pulsed ED. Here, the working electrodes are supplied with a pulsed electric current varying with a pulse length of milliseconds to minutes between zero and a nominal potential value. A major advantage of pulsed ED in comparison to EDR are the lower investment costs as the distribution system of the module allowing for the inversion of the concentrate and diluate streams is not required. Some authors reported a significant reduction of both fouling and scaling (e.g., Casademont et al. (2009), Gurtler et al. (2008), Mikhaylin et al. (2014), Ruiz et al. (2007)) for pulsed ED compared to processes operated with a constant current. Further, Malek et al. (2013) found a reduction of concentration polarization effects in experiments for the electrodialytic desalination of NaCl solutions. To what extent this reduction affects the energy consumption of the process is still not clear. Whereas Malek et al. (2013) found no improvement by using a pulsed applied current, Ruiz et al. (2007) and Mishchuk et al. (2001a) found a positive effect for this operational mode. This disagreement comes along with a significant lack of insight concerning the effect of the pulsed operations on the underlying transport mechanisms.

As no experimental assessment of the local phenomena is possible, the experimental findings are commonly interpreted with vague theoretical hypotheses. Malek et al. (2013) associate the observed dynamic process behavior solely to isolated polarization phenomena occurring in the flow channels. A sound analysis of the observed dynamic behavior also including dynamic effects in the IEM and at the membrane-electrolyte interphase is not available. This lack of insight into the mechanisms governing the performance of transient ED processes comes along with a very restricted knowledge concerning the dynamic behavior of the ionic transport in ED systems. It is in particular widely unknown in which way the integral transient behavior of ED systems results from the transport occurring in the IEM, the electrolyte solution or the membrane-electrolyte interface. To thoroughly identify these individual contributions in the absence of local in-situ measurements, a valuable tool can be provided in the form of predictive models describing the dynamic behavior of transient ED processes.

1.3 Modeling ionic mass transport and electrodialysis processes

As illustrated in Sections 1.1 and 1.2, ED is governed by transport processes where the interactions of electric field, convective and diffusive transport as well as the strongly non-ideal thermodynamics are complex and have a decisive impact. The phenomena arise in coupled phases, i.e., flow channel and the membranes, and on different spatial and temporal scales placing severe constraints on an effective experimental analysis. Hence, modeling and simulation are important and well accepted tools in the analysis and design of ED processes (Nikonenko et al., 2010, Strathmann, 2010).

However, the complexity of the large number of distinct phenomena and their strong interactions also complicates the development of physically consistent models for ED systems. A rigorous model allowing the integrated description of all relevant phenomena and transport processes with an adequate temporal and spatial resolution is not available. To reduce both the complexity in the model development and the computational effort in simulation studies, two distinct strategies can be identified in current literature. The first approach results in a reduction of model complexity by focusing on a single isolated phenomenon in a specific scenario. Here, particular examples are the investigation of the transport in a single spacer-filled channel by computational fluid dynamics (CFD) simulations and the model-based analysis of the transport in a single IEM. A brief overview of relevant works is given in Sections 1.3.1 and 1.3.2. In the second approach, the description of the coupled phenomena is strongly simplified to allow for an integral description of the entire process in a process model (cf. Section 1.3.3).

1.3.1 Investigation of spacers by CFD methods

A particularly well-studied field in the context of a model-based analysis of ED processes is the analysis of the hydrodynamics in a single spacer-filled channel using computational fluid dynamics (CFD) techniques (e.g., Fimbres-Weihs (2008), Koutsou et al. (2007), Schock and Miquel (1987)). An excellent review is provided by Fritzmann (2012). The focus of the majority of CFD studies (Cao, 2001, Fimbres-Weihs and Wiley, 2007, Koutsou et al., 2004, Schwinge et al., 2002; 2004) has been directed at a qualitative description of the flow fields arising in different Reynolds regimes.

In more detailed studies, the simulation of the hydrodynamics in the channel is extended to include additional physical principles. The simulation of the diffusive and convective mass transport of infinitely diluted solutes is included in few simulation studies (Fimbres-Weihs and Wiley, 2007, Fritzmann, 2012, Koutsou et al., 2009). Picioreanu et al. (2009) and Radu et al. (2010) use coupled simulations of hydrodynamics and biofilm growth in the channel to study the formation of fouling. Similar studies, focusing on particulate fouling, have been reported by Chaumeil and Crapper (2013) and Li et al. (2012).

The evaluation of the simulated pressure drop and mass transport rates is commonly assisted by simple algebraic models (Fimbres-Weihs and Wiley, 2007, Isaacson and Sonin, 1976, Koutsou et al., 2009). These models correspond to power laws relating well-known dimensionless quantities such as friction factors, Reynolds, Sherwood and Schmidt numbers by empirical parameters. The

comparison of these empirical parameters for different spacer geometries allows for a resonable evaluation of the geometries in the entire range of Reynolds or Schmidt numbers. However, an important limitation of the models for the prediction of pressure drop and mass transport rates is their restriction to a fixed spacer geometry. A general model for the prediction of the pressure drop or mass transfer rate for a wide range of design parameters is still missing (Fritzmann, 2012).

1.3.2 Modeling of ion exchange membranes

The model-based analysis of transport processes in IEM is investigated in current literature with a widely varying level of detail. Molecular dynamic simulations were used, e.g., by Brandell et al. (2007), Kotelyanskii et al. (1999) and Karo et al. (2010) to investigate the interaction of the membrane material and perfusing solutes. Psaltis and Farrell (2011) applied molecular dynamic methods in order to determine diffusion coefficients in a coupled simulation with a model describing the transport of solutes on a macroscopic level. Model-based studies investigating the effect of the meso- and microscopic morphology on the transport of solutes were conducted by Weber and Newman (2004) and Elliott et al. (2011).

Models describing the charge-selective transport in the IEM not explicitly accounting for the nanostructured morphology of the membrane material were proposed, e.g., by Nikonenko et al. (2009), Ramírez (2001), Weber and Delacourt (2008), Weber and Newman (2003) and Hogendoorn et al. (2001). Macroscopic transport models specifically focusing on the dynamic behavior of an IEM were presented by Moya and Horno (1999) and Moya and Sistat (2013). All these models employ a solution-diffusion approach based on the assumption of a pseudo-homogenous membrane phase. Effects resulting from the micro- or nanostructure of the polymeric membrane material are incorporated by means of effective diffusion coefficients and effective thermodynamic states. The charged polymeric membrane material is considered as an additional species in the electrolyte system.

In addition to these transport models, numerous authors presented models for the description of the phase equilibrium between IEM and adjacent electrolyte solution (Shiryaeva and Victorov, 2001, van der Stegen, J.H.G. et al., 1999) and the associated membrane swelling (Okeowo and Dorgan, 2006, Saarinen et al., 2007). For the evaluation of impedance spectroscopic measurements, the membrane and the adjacent electrolyte solution are commonly modeled by equivalent electric circuits (cf. e.g. Dlugolecki (2009) and Freger and Bason (2007)). A common problem in the evaluation of an isolated IEM model with experimental data results from the interaction of the transport in the membrane with polarization phenomena occurring in the adjacent electrolyte solution (cf. Section 1.1.1).

1.3.3 Electrodialysis process modeling

Within the last decades, significant attention has been paid to the modeling of entire ED processes. Empiric data-driven models in the form of surface response models (Wang et al., 2010, Zhang et al., 2008), neural networks (Jing et al., 2012, Sadrzadeh et al., 2009) or a fuzzy-logic (Borges

et al., 2009) have been proposed to model the input-output behavior without any resolution of the phenomena inside the process. Model formulations relying on the simplified description of the concentration distribution in a single representative flow channel have been proposed e.g. by Kuppinger et al. (1995), Lee et al. (2002), Ortiz et al. (2005), Yu and Admassu (2000) and Strathmann (2004). In these models, integral properties of the membranes, such as the selectivity or the electric resistance, are described by simple empirical correlations. In the case of a dynamic batch process, the model for the representative flow channel is commonly replaced by an ideally stirred tank model (cf. e.g. Fidaleo and Moresi (2005; 2010), Kaláb and Palatý (2012)).

Structured process models have been proposed for electrodialysis by Kraaijeveld et al. (1995), Kuppinger (1997), Neubrand (1999), Rype (2002) and Visser (2001) and for a strongly related process by Prado-Rubio (2010). These models are based on an either mechanistic or empiric description of all important process components, i.e., electrodes, spacer-filled flow channels and IEM. This allows to establish a sound relation between the phenomena in the distinct process components and the integral process behavior. This fact is a major advantage of the structured process models over the empiric formulations when a model-based analysis is targeted. However, in particular when a rigorous mechanistic description of phenomena in the membranes and flow channels is addressed, the development of structured process models is significantly more involved. Hence, the development of structured process models is commonly associated with the introduction of distinct simplifying assumptions.

A common simplification used in structured process models is the approximation of the complex hydrodynamics in the flow channels by the film-theory approach. Accordingly, the channels are segmented into a bulk phase and two polarization films adjacent to the membranes. This segmentation reduces the complexity of the modeling problem significantly as it circumvents a local resolution of the complex spacer geometry. Further, it facilitates the description of the hydrodynamics with strongly simplifying assumptions. The bulk phase is commonly described with a one-dimensional model using a plug flow assumption (Neubrand, 1999) or even an ideally mixed volume which is not resolved spatially at all (Kraaijeveld et al., 1995, Visser, 2001). In the polarization films convective transport is commonly neglected resulting in a one-dimensional diffusion problem in a stagnant electrolyte solution. As a result, the major effort in the modeling of the spacer-filled flow channels is associated with the description of the diffusive transport in the liquid electrolyte phase.

The transport in the IEM is described in the structured models by using the assumption of a pseudo-homogenous membrane phase (cf. Section 1.3.2) in which transport occurs only in the direction orthogonally to the working electrodes. This way, the description of the transport in the IEM also reduces to a one-dimensional diffusion problem in a homogenous electrolyte phase. Correspondingly, the central element of structured ED process models is the description of the transport of ionic species in a homogenous phase corresponding to either the ion exchange membranes or the electrolyte solution in the flow channels.

1.3.4 Modeling ionic mass-transport in a homogenous phase

The fundamentals of ionic mass transfer are well described in a number of monographs (Bird et al., 2002, Kontturi et al., 2008, Newman and Thomas-Alyea, 2004, Rubinstein, 1990). In general, the established concepts for the transport of uncharged species can be generalized to ionic mass transport problems in a straightforward manner. However, with the emerging electric charges associated with ionic species, additional physical principles need to be accounted for in constitutive equations and physico-chemical property models (Chen et al., 1982, Newman and Thomas-Alyea, 2004). To describe the propagation of electric fields, supplementary equations have to be incorporated in the model formulation such as the well-known electroneutrality condition (Kontturi et al., 2008). In particular, these additional relations and the resulting strong coupling of mass and charge transport seriously complicate the development of physically consistent models.

Due to this increased model complexity, models that are developed in an unstructured approach and on a rough theoretical basis easily fail to fulfill important physical consistency requirements such as the conservation of species masses or electric current. Further, the physical interpretation of the model and the corresponding simulation results is often difficult, as important model properties are not explicitly depicted in the model structure. An important example is the electroneutrality equation implicitly describing the propagation of the electric potential without accounting for it in its model structure (Feldberg, 2000).

A common approach to reducing the complexity of ionic transport models is either (i) to limit the amount of physical phenomena depicted in the model by considering specific simplified scenarios or (ii) to severely restrict the geometric extension of the modeled physical system. A particular example in the context of ED processes for the first class of simplifications is the ionic mass transport model proposed by Neubrand (1999). The model is based on the well-known Nernst-Planck approach for infinitesimally diluted electrolyte solutions and accordingly is not applicable to electrolyte solutions with concentrations typically encountered in industrial applications. An example of the second class of simplifications is the transport model proposed by Kraaijeveld et al. (1995) and Visser (2001). The model is based on the rigorous Maxwell-Stefan approach and includes detailed models for important thermodynamic properties. However, the description of the transport processes is restricted to one spatial coordinate and all storage terms are neglected, which results in a quasi-stationary model formulation.

As a first important step to overcome this unsatisfactory situation, Kakhu and Pantelides (2003) proposed a systematic methodology for the development of dynamic models for electrolyte systems with multiple phases and an arbitrary number of species. Their approach combines model development with a detailed analysis of important mathematical model properties. This way, it strongly supports both the formulation of a physically consistent model and the subsequent numerical treatment of the dynamic model with generic methods. However, a major limitation of the method is its restriction to concentrated systems, i.e., to systems in which the physical phenomena are not spatially resolved. Hence, the methodology is not suitable for mass transport problems. A methodology based on network theory that is applicable to distributed systems has

been proposed by Hanke-Rauschenbach (2007). However, the methodology is strongly tailored to proton exchange membrane fuel-cells and does not address liquid electrolyte solutions with multiple ionic species.

1.4 Conclusions and scope of this work

The discussion in this chapter has shown that the efficiency of the ED process is determined by the intensity of the ionic mass transport in the electrolyte-membrane system. The underlying mechanisms of this transport are not entirely understood although the process has been established in industry for several decades (Newman and Thomas-Alyea, 2004, Strathmann, 2010). The strong coupling of the different physico-chemical phenomena and the usually very compact design of electrodialysis stacks represent large challenges for an experimental in-situ observation of the local transport phenomena. This results in a severe lack of process insight, especially if multi-species electrolytes such as seawater are processed (Strathmann, 2010).

Specific effects strongly limiting the performance of ED processes are fouling, scaling or concentration polarization (cf. Section 1.1.2). A successful strategy to reduce the influence of these effects on the process performance is the operation of the ED process in a transient mode (cf. Section 1.2.2). However, in particular the dynamic process behavior and the dynamics of the local transport mechanisms are poorly understood. A second strategy to limit the impact of these effects on the process performance is the improvement of the spacer and module design (cf. Section 1.2.1). However, in such a design approach a large number of design parameters need to be considered which poses hard constraints on purely experimental design studies.

The identification of rigorous mechanistic models for ED processes can contribute to overcoming this unsatisfactory situation. Dedicated simulation studies and sensitivity analyses reveal profound insight into both the dynamic process behavior and the underlying mechanisms. Further, predictive models constitute the basis for model-based approaches addressing the optimal design and control of ED processes. However, a large number of models has been developed for the investigation of isolated phenomena in the flow channels or the IEM only (cf. Sections 1.3.1 and 1.3.2). The insight obtained by these isolated models is limited as it is commonly difficult to relate the behavior of the isolated phenomena to the behavior of the entire process. Further, as shown in Section 1.1.3, recent findings emphasize the importance of transport mechanisms arising from the interaction of phenomena occurring at the interphase between the membranes and electrolyte phases. Models for the isolated description of transport phenomena in the membranes or flow channels cannot assess these important mechanisms.

The drawbacks associated with the isolated models can be overcome by targeting at an integrated description of the integral process behavior and the underlying local mechanism in a structured process model. The development of structured process models has been addressed by a few authors (cf. Section 1.3.3). The process model describing the underlying transport phenomena with the highest level of detail was developed by Kraaijeveld et al. (1995) and Visser (2001). However, even in this model an important limitation results from the one-dimensional,

quasi-stationary description used for the underlying transport processes. Both factors limit the amount of information which can be obtained from the model in particular when describing innovative process configurations operated in a dynamic mode. Further, the missing resolution of the spacer geometry in the film-theory model limits the applicability of the process model in a design process.

The substantial limitations of currently existing process models for ED systems constitute the main motivation of this work. In particular, the limited insight provided by the models concerning the process dynamics and their limited applicability to processes operated in a transient mode motivates the generalization of the commonly used transport models. By this means, one particular objective is the development of a generalized dynamic process model based on a dynamic multi-dimensional description of the underlying mass transport processes.

For the final development of such a dynamic generalized process model in Chapter 5 several important prerequisites are systematically elaborated in the following chapters. To support the modeling process, an experimental analysis with a lab-scale ED plant is conducted in Chapter 2 to yield a first important insight into the dynamic process behavior. This includes, next to the collection of experimental data for the evaluation of the developed model, the identification of the sensitivity of the dynamic process behavior with respect to the numerous operational and design parameters. Further, the study aims at the identification of the temporal scales and the qualitative shape characterizing the dynamic response to a pulsewise increase in the electric field applied by the working electrodes.

Section 1.3.4 discusses the difficulties associated with the development of unsimplified ionic mass transport models which are both physically consistent and allow for a reliable numerical treatment in established modeling environments. To address these issues, the general idea of Kakhu and Pantelides (2003) is followed combining the model development with a thorough analysis of important mathematical properties. This approach is of specific relevance since the generalization of the transport models is accompanied by major changes to the mathematical model structure. Whereas the pseudo-stationary one-dimensional formulations used in the models developed by Kraaijeveld et al. (1995) and Visser (2001) correspond to systems of differential-algebraic equations (DAE) in a single independent variable, the generalized models form systems of partial differential-algebraic equations (PDAE) in multiple independent variables. The reliable numerical solution of PDAE systems is significantly more complex and additional issues arise in the consistent specification of initial and boundary conditions. In particular, the latter is known to be non-trivial and is commonly supported by mathematical concepts such as the differential index (Martinson and Barton, 2000, Neumann and Pantelides, 2005). However, systematic procedures integrating these concepts into a general modeling work flow are not yet available. In this context, Chapter 3 is devoted to the development of a new procedure for index analysis and reduction of general PDAE systems in the context of a systematic modeling work flow. The method is introduced for general PDAE systems and illustrated by considering a simplified ionic mass transport model. Readers with a major interest in the modeling and application-oriented results are referred directly to Chapter 4.

The resulting procedure is used in Chapter 4 for the development of the generalized transport models. These models are based on a rigorous description of the diffusive transport phenomena using the Maxwell-Stefan approach. The propagation of the electric field is described by the well-known electroneutrality condition. Significant effort is directed to the reformulation of the resulting transport models to yield PDAE systems suitable for a reliable numerical treatment in commercial modeling environments.

These transport models form the basis for the description of the IEM and the spacer-filled flow channels in the process model developed in Chapter 5. The model development includes the derivation of an appropriate model structure allowing for the description of distinct process configurations. The prediction of the developed model is examined to obtain a first important insight into the underlying phenomena in the membrane-electrolyte system.The reliability of these results is investigated in a comparison with experimental data obtained from the experiments reported in Chapter 2.

Finally, Chapter 6 further extends the scope of the considered transport models with the objective of incorporating a fully three-dimensional description of the hydrodynamics in the spacer-filled flow channels. In this context, first important aspects are addressed contributing to the development of an integrated highly detailed model which incorporates all relevant transport mechanisms as a long-term objective. One central element of such an integrated model is an efficient CFD solver with a high spatio-temporal resolution. For this purpose a novel software tool is currently being developed which is based on the Lattice-Boltzmann Method (LBM) allowing the simulation of the hydrodynamic problem on high performance computers. The tool provides the possibility of assessing the effect of geometrical design parameters of the spacers on important performance measures. The relations between the performance measures and the multiple design parameters obtained from the detailed simulations can be effectively represented in simple algebraic models. The systematic identification of such algebraic models will constitute the focus of this chapter. A systematic work flow for model identification is proposed which is used for the identification of predictive pressure drop models for both non-woven and woven spacer geometries.

This way, this thesis contributes to a model-based analysis of the underlying dynamic transport phenomena in transient ED processes. Further, the development of predictive models can be seen as a first important step towards a model-based optimization of process design and operations. Due to the general modeling approaches and widely accepted paradigms used in this work, the findings can easily be generalized to related electrochemical processes such as fuel cells or batteries. Furthermore, the new method for the analysis and reduction of PDAE systems reported in Chapter 3 supports the development of reliable distributed models for general dynamics systems.

2 Experimental analysis of electrodialysis process dynamics

This chapter investigates the dynamic behavior of ED processes by means of an experimental analysis. The analysis targets to support the model development by revealing the qualitative patterns and the temporal scales governing the dynamic response to transients in the operational mode. The set-up of the lab-scale ED plant and the experimental methods used are introduced in Section 2.1. On this basis, in Section 2.2 the scope of the experimental study is discussed and its relevance for the development of the dynamic process model is illustrated. The dynamic current-voltage behavior of the ED process is addressed in Section 2.3. Section 2.4 introduces the results of an experimental sensitivity analysis with respect to operational and design parameters. Sections 2.5 and 2.6 present the results of desalination experiments operated with transient and pulsed currents, respectively. The focus is here on the identification of the temporal scales and the qualitative patterns of the dynamic response to the discontinuous transitions in the operational controls.

2.1 Experimental set-up and methods

The lab-scale ED plant introduced in Section 2.1.1 is used for both batch desalination and current-voltage experiments. Batch desalination experiments presented in Section 2.1.2 allow the investigation of the process in a realistic application. The current-voltage experiments described in Section 2.1.3 are designed to investigate the current-voltage behavior of the ED module.

2.1.1 Experimental set-up

Experiments are carried out using a lab-scale electrodialysis plant illustrated by a simplified piping and instrumentation diagram in Fig. 2.1. The concentrate, diluate and electrode rinsing solution streams are pumped by centrifugal pumps (IWAKI Co., Japan) from the storage tanks through the membrane module. The plant is equipped with capacitive pressure sensors $PIR1006$, $PIR2006$, $PIR1007$ and $PIR2007$ (Endress+Hauser GmbH, Germany) located in the feed and effluent streams before and after the module. The total volumetric flow rates $Q^{FIRC1002}$ and $Q^{FIRC2002}$ are measured by the turbine flow-meters $FIRC1002$ and $FIRC2002$ (Bio-tech e.K., Germany), respectively. The signals of the flow rate sensors are supplied to a software-based PD-controller controlling the volumetric flow rates $Q^{FIRC1002}$ and $Q^{FIRC2002}$ by acting on the control valves $V1101$ and $V2101$ (ASV Stuebbe GmbH, Germany) in bypass configurations. To operate in EDR

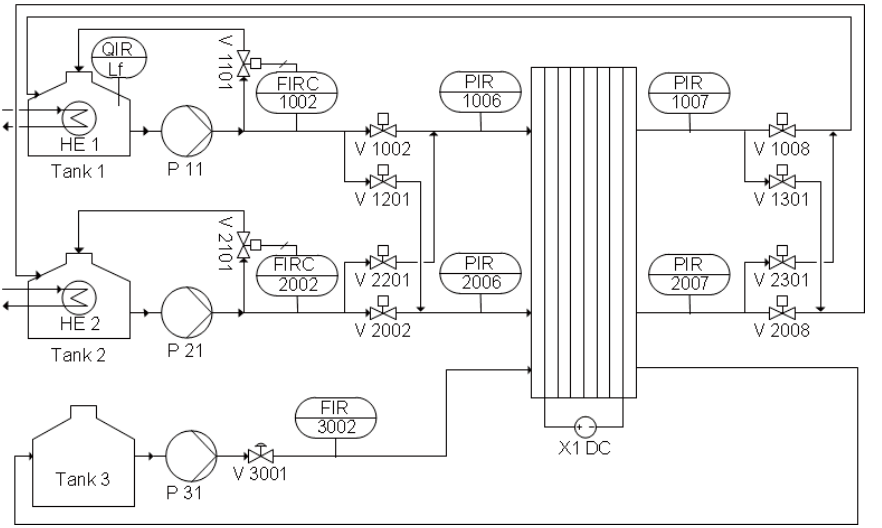

Figure 2.1: Simplified piping and instrumentation diagram of the lab-scale ED plant.

mode, the plant is equipped with a series of magnetic valves (ASV Stuebbe GmbH, Germany) in the feed and effluent streams of the concentrate and diluate, respectively.

The temperature in the tanks is controlled to $25 \pm 1°C$ using the heat exchangers *HE1* and *HE2* and a thermostat (VWR GmbH, Germany). The conductivity in the diluate tank (Tank 1) is measured using an electrode sensor (Meinsberg GmbH, Germany). The working electrodes are connected to a programmable power supply *X1 DC* (Hameg Instruments GmbH, Germany) operating in either amperostatic or galvanostatic mode. Data logging and the software-based control system are realized in LabVIEW (National Instruments, USA). Experiments are conducted using the module ED-200 (PCCELL GmbH, Germany) equipped with 6 to 14 cellpairs and Neosepta CMX and AMX membranes (Tokuyama Co., Japan). The geometric properties of the stack and the used woven spacers are summarized in Tables A.1 and A.2 in Appendix A. In each experiment, the working electrodes are rinsed with $0.5\,\frac{kmol}{m^3}$ Na_2SO_4 solution from Tank 3.

The design of the plant and particularly the development of the software for data logging and control purposes has been opted with regard to model identification and evaluation as the principal objective of the experiments. This includes the dimensioning of actuators, sensors and connection tubes with the objective of obtaining a minimal, in comparison to the volume in the tank and module negligible, volume in these process elements. This is of specific importance, since the modeling of the transport and dispersion processes in these process elements would be very difficult. Data logging is realized in the developed software with a sampling rate of 0.1 to $1\,Hz$ to enable a high resolution of the dynamic phenomena. Further, the software enables

the import of transient input trajectories, e.g., generated from measured sunlight intensities (cf. Sec. 2.5) or from methods for the optimal design of experiments, to operate the plant in a transient mode. This import of transient input trajectories and the automated control system of the plant are essential aspects for execution of the transient experiments in a reproducable manner. An automated export of experimental settings and measurements allows the straight forward comparison between the experiments and simulation results from the developed process model.

2.1.2 Batch desalination experiments

In batch desalination experiments the storage tanks of diluate and concentrate are filled with aqueous electrolyte solution with a specific initial concentration. The volume of the solution in both tanks is adjusted to $17.6 \cdot 10^{-3}\, m^3$. After setting the flow rates and temperature to the nominal values, the system is equilibrated for at least 15 minutes. The experiment begins by starting the power supply with a specific current profile with admissible values in the range of $0 - 3\ A$.

In the course of the desalination experiments the $NaCl$ concentration is determined by the calibrated conductivity measurements in the diluate tanks. For the experiments with $NaCl - Na_2SO_4$ mixtures $5\, ml$ samples are drawn additionally at specific conductivities from the diluate tank for an ex-situ analysis. In this analysis, the concentrations of the different ionic species are determined by ion-chromatography. As a result of the decreasing concentration of ionic species in the diluate cycle the voltage drop over the stack increases in the course of the experiment. The experiments are stopped after the voltage applied to the working electrodes reaches the limit of $20\, V$.

2.1.3 Current-voltage experiments

Current-voltage experiments are carried out to investigate the current-voltage behavior of the stack at constant inlet concentrations in the diluate and concentrate channels. To this end, only the diluate cycle is filled with electrolyte solution with a specific initial concentration. The solution is distributed to both the concentrate and diluate channels by opening the magnetic valves $V1002$ and $V1201$, respectively. After the stack, the solution is recycled to the diluate tank via the valves $V1008$ and $V2301$. The experiment is operated by specific voltage profiles with admissible values in the range of $3 - 20\ V$.

2.1.4 Degrees of freedom, measurements and performance measures

The degrees of freedom of the experimental set-up and the measurements taken are summarized in Fig. 2.2. The developed set-up allows the variation of the spacer type and the number of cells in the ED module n_{cells} as constructional degrees of freedom. The operational degrees of freedom are formed by the volumetric flow rate $Q = Q^{FIRC1002} = Q^{FIRC2002}$, the initial species concentrations in the storage tanks $\mathbf{c}\,(t = 0)$, either the current $I\,(t)$ or voltage difference $U\,(t)$ applied to the

electrodes and, in case of experiments with a pulsed applied current, the interval length of a largely rectangular pulse. The measurements consists of the profiles of species concentrations in the storage tanks $\mathbf{c}(t)$, either the current $I(t)$ or voltage difference $U(t)$ at the electrodes and the pressure drop $\Delta p = p^{PIR1006} - p^{PIR1007}$ over the ED module.

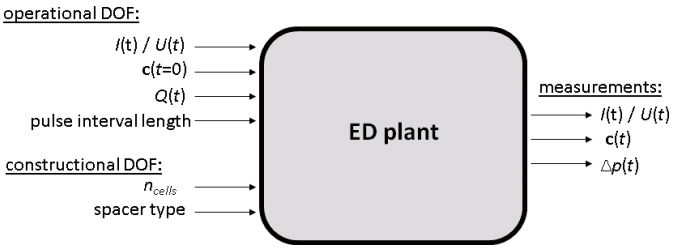

Figure 2.2: Constructional and operational degrees of freedom and measured output in the experiments.

Performance measures of ED batch processes significantly affecting the process cost are the desalination time t^e and the total energy consumption E_t. The latter constitutes the sum of the energy consumption of the electrodes E_e and the pumps E_p, i.e.,

$$E_t = E_e + E_p. \tag{2.1}$$

The energy consumption of the electrodes is determined as

$$E_e = \int_{\tau=0}^{\tau=t^e} U(\tau)\, I(\tau)\, d\tau, \tag{2.2}$$

and the energy consumption of the pumps is given by

$$E_p = \int_{\tau=0}^{\tau=t^e} Q(\tau)\, \Delta p(\tau)\, d\tau. \tag{2.3}$$

2.2 Scope of the experimental study

The experiments carried out in the context of this work are designed to support the development of the dynamic ED process model. As a first objective the experiments are supposed to yield appropriate data for the identification of model structures or parameters and the evaluation of the model accuracy. As a second objective the experimental study is intended to support the model development process by revealing essential process insight. The experiments on their own do not aim at an encompassing investigation of process principles, e.g., the discrimination and quantification of specific mechanisms, as the measurements will not provide any insight into the local phenomena. However, in this context the results of the experimental study will provide

important information, when they are combined with additional experimental or simulated data for quantifying the local phenomena.

A first important aspect of the process insight supporting a systematic model development is information about the sensitivities of the measurements with respect to the degrees of freedom. The sensitivities are important to assess the impact of simplifying assumptions or competing model candidates. Further, the sensitivity information constitutes important benchmarks for the evaluation of the model or model components within the model development process. The large number of operational and design degrees of freedom constitutes a major challenge for a thorough sensitivity analysis. To the author's knowledge no coherent sensitivity analysis has been reported which includes all degrees of freedom. The majority of prior studies focusing on ED or related processes have considered only specific aspects of the process. Particular examples are the investigation of the steady-state current-voltage characteristics (Valerdi-Pérez et al., 2001, Valerdi-Pérez and Ibáñez-Mengual, 2001), the pressure drop in the ED module (Pawlowski et al., 2014) or the competitive transport in multi-species solutions (Kim et al., 2012, Moon et al., 1998) in detailed isolated studies. The experiments conducted in Section 2.4 aim at the development of less detailed, however coherent sensitivity information covering all degrees of freedom.

A second aspect of the required process insight concerns the response of the measured output to dynamic variations of the applied current and voltage, respectively. The temporal scales and the qualitative shape characterizing this dynamic response constitute important information for the evaluation of the model or model components. The response of a single IEM in a dedicated test-cell to dynamic input trajectories has been thoroughly studied, e.g., by Długołęcki et al. (2010), Krol (1999), Wilhelm et al. (2002) or Moya and Sistat (2013). However, the dynamic response of an entire ED process has been rarely investigated. A particular exception is the work of Malek et al. (2013), who investigate the dynamic current-voltage behavior of the electrodialytic desalination of $NaCl$ solution with a pulsed applied voltage. Here a first important insight is found concerning the qualitative shape of the dynamic response. The experiments in Section 2.6 extend their work by analyzing the sensitivity of the dynamic response with respect to the remaining degrees of freedom. Further, Section 2.5 investigates the dynamic response in desalination experiments with more general dynamic input trajectories, e.g., relevant for solar powered ED processes (Li and Zhang, 2009).

The lack of information concerning the sensitivities and the dynamic response is even more significant for ED plants processing multi-salt solutions as the majority of studies focusing on ED restrict their considerations to $NaCl$ solutions. However, it is well known that the behavior of ED systems processing multi-salt solutions such as sea or brackish water can differ substantially (Post et al., 2009, Strathmann, 2010). Further, it has been found that the selectivity of the transport processes in the membrane-electrolyte system for specific ionic species can be strongly influenced by the application of a pulsed applied current (Gurtler et al., 2008, Mishchuk et al., 2001b). To this end, the experimental study in this chapter includes, in addition to numerous experiments with $NaCl$ solutions, experiments with $NaCl$-Na_2SO_4 solutions. Next to the identification of the sensitivities and the characterization of the dynamic response, an additional objective is here

to quantify the competing transport of the Cl^- and SO_4^{2-} anions. This information is relevant for the selection of an adequate transport model to describe ED processes for the desalination of multi-salt mixtures.

To relate the gained process insight to industrial processes, the sensitivity analysis and a thorough evaluation of the dynamically operated experiments will include the evaluation of the performance measures of the process. In this context, the experimental study contributes to the question whether a transient or pulsed operation can affect the performance of ED processes positively. Further, the analysis of the experimental study includes the assessment of the amount of information in the measurements. In this context, it is evaluated in which way a detailed dynamic model can contribute to investigating open questions concerning ED processes.

2.3 Current-voltage behavior

Current-voltage experiments are carried out to investigate the dynamic response of the electric current to a stepwise increase of the applied voltage. In these experiments, the plant is operated with $NaCl$ solutions with concentrations of either $c_{NaCl} = 192\,\frac{mol}{m^3}$, $c_{NaCl} = 96\,\frac{mol}{m^3}$ or $c_{NaCl} = 48\,\frac{mol}{m^3}$. For each concentration two experiments are carried out with volumetric flow rates $Q_{high} = 2.5 \cdot 10^{-5}\,\frac{m^3}{s}$ and $Q_{low} = 0.83 \cdot 10^{-5}\,\frac{m^3}{s}$, respectively. Details concerning the module configuration and the remaining operational parameters in these experiments are summarized in Table A.7, Exp. 1-6. The repeatability [1] of the experiments and the expected measurement error is discussed in Appendix A.2.3. The electric potential difference over the stack is increased stepwise from initially $3\,V$ by an increment of $0.5\,V$ every $60s$. The resulting profile of the applied potential difference is shown in Fig. 2.3 a.

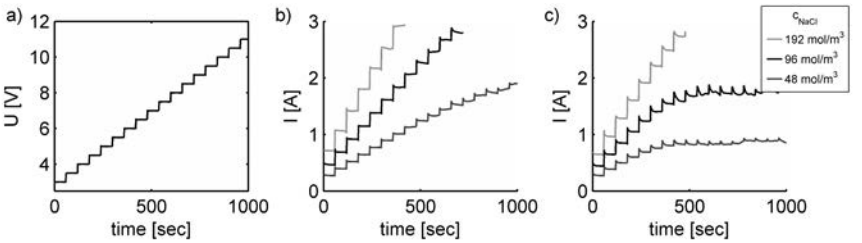

Figure 2.3: Current-voltage experiments with $NaCl$ solutions with concentrations $c_{NaCl} = 192\,\frac{mol}{m^3}$, $c_{NaCl} = 96\,\frac{mol}{m^3}$ and $c_{NaCl} = 48\,\frac{mol}{m^3}$. a) Profile of applied potential difference; measured current I for b) $Q_{high} = 2.5 \cdot 10^{-5}\,\frac{m^3}{s}$ and c) $Q_{low} = 0.83 \cdot 10^{-5}\,\frac{m^3}{s}$.

The measured profiles of electric current are shown for the different flow rates in Figs. 2.3 b and 2.3 c, respectively. A common characteristic is found here in the monotonically increasing current with increasing $NaCl$ concentration. Further, it is seen that in the experiments with Q_{high} the

[1] Here, repeatability is analyzed to quantify the variation of repeated experiments under identical conditions as defined by Bartlett and Frost (2008).

current is significantly higher when compared to the analogous experiments with Q_{low}. Whereas this difference appears to be small at the beginning of the experiments at relatively low applied potential differences, large deviations are found for high potential differences at the end of the experiment. Here, the measured current approaches a finite limit in the experiments with Q_{low} and concentrations of $c_{NaCl} = 96\,\frac{mol}{m^3}$ and $c_{NaCl} = 48\,\frac{mol}{m^3}$. This limiting behavior is not observed in the analogous experiments operated with Q_{high}.

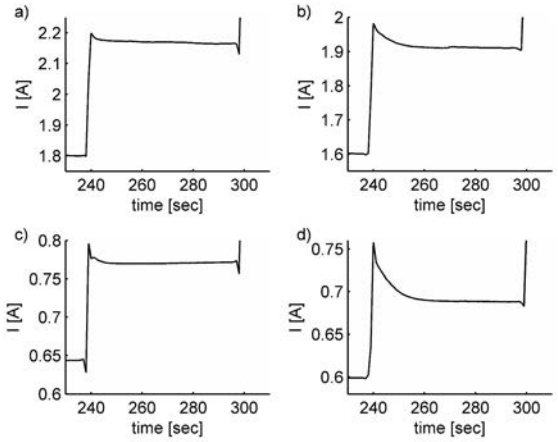

Figure 2.4: Transient response in current-voltage experiments with $NaCl$ solutions: a) $c_{NaCl} = 192\,\frac{mol}{m^3}$ and $Q_{high} = 2.5 \cdot 10^{-5}\,\frac{m^3}{s}$ b) $c_{NaCl} = 192\,\frac{mol}{m^3}$ and $Q_{low} = 0.83 \cdot 10^{-5}\,\frac{m^3}{s}$, c) $c_{NaCl} = 48\,\frac{mol}{m^3}$ and $Q_{high} = 2.5 \cdot 10^{-5}\,\frac{m^3}{s}$ and d) $c_{NaCl} = 48\,\frac{mol}{m^3}$ and $Q_{low} = 0.83 \cdot 10^{-5}\,\frac{m^3}{s}$.

Major differences are also found in the dynamic response to the stepwise increase of the potential differences. In all experiments a peak in the current signal is found immediately after the increase in the applied potential difference. However, the magnitude and length of this peak apparently depends strongly on both the concentration and the flow rate. Fig. 2.4 illustrates this dependence by showing the measured dynamic response in the interval $t = [230, 310]\,s$ for selected flow-rates and concentrations. The peak is significantly bigger and the transition to the steady-state is much slower in the experiments with the lower flow rate. Further, the extension of the peak decreases slightly with increasing concentration.

In a second series of experiments current-voltage experiments are conducted with a varying number of cells in the ED module (Exp. 1, 10 and 12 in Table A.7). The measured current profiles for 6, 10 and 14 cells are shown in Fig. 2.5 a. Here, the current profiles decrease monotonically with an increasing number of cells. The shape of the dynamic response largely coincides for the different experiments as illustrated in 2.5 b and c where the response of the experiments with 6 and 14 cells are shown in the interval $t = [110, 190]\,s$.

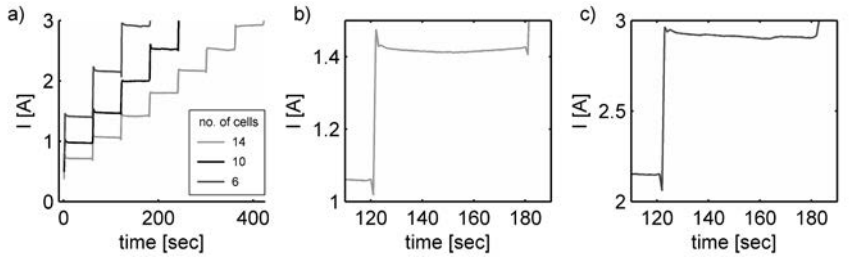

Figure 2.5: Current-voltage experiments with $NaCl$ solution with a concentration of $c_{NaCl} = 192\,\frac{mol}{m^3}$. a) Comparison of a varying number of cells in the ED stack, b) measured current for 14 cells and c) measured current for 6 cells.

The current-voltage behavior of the complete stack is compared in Fig. 2.6 for the aqueous electrolyte systems $NaCl$ and $NaCl - Na_2SO_4$ (Exp. 3, 6 and 9 in Table A.7 and Exp. 1-3 in Table A.6). For both systems the conductivity in the inlet is adjusted to $5\,\frac{mS}{cm}$ and the experiments are operated with volumetric flow rates $Q = 2.5{\cdot}10^{-5}\,\frac{m^3}{s}$, $Q = 1.6{\cdot}10^{-5}\,\frac{m^3}{s}$ and $Q = 0.83{\cdot}10^{-5}\,\frac{m^3}{s}$, respectively. As a general trend, the current measured in the experiments with $NaCl - Na_2SO_4$ solution exceeds the current measured in the $NaCl$-experiments. However, the difference between the current profiles decreases considerably with decreasing volumetric flow rate. The shape of the dynamic response to the stepwise increase in the applied potential difference coincides to a large extent for both systems.

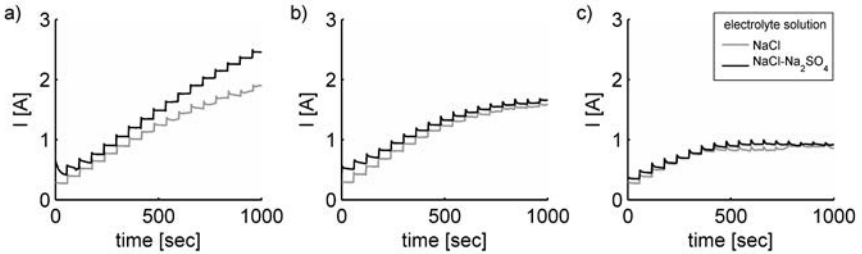

Figure 2.6: Measured current profiles of experiments with $NaCl$ and $NaCl - Na_2SO_4$ solutions for volumetric flow rates of a) $Q = 2.5 \cdot 10^{-5}\,\frac{m^3}{s}$, b) $Q = 1.6 \cdot 10^{-5}\,\frac{m^3}{s}$ and c) $Q = 0.8 \cdot 10^{-5}\,\frac{m^3}{s}$.

Discussion

The current-voltage experiments illustrate the well-known phenomena of a limiting current which can be observed in electrodialysis systems (Valerdi-Pérez and Ibáñez-Mengual, 2001) or in test cells for single IEM, e.g., (Krol, 1997). This limiting behavior constitutes a first important benchmark for the physical plausibility of the models developed in this work. The results extend the extensive

amount of information concerning the steady-state current-voltage behavior by focusing on the dynamic response to the stepwise increase of the applied potential difference. The response is characterized by a relaxation to a stationary current lasting 2 to 20s. These temporal scales and the qualitative shape of the relaxation strongly depend on both the flow rate and the ion concentration. To properly understand the mechanisms governing the response, dynamic models are needed with a temporal resolution in the (sub-)second range. A comparably small sensitivity of the dynamic response is found with respect to the number of cells and the type of ionic species in the electrolyte solution. These sensitivities constitute further important benchmarks for the developed models.

2.4 Sensitivities with respect to operational and design parameters

The sensitivity of batch desalination processes is analyzed in Section 2.4.1 with respect to the applied electric current and in Section 2.4.2 with respect to the volumetric flow rate. Section 2.4.3 compares the results of experiments with different spacers to obtain an estimate of the sensitivities with respect to the geometric spacer design.

2.4.1 Applied current

Desalination of $NaCl$ solution

To investigate the sensitivity with respect to the applied current, $NaCl$ solution is desalinated with a constant electric current of $1\,A$, $2\,A$ and $3\,A$, respectively. Details concerning the module configuration and the remaining operational parameters in these experiments are summarized in Table A.9, Exp. 1-3. The repeatability of desalination experiments with constant current and the expactable measurement error is discussed in Appendix A.2. The measured profiles of the $NaCl$ concentration in the diluate tank c_{NaCl} and the potential drop over the stack U are shown in Fig. 2.7. Here, a common characteristic is found in the linear decrease of c_{NaCl} in the diluate tank. The slopes of these linear trends depend strongly on the applied current. The measured voltage profiles increase monotonically in the course of the experiment. Apparently, this increase in the potential is a direct consequence of the decreasing concentration in the diluate cycle. Further, the sensitivity of the potential drop with respect to the applied current increases significantly as the concentration in the diluate tank decreases.

The energy demand of the total process, the working electrodes and the pumps are compared in Fig. 2.8 a. In comparison to the experiment with $I = 1\,A$ the electrode energy demand of the experiments with $I = 3\,A$ and $I = 2\,A$ is 112.2 % and 54.4 % higher, respectively. As the energy demand of the electrodes dominates the total energy demand, the latter decreases continuously with decreasing current. At the same time, the energy demand of the pumps increases substantially with decreasing current. This increase in the pumping energy demand results from a significant increase of the desalination time with decreasing applied current (cf. Fig. 2.8 b).

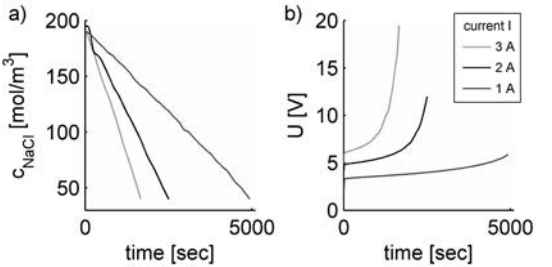

Figure 2.7: Measured profiles of $NaCl$ concentration c_{NaCl} in the diluate tank (a) and voltage drop U (b) for desalination experiments with constant applied currents of $3\,A$, $2\,A$ and $1\,A$.

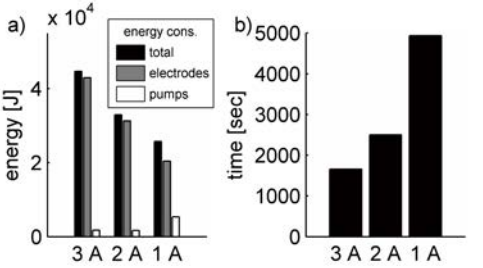

Figure 2.8: Comparison of a) the energy consumption of the total process (t), the electrodes (e) and the pumps (p) and b) the desalination time for the desalination of $NaCl$ with a constant current of $3\,A$, $2\,A$ and $1\,A$.

Desalination of $NaCl - Na_2SO_4$ solution

Similar trends are identified in two experiments (Exp. 1 and 2 in Table A.8) for the desalination of aqueous $NaCl - Na_2SO_4$ solution with an initial concentration of $c_{NaCl} = 0.049\,\frac{mol}{l}$ and $c_{Na_2SO_4} = 0.046\,\frac{mol}{l}$. In these experiments, a constant current of $1\,A$ and $2\,A$ is applied, respectively.

The measured profiles for the conductivity in the diluate tank κ, the potential drop U and the concentrations of the ionic species c_{Na^+}, c_{Cl^-} and $c_{SO_4^{2-}}$ are shown in Fig. 2.9. As in the $NaCl$ experiments, the potential drop U increases monotonically during the experiment (cf. Fig. 2.9 b). As shown in Fig. 2.9 a, the conductivity κ decreases linearly with time where the slope depends significantly on the applied current. Subject to the comparably small number of measurements and the measurement uncertainty (cf. Appendix A.2.2) similar nearly linear trend can be identified for the decrease of c_{Na^+} (cf. Fig. 2.9 d), whereas nonlinear profiles are found for the decrease of c_{Cl^-} and $c_{SO_4^{2-}}$ (cf. Fig. 2.9 c). Apparently, c_{Cl^-} decreases much faster than $c_{SO_4^{2-}}$ at the beginning of the experiments. At the end of the experiments, as the concentration in the diluate tank declines, $c_{SO_4^{2-}}$ decreases in a comparable manner or even faster than c_{Cl^-}.

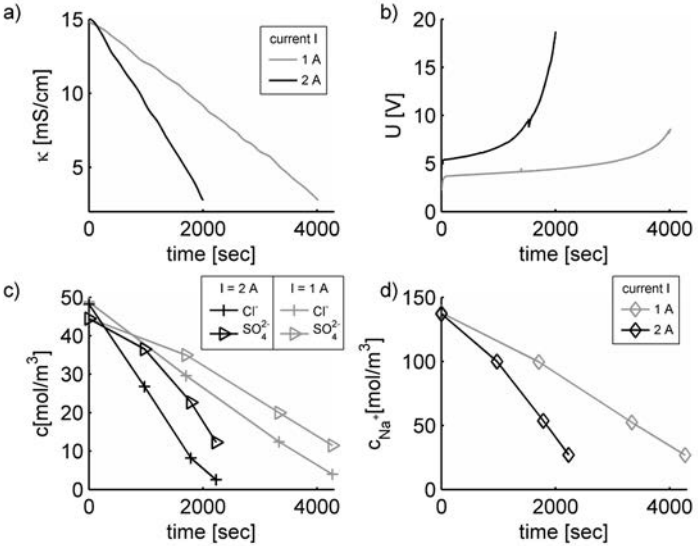

Figure 2.9: Measured profiles of the conductivity κ (a), the voltage drop U (b) and concentrations of the ionic species Cl^-, SO_4^{2-} (c) and Na^+ (d) in the diluate tank for desalination experiments with constant applied currents of $2\,A$ and $1\,A$.

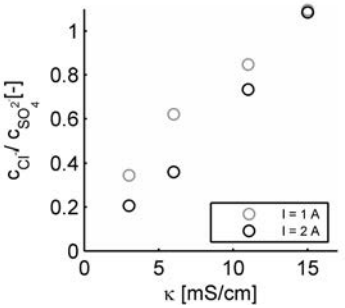

Figure 2.10: Measured concentration ratio $\frac{c_{Cl^-}}{c_{SO_4^{2-}}}$ in the diluate tank in the desalination experiments with constant applied currents of $2\,A$ and $1\,A$.

The sensitivity of this competitive transport of the two anions Cl^- and SO_4^{2-} with respect to the applied current is illustrated in Fig. 2.10. Here, the concentration ratio $\frac{c_{Cl^-}}{c_{SO_4^{2-}}}$ is plotted against the corresponding conductivity in the diluate tank κ. In the entire range, the ratio is significantly higher for the experiment with $I = 1\,A$. From the initial conductivity of $\kappa = 15\,\frac{mS}{cm}$ the difference in the ratio increases until a maximal difference at $\kappa = 6\,\frac{mS}{cm}$ is reached. At the

last sample at $\kappa = 3\,\frac{mS}{cm}$ the difference is slightly smaller. These results indicate that the applied current has a significant effect on the transport of the two competing anions.

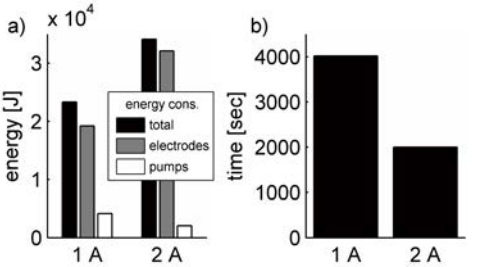

Figure 2.11: Comparison of a) the energy consumption of the total process (t), the electrodes (e) and the pumps (p) and b) the desalination time for the desalination of aqueous $NaCl - Na_2SO_4$ solution with a constant current of $2\,A$ and $1\,A$.

The energy demands of the two experiments are compared in Fig. 2.11 a. The energy demand of the electrodes is 71.5 % higher for the experiment operated with a current of $2\,A$. Hence, the sensitivity of the electrode energy demand with respect to the applied current is significantly higher for the $NaCl - Na_2SO_4$ system in comparison to the sensitivity found for the $NaCl$ system. The increase of the desalination time and pumping energy demand by 101.15 % for the experiment with $I = 1\,A$ (cf. Fig. 2.11 b) is similar to the increase found for the $NaCl$ system.

2.4.2 Volumetric flow rate

The sensitivity with respect to the volumetric flow rate is investigated in two additional desalination experiments with flow rates $Q_{high} = 2.5 \cdot 10^{-5}\,\frac{m^3}{s}$ and $Q_{low} = 0.83 \cdot 10^{-5}\,\frac{m^3}{s}$, respectively (cf. Exp. 4 and 5 in Table A.9). The resulting concentration and voltage drop profiles are shown in Fig. 2.12. Apparently, the flow rate has little effect on the profiles in a wide range of the experiment. However, the increase in the potential drop U at the end of the experiment is significantly more pronounced in the experiment with the lower flow rate. Hence, the sensitivity of the potential drop U with respect to the volumetric flow rate is only of significant order at low concentrations in the diluate cycle.

The small sensitivity of the flow rate is seen in an analogous manner in the energy demand of the electrodes and the desalination time (cf. Fig. 2.13 a). Resulting from the higher energy consumption of the pumps, the total energy demand is 7.1 % higher for the experiment with the higher volumetric flow rate (cf. Fig. 2.13 b).

2.4.3 Comparison of different spacers

The sensitivity with respect to the spacer design is determined in desalination experiments (Exp. 6 and 7 in Table A.9) using either the woven spacer A or B with geometrical properties given in

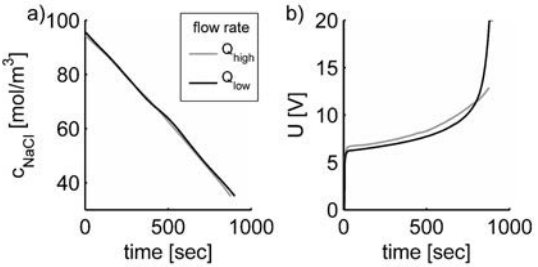

Figure 2.12: Profiles of the measured concentration c_{NaCl} (a) and voltage drop U (b) for the desalination experiments with flow rates $Q_{high} = 2.51 \cdot 10^{-5}\ \frac{m^3}{s}$ and $Q_{low} = 0.83 \cdot 10^{-5}\ \frac{m^3}{s}$.

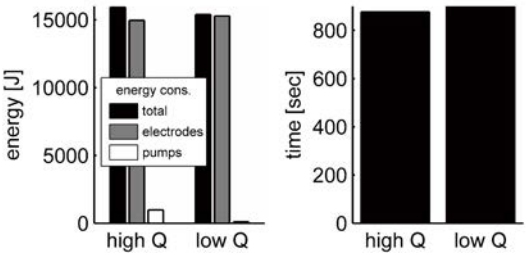

Figure 2.13: a) Total energy consumption (t), energy consumption of the electrodes (e) and pumps(p) and b) desalination time for the desalination experiments with flow rates $Q_{high} = 2.5 \cdot 10^{-5}\ \frac{m^3}{s}$ and $Q_{low} = 0.83 \cdot 10^{-5}\ \frac{m^3}{s}$.

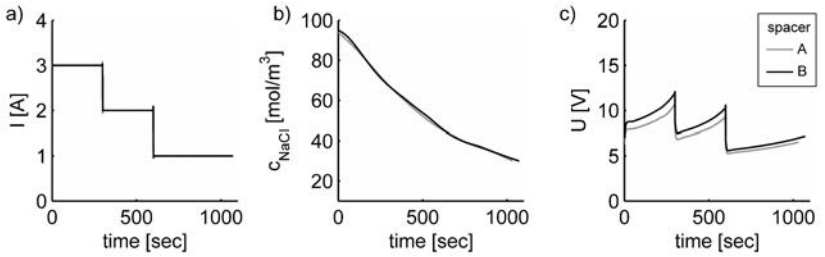

Figure 2.14: Applied current profile (a), measured $NaCl$ concentration in the diluate tank c_{NaCl} (b) and measured potential drop over the stack U (c) for desalination experiments with spacer A and spacer B.

Tab. A.2. These experiments are operated with a stepwise varying applied current as shown in Fig. 2.15 a.

The resulting profiles for the measured c_{NaCl} and measured U are depicted in Fig. 2.14 b and c. The c_{NaCl} profile coincides in the entire range of experiments whereas the potential drop U is

significantly higher for spacer B. Apparently, the different geometrical design parameters of the spacer significantly affect the transport and the propagation of the electric field in the spacer-filled channels. The higher potential drop results in an increased energy consumption of the electrodes (10.8 %) and the total process (10.7 %, cf. Fig. 2.15 a). Further, the pumping energy is 3.8 % higher for the experiment with spacer B resulting from both a higher desalination time and higher pressure drop.

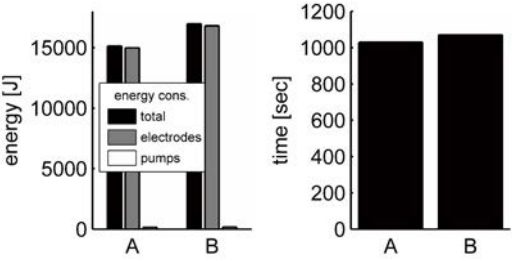

Figure 2.15: a) Total energy consumption (t), energy consumption of the electrodes (e) and pumps(p) and b) desalination time for the desalination experiments with spacer A and spacer B.

2.4.4 Discussion

Comparably small sensitivities have been found with respect to the flow rate which is in contrast to the common assumptions that it effects the local transport phenomena in the flow channels significantly (Koutsou et al., 2009, Strathmann, 2004). Concerning the contribution of these transport phenomena to the behavior of the entire process, these experimental results give rise to two major hypotheses: (i) The contribution of the transport in the flow channels is negligibly small in the investigated experimental scenario. (ii) The flow rate affects the transport in the flow channels only slightly. The significant sensitivity with respect to the spacer geometry found in Section 2.4.3 and the results of the current-voltage experiments in Section 2.3 contradict the first hypothesis. However, a thorough investigation of the hypotheses on the basis of the experimental data is not possible. This fact constitutes a major motivation for the development of a process model which thoroughly discriminates the different contributions to the total process performance.

The pronounced sensitivity with respect to the applied current has been found in the experiments in accordance with previous results (Parulekar, 1998, Tanaka, 2003). It emphasizes the necessity for a thorough representation of the charge transport in the developed models. The effect of the applied current on the competing transport of Cl^- and SO_4^{2-} ions is found in agreement with the results of Moon et al. (1998) and Tanaka et al. (2012). In these works the sensitivity of the competitive transport with respect to the applied current is studied by analyzing the concentrations in the diluate tank at the final time of the desalination experiment. Their results are extended by the experiments in Section 2.4.1 by providing a first temporal resolution of the concentrations. With regard to the model development addressed in this work, the results high-

light the fact that the commonly used description of the perm-selective transport through the membrane by constant transport or transference numbers, e.g., in (Fidaleo and Moresi, 2005, Lee et al., 2002), is not adequate for the chosen scenario. It rather provides a strong motivation for the development of the rigorous multi-species transport model for the transport in the membrane phase.

2.5 Operation with transient applied currents

The results of the sensitivity analysis are generalized in this section to desalination processes operated in a transient mode. An operational mode with a time-variant applied current arises naturally if the electric energy for the working electrodes is directly provided by a solar power system (AlMadani, 2003, Li and Zhang, 2009). Such a system is investigated with respect to the arising dynamic process behavior in an additional experiment for the desalination of $NaCl$ solution (Exp. 22 in Table A.9). Here, a scenario is considered where the applied current is chosen to be proportional to measured sunlight intensities. The intensities are taken from data of the Oahu Solar Measurement Grid published by the National Renewable Energy Laboratory[2]. From these data one minute piecewise-constant intensities are formed by averaging and used to scale the applied current signal with a minimal and maximal value of $1\,A$ and $2\,A$, respectively. The resulting applied current profile is shown in Fig. 2.16 a.

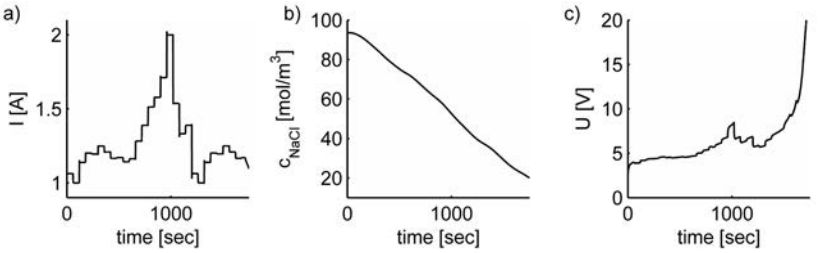

Figure 2.16: Profiles of applied current (a), measured $NaCl$ concentration in the diluate tank (b) and measured potential drop over the stack U (c) for a desalination experiment with an applied current proportional to measured sun intensities.

The measured profiles of concentration in the diluate tank c_{NaCl} and potential drop U are shown in Fig. 2.16 b and c. The transitions in the applied current are not resolved in the c_{NaCl} profile where a nearly linear trend is seen. This highlights important limitations of the information content in the concentration data, as a reconstruction of the transient fluxes across the membranes is not possible. A valid mechanistic model can contribute to enriching the measured information. The measured potential-drop reacts almost instantaneously to the transitions in the

[2] The used data have been measured at location *DHHL3* on 1^{st} December 2011 from 1:42 pm till 2:03 pm. Consider (National Renewable Energy Laboratory) for details concerning the measurement.

applied current. However, the dynamic response of the potential-drop is substantially affected by the decreasing concentration in the diluate cycle. Correspondingly, the transitions of the applied current are more strongly resolved at the end of the experiment. This varying sensitivity of the measured potential difference constitutes an important benchmark for the developed model.

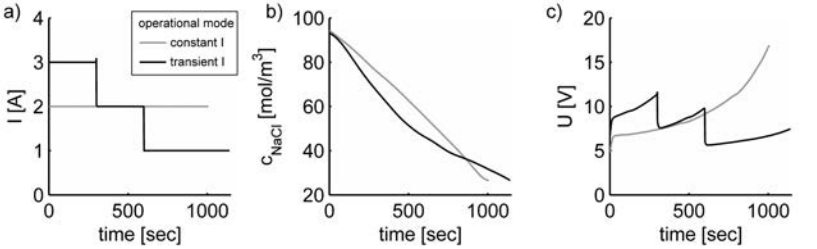

Figure 2.17: Profiles of applied current (a), measured $NaCl$ concentration in the diluate tank (b) and measured potential-drop (c) over the stack U for a desalination experiment with constant and varying applied current.

A desalination experiment with a constant applied current of $2\,A$ (Exp. 6 in Table A.9) is compared with an experiment operated with a time-variant applied current (Exp. 7 in Table A.9). In the latter, the current is reduced stepwise from initially $3\,A$ to $1\,A$ with a step length of five minutes (cf. Fig. 2.17 a). The profiles of measured concentration c_{NaCl} and measured potential drop U are depicted in Fig. 2.17 b and c. In the experiment with the time-variant operational mode the steps in the applied current result in a nearly instantaneous drop in the voltage signal. The corresponding concentration profile shows a significantly non-linear trend (cf. Fig. 2.17 b).

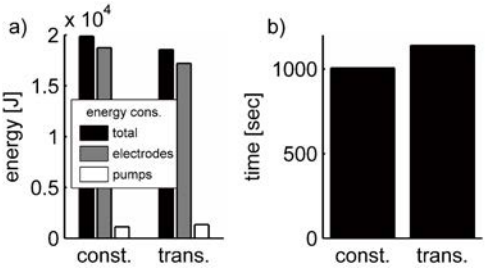

Figure 2.18: a) Total energy consumption (t), energy consumption of the electrodes (e) and pumps(p) and b) the desalination time for the desalination experiments with constant applied current of $2\,A$ and a time-variant applied current.

The energy consumption and the desalination time of the experiments are compared in Fig. 2.18. For the experiment with constant applied current, the energy demand of the total process and the electrodes is 7.15 % and 8.95 % higher, respectively. This observation indicates that

the use of a dynamically varying applied current can increase the energy efficiency of the ED process. Thus, the results confirm the findings of the theoretical and numerical analysis on the energy consumption of ED batch processes by Parulekar (1998). However, it has to be noted that the desalination time is 13.33 % higher for this operational mode. Hence, for the design of a time-variant current trajectory with the objective of increasing the entire process performance a systematic approach is required accounting for both aspects.

2.6 ED with pulsed current

Desalination experiments operated with a pulsed applied current are investigated in Sections 2.6.1 and 2.6.2 for aqueous $NaCl$ and $NaCl - Na_2SO_4$ solutions, respectively. The focus is here to investigate the temporal scales and qualitative patterns of the dynamic response to the current pulses.

2.6.1 Desalination of $NaCl$ solution using a pulsed applied current

The effect of a pulsed applied current is investigated in a comparison of two desalination experiments (Exp. 10 and 11 in Table A.9). In the first experiment a pulsed current is applied to the working electrodes varying between $0\,A$ and $2\,A$ with a pulse length of $60s$. The second experiment is operated with a constant applied current of $2\,A$. The resulting profiles of applied current I, measured concentration c_{NaCl} and potential drop U are compared in Fig. 2.19. Both experiments are characterized by a nearly linear decrease of the concentration c_{NaCl}. However, the decrease is significantly faster in the experiment with a constant applied current. In the pulsed current experiment the pulsed operation is not resolved in the profile of the measured concentration. The dynamic response of the measured potential drop to the pulsed current signal is characterized by a fast transition in the range of seconds.

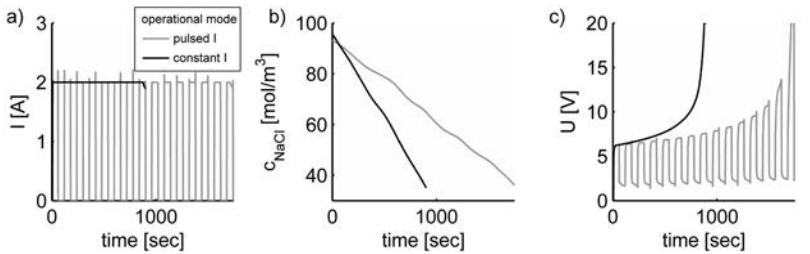

Figure 2.19: Profiles of applied current (a), measured $NaCl$ concentration in the diluate tank (b) and measured potential drop over the stack U (c) for a desalination experiment with constant and pulsed applied current.

The energy consumption and desalination time of the two experiments are compared in Fig. 2.20. The total energy consumption and the energy consumption of the electrodes are nearly

identical. The desalination time of the experiment with pulsed applied current is 101.2 % higher resulting in an analogous increase in the energy demand of the pumps.

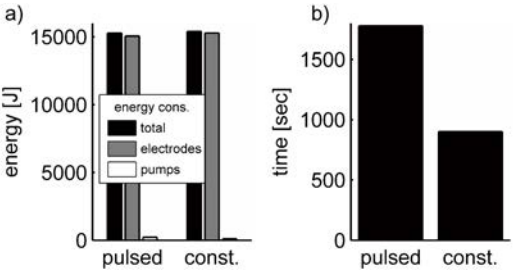

Figure 2.20: a) Total energy consumption (t), energy consumption of the electrodes (e) and pumps(p) and b) the desalination time for the desalination experiments with constant and pulsed applied current.

Additional experiments are conducted to obtain more profound insight into the temporal scales and the qualitative patterns of the dynamic response to a pulsed applied current. This includes the evaluation of the sensitivity of these two aspects with respect to the pulse interval length, the volumetric flow rate and the geometrical properties of the spacer.

Effect of pulse interval length

The effect of the pulse interval of the applied current is investigated in three experiments (Exp. 12-14 in Table A.9), where the pulse rates of the on-off signal are chosen as 10s-10s, 30s-30s and 60s-60s. Fig. 2.21 shows the profiles of the applied current and the measured potential drop in the in the entire experiment as well as in the interval $t = [710, 850]\,s$. The latter allows to investigate the characteristic shape of the dynamic response of the voltage drop to a current pulse. Here, a common pattern is found in the nearly spontaneous increase to approximately two third of the maximal voltage value followed by a transient response with a decreasing slope. For the 60s-60s pulse rate the transient settles after approximately $35s$ into a monotonous flat increase of the potential drop. For the shorter pulse rates the transients are interrupted by the following $0\,A$ interval before settling into this flat increase.

Effect of the flow rate on pulsed experiments

The sensitivity of the dynamic response with respect to the volumetric flow rate is investigated in two experiments (Exp. 18 and 19 in Table A.9) operated with $Q_{high} = 2.51 \cdot 10^{-5}\,\frac{m^3}{s}$ and $Q_{low} = 0.83 \cdot 10^{-5}\,\frac{m^3}{s}$, respectively. The pulsed applied current I and measured voltage drop U are shown in Fig. 2.22 a and b. In the first $800s$ of the experiments the potential drops largely coincide. For $t > 800s$ the experiment with Q_{low} is characterized by a significantly faster increase of the potential drop in a manner comparable to the results of the constant current experiments in Section 2.4.2. Also, the effect of the volumetric flow rate on the shape of the dynamic response

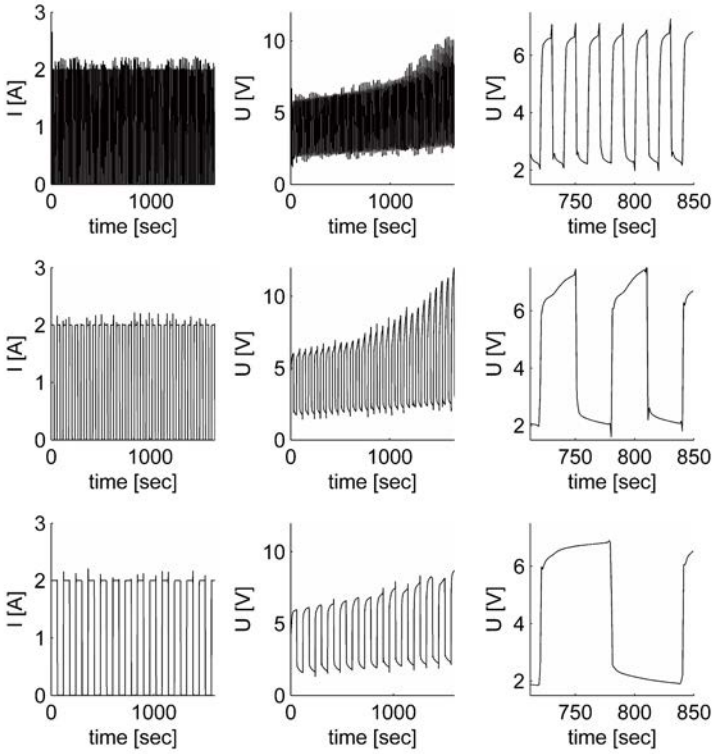

Figure 2.21: Applied pulsed current profiles, measured potential drop U in the entire experiment and measured potential drop in the interval from $t_1 = 710s$ to $t_2 = 850s$ for pulse rates: 10s-10s, 30s-30s and 60s-60s.

depends heavily on the desalination time. Whereas nearly no difference is found for the profiles at the beginning of the experiment (cf. Fig. 2.22 c), significant deviations are seen towards the end of the experiments (cf. Fig. 2.22 d).

Effect of the spacer geometry on pulsed experiments

The effect of the spacer geometry on the dynamic response to a pulsed applied current is investigated in two desalination experiments (Exp. 20 and 21 in Table A.9) carried out with spacer A and spacer B, respectively. The resulting profiles of applied current and measured potential drop are illustrated in Fig. 2.23 a and b. In the entire range of the experiment a significantly higher voltage drop is found for spacer B, which is in accordance with the expermeriments operated with

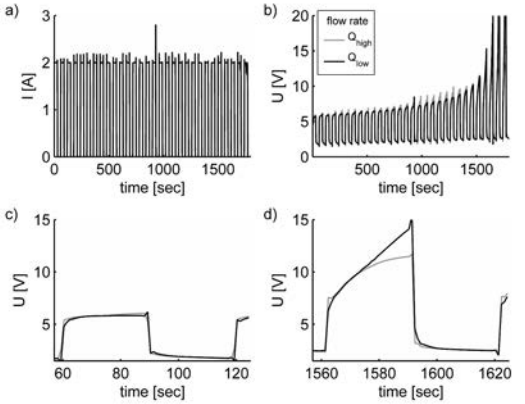

Figure 2.22: Profiles of the pulsed applied current (a), measured voltage drop U (b) and measured voltage drop U in the intervals $t = [55, 125]$ (c) and $t = [1555, 1625]\, s$ (d) for desalination experiments with flow rates $Q_{high} = 2.51 \cdot 10^{-5}\, \frac{m^3}{s}$ and $Q_{low} = 0.83 \cdot 10^{-5}\, \frac{m^3}{s}$.

constant applied current in Section 2.4.3. The shape of the dynamic response coincides to a large extent at the beginning as well as at the end of the experiment (cf. Fig. 2.23 c and d). The shape is characterized by initially rapidly increasing transients, which after approx. $30s$ settle in a moderate increase of the applied potential.

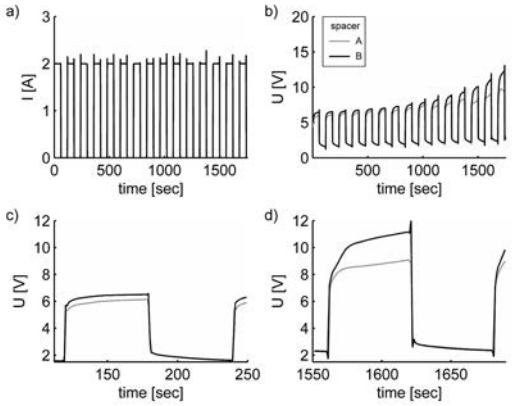

Figure 2.23: Profiles of applied current (a), measured potential drop over the stack U (b) and measured potential drop for a single pulse interval at the beginning (c) and end (d) of the desalination experiments with spacer A and spacer B.

Effect of the applied current on pulsed experiments

The sensitivity of the dynamic response is further analyzed with respect to the magnitude of the pulsed applied current. Here, experiments are conducted with a pulse rate of $180s - 60s$ for the on-off signal and magnitudes of $3\,A$, $2\,A$ and $1\,A$ (Exp. 15-17 in Table A.9). The applied current profiles, measured potential-drop and measured potential-drop in the first $280s$ are illustrated in Fig. 2.24. The nearly instantaneous increase to approximately two-thirds of the maximal potential-drop value is found in the response of all experiments. The following transients are characterized by significantly different slopes with the highest slope found for the highest magnitude. The transient corresponding to the experiment with a magnitude of $3\,A$ settles after $20s$ into a flat increase with a nearly linear trend. This transition is significantly slower in the experiments with $2\,A$ and $1\,A$.

2.6.2 Desalination of $NaCl - Na_2SO_4$ solution using a pulsed applied current

The effect of a pulsed applied current on the transport of competing ionic species is investigated in two experiments (Exp. 1 and 3 in Table A.8) for the desalination of aqueous $NaCl - Na_2SO_4$ solution with initial concentrations of $c_{NaCl} = 0.049\,\frac{mol}{l}$ and $c_{Na_2SO_4} = 0.046\,\frac{mol}{l}$. In the first experiment a pulsed current is applied varying between $2\,A$ and $0\,A$ with a pulse length of $60s$; in the second a constant current of $2\,A$ is applied.

The measured profiles for the conductivity in the diluate tank κ, the potential drop U and the concentrations of the ionic species c_{Na^+}, c_{Cl^-} and $c_{SO_4^{2-}}$ are shown in Fig. 2.25. The trends of the linearly decreasing conductivity and increasing potential drop resemble to a large extent the results of the $NaCl$ desalination experiments (cf. Section 2.6.1). Further, nearly linear trends can be identified for the decrease of c_{Na^+} in the diluate tank (cf. Fig. 2.25 d). The decrease of c_{Cl^-} and $c_{SO_4^{2-}}$ follows a significantly non-linear trend (cf. Fig. 2.25 c) indicating a competitive transport of these anions as analogously found in Section 2.4.1.

The effect of the pulsed current on this competitive transport is illustrated in Fig. 2.26. At the beginning of the experiments ($\kappa = 15\,\frac{mS}{cm}$) the concentration ratio $\frac{c_{Cl^-}}{c_{SO_4^{2-}}}$ nearly coincides with values of 1.03 and 1.02, respectively. In the course of the experiment the ratio decreases significantly faster for the non-pulsed operational mode. The samples drawn at the end of the pulsed and non-pulsed experiments at a conductivity of $\kappa = 2.8\,\frac{mS}{cm}$ consists of 57.1 % and 19.4 % chloride ions, respectively. Hence, the amount of transported sulfate ions is significantly higher in the pulsed experiment.

2.6.3 Discussion

The comparison of experiments operated with either pulsed or constant applied current showed no significant difference in the energy demand. These findings are in accordance with recent findings of Malek et al. (2013) and illustrate that the significant reduction of the total energy demand found by Mishchuk et al. (2001a) is restricted to processes for the desalination of strongly diluted electrolyte solutions. In the investigated concentration range, the pronounced dynamic response

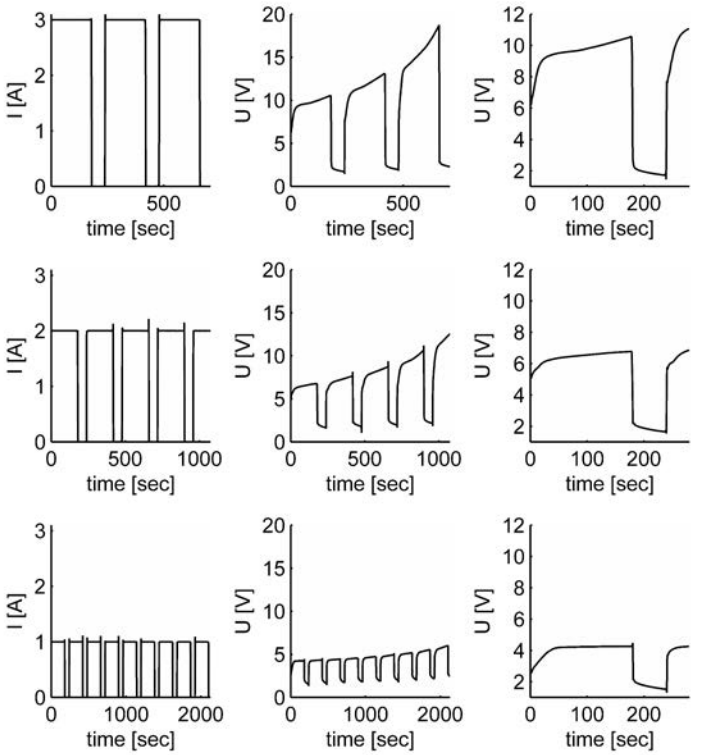

Figure 2.24: Profiles of the pulsed applied current, measured voltage drop U and measured voltage drop U in the interval from $t = [0, 280]$ for desalination experiments with a maximal current $3\,A$, $2\,A$ and $1\,A$.

of the measured voltage apparently makes only a minor contribution to the total energy demand. The rigorous assessment of the transient behavior on the process performance requires a more profound investigation of the underlying mechanisms. For the analysis of these mechanisms the integral measurements obtained in this study are to be combined with information concerning the local phenomena in the ED module, preferably by high-resolution measurements or from detailed dynamic models developed in this work.

The dynamic response to the pulsed operational transitions has been found to show a significant sensitivity with respect to the operational parameters. These sensitivities, the characteristic shape and the temporal scales of the response constitute important benchmarks for the developed dynamic models. Further, it has been found that the operation of the process with a pulsed

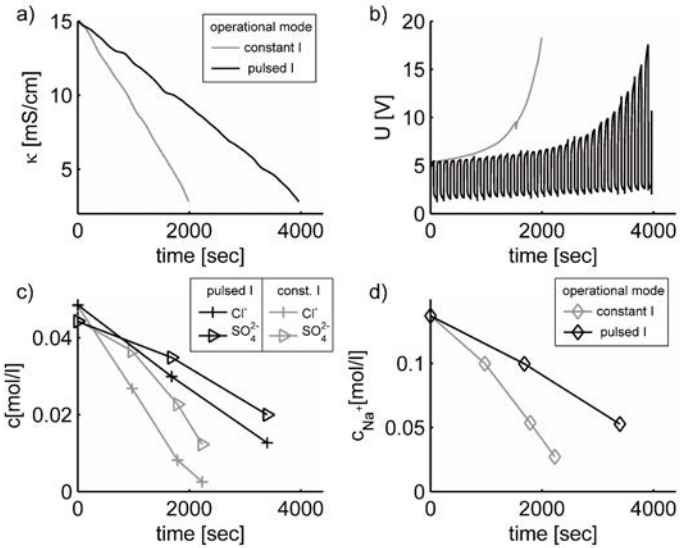

Figure 2.25: Measured profiles of the voltage drop U (a), the conductivity κ (b) and concentrations of the ionic species Cl^-, SO_4^{2-} (c) and Na^+ (d) in the diluate tank for desalination experiments with constant applied currents of $2\,A$ and $1\,A$.

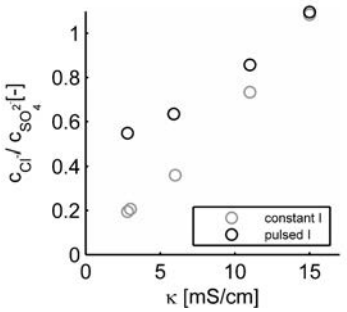

Figure 2.26: Measured concentration ratio $\frac{c_{Cl^-}}{c_{SO_4^{2-}}}$ in the diluate tank in the desalination experiments with constant and pulsed applied currents.

applied current also strongly effects the competitive transport. The transport of sulphate ions is significantly increased by the pulsed operational mode. These findings are in accordance with previously reported studies investigating the selective transport of Na^+ and Ca^{2+} ions (Gurtler et al., 2008, Karlin and Kropotov, 1995). The results emphasize the importance of considering dynamic effects in a model-based analysis of the process to understand the selective transport in

the membrane-electrolyte system properly.

2.7 Conclusions

The experimental study in this chapter has illustrated the complexity arising in the systematic investigation of ED processes from the large number of operational and design parameters. This emphasizes the potential of a predictive process model to support a systematic investigation, particularly of the dynamic process behavior. For the identification of model structures and parameters in a model development process the experiments have provided a large amount of coherent experimental data with a fine temporal resolution.

As important process insight for a systematic model development, the analysis has revealed the sensitivity of the measured output and important performance measures with respect to operational and design parameters. The results provide for the first time coherent sensitivity information with respect to all relevant degrees of freedom. Further, in contrast to prior work (cf. the discussion in Section 2.2), the findings include the sensitivities of the dynamic response of the measured voltage with respect to the flow rate, spacer geometry, pulse rate and current. Table 2.1 illustrates the measured sensitivities in a qualitative sense. The sensitivities constitute important benchmarks for the evaluation of the physical consistency of the developed models.

Table 2.1: Summary of qualitative sensitivities measured at the lab-scale ED plant: ++ has strong effect, + has effect, ○ has negligible effect , n.m. not measured.

	energy demand	desalination time	selectivity	dynamic response
I	++	++	++	+
Q	○	○	n.m.	+
spacer type	+	○	n.m.	○
pulse interval	○	++	+	+

On the basis of the sensitivity information, it has been possible to identify a first set of specific requirements for an accurate model-based description of the process in Section 2.4.4. Accordingly, significant effort should in the model development process be directed to the description of the charge transport in the membrane-electrolyte system and its substantial dependence on the ionic species concentrations. Hence, rather than employing simplified charge transport models on the basis of empirical resistance parameters, it appears useful to consider a mechanistic description mutually integrating charge transport and the diffusion of ionic species. Further, for multi-salt systems the modeling of the selective transport in the membranes has to go beyond the introduction of constant transport numbers in order to describe the identified sensitivities with respect to both the species concentrations and the current density properly. A mechanistic spatially distributed transport model which is expected to fulfill these requirements is the Maxwell-Stefan approach coupled to the electroneutrality condition.

The results in Section 2.5 show that a time-variant applied current can influence the energy consumption of the process significantly . In addition it has been found in 2.6.3 that dynamic effects even affect the competitive transport in multi-salt solutions considerably. Hence, the development of a thoroughly dynamic model formulation not only allows the investigation of processes operated in a dynamic mode, but is in a general sense of significant importance to understand the mechanisms governing the selectivity of the transport processes properly. The temporal scales in which the dynamic effects affect the process substantially have been found to be in the subsecond to second range. This range constitutes an important requirement for the temporal resolution of the developed model.

An additional important benchmark for the physical plausibility of the developed model has been identified in Section 2.3 in terms of the limiting behavior of the measured current. The established theory relates this limiting behavior to the depletion of ionic species at the membrane-electrolyte interphase, cf. e.g. (Balster et al., 2007, Melin and Rautenbach, 2004). In the experimental setting – and analogously in a typical industrial ED plant – the depletion of ionic species occurs in the main direction of the electric field (orthogonal to the membranes) and along the flow-path (parallel to the membranes). Hence, for an accurate resolution of the limiting behavior in the developed model the description of the local transport processes has to occur in at least two spatial dimensions.

In summary, the experimental results presented in this chapter impose the following requirements on the developed model: (i) the thorough mechanistic description of the transport processes, (ii) the fully dynamic model formulation and (iii) the – at least – two-dimensional resolution of the transport processes. To fulfill these requirements it is inevitable to consider models, e.g., in the form of the Maxwell-Stefan approach coupled to the electroneutrality constraint, which constitute systems of partial-differential algebraic equations. However, with the use of PDAE models, next to issues related to the physical plausibility, it is well-known (Chudej et al., 2005, Martinson and Barton, 2003, Sternberg, 2006), that essential problems emerge in the modeling process concerning the mathematical classification and the reliable numerical treatment. These aspects have not been considered thoroughly before in the context of ED and electromembrane processes as commonly strongly simplified, e.g., quasi-stationary or one-dimensional models, have been used. To this end, before actually addressing the development of a transport model fulfilling the requirements (i)-(iii) in Chapter 4 and the incorporation of these transport models into a hierarchically structured process model in Chapter 5, Chapter 3 introduces a novel method for the characterization of general PDAE systems. As illustrated in the course of the elaboration of the method for a simplified dynamic charge transport model, the developed method is of essential importance for the systematic mathematical analysis of models developed in Chapter 4.

3 Index analysis and reduction of PDAE systems

This chapter introduces a new procedure for index analysis and reduction of PDAE systems. The method is considered as a central element of a modeling work-flow for rigorous transport models and is therefore introduced in this general context. Its specific relevance for the modeling of ionic charge transport is illustrated by considering the well-known Nernst-Planck approach together with the electroneutrality constraint. The elaboration of the method includes a brief review of different concepts of index analysis of DAE and PDAE systems in Section 3.2. Different definitions of index are introduced and evaluated as a concept to support the modeling process, the numerical treatment *and* the physical interpretation of PDAE systems. In Section 3.3, the underlying theory of a novel index reduction procedure is introduced and illustrated. In Section 3.4 the role of index reduction as a major task in any modeling work flow is discussed. Elements of this chapter have been published previously (Johannink et al., 2016b).

3.1 Introduction

Rigorous models for the description of transport phenomena in chemical processes frequently result in systems of partial differential and algebraic equations (PDAE) (Bird et al., 2002, Curtiss and Bird, 1999, Martinson and Barton, 2001b). For the numerical treatment of PDAE systems various equation-oriented modeling environments (e.g., Aspen Plus (Aspentech, 1994-2013) or gPROMS (Process Systems Enterprise, 1997-2009)) provide suitable methods which are based on the semi-discretization of the PDAE in the spatial coordinates and the numerical integration of the resulting system of differential-algebraic equations (DAE). From a technical point of view, such a vertical method of lines (MOL) approach is very attractive: (i) The discretization of the spatial coordinates is carried out by generic schemes resulting in a simple implementation of the PDAE. (ii) The representation of the distributed model in the semi-discretized form as a DAE allows for the straightforward coupling with other DAE models and the simultaneous numerical treatment of these models. Such an approach has become a standard procedure in flowsheet or plant-wide modeling in chemical engineering. (iii) The main effort in the numerical treatment of the model is the integration of the semi-discretized and possibly coupled DAE. For this purpose efficient (semi)-implicit integrators are available (Campbell and Marszalek, 1996, Deuflhard et al., 1987, Hairer et al., 1993, Petzold, 1982a, Schlegel et al., 2004).

The development of these generic numerical techniques results in an increasing application of

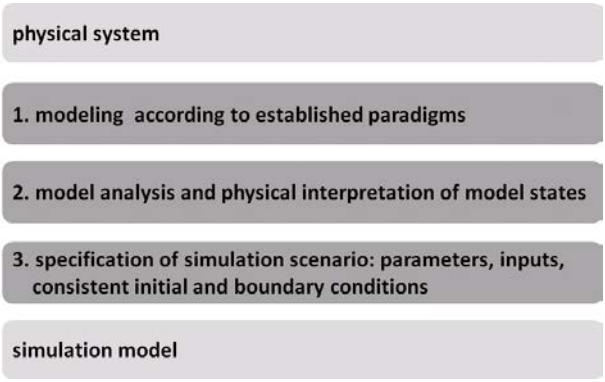

Figure 3.1: A general work flow for the modeling of distributed models.

detailed distributed models in the form of PDAE systems in simulation, model-based design and control. However, two major challenges can be identified complicating the use of these models: (i) The generic numerical treatment fails easily, if the PDAE system is not characterized by certain mathematical properties. It is generally required that the PDAE system is well-posed in the sense of Hadamard (Hadamard, 1902, Vitillaro and Fiscella, 2013), demanding a consistent specification of initial and boundary conditions. Further, depending on the specific numerical methods applied, additional requirements arise with respect to the structural properties of the PDAE system. (ii) Especially when large and strongly coupled models are concerned, important physical principles are not explicitly depicted in the model structure. Hence, even if a numerical solution is obtained in a straightforward manner, it is difficult to develop a proper relation between the model states and the physical phenomena.

These challenges emphasize the importance of a systematic approach to derive a well-posed distributed simulation model for a given physical system. A typical work flow used for such a systematic model development is shown in Fig. 3.1 (Marquardt, 1994). Here, the model developed by established modeling paradigms in step 1 is subject to a theoretical analysis in step 2. The first objective of this analysis is the identification of important mathematical model properties. The second objective is to analyze the model with respect to the physical interpretation of the states in the model. In step 3 the final simulation scenario is specified by formulating appropriate initial and boundary conditions as well as model parameters and input functions. The significance of such a structured modeling approach even for a simplified charge transport model is illustrated in the following example.

Example 1: Simplified ionic charge transport model. *The transport of n ionic species in a liquid electrolyte is described by the PDAE system* (Johannink et al., 2011, Newman and

Thomas-Alyea, 2004)

$$\frac{\partial c_k}{\partial t} = -\nabla \cdot \mathbf{J}_k - \nabla \cdot (\mathbf{v}\, c_k), \qquad k = 1, ..., n, \tag{3.1}$$

$$\mathbf{J}_k = -D_k \nabla c_k + \frac{z_k\, c_k}{RT} D_k\, F\, \mathbf{E}, \quad k = 1, ..., n, \tag{3.2}$$

$$\mathbf{E} = -\nabla \phi, \tag{3.3}$$

$$0 = \sum_{k=1}^{n} z_k\, c_k. \tag{3.4}$$

The scenario of an infinitely diluted isothermal solution is considered, so that the species balance equation for the solvent is trivially fulfilled and the transport processes do not affect the velocity $\boldsymbol{v}$ of the solvent. To simplify the problem, $\boldsymbol{v}$ is considered as a known input, e.g., provided by a possibly analytical solution of the Navier-Stokes equation. Next to the n species balance equations (3.1), the Nernst-Planck equations (3.2) are introduced to describe the flux densities $\boldsymbol{J}_k$ of ionic species as a superposition of transport induced by diffusion and by the electric field $\boldsymbol{E}$. Eq. (3.3) defines the electric field $\boldsymbol{E}$ as the negative gradient of the electric potential ϕ (Kontturi et al., 2008). The algebraic equation (3.4) corresponds to the well-known electroneutrality condition (Newman and Thomas-Alyea, 2004) enforcing a local space charge of zero. c_k is the volumetric concentration, D_k is the diffusion coefficient and z_k is the charge number of species k. The Faraday constant F, the gas constant R and the temperature T are constant model parameters.

On first inspection the model (3.1)-(3.4) appears to constitute no particular challenges neither for the physical interpretation of the model states nor for the numerical treatment using established modeling environments. However, first problems might get apparent when addressing the question which initial and boundary conditions are to specified to complete the problem formulation. The number of differential states in the Eqs. (3.1), (3.2) and (3.3) might lead to the assumption that n initial conditions, e.g., one for each concentration, and in total $2n + 1$ boundary conditions for each coordinate can be specified independently. However, as shown in the following such a specification is definitely inconsistent. With a certain amount of experience in modeling dynamic systems this inconsistency might be discovered right away by reasoning that the electroneutrality constraint (3.4) couples n apparently independent concentrations. However, even if this issue is identified right away, no ad hoc solution is available to overcome this problem.

Difficulties will certainly become apparent when the numerical treatment of the model (3.1)-(3.4) is directly addressed with standard methods. The application of a standard finite-difference scheme to discretize the spatial coordinates, e.g., the central finite-difference method (Strikwerda, 2004), implicating the specification of the eight boundary conditions, will yield a singular DAE model which cannot be solved at all. If a well-posed DAE model can be obtained, e.g., by applying a modified discretization scheme, it is very likely that a standard DAE integrator will fail as a consequence of the inconsistent specification of four initial conditions and the structural properties of the model (3.1)-(3.4). □

In recent works (Angermann and Rang, 2007, Martinson and Barton, 2000, Neumann, 2004, Neumann and Pantelides, 2008) powerful concepts have been developed to support the different

tasks in such a modeling work flow for distributed models. The focus has largely been directed toward criteria to assess important mathematical properties of the model and to support the consistent specification of initial and boundary conditions. An important theory in this context is the concept of the differential or perturbation index. Different definitions of these indices are reviewed in detail in Section 3.2. The essence of the concept of index is to distinguish PDAE systems that are characterized by a weak coupling of the partial-differential and the algebraic part from those where this coupling is more involved. The latter case is commonly denoted as a PDAE characterized by high index behavior.

In general, high index behavior is associated with several problems (Johannink et al., 2011, Martinson and Barton, 2001b): (i) From physical considerations it would be expected that all differential quantities with respect to time characterize the storage of extensive quantities and determine the dynamics of the system. However, some of these terms are coupled implicitly and the number of dynamic degrees of freedom is smaller than the apparent number of states occurring as differentials with respect to time. Likewise, not all states appearing in the model formulation as differential quantities with respect to the spatial coordinates show the behavior of evolution variables in space. (ii) Correspondingly, the specification of a consistent set of initial and boundary conditions is subject to "hidden" constraints, which are generally not satisfied by an intuitive approach. (iii) Quantities showing invariant behavior with respect to a specific independent variable (i.e., either time or space) do not get explicit from the model formulation or simulation results, hindering the physical interpretation of the model. (iv) Many of the established numerical methods based on the MOL approach fail, or even worse, will yield numerical solutions with an unbounded error.

All these critical aspects can be overcome if it is possible to derive equivalent model formulations which are characterized by indices not exceeding one. Such procedures are commonly known as index reduction. However, especially if the considered PDAE systems are large, this is a non-trivial task: The reduction of the index by remodeling (e.g., changing the reference frame or dropping a simplifying assumption) involves knowledge in numerical analysis, profound insight into the underlying physical phenomena and advanced modeling skills. An algorithmic index reduction usually increases the size – e.g., by introducing dummy-derivatives (Mattsson and Soderlind, 1993) – or the complexity – e.g., by repeated differentiation and substitution (Unger et al., 1995) – of the model. Thus, the numerical treatment is more involved and – more importantly – the explicit relation between the model states and the physical phenomena gets easily lost. In this chapter, a new method for a systematic index reduction of quasi-linear PDAE systems (Zauderer, 2006) is proposed. The procedure is based on the generalization of the concepts for index reduction of differential-algebraic equations which have been developed by Asbjørnsen and Fjeld (1970), Bachmann et al. (1990) and Moe (1995). The general idea of the index reduction method is to reveal quasi-linear combinations of the differential quantities in the high-index model which are invariant with respect to a specific independent variable. By using these quasi-linear combinations as templates for symbolic manipulations applied to the differential equations in the model, additional algebraic constraints become explicit. As these quasi-linear operations preserve the

physical information of the original differential equations, these hidden constraints can be used to substitute differential equations in order to reduce the index. In that manner, the reduction method does not increase the number of equations in the PDAE system. Further, the symbolic manipulations applied to the modeling equations are constructed to eliminate invariant terms and thus are simplifying the model. As the index reduction method is based on simple linear algebra concepts and symbolic manipulation, it can easily be implemented in a procedural manner.

The proposed method yields a reformulated PDAE system that is characterized by differential indices of one, which is an important prerequisite for the applicability of many MOL-based numerical methods. Further, since the additional constraints reduce the number of independent differential quantities in the model, the method provides valuable information for the specification of consistent initial and boundary conditions. Moreover, important information is obtained regarding those extensive quantities, which are invariant with respect to a specific independent variable, and hence reveal important physical principals represented in the model. As such, the reduction method is considered as a key component in any work flow for the development of distributed models.

3.2 Index concepts for DAE and PDAE systems

This section briefly introduces the established index concepts for DAE systems and their generalization to PDAE systems. As most of the indices are defined for specific scenarios and require a tailored terminology, the description is restricted to a conceptual level. For a formal description of the concepts, it is referred to the original publications.

3.2.1 Index concepts for DAE systems

The concept of an index has initially been developed for the characterization of DAE systems (Gear and Petzold, 1984, Petzold, 1982b). In the most general case, a DAE system is represented in the nonlinear implicit form $\mathbf{F}\left(\mathbf{z}, \frac{\partial \mathbf{z}}{\partial t}, \mathbf{u}\right) = \mathbf{0}$, $\mathbf{z}(t) \in \mathbb{R}^{n_z}$, $\mathbf{u}(t) \in \mathbb{R}^{n_u}$, $\mathbf{F} : \mathbb{R}^{n_z} \times \mathbb{R}^{n_z} \times \mathbb{R}^{n_u} \rightarrow \mathbb{R}^{n_z}$. Here, $\mathbf{z}(t)$ represents the vector of unknown state variables; $\mathbf{u}(t)$ is the vector of known inputs.

In the mathematical and application-oriented literature, a large number of different indices have been defined. Numerous different definitions are reviewed in detail in Campbell and Marszalek (1999) and Gear (1990). Principally, two index definitions are to be distinguished: the differential index ν_d and the perturbation index ν_p.

The perturbation index ν_p

The perturbation index has been introduced by Hairer et al. (1989) and is formalized in

Definition 1 (Unger et al., 1995): *The DAE system* $\boldsymbol{F}\left(\boldsymbol{z}, \frac{\partial \boldsymbol{z}}{\partial t}, \boldsymbol{u}\right) = \boldsymbol{0}$ *has the perturbation index* ν_p *along a solution* $\boldsymbol{z}(t)$ *for* t *in a bounded interval* I *and given forcing function* $u(t)$*, if* ν_p *is the smallest integer, so that, for all functions* $\hat{\boldsymbol{z}}(t)$ *having a defect*

$$\mathbf{F}\left(\hat{\mathbf{z}}, \frac{\partial \hat{\mathbf{z}}}{\partial t}, \mathbf{u}\right) = \delta(t),$$

there exists an estimate

$$\|\hat{\mathbf{z}}(t) - \mathbf{z}(t)\| \leq C \|\hat{\mathbf{z}}(0) - \mathbf{z}(0)\| + \max_{0\leq\tau\leq t} \|\delta(\tau)\| + ... + \max_{0\leq\tau\leq t} \left\|\delta^{\nu_p - 1}(\tau)\right\|$$

on I, whenever $\delta(t)$ is sufficiently small. C denotes a constant which depends only on $\boldsymbol{F}(\cdot)$ and the length of the interval I.

According to this definition, the perturbation index ν_p represents a quantitative measure of the sensitivity of the solution with respect to the model structure (Unger et al., 1995). In the context of the numerical solution of DAE systems with (semi-) implicit integrators, ν_p characterizes the behavior of the roundoff error (Campbell and Marszalek, 1999). Hence, the perturbation index can be seen as the key quantity characterizing the effort associated with a numerical solution of the DAE system.

The differential index ν_d

The concept of differential index ν_d (Brenan et al., 1996) is based on solvability arguments of a linear constant coefficient DAE system $\mathbf{M}\frac{\partial \mathbf{z}}{\partial t} + \mathbf{L}\mathbf{z} + \mathbf{u}(t) = \mathbf{0}$, $\mathbf{u}(t) \in \mathbb{R}^{n_z}$. Here, $\mathbf{M}, \mathbf{L} \in \mathbb{R}^{n_z \times n_z}$ are constant coefficient matrices forming the matrix pencil $\lambda\mathbf{M} + \mathbf{L}$. This pencil provides important information concerning the solvability of the considered DAE system: A constant coefficient DAE system has a unique solution, if the pencil $\lambda\mathbf{M} + \mathbf{L}$ fulfills the regularity condition $\det(\lambda\mathbf{M} + \mathbf{L}) \neq 0$, $\exists\, \lambda \in \mathbb{R}$.[1] If this condition is fulfilled for a given DAE system, the structure of its solution can be examined by exploiting the nilpotency ν_M of the pencil. The nilpotency ν_M corresponds to the number of differentiations required to transform the DAE system into a system of ordinary differential equations (ODE). The derivation of this underlying ODE system reveals that for $\nu_M > 1$ (Brenan et al., 1996): (i) The number of differential quantities in the DAE system does not correspond to the number of independent initial conditions. (ii) The model formulation implicitly defines additional algebraic relations. These 'hidden' constraints have to be fulfilled by every solution of the DAE system. (iii) The solution of the DAE system depends on $\nu_M - 1$ derivatives of the forcing function $\mathbf{u}(t)$. Thus, for non-smooth forcing, the solution contains discontinuous modes.

The solvability properties of linear constant coefficient DAE systems cannot be generalized to the general nonlinear case. However, it turned out useful to consider the concept of the nilpotency index ν_M in a generalized form, resulting in the differential index ν_d defined as follows:

Definition 2 (cf. Brenan et al. (1996)): *The minimal number of differentiations with respect to time that are to be applied upon all or a subset of the equations of the DAE system $\boldsymbol{F}\left(\boldsymbol{z}, \frac{\partial \boldsymbol{z}}{\partial t}, \boldsymbol{u}\right) = \boldsymbol{0}$ in order to determine $\frac{\partial \boldsymbol{z}}{\partial t}$ as a continuous function of $\boldsymbol{z}$ and $\boldsymbol{u}$ is called the differential index ν_d of the DAE system.*

The differential index reflects – in analogy to ν_M – important characteristics of the structure of the equations forming the DAE system. In case a given DAE system is characterized by $\nu_d > 1$, the same problems (i)-(iii) are encountered as for linear DAE systems with $\nu_M > 1$ (Unger et al., 1995).

[1] This condition is both necessary and sufficient.

For nonlinear DAE systems, ν_d can vary locally along the solution trajectory $\mathbf{z}(t)$. A common approach to obtain a global estimate of the differential index for the entire solution space, is the introduction of the structural index ν_s (cf. e.g., Pantelides (1988), Unger et al. (1995)). Whereas the concept of ν_s is based on the definition of ν_d, a conceptually different approach is used in the technical realization of the index analysis. The analyses differ with respect to a qualitative or quantitative evaluation of the dependent variables: In case of ν_d the analysis considers the numerical values of the dependent variables, while in case of ν_s the analysis only considers their structural occurrence. That way, local changes of the modeling equations, e.g., if the numerical value of certain quantities becomes zero, are excluded from the analysis. As a result an estimate of a non-local approximation of the differential index is obtained. However, it is to be noted that for specific DAE systems ν_s can strongly differ from ν_d (Reissig et al., 2000).

Perturbation vs. differential index

For a linear constant coefficient DAE the perturbation and differentiation index coincide, i.e. $\nu_p = \nu_d$ (Strehmel, 1992). In the nonlinear case, the differential index possibly underestimates the perturbation index (Campbell and Marszalek, 1999). Thus, for the characterization of general nonlinear DAE, some authors (Angermann and Rang, 2007, Campbell and Marszalek, 1999) consider the perturbation index as the more appropriate measure. However, Gear (1990) has shown that the coincidence of ν_d and ν_p also holds for nonlinear semi-explicit DAE systems,

$$\dot{\mathbf{x}} = \mathbf{f}(\mathbf{x},\, \mathbf{y},\, \mathbf{u})\,, \tag{3.5}$$

$$0 = \mathbf{g}(\mathbf{x},\, \mathbf{y},\, \mathbf{u})\,, \tag{3.6}$$

where the quantities $\mathbf{z}$ and $\mathbf{F}$ have been split up according to $\mathbf{z} = \left[\mathbf{x}^T,\, \mathbf{y}^T\right]^T$ and $\mathbf{F} = \left[\mathbf{f}^T,\, \mathbf{g}^T\right]^T$ with $\mathbf{x} \in \mathbb{R}^{n_x}$, $\mathbf{y} \in \mathbb{R}^{n_y}$, $n_x + n_y = n_z$, $\mathbf{f}\colon \mathbb{R}^{n_x} \times \mathbb{R}^{n_y} \times \mathbb{R}^{n_u} \to \mathbb{R}^{n_x}$ and $\mathbf{g}\colon \mathbb{R}^{n_x} \times \mathbb{R}^{n_y} \times \mathbb{R}^{n_u} \to \mathbb{R}^{n_y}$. Here, it is important to note that, at least locally, every nonlinear implicit DAE-system can be represented in semi-explicit form, e.g., by introducing the additional states $h(t) \in \mathbb{R}^{n_z}$ and the transformation (Otter, 1996)

$$\mathbf{0} = \mathbf{F}\left(\mathbf{z},\, \frac{\partial \mathbf{z}}{\partial t},\, \mathbf{u}\right) \quad \Longrightarrow \begin{pmatrix} \dot{\mathbf{z}} \\ \mathbf{0} \end{pmatrix} = \begin{pmatrix} \mathbf{h} \\ \mathbf{F}\,(\mathbf{z},\, \mathbf{h},\, \mathbf{u}) \end{pmatrix}. \tag{3.7}$$

Accordingly, for nonlinear DAE systems ν_d and ν_p always coincide if the index analysis is applied to the semi-explicit representation of the system. Thus, concerning the characterization of a given DAE system in the modeling process, the same results can be expected from both concepts. However, the concept of ν_p has severe limitations (Martinson and Barton, 2000):

(i) The definition of ν_p is based directly on the solution of the DAE system. Thus, its quantification requires a closed expression of the solution or at least its structural form. For general DAE systems, this is not available.

(ii) Even if the solution were available, it relies on an a priori specification of the initial conditions. Hence, the concept is inadequate to evaluate the consistency of initial conditions.

(iii) The actual evaluation of ν_p for nonlinear DAE systems with known analytical solution still requires a high level of expertise in order to evaluate the different norms properly.

Thus, ν_p is inadequate for a rapid and possibly automated evaluation of large DAE systems.

Differential index and consistent initialization

An important problem when working with DAE models is the identification of consistent initial conditions. The consistent initialization problem is best illustrated if the DAE system is considered as an ODE system defined on a manifold in the state space (Rheinboldt, 1984). The dimension and the shape of the manifold is most easily accessible for semi-explicit DAE systems (3.5), (3.6) of $\nu_d = 1$. Here, the n_y-dimensional manifold can be explicitly represented by

$$M = \{\mathbf{x},\, \mathbf{y},\, \mathbf{u}(t = t_0) = \mathbf{u}_0 \,|\, 0 = \mathbf{g}\,(\mathbf{x},\, \mathbf{y},\, \mathbf{u}_0)\}. \tag{3.8}$$

The ODE system defined on this manifold is then given by Eq. (3.5).

For this setting it is obvious that the maximal number of independent initial conditions, also referred to as dynamic degrees of freedom (Unger et al., 1995), corresponds to the dimension of the system of underlying ODE. In order to be consistent, these initial conditions are to be specified according to:

Definition 3: *The vectors $\boldsymbol{x}_0$, $\dot{\boldsymbol{x}}_0$ and $\boldsymbol{y}_0$ are consistent initial conditions of a DAE system in semi-explicit form with $\nu_d = 1$ if they uniquely solve the DAE system (3.5) and (3.6) at $t = t_0$.*

The connection of index and consistent initialization gets obvious recalling that in case $\nu_d > 1$ 'hidden' constraints are to be satisfied by any solution of the DAE system. Accordingly, the manifold M associated to the consistent initialization problem is in general not only formed by the explicit algebraic equations but also by the 'hidden' constraints implicitly defined in the DAE system. Thus, the properties – especially the dimension – of the manifold are not directly accessible for a DAE system with $\nu_d > 1$. Hence, in order to identify a consistent set of initial conditions, the algebraic manifold M has to be made explicit. One approach is to apply index reduction to derive an equivalent formulation of the DAE system, which is characterized by $\nu_d = 1$. This way, the manifold (3.8) is explicitly derived and the consistent initialization problem can be solved according to Definition 3.

An alternative approach for the identification of consistent initial conditions is based on the derivation of an extended system as suggested by Unger et al. (1995).

3.2.2 Index concepts for PDAE systems

The generalization of the introduced index concepts to PDAE systems have been addressed in numerous works. Similar to DAE systems, perturbation indices (Campbell and Marszalek, 1999, Marszalek and Trzaska, 1995, Matthes, 2012, Rang and Angermann, 2005) and differential indices (Lucht et al., 1999, Martinson, 2000, Sternberg, 2006) have been defined for specific types of PDAE systems. Before presenting the different concepts, the formal representation of the PDAE systems considered in this work is briefly introduced.

Formal representation of PDAE systems

If not otherwise stated, it is referred to PDAE systems defined in the independent variables $\zeta = \{t, x_1, ..., x_d\}$, where $t \in [t_0, t_f]$ is time and $x_k \in \left[x_k^L, x_k^U\right]$, $k = 1, ..., d$, are the spatial coordinates with appropriate lower and upper bounds. The general structure of a first-order, possibly nonlinear, PDAE system is

$$0 = \mathbf{F}\left(\frac{\partial \omega}{\partial \zeta}, \omega, \mathbf{u}, \mathbf{p}, \zeta\right) \tag{3.9}$$

with states $\omega(\mathbf{x}, t) \in \mathbb{R}^{n_\omega}$, inputs $\mathbf{u}(t) \in \mathbb{R}^{n_u}$, parameters $\mathbf{p} \in \mathbb{R}^{n_p}$ and state derivatives

$$\frac{\partial \omega}{\partial \zeta} = \left[\frac{\partial \omega}{\partial t}, \frac{\partial \omega}{\partial x_1}, ..., \frac{\partial \omega}{\partial x_d}\right]. \tag{3.10}$$

The system has to be completed by consistent initial and boundary conditions. Initial conditions are specified as

$$0 = \mathbf{f}^{IC}\left(\phi_0^{IC}, \left.\frac{\partial \omega}{\partial \zeta}\right|_{t=t_0}, \omega|_{t=t_0}, \mathbf{u}, \mathbf{p}, \mathbf{x}\right), \tag{3.11}$$

where $\phi_0^{IC}(\mathbf{x}) \in \mathbb{R}^{n_{IC}}$ is a vector of known initial values and $\mathbf{f}^{IC} : \mathbb{R}^{n_{IC}} \times \mathbb{R}^{n_\omega} \times \mathbb{R}^{n_\omega} \times \mathbb{R}^{n_u} \times \mathbb{R}^{n_p} \times \mathbb{R}^d \to \mathbb{R}^{n_{IC}}$ is an arbitrary function. n_{IC} corresponds to the number of initial conditions that can be specified independently. It is important to note that in general $n_{IC} \neq n_\omega$.

Boundary conditions are specified at the lower and upper bounds x_k^L and x_k^U, $k = 1, ..., d$, as

$$0 = \mathbf{f}_k^{BC,L}\left(\phi_k^{BC,L}, \left.\frac{\partial \omega}{\partial \zeta_i}\right|_{x_k = x_k^L}, \omega|_{x_k = x_k^L}, \mathbf{u}, \mathbf{p}, t\right), k = 1, ..., d, \tag{3.12}$$

$$0 = \mathbf{f}_k^{BC,U}\left(\phi_k^{BC,U}, \left.\frac{\partial \omega}{\partial \zeta_i}\right|_{x_k = x_k^U}, \omega|_{x_k = x_k^U}, \mathbf{u}, \mathbf{p}, t\right), k = 1, ..., d, \tag{3.13}$$

where $\phi_k^{BC,L}\left(t, \mathbf{x}|_{x_k = x_k^L}\right) \in \mathbb{R}^{n_{BC,x_k^L}}$ and $\phi_k^{BC,U}\left(t, \mathbf{x}|_{x_k = x_k^U}\right) \in \mathbb{R}^{n_{BC,x_k^U}}$ are prescribed values possibly varying in time and the spatial coordinates. $\mathbf{f}_k^{BC,x_k^L} : \mathbb{R}^{n_{BC,L}} \times \mathbb{R}^{n_\omega} \times \mathbb{R}^{n_\omega} \times \mathbb{R}^{n_u} \times \mathbb{R}^{n_p} \times \mathbb{R} \to \mathbb{R}^{n_{BC,x_k^L}}$ and $\mathbf{f}_k^{BC,U} : \mathbb{R}^{n_{BC,x_k^U}} \times \mathbb{R}^{n_\omega} \times \mathbb{R}^{n_\omega} \times \mathbb{R}^{n_u} \times \mathbb{R}^{n_p} \times \mathbb{R} \to \mathbb{R}^{n_{BC,x_k^U}}$ are arbitrary functions. The number of boundary conditions that can be specified independently at x_k^L and x_k^U are n_{BC,x_k^U} and n_{BC,x_k^L}, respectively.

The consistent specification of initial and boundary conditions (3.11), (3.12) and (3.13) will be discussed in Section 3.4.2. For all specific PDAE systems introduced in the remainder of this paper, it is assumed that initial and boundary conditions are specified in order to obtain a closed problem formulation.

MOL-based indices

MOL-based indices have been introduced for initial-boundary value problems, where the independent variables in the PDAE system are time t and spatial coordinates $\mathbf{x}$, i.e., $\zeta = \{t, x_1, ..., x_d\}$ in a d-dimensional spatial domain (Campbell and Marszalek, 1996, Sternberg, 2006, Weickert, 1996). The different index concepts for DAE systems can be directly applied if a MOL approach is used

to discretize the spatial derivatives, e.g., by finite difference or finite element approximations. This semi-discretization transforms the PDAE (3.9) into the MOL-DAE

$$\mathbf{G}\left(\dot{\mathbf{m}},\, \mathbf{m},\, \mathbf{u},\, \mathbf{p}\right) = 0, \tag{3.14}$$

where $\mathbf{m}\left(t\right)$ are function vectors concatenating all unknown functions $\omega\left(t,\, \mathbf{x}\right)$ on lines through the gridpoints of the spatial discretization (Sternberg, 2006). Index analysis with respect to time as the only remaining independent variable can then be applied to the semi-discretized system (3.14).

An evaluation of the concept of MOL-based index for linear PDAE is reported by Campbell and Marszalek (1996). In summary, mostly the index of the MOL-DAE (3.14) can be associated with the structural properties of the original PDAE (3.9). However, it is pointed out that the MOL-based index might depend on the specific domain considered or on the specific spatial discretization method applied.

Perturbation indices for abstract DAE

Following the general concept of semi-discretization, however leaving the actual approximation of the partial derivatives with respect to the spatial coordinates on a more abstract level, concepts for the perturbation index of a PDAE system have been worked out. Abstract DAE systems are derived from PDAE systems, which are quasi-linear with respect to time, by representing the spatial operators in the form of eigenfunctions (Marszalek and Trzaska, 1995), an orthogonal basis (Campbell and Marszalek, 1999) or a weak formulation (Rang and Angermann, 2005).

For these abstract DAE systems, the perturbation index with respect to time is defined as a straightforward generalization of Definition 1. The resulting index with respect to time characterizes the sensitivity with respect to perturbations in the initial values, boundary conditions and forcing functions.

Differential indices for linear and quasi-linear PDAE systems

Differential indices for time t and spatial coordinate x as the independent variables in the linear second-order PDAE system a in one-dimensional spatial domain

$$\mathbf{A}\,\frac{\partial \omega}{\partial t} + \mathbf{B}\,\frac{\partial^2 \omega}{\partial x^2} + \mathbf{C}\,\omega + \mathbf{f}\left(t,\, x\right) = 0, \quad \omega\left(x,\, t = 0\right) = \omega_0\left(x\right) \tag{3.15}$$

with constant coefficient matrices $\mathbf{A},\, \mathbf{B}, \mathbf{C} \in \mathbb{R}^{n_\omega \times n_\omega}$ has been introduced by Eichler-Liebenow (1999). Here, the Laplace transformation

$$\omega_\xi\left(x\right) = \int_0^\infty e^{-t\,\xi} \omega\left(x, t\right) dt, \tag{3.16}$$

is used to transform the differential operator with respect to time t. For the resulting transformed system

$$\mathbf{B}\,\frac{\partial^2 \omega_\xi}{\partial x^2} + \left(\xi\,\mathbf{A} + \mathbf{C}\right)\omega_\xi + \mathbf{f}_\xi\left(t,\, x\right) + \mathbf{A}\,\omega_0 = 0, \tag{3.17}$$

a differential index with respect to the spatial coordinate is defined. The definition is based on the nilpotency of the pencil $(\lambda \mathbf{B} + \xi\, \mathbf{A} + \mathbf{C})$ and the established theory for linear constant coefficient DAE systems (cf. Section 3.2.1). In an analogous manner, a Fourier transformation is used to transform the spatial operator, which allows the definition of a differential index with respect to time.

A similar approach has been proposed by Campbell and Marszalek (1999), who define algebraic indices for the linear PDAE system

$$\mathbf{A}\,\frac{\partial \omega}{\partial t} + \mathbf{B}\,\frac{\partial^2 \omega}{\partial x^2} + \mathbf{D}\,\frac{\partial \omega}{\partial x} + \mathbf{C}\,\omega + \mathbf{f}(t,\, x) = 0, \tag{3.18}$$

which differs from (3.15) by the first order term $\mathbf{D}\,\frac{\partial \omega}{\partial x}$, $\mathbf{D} \in \mathbb{R}^{n_\omega \times n_\omega}$. For the definition of the algebraic indices Campbell and Marszalek (1999) consider the algebraic system resulting from a Laplace transformation of (3.18) in the form of the resolvent

$$R\,(\psi, \xi) = \left(\psi \mathbf{A} + \xi^2 \mathbf{D} + \xi \mathbf{C} + \mathbf{B}\right)^{-1}. \tag{3.19}$$

With this representation of Eq. (3.18), the algebraic indices are defined as follows:

Definition 4 (Campbell and Marszalek, 1999): *For the linear PDAE system (3.18) the smallest integer $\nu_{a,t}$ yielding $\lim_{|\psi|\to\infty} \psi^{\nu_{a,t}} R\,(\psi, \xi) = 0$ is the algebraic index with respect to time. The algebraic index with respect to the spatial coordinate x is defined as the smallest integer $\nu_{a,x}$, so that $\lim_{|\xi|\to\infty} \xi^{\nu_{a,x}} R\,(\psi, \xi) = 0$.*

Differential indices for PDAE as pseudo-DAE on hyperplanes

A conceptually different approach for the definition of differential indices of PDAE systems has been proposed by Martinson and Barton (2000). The theory is applicable for first-order, possibly nonlinear, PDAE (3.9) in n_l independent variables $\zeta = \{\zeta_1, ..., \zeta_{n_l}\}$. It is assumed that a unique solution exists over a rectangular domain defined by $\zeta_i \in \mathcal{I}_i \subset \mathbb{R}$, $i = 1, ..., n_l$. The approach is motivated by generalizing the consistent initialization problem of DAE systems (cf. Section 3.2.1) to a scenario with n_l independent variables as encountered in PDAE systems. In this context, Martinson and Barton (2000) consider a $(n_l - 1)$-dimensional hyperplane specified by $\zeta_j = const.$ and $\zeta_i \in \mathcal{I}_i$, $i \in \{1, ..., n_l\}$, $i \neq j$, in the n_l-dimensional space spanned by the independent variables. This hyperplane is regarded as a generalization of the zero-dimensional initial point $t = 0$ in the case of a DAE system.

The key element of the index definition is the discrimination of interior and exterior derivatives with respect to a specific hyperplane. Here, the partial derivative $\left.\frac{\partial \omega}{\partial \zeta_j}\right|_{\zeta_j = const.}$ is the (only) exterior derivative; the derivatives $\left.\frac{\partial \omega}{\partial \zeta_i}\right|_{\zeta_j = const.}$, $i \in \{1, ..., n_l\}$, $i \neq j$, are interior derivatives. It is important to note that the values of the dependent variables $\omega|_{\zeta_j = const.}$ over the hyperplane completely determine the interior derivatives $\left.\frac{\partial \omega}{\partial \zeta_i}\right|_{\zeta_j = const.}$, $i \in \{1, ..., n_l\}$, $i \neq j$. This allows the definition of the differential index with respect to the exterior direction of the hyperplane without the introduction of a detailed concept for the approximation of the interior derivatives as follows:

Definition 5 (Martinson and Barton, 2000): *The differentiation index with respect to* ζ_j, ν_{d,ζ_j}, *is the smallest number of times* $\boldsymbol{F}(\cdot)$ *in (3.9) must be differentiated with respect to* ζ_j *in order to determine* $\frac{\partial \omega}{\partial \zeta_j}$ *as a continuous function of* ω, $\frac{\partial \omega}{\partial \zeta_i}$, $i \in \{1, ..., n_l\}$, $i \neq j$, $\boldsymbol{u}(t)$, $\boldsymbol{p}$ *and* ζ_i, $i \in \{1, ..., n_l\}$, $i \neq j$.

This definition motivates the characterization of a PDAE system by systematically evaluating the differential indices ν_{d,ζ_j} on all hyperplanes $\zeta_j = const.$, $j = 1, ..., n_l$. For an analytic or algorithmic index analysis based on Definition 5, a formal representation of the interior derivatives is still needed. The approach used by Martinson and Barton (2000) considers the interior derivatives $\frac{\partial \omega}{\partial \zeta_i}$, $i \in \{1, ..., n_l\}$, $i \neq j$, as instances of the dependent variable ω itself multiplied with nonzero operator-valued coefficients $\frac{\partial}{\partial \zeta_i}$, $i \in \{1, ..., n_l\}$, $i \neq j$. Accordingly, in the course of index analysis with respect to ζ_j, the PDAE system is considered as the pseudo-DAE system

$$0 = \bar{\mathbf{F}} \left(\frac{\partial \omega}{\partial \zeta_j}, \omega, \mathbf{u}, \mathbf{p}, \zeta \right) \tag{3.20}$$

with $\bar{\mathbf{F}} : \mathbb{R}^{n_\omega} \times \mathbb{R}^{n_\omega} \times \mathbb{R}^{n_u} \times \mathbb{R}^{n_p} \times \mathbb{R}^{n_l} \rightarrow \mathbb{R}^{n_\omega}$ containing the operator-valued coefficients $\frac{\partial}{\partial \zeta_i}$, $i \in \{1, ..., n_l\}$, $i \neq j$.

The occurrence of the operator-valued coefficients in $\bar{\mathbf{F}}$ affects the technical realization of an algorithmic analysis of the differential index. However, as shown by Martinson (2000), it does not constrain any symbolic manipulation of equations in the course of the analysis. The concept and algorithms for a structural index analysis (e.g., Pantelides (1988), Unger et al. (1995)) can readily be applied to the pseudo-DAE systems (3.20) as the corresponding structural representation of the interior derivatives $\frac{\partial \omega}{\partial \zeta_i}$, $i \in \{1, ..., n_l\}$, $i \neq j$, coincides with the structural representation of the variables ω themselves.

3.2.3 Comparison of the index concepts for PDAE systems

PDAE systems differ from DAE systems by a larger number of independent variables. Hence, the generalization of the DAE index concepts to PDAE systems is generally approached by deriving a transformed system, in which all derivatives of the dependent variables with respect to $n_l - 1$ independent variables are completely determined by the values of the dependent variables themselves. This is achieved by either introducing adequate finite-dimensional approximations of these derivatives or defining a specific scenario on lower-dimensional hyperplanes. The index is then defined for this transformed abstract or pseudo-DAE, using the same definitions as for DAE systems.

In analogy to the DAE case, the conceptually different perturbation and differential indices are distinguished. The concept of a perturbation index for PDAE requires the introduction of a specific approximation of the spatial operators, the analytical solution of the resulting abstract DAE system and an a priori specification of initial and boundary conditions. The concepts of a differential index for PDAE systems neither require such a priori specification and nor the solution of the problem. Further, the approximation of the remaining differential operators or interior derivatives is addressed on a rather conceptual level so that the index analysis does not

depend on the introduction of a specific representation. Correspondingly, the latter concept is considered more useful for the identification of consistent initial and boundary conditions of a given PDAE system in a modeling process.

From the different definitions of a differential index the approach of Martinson and Barton (2000) stands out as it is applicable to general nonlinear PDAE systems. Further, its relation to consistent initialization of DAE systems makes it useful for the identification of a consistent set of initial and boundary conditions of PDAE systems. Hence, in the remainder of this work Definition 5 and the corresponding theory developed by Martinson and Barton (2000) is used. However, a formally different nomenclature is introduced which is tailored to PDAE systems in semi-explicit form with respect to all independent variables. As shown in the following, an efficient method for the reduction of the index can be derived for such semi-explicit systems. Further, it can be expected that the differential indices defined in this way are better estimates for the perturbation index, generalizing the reasoning of Gear (1990) and Otter (1996) to the PDAE case.

3.3 Index analysis and reduction for semi-explicit PDAE systems

This section first introduces the definition of the differential index for PDAE systems cast in semi-explicit pseudo-DAE on hyperplanes. This definition motivates the characterization and – if required – the reformulation of the PDAE system by means of a successive treatment of the pseudo-DAE. Following this idea, a systematic procedure for index analysis and reduction is derived. Before depicting the procedure in detail, the two principal tasks are introduced: (i) index analysis and (ii) index reduction of a pseudo DAE with respect to an independent variable ζ_j.

3.3.1 Differential index

For the definition of the differential index a PDAE system (3.9) is considered, for which a solution is assumed to exist if a set of consistent initial and boundary conditions is specified. Further, the solution is assumed to be sufficiently differentiable to allow the interchangeability of partial derivatives according to Young's theorem (Young, 1912), i.e., $\frac{\partial^2 \omega_k}{\partial \zeta_j \partial \zeta_i} = \frac{\partial^2 \omega_k}{\partial \zeta_i \partial \zeta_j}$ holds for all i, j. For notational simplicity the explicit dependence of the PDAE system (3.9) on ζ will be dropped as this can easily be eliminated by introducing additional states.

Following Definition 5, the PDAE system (3.9) is considered as a set of pseudo-DAE on hyperplanes in the course of the index analysis. However, it is required that all n_l pseudo-DAE can be transformed into the semi-explicit form

$$\frac{\partial \mathbf{w}}{\partial \zeta_j} = \mathbf{f}\left(\frac{\partial \mathbf{w}}{\partial \zeta_i}, \mathbf{w}, \frac{\partial \mathbf{y}_1}{\partial \zeta_i}, \mathbf{y}_1, \frac{\partial \mathbf{y}_2}{\partial \zeta_i}, \mathbf{y}_2, \mathbf{u}, \mathbf{p}\right), \tag{3.21}$$

$$\mathbf{0} = \mathbf{g}\left(\frac{\partial \mathbf{w}}{\partial \zeta_i}, \mathbf{w}, \frac{\partial \mathbf{y}_1}{\partial \zeta_i}, \mathbf{y}_1, \mathbf{u}, \mathbf{p}\right), \quad j, i \in \{1, ..., n_l\},\ i \neq j, \tag{3.22}$$

with $\mathbf{w}\left(\mathbf{x}, t\right)$, $\mathbf{f}: \mathbb{R}^{n_w} \times \mathbb{R}^{n_w} \times \mathbb{R}^{n_{y_1}} \times \mathbb{R}^{n_{y_1}} \times \mathbb{R}^{n_{y_2}} \times \mathbb{R}^{n_{y_2}} \times \mathbb{R}^{n_u} \times \mathbb{R}^{n_p} \to \mathbb{R}^{n_w}$ and $\mathbf{y} = \left[\mathbf{y}_1^T, \mathbf{y}_2^T\right]^T$, $\mathbf{g}: \mathbb{R}^{n_w} \times \mathbb{R}^{n_w} \times \mathbb{R}^{n_{y_1}} \times \mathbb{R}^{n_{y_1}} \times \mathbb{R}^{n_u} \times \mathbb{R}^{n_p} \to \mathbb{R}^{n_y}$, $n^\omega = n^w + n^y$. In this form, the

model equations are assorted into differential (3.21) and pseudo-algebraic equations (3.22) with respect to the independent variable ζ_j. The pseudo-algebraic equations (3.22) possibly contain partial differential operators $\frac{\partial}{\partial \zeta_i}$, $i \in \{1, ..., n_l\}$, $i \neq j$. The vector $\mathbf{w}$ comprises the differential quantities with respect to ζ_j, $j = 1, ..., n_l$. All the remaining dependent variables, i.e., the variables for which no derivatives with respect to ζ_j occur, are referred to as pseudo-algebraic variables $\mathbf{y}$. These pseudo-algebraic variables are further distinguished whether they occur only in the differential equations or in both the differential and the pseudo-algebraic equations. According to this criterion the variables are assorted to the vectors $\mathbf{y}_2$ and $\mathbf{y}_1$, respectively.

Example 1 (cont.): *The model (3.1)-(3.4) corresponds to a PDAE system in the set of independent variables* $\zeta = \{t, x_1, x_2, x_3\}$. *With respect to the independent variable* $\zeta_j = t$, *it is in semi-explicit form (3.21), (3.22) already, with* $\boldsymbol{w} = [c_1 \dots c_n]^T$, $\boldsymbol{y}_1 = [\boldsymbol{J}_1, \dots, \boldsymbol{J}_n, \boldsymbol{E}, \phi]^T$, $\boldsymbol{u} = v$ *and* $\boldsymbol{p} = [z_1 \dots z_n, D_1 \dots D_n, R, T, F]^T$. *The system can easily be reformulated to a first-order system which is semi-explicit with respect to* $\zeta_j = x_1$, $\zeta_j = x_2$ *and* $\zeta_j = x_3$, *respectively.* □

For the set of pseudo-DAE (3.21), (3.22) differential indices with respect to all independent variables $\zeta_j, j = 1, ..., n_l$, can be defined following Definition 6.

Definition 6 (Martinson and Barton, 2000): *The differential index* ν_{d,ζ_j} *with respect to the independent variable* ζ_j *is defined as the minimal number of differentiations that have to be applied to (3.21), (3.22) or a subset of equations in (3.21), (3.22) to determine* $\frac{\partial \boldsymbol{w}}{\partial \zeta_j}$, $\frac{\partial \boldsymbol{y}_1}{\partial \zeta_j}$ *and* $\frac{\partial \boldsymbol{y}_2}{\partial \zeta_j}$ *as continuous functions of* $\frac{\partial \boldsymbol{w}}{\partial \zeta_i}$, $\frac{\partial \boldsymbol{y}_1}{\partial \zeta_i}$, $\frac{\partial \boldsymbol{y}_2}{\partial \zeta_i}$, $i \in \{1, ..., n_l\}, i \neq j$, $\boldsymbol{w}, \boldsymbol{y}_2$ *and* $\boldsymbol{y}_1$ *for given* $\boldsymbol{u}(t)$ *and* $\boldsymbol{p}$.

Following Martinson (2000), by introducing operator-valued coefficients for the formal representation of the interior derivatives $\frac{\partial \mathbf{w}}{\partial \zeta_i}$, $\frac{\partial \mathbf{y}_1}{\partial \zeta_i}$ and $\frac{\partial \mathbf{y}_2}{\partial \zeta_i}$, $i \in \{1, ..., n_l\}$, $i \neq j$, the semi-explicit pseudo-DAE system (3.21), (3.22) can be represented as

$$\frac{\partial \mathbf{w}}{\partial \zeta_j} = \bar{\mathbf{f}}\left(\mathbf{w}, \mathbf{y}_1, \mathbf{y}_2, \mathbf{u}, \mathbf{p}\right), \tag{3.23}$$

$$\mathbf{0} = \bar{\mathbf{g}}\left(\mathbf{w}, \mathbf{y}_1, \mathbf{u}, \mathbf{p}\right), \quad j = 1, ..., n_l, \tag{3.24}$$

with $\bar{\mathbf{f}}\colon \mathbb{R}^{n_w} \times \mathbb{R}^{n_{y1}} \times \mathbb{R}^{n_{y2}} \times \mathbb{R}^{n_u} \times \mathbb{R}^{n_p} \to \mathbb{R}^{n_w}$ and $\bar{\mathbf{g}}\colon \mathbb{R}^{n_w} \times \mathbb{R}^{n_{y1}} \times \mathbb{R}^{n_u} \times \mathbb{R}^{n_p} \to \mathbb{R}^{n_y}$.

3.3.2 Index analysis

The criterion for the pseudo-DAE system (3.23), (3.24) to be of index $\nu_{d,\zeta_j} > 1$ is

$$\det\left(\frac{\partial \bar{\mathbf{g}}\left(\mathbf{w}, \mathbf{y}_1, \mathbf{u}, \mathbf{p}\right)}{\partial \mathbf{y}_1}\right) = 0. \tag{3.25}$$

It expresses the fact that the pseudo-algebraic variables $\mathbf{y}_1$ are not uniquely determined by the set of pseudo-algebraic equations, i.e., the set of equations (3.24) is structurally singular with respect to $\mathbf{y}_1$.

In many cases, the structural singularity of the pseudo-algebraic equations (3.24), and thus the high-index behavior, is caused by a subsystem of pseudo-algebraic equations

$$\mathbf{0} = \Omega_{\zeta_j}\left(\mathbf{w}, \mathbf{y}_1, \mathbf{u}, \mathbf{p}\right), \tag{3.26}$$

of (3.24) with $\Omega_{\zeta_j} : \mathbb{R}^{n_w} \times \mathbb{R}^{n_{y_1}} \times \mathbb{R}^{n_u} \times \mathbb{R}^{n_p} \to \mathbb{R}^{n_{\Omega_{\zeta_j}}}$, $n_\Omega \leq n_y$. Formally, such a subsystem, – referred to as minimal structurally singular subsystem (MSSS)– is defined as the smallest subsystem of the pseudo-algebraic equations (3.24) which is structurally singular (Neumann, 2004), i.e. which has the property

$$\det\left(\frac{\partial \Omega_{\zeta_j}\left(\mathbf{w}, \tilde{\mathbf{y}}_1, \mathbf{u}, \mathbf{p}\right)}{\partial \tilde{\mathbf{y}}_1}\right) = 0 \tag{3.27}$$

for any pseudo-algebraic variables $\tilde{\mathbf{y}}_1$ taken from $\mathbf{y}_1$ with $\dim\left(\tilde{\mathbf{y}}_1\right) \leq \dim\left(\mathbf{y}_1\right)$ and $\dim(\tilde{\mathbf{y}}_1) \leq n_\Omega$ (Neumann, 2004). Due to this property, the MSSS couples differential quantities by algebraic constraints. An important special case where this coupling is obvious is the MSSS

$$\mathbf{0} = \Omega_{\zeta_j}\left(\mathbf{w}, \mathbf{u}, \mathbf{p}\right). \tag{3.28}$$

As (3.28) does not show any dependence on $\tilde{\mathbf{y}}_1$, criterion (3.27) is trivially fulfilled.

Example 1 (cont.): *Consider the pseudo-DAE system with respect to $\zeta_j = t$ of the ionic charge transport model (3.1)-(3.4) . Obviously, criterion (3.27) is fulfilled and the algebraic equation (3.4) forms the scalar MSSS*

$$\Omega_t = \sum_{k=1}^{n} z_k\, c_k. \tag{3.29}$$

Correspondingly, it is found $\nu_{d,t} > 1$. A similar result is obtained for reformulation of Eqs. (3.1)-(3.4) to a pseudo-DAE system with respect to x_1, x_2 and x_3. A MSSS is formed in each case by (3.4) and correspondingly $\nu_{d,x_1} > 1$, $\nu_{d,x_2} > 1$ and $\nu_{d,x_3} > 1$. □

3.3.3 Generalization of the index reduction algorithm

The procedure for a systematic index reduction that is used here is based on the work of Asbjørnsen and Fjeld (1970) and Bachmann et al. (1990). It corresponds to an extension of the algorithm proposed by Moe (1995) for the index reduction of DAE systems to PDAE systems. Further, the algorithm is modified by tailoring it to the concept of MSSS causing the structural singularity. The latter improves the method significantly, as not all algebraic equations have to be used in the reformulation procedure.

The basis for the reduction procedure is to exploit the fact that an MSSS (3.26) is characterized by its structural singularity with respect to the pseudo-algebraic variables $\tilde{\mathbf{y}}_1$. If (3.26) is differentiated with respect to ζ_j, it is obvious that also the differentiated MSSS

$$0 = \frac{\partial \Omega_{\zeta_j}}{\partial \zeta_j} = \frac{\partial \Omega_{\zeta_j}}{\partial \mathbf{w}}\frac{\partial \mathbf{w}}{\partial \zeta_j} + \frac{\partial \Omega_{\zeta_j}}{\partial \mathbf{y}_1}\frac{\partial \mathbf{y}_1}{\partial \zeta_j} + \frac{\partial \Omega_{\zeta_j}}{\partial \mathbf{u}}\frac{\partial \mathbf{u}}{\partial \zeta_j} \tag{3.30}$$

does not determine $\frac{\partial \tilde{\mathbf{y}}_1}{\partial \zeta_j}$ uniquely. Eq. (3.30) can be rewritten as an underdetermined linear system

$$\mathbf{A}\,\frac{\partial \tilde{\mathbf{y}}_1}{\partial \zeta_j} = \mathbf{b} \tag{3.31}$$

with

$$\mathbf{A} = \frac{\partial \Omega}{\partial \tilde{\mathbf{y}}_1} \in R^{n_\Omega \times n_{\tilde{y}_1}}, \quad \mathbf{b} = -\frac{\partial \Omega}{\partial \mathbf{w}}\frac{\partial \mathbf{w}}{\partial \zeta_j} - \frac{\partial \Omega}{\partial \mathbf{u}}\frac{\partial \mathbf{u}}{\partial \zeta_j} \in R^{n_\Omega}. \tag{3.32}$$

Note that $\frac{\partial \mathbf{w}}{\partial \zeta_j}$ is given by Eq. (3.23) and $\frac{\partial \mathbf{u}}{\partial \zeta_j}$ is the derivative of the known inputs $\mathbf{u}$ and thus a known function itself. Hence, $\mathbf{b}$ corresponds to a quasi-linear combination of the righthand side of the differential equations and the derivatives of the inputs. A necessary solvability condition for Eq. (3.31) is

$$\Gamma^T \mathbf{b} = 0. \tag{3.33}$$

Here Γ is a matrix of basis vectors of the nullspace of $\mathbf{A}^T$ (Moe, 1995), which is defined as the set of linearly independent vectors $\{\gamma_1, ..., \gamma_{n_n}\}$, $n_n = n_\Omega - \mathrm{rank}(\mathbf{A})$, satisfying

$$\mathbf{A}\,\gamma_i = 0, \quad i = 1, ..., n_n. \tag{3.34}$$

If the MSSS has the form (3.28), $\mathbf{A} = \frac{\partial \Omega}{\partial \dot{\mathbf{y}}_1}$ is not properly defined. For this particular case the definition $\Gamma = \mathbf{I}$ is introduced with $\mathbf{I} \in \mathbb{R}^{n_\Omega \zeta_j}$ as the unity matrix.

The criterion (3.33) together with (3.32) reveals an additional system of equations

$$\Gamma^T \mathbf{b} = \mathbf{g}_{add,\zeta_j}(\mathbf{w}, \mathbf{y}_1, \mathbf{u}, \mathbf{p}) = 0, \tag{3.35}$$

linking differential and algebraic variables of the model, which every solution of the PDAE system has to fulfill. The differential index of the pseudo-DAE systems (3.23), (3.24), can be reduced, if the additional constraints (3.35) are used to substitute the corresponding number of differential equations. As (3.35) corresponds to quasi-linear combinations of the original model equations, this procedure preserves the physical information of the original formulation.

Example 1 (cont.): *The index reduction method is applied to the high-index model of the ionic mass transport problem. First, the pseudo-DAE with respect to $\zeta_j = t$ is considered. Symbolic differentiation of the MSSS (3.29) yields*

$$\frac{\partial \Omega_t}{\partial \mathbf{w}} = [z_1 \ \ ... \ \ z_n], \tag{3.36}$$

and, as $\frac{\partial \Omega_t}{\partial \boldsymbol{u}} = 0$, (3.32) is evaluated to

$$b = -\sum_{k=1}^{n} z_k \nabla \cdot \mathbf{J}_k + \sum_{k=1}^{n} z_k \nabla \cdot (\mathbf{v}\, c_k). \tag{3.37}$$

Note that the convective terms in (3.37) comprising first derivatives with respect to x cancel out, because

$$\nabla \Omega_t = \sum_{k=1}^{n} z_k \nabla c_k = \mathbf{0}. \tag{3.38}$$

As the MSSS (3.29) is of the form (3.28), the nullspace is defined as $\Gamma = 1$. Thus, the additional constraint

$$g_{add,t} = -\sum_{k=1}^{n} z_k \nabla \cdot \mathbf{J}_k = 0 \tag{3.39}$$

is obtained as a quasi-linear combination of the original species balance equations (3.1). If one of the species balance equations (3.1) – for instance the one of species 1 – is substituted by Eq. (3.39), a reformulated system of $\nu_{d,t} = 1$ is obtained. As one differentiation has been applied in the course of the index-reduction, the differential index of the original model (3.1) - (3.4) with respect to time is $\nu_{d,t}^{orig} = 2$. □

3.3.4 Systematic procedure for the index analysis and reduction

Based on the concepts and procedures introduced above, a systematic procedure for the index analysis and reduction of PDAE systems is proposed as illustrated in Algorithm 1. It starts with a given model in the form of a PDAE system in the independent variables $\zeta_1, \ldots, \zeta_{n_l}$. In step 4 of the procedure a first-order pseudo-DAE is formulated with respect to the first independent variable ζ_1. For this system, the differential index ν_{d,ζ_1} is calculated in step 5 using the framework introduced in Section 3.3.2. In case $\nu_{d,\zeta_1} > 1$, the model is reformulated in steps 7-9 using the index reduction described in Section 3.3.3. This yields a reformulated model which is subject to another index analysis in step 10. The index reduction process is successively carried out until a reformulated model is obtained that is characterized by $\nu_{d,\zeta_1} = 1$. From the number of times the index reduction procedure has been applied, which is equivalent to the number of differentiations $n_{diff,j}$ applied to the model, the index $\nu_{d,j}^{orig}$ is calculated in step 12. Then the procedure is restarted in step 3 for the next independent variable ζ_2. The procedure terminates after sequentially going through each independent variable $\zeta_j \in \zeta$.

Algorithm 1: Index reduction algorithm for PDAE systems

1 formulate PDAE system in the general form Eq. (3.9) in the independent variables $\zeta_1, \ldots, \zeta_{n_l}$
2 **for** $j = 1, \ldots, n_l$ **do**
3 reformulate the PDAE system as a pseudo-DAE with respect to ζ_j in the form (3.23), (3.24)
4 **analyze** if $\nu_{d,\zeta_j} > 1$ by evaluating (3.25)
5 **set** $n_{diff,j} = 0$ `/* init. number of differentiations */`
6 **while** $\nu_{d,\zeta_j} > 1$ **do**
7 **identify** the MSSS Ω_{ζ_j}
8 **apply** systematic index reduction as described in Section 3.3.3
9 **set** $n_{diff,j} = n_{diff,j} + 1$
10 **analyze** if $\nu_{d,\zeta_j} > 1$ by evaluating (3.25)
11 **end while**
12 **set** $\nu_{d,j}^{orig} = n_{diff,j} + 1$ `/* calc. index of original model */`
13 **end for**

Example 1 (cont.): *The procedure is illustrated by considering the ionic mass transport model, where the results obtained in the previous sections can be already included. Thus, the results for steps 1-9 in Algorithm 1 for $\zeta_j = t$ have been already found: The index of the original modeling equations with respect to time is $\nu_{d,t} > 1$. The index reduction procedure identifies the additional constraint (3.39) which is used to eliminate one of the original balance equations, e.g., the balance equation for species* 1. *As the resulting reformulated model is characterized by $\nu_{d,t} = 1$, the method exits the index-reduction loop and determines the index of the original model $\nu_{d,t}^{orig} = 2$.*

The method returns to step 4 in order to obtain a PDAE system in semi-explicit form with respect to the next independent variable, i.e. x_1, by symbolic manipulation. In step 5, the analysis reveals that the index of the reformulated model with respect to x_1 is larger than one. The index reduction method applied in the steps 7-10 yields the additional constraint

$$g_{add,x_1} = -\sum_{k=1}^{n} z_k \frac{J_{x_1,k}}{D_k} + \sum_{k=1}^{n} \frac{z_k^2 c_k}{RT} F\, E_{x_1} = 0, \tag{3.40}$$

where $J_{x_1,k}$ and E_{x_1} are the scalar entries of the flux density $\boldsymbol{J}_k$ and electric field $\boldsymbol{E}$ vectors in the x_1-direction. To reduce the index ν_{d,x_1}, the constraint (3.40) is used to substitute one scalar element of the vectorial Nernst-Planck equation (3.2) for any species in the set of species, e.g., for the first species

$$J_{x_1,1} = -D_1 \nabla c_1 + \frac{z_1\, c_1}{RT} D_1\, F\, E_{x_1}. \tag{3.41}$$

The method continues in step 11 to analyze the index of the reformulated model yielding $\nu_{d,x_1} = 1$. Thus, the index of the original formulation with respect to x_1 is $\nu_{d,x_1}^{orig} = 2$. In the next few steps the method is continued by analyzing and reducing the index with respect to the remaining independent variables x_2 and x_3. As the model is symmetric in the spatial coordinates, it is conclusive that the method in an analogous manner identifies the high-index behavior and reveals additional constraints similar to Eq. (3.40) for x_2 and x_3. In vectorial notation these three scalar additional constraints obtained in the reduction process with respect to x_1, x_2 and x_3 are expressed as

$$\mathbf{g}_{add,\mathbf{x}} = -\sum_{k=1}^{n} z_k \frac{\mathbf{J}_k}{D_k} + \sum_{k=1}^{n} \frac{z_k^2 c_k}{RT} F\, \mathbf{E} = 0. \tag{3.42}$$

For the reduction of the index with respect to all spatial coordinates (3.42) is used to substitute the vectorial Nernst-Planck equation (3.2) of the first species. As a final result, the method yields the reformulated model

$$\frac{\partial c_k}{\partial t} = -\nabla \cdot \mathbf{J}_k - \nabla \cdot (\mathbf{v}\, c_k), \qquad k = 2, ..., n, \tag{3.43}$$

$$0 = -\sum_{k=1}^{n} z_k\, \nabla \cdot \mathbf{J}_k, \tag{3.44}$$

$$\mathbf{J}_k = -D_k \nabla c_k + \frac{z_k\, c_k}{RT} D_k\, F\, \mathbf{E}, \quad k = 2, ..., n, \tag{3.45}$$

$$0 = -\sum_{k=1}^{n} z_k \frac{\mathbf{J}_k}{D_k} + \sum_{k=1}^{n} \frac{z_k^2 c_k}{RT} F\, \mathbf{E}, \tag{3.46}$$

$$\mathbf{E} = -\nabla \phi, \tag{3.47}$$

$$0 = \sum_{k=1}^{n} z_k\, c_k, \tag{3.48}$$

and the indices of the original model formulation $\nu_{d,t} = 2$ and $\nu_{d,x_j} = 2,\ j = 1, ...3$. □

3.4 Index analysis and reduction in the modeling work flow

This section illustrates the relevance of the systematic index analysis and reduction procedure in a modeling work flow for distributed models. In Section 3.4.1 it is shown how the results of the proposed method support the physical interpretation of the model. With respect to the evaluation of the consistency of initial and boundary conditions Section 3.4.2 discusses the benefits and the limitations of the results obtained from the method.

3.4.1 Physical interpretation of the reformulated model

The index analysis of a DAE system provides important information on its dynamic degrees of freedom (cf. Section 3.2.1) corresponding to the maximal number of independent initial conditions. Next to the specification of initial conditions, the dynamic degrees of freedom constitute an important model property with respect to its physical interpretation. Most important in this context is the coincidence between the dynamic degrees of freedom and the number of model states independently describing extensive quantities in the model. Thus, if it is assumed that the system is described correctly by the model, the dynamic degrees of freedom can help to identify the number of extensive quantities in the physical system that are truly independent. The other way round, if the number of independent extensive quantities is known, e.g., by theoretical considerations or experiments, the dynamic degrees of freedom give a criterion to evaluate the potential of the model to describe the underlying relations correctly.

The concept of dynamic degrees of freedom for DAE can be generalized to PDAE systems in a straightforward manner. The key aspect allowing this generalization, is the definition of the differential index for semi-explicit pseudo-DAE systems (3.23), (3.24). If the pseudo-DAE with respect to the independent variable ζ_j is characterized by $\nu_{d,j} = 1$, the dimension of the differential system (3.23) directly provides the number of truly independent differential quantities with respect to ζ_j. For this measure, the notion of differential degrees of freedom with respect to an independent variable ζ_j is introduced as follows:

Definition 7: *For a given pseudo-DAE with respect to ζ_j, (3.23), (3.24), characterized by $\nu_{d,j} = 1$, the differential degrees of freedom $d_{f,j}$ with respect to ζ_j correspond to the dimension of the differential system (3.23).*

According to this definition the differential degrees of freedom are a direct result of the procedure for the systematic index analysis and reduction to pseudo-DAE systems characterized by $\nu_{\zeta_j} = 1$.

Example 1 (cont.): *The reduction process and the additional constraints (3.44) and (3.46) reveal important physical principles tacitly represented in the model. In the first reduction step, the lumped storage term $\frac{\partial \sum_{k=1}^{n} z_k c_k}{\partial t}$ is formed as a linear combination of the original storage terms $\frac{\partial c_k}{\partial t}$, $k = 1, ..., n$, highlighting the invariance of the volumetric space charge $\rho^e = F \sum_{k=1}^{n} z_k c_k = 0$. To express this explicitly in the model, the method derives equation (3.44) as a linear combination of the species balance equations (3.1). By introducing the definition of the current density*

(Newman and Thomas-Alyea, 2004)

$$\mathbf{i} = F \sum_{k=1}^{n} z_k \mathbf{J}_k, \tag{3.49}$$

it becomes obvious that (3.44) corresponds to the stationary charge balance

$$0 = \nabla \cdot \mathbf{i}. \tag{3.50}$$

The invariance of the charge density with respect to the spatial coordinates is expressed in the constraint (3.46). The number of independent driving forces for the diffusive transport is $n-1$ rather than n suggested by the original model. Further, it is interesting to note that the constraint (3.46) gives an implicit algebraic relation between the current density and the electric field as a generalization of Ohm's law, i.e.,

$$\mathbf{i} = \kappa \, \mathbf{E}. \tag{3.51}$$

It can easily be verified that (3.46) really corresponds to the generalization of (3.51), if a scenario with equal diffusion coefficients $D_k = \tilde{D}$, $k = 1, ..., n$, is considered and the local conductivity of the solution is introduced as $\kappa = \sum_{k=1}^{n} \frac{z_k^2 \, c_k}{RT} \tilde{D} \, F$ (cf. Newman and Thomas-Alyea (2004)). □

In addition to the differential degrees of freedom, the index reduction method provides further insight into physically relevant model properties. These properties are found in the invariant expressions with respect to certain independent variables revealed as additional constraints in the index reduction. In many cases, it is even possible to obtain a physical interpretation of these invariants highlighting important physical principles that are depicted in the model. Assuming that the model describes the underlying physical phenomena correctly, the revealed physical principles contribute to a better understanding of the phenomena themselves.

Example 1 (cont.): *The index reduction with respect to time reveals the additional constraint (3.44) by means of a quasi-linear combination of the original species balance equations. From a technical point of view, this is achieved by lumping the holdup terms $\frac{\partial c_k}{\partial t}$, $k \in \{1, ..., n\}$, into the term $\sum_{k=1}^{n} z_k \frac{\partial c_k}{\partial t}$, which is characterized by an invariant behavior with respect to time. The invariance of the electric charge density $F \sum_{k=1}^{n} z_k \, c_k$ is revealed in an analogous manner in the index reduction with respect to the spatial coordinates. Hence, only $n-1$ of the diffusive fluxes $\boldsymbol{J}_k \in k \in \{1, ..., n\}$ defined in (3.2) are independent.*

Here, it is interesting to recall that the Nernst-Planck equations (3.2) correlate the diffusive fluxes to their driving forces, which are the concentration gradients and the electric field. In this context, the derivation of the additional constraints illustrates that only $n-1$ driving forces are independent in order to preserve local electroneutrality imposed by (3.4). □

3.4.2 Identification of consistent initial and boundary conditions

The PDAE model equations have to be completed by a consistent set of initial and boundary conditions in the form (3.11), (3.12) and (3.13). From a technical point of view, the specification targets at obtaining a complete problem formulation that matches a specific physical scenario, e.g., specific concentrations in the reaction media at $t = t_0$ or a free outflow at the end of the

tubular reactor. From a mathematical perspective, the specified initial and boundary conditions represent additional data that either (i) select a unique member of a set of solutions or (ii) construct the functional form of the solution. In the former case, it is referred to as a restricted solution (Martinson, 2000) while in the latter case it is referred to as an unrestricted solution. To accomplish this role, the set of initial and boundary data has to be in agreement with specific criteria, i.e., it has to be consistent to yield a well-posed problem.

A closed theory and appropriate methods for testing the consistency of initial and boundary conditions for a general PDAE system is still missing. However, the procedure for the index reduction provides valuable information to support the consistent specification of initial and boundary conditions: The number of differential degrees of freedom with respect to time, $d_{f,t}$, corresponds to the maximal number of initial conditions n^{IC} that can be specified independently. Further, the results of the method support the analysis of the consistency of the initial conditions, as the resulting pseudo-DAE with respect to time is characterized by $\nu_{d,t} = 1$ and is in semi-explicit form (3.23), (3.24). Hence, Definition 3 can be generalized to the pseudo-DAE in a straightforward manner. Accordingly, the initial conditions in combination with the model equations (3.23), (3.24) have to uniquely determine the algebraic variables $\mathbf{y}|_{t=t_0}$, the differential variables $\mathbf{w}|_{t=t_0}$ and their gradients $\frac{\partial \mathbf{w}}{\partial t}\big|_{t=t_0}$ on the hyperplane $t = t_0$.

The number of differential degrees of freedom with respect to a spatial coordinate corresponds to the total number of boundary conditions $n_{BC,x_k} = n_{BC,x_k^U} + n_{BC,x_k^L}$ that can be specified independently at the upper or lower bounds of the coordinate x_k, x_k^U and x_k^L.

Example 1 (cont.): *The number of differential degrees of freedom with respect to time is* $d_{f,t} = n - 1$*; hence,* $n^{IC} = n - 1$ *initial conditions have to be specified. The specification of four initial conditions as suggested by the four differential states in the original model formulation would easily result in inconsistent initial conditions and thus in a badly posed problem. The initial conditions*

$$c_k\left(t = 0, \mathbf{x}\right) = c_{k,0}\left(\mathbf{x}\right), \quad k = 2, ..., n. \tag{3.52}$$

and the reformulated model (3.43)-(3.48) uniquely determine the algebraic variables $\boldsymbol{y} = \boldsymbol{y}_1 = [\boldsymbol{J}_1, ... \boldsymbol{J}_n, c_1, \boldsymbol{E}, \phi]^T$*, the differential variables* $\boldsymbol{w} = [c_1, ... c_n]^T$ *and their gradients* $\frac{\partial \boldsymbol{w}}{\partial t}\big|_{t=t_0} = \left[\frac{\partial c_2}{\partial t}\Big|_{t=t_0}, ..., \frac{\partial c_n}{\partial t}\Big|_{t=t_0}\right]$ *on the hyperplane* $t = t_0$*.*

The identification of a consistent set of boundary conditions is more involved. However, the reformulated model provides an adequate basis for investigating this question. The differential degrees of freedom with respect to the spatial coordinates are determined as $d_{f,x_k} = 2n$, $k = 1, ..., 3$*. Hence, in total* $n_{BC,x_k} = 2n$, $k = 1, ..., 3$*, boundary conditions can be specified independently.* □

No information is provided by the proposed procedure concerning the distribution of the specified boundary conditions to the lower or upper bound of the spatial coordinates. Hence, additional information has to be added to evaluate the consistency of the boundary conditions. In the case of a linear PDAE system, a comprehensive theory for the consistent specification of boundary conditions has been developed by Martinson and Barton (2003). These authors derive criteria for the well-posedness of a given specification of initial and boundary conditions by generalizing

characteristic analysis of hyperbolic PDE to general PDAE systems. The essence of the method is to use a block decomposition method to transform the system into a canonical form. In this form, the resulting block rows can be distinguished by showing either hyperbolic, parabolic or differential characteristics. According to the characteristics, the boundary conditions are to be specified at the upper or lower boundary of the domain.

However, in addition to its restriction to linear PDAE systems, the method has two major limitations: (i) PDAE systems are considered which are characterized by an unrestricted solution and (ii) the theory only holds for $n_l = 2$ and can not be generalized to higher-dimensional PDAE systems. Hence, PDAE systems classified as ill-posed according to the results of the characteristic analysis can be well-posed if they are considered as restricted problems. A particular example of the latter case is the well-known heat equation (Martinson and Barton, 2003).

For general PDAE systems, methods for investigating the consistency of a given specification of boundary conditions are typically system-specific and require a high level of expertise. A particular exception is the evaluation of the consistency for specific standard types of PDAE systems. Hence, a useful approach to characterize a given PDAE system is to apply explicit transformations to yield a reformulated system in standard form.

Example 1 (cont.): *To investigate if the boundary conditions are to be specified on the lower or upper bound of the coordinates x_k, $k = 1, ..., 3$, the reformulated PDAE system (3.43) - (3.48) is transformed into a standard type by algebraic manipulation. To this end, the electric field $\boldsymbol{E}$ and the concentration of the first species c_1 is eliminated from the model by introducing (3.47), (3.48) into (3.45), (3.46). Further, eliminating the diffusive fluxes by introducing (3.45), (3.46) into the balances (3.43), (3.44) yields*

$$\frac{\partial c_k}{\partial t} = D_k \Delta c_k - \frac{z_k F}{RT} D_k \nabla \cdot (c_k \nabla \phi) - \nabla \cdot (\mathbf{v}\, c_k), \qquad k = 2, ..., n, \tag{3.53}$$

$$\begin{aligned} 0 = &- \sum_{k=2}^{n} z_k \left(D_k - D_1\right) \Delta c_k \\ &+ \sum_{k=2}^{n} \frac{z_k F}{RT} \left(z_k \left(D_k - D_1\right) + D_k \left(z_k - z_1\right)\right) \nabla \cdot (c_k \nabla \phi). \end{aligned} \tag{3.54}$$

Hence, the reformulated PDAE is reduced to a set of $n-1$ parabolic advection-diffusion PDE (3.53) and an elliptic PDE (3.54) showing the structure of Poisson's equation. Thus, the $2n$ boundary conditions that can be specified independently for each coordinate are to be distributed equally at the lower and upper bounds of the coordinates, e.g., in the form of the surface balance equations

$$\mathbf{n}_l^L \cdot \left[-D_k \nabla c_k + \frac{z_k c_k}{RT} D_k F \nabla \phi + \mathbf{v}\, c_k \right]_{x_l = x_l^L} - \Phi_{k,l}^U \left(t,\, x_l \neq x_j\right) = 0, \tag{3.55}$$

$$\mathbf{n}_l^U \cdot \left[-D_k \nabla c_k + \frac{z_k c_k}{RT} D_k F \nabla \phi + \mathbf{v}\, c_k \right]_{x_l = x_l^U} - \Phi_{k,l}^L \left(t,\, x_l \neq x_j\right) = 0, \tag{3.56}$$

$$k = 2, ..., n, \qquad j = l = 1, ..., 3,$$

and the Dirichlet conditions for the electric potential

$$\phi|_{x_l = x_l^L} = \phi_l^L, \tag{3.57}$$

$$\phi|_{x_l=x_l^L} = \phi_l^U, \qquad l = 1, ..., 3. \tag{3.58}$$

Here, $\boldsymbol{n}_l^L$ and $\boldsymbol{n}_l^U$ correspond to normal vectors in the direction of x_l pointing into the domain at the lower and upper bounds of x_l. $\Phi_{k,l}^L$ and $\Phi_{k,l}^U$ are known fluxes entering or leaving the domain across the boundaries. The electric potential at the boundaries is prescribed by ϕ_l^L and ϕ_l^U.

As a final result the modeling work flow results in the reformulated model (3.43) - (3.48) with initial conditions (3.52) and boundary conditions (3.55), (3.56), (3.57) and (3.58). □

3.5 Conclusions

In this chapter a new procedure for index analysis and reduction of distributed PDAE models has been developed. It is based on the generalization of established concepts for the index analysis and reduction of DAE systems. For this generalization the PDAE system is considered as a set of pseudo-DAE defined on hyperplanes. This motivates the analysis and, if necessary, the reduction of the indices of the pseudo-DAE with respect to the different independent variables in a sequential procedure. In contrast to recent works (Angermann and Rang, 2007, Rang and Angermann, 2005) focusing on a perturbation index for linear PDAE systems, the concept of a differential index is used as it is applicable without any a priori knowledge of the solution of the PDAE system, which is not available in the nonlinear case. Further, the method is tailored to a semi-explicit representation of the pseudo-DAE allowing the development of an efficient procedure for index reduction. The latter is based on symbolic manipulation of the original model equations and eliminates terms that show invariant behavior with respect to specific independent variables. As a result, a reformulated model is obtained which is characterized by differential indices of one with respect to all independent variables.

The procedure can be embedded in a general modeling work flow for distributed PDAE models. The reformulated model constitutes an appropriate basis for the specification of consistent initial and boundary conditions and for investigating the applicability of general MOL-based numerical methods. Even more important, the hidden constraints revealed by index reduction provide important information concerning the physical principles implicitly encoded in the model. As such, the method contributes to an improved understanding of complex coupled PDAE models prior to any numerical studies.

The suggested procedure is illustrated for a simplified charge transport model based on the Nernst-Planck equation and the electroneutrality condition. For this model the proposed method identifies high-index behavior with respect to time and spatial coordinates. The reduction method is capable of deriving an equivalent model formulation which is characterized by differential indices of one. Further, a sound physical interpretation has been obtained for the hidden constraints that become explicit in the reduction process. The true number of differential degrees of freedom are identified, which are less than the apparent number in the original model formulation. These results of the proposed method support the consistent specification of initial conditions in a comprehensive manner. Valuable information for consistent specification of boundary con-

ditions is obtained, including the maximal number of boundary conditions that can be specified independently for a spatial coordinate.

To the author's knowledge, the high index behavior found for the Nernst-Planck/electroneutrality model, has not been reported in prior works. These findings provide for the first time a possible explanation for the difficulties reported, e.g., by Neubrand (1999), in the context of the numerical solution of these models. Further, it illustrates the relevance of the derived methods for the modeling of electrochemical systems or electro-membrane processes even if simplified modeling approaches are applied. Correspondingly, for the derivation of transport models in Chapter 4, where the more rigorous Maxwell-Stefan approach is applied and the assumption of an infinitesimally diluted solution is dropped, the developed method constitutes a central element.

4 Modeling of ionic transport in electrolytes

This chapter presents rigorous models for the description of ionic mass transport in a liquid electrolyte solution and a homogeneous membrane phase. The models enable the accurate dynamic description of the local transport in the flow channels and the ion exchange membranes in the ED process. The underlying modeling equations and the theoretical framework are introduced in Section 4.1. On this basis closed mathematical models are derived and analyzed in Section 4.2 with respect to their differential indices. This index analysis and the subsequent reduction is carried out using the systematic procedure developed in Chapter 3. In Section 4.3 the results of the index reduction are used to investigate the structure of the PDAE models and to derive an appropriate representation for an efficient numerical treatment.

4.1 Modeling equations and theoretical framework

This section introduces the fundamental equations for a mechanistic description of multicomponent mass transfer in an isothermal homogeneous electrolyte phase. The theoretical framework largely coincides with the one used by Kraaijeveld et al. (1995), Visser (2001) and Hogendoorn et al. (2001). However, a more accurate model for the activity coefficients and the excess volume in the electrolyte solution are introduced in Section 4.1.2. Further, in contrast to the prior works a rigorous dynamic model formulation is addressed. Moreover, instead of the one-dimensional spatial domain, a general setting of a three-dimensional spatial domain is considered, with coordinates $x_l \in \left[x_l^L, x_l^U\right], l = 1,2,3$, where x_l^L and x_l^U are fixed lower and upper bounds. The description accounts for a set $S = \{1, ..., n\}$ of charged or charge-neutral species with specific charge numbers z_k, $k = 1, ..., n$.

This general setting is discussed with particular emphasis on two specific scenarios: (i) a scenario of a liquid solution, where the transport occurs in a charge-neutral solvent and (ii) a scenario of a pseudo-homogeneous IEM, where the transport occurs in an immobile polymeric membrane material[1]. For the first scenario it is demanded – without a loss of generality – that the charge-neutral solvent is the first species in S, i.e., $z_1 = 0$. For the second scenario the charged membrane material is considered as the first species in S. In both cases, again without a loss of generality, species n is required to be an ionic species of arbitrary charge which implies $z_n \neq 0$.

[1] Here it is assumed that swelling effects in the membrane are negligibly small, which allows to consider the membrane as immobile. Without this assumption the model for the description of ionic transport in the membrane results in a moving boundary problem (cf. (Bausa and Marquardt, 2001) for a model with charge-neutral species), which is out of the scope of this work.

4.1.1 Species balance equations and definition of the reference velocity

Mass conservation is enforced by the introduction of n species balance equations

$$\frac{\partial c_k(\mathbf{x},t)}{\partial t} = -\nabla \cdot \mathbf{J}_k(\mathbf{x},t) - \nabla \cdot \Big(c_k(\mathbf{x},t)\, \mathbf{v}(\mathbf{x},t) \Big) + r_k^V(\mathbf{x},t), \quad k = 1,...,n. \tag{4.1}$$

Here, $c_k(\mathbf{x},t)$ is the molar volumetric density, $\mathbf{J}_k(\mathbf{x},t)$ is the molar flux density and $r_k^V(\mathbf{x},t)$ is the local volumetric reaction flux density of species $k \in S$. The molar diffusive flux densities $\mathbf{J}_k(\mathbf{x},t), k = 1,...,n$, are defined as

$$\mathbf{J}_k(\mathbf{x},t) = c_k(\mathbf{x},t) \Big(\mathbf{v}_k(\mathbf{x},t) - \mathbf{v}(\mathbf{x},t) \Big), \quad k = 1,...,n, \tag{4.2}$$

with respect to the absolute species velocity $\mathbf{v}_k(\mathbf{x},t)$ and the reference velocity $\mathbf{v}(\mathbf{x},t)$. The reference velocity is defined as

$$\mathbf{v}(\mathbf{x},t) = \frac{\sum_{j=1}^{n} w_j(\mathbf{x},t)\, c_j(\mathbf{x},t)\, \mathbf{v}_j(\mathbf{x},t)}{\sum_{j=1}^{n} w_j(\mathbf{x},t)\, c_j(\mathbf{x},t)}, \tag{4.3}$$

by introducing appropriate weights $w_k(\mathbf{x},t), k = 1,...,n$. As an alternative to the explicit definition in Eq. (4.3), the reference velocity can be implicitly defined by the introduction of the closure relation

$$0 = \sum_{j=1}^{n} w_j(\mathbf{x},t)\, \mathbf{J}_j(\mathbf{x},t). \tag{4.4}$$

In the modeling of transport phenomena the barycentric velocity $\mathbf{v}^{bar}(\mathbf{x},t)$ is widely used. It results from the specification of the weights as $w_k^{bar} = M_k,\ k = 1,...,n$, with M_k as the molecular weight of species $k \in S$. However, as shown in the following, in the scenario of ionic transport in a charge-neutral solvent it is beneficial to introduce a volume-averaged reference velocity by choosing

$$w_k^{va}(\mathbf{x},t) = \tilde{V}_k + V^E(\mathbf{x},t), k = 1,...,n. \tag{4.5}$$

Here, $\tilde{V}_k$ is the infinite dilution partial molar volume of species $k \in S$ and $V^E(\mathbf{x},t)$ is the excess volume of the mixture. With Eq. (4.5) the implicit definition of the reference velocity (4.4) yields

$$0 = \sum_{j=1}^{n} \Big(\tilde{V}_j + V^E(\mathbf{x},t) \Big) \mathbf{J}_j(\mathbf{x},t). \tag{4.6}$$

The relation between the barycentric and the volume-averaged velocity can be derived (cf. Appendix B.1) as

$$\mathbf{v}^{bar}(\mathbf{x},t) = \mathbf{v}^{va}(\mathbf{x},t) + \frac{\sum_{j=1}^{n} \mathbf{J}_j(\mathbf{x},t)\, M_j}{\sum_{j=1}^{n} c_j(\mathbf{x},t)\, M_j}. \tag{4.7}$$

For the scenario of ionic transport in a pseudo-homogenous membrane it is beneficial to specify the reference velocity as the absolute species velocity of the stagnant membrane material $\mathbf{v}_1 = 0$. This implies, $w_1 = 1,\ w_j = 0,\ j = 2,...,n$, which specifies Eq. (4.4) as

$$0 = \mathbf{J}_1(\mathbf{x},t). \tag{4.8}$$

Further, the species balance equation (4.1) for species 1 degenerates and is trivially fulfilled for $c_1(\mathbf{x},t) = const.$

4.1.2 Constitutive equations

Constitutive equations are introduced describing the thermo-physical properties of the electrolyte phase and the diffusive transport mechanisms.

Thermo-physical properties

The total concentration $c_T(\mathbf{x},t)$ is defined as

$$c_T(\mathbf{x},t) = \sum_{j=1}^{n} c_j(\mathbf{x},t)\,. \tag{4.9}$$

In case of a liquid electrolyte solution, $c_T(\mathbf{x},t)$ is related to the local composition by the equation of state (Djordjević et al., 1994, Rouquerol and Sabbah, 1977)

$$1 = \sum_{j=1}^{n} c_j(\mathbf{x},t)\,\tilde{V}_j + V^E(\mathbf{x},t)\; c_T(\mathbf{x},t). \tag{4.10}$$

The excess volume of the mixture $V^E(\mathbf{x},t)$ is described by means of a multi-component density model for electrolyte solutions (Mathias, 2004) (cf. Section B.3). For the scenario of a pseudo-homogenous membrane phase, the assumption of a stagnant membrane material with $c_1 = const.$ implies that the total $c_T(\mathbf{x},t)$ is not bounded by an additional equation of state (cf. Hogendoorn et al. (2001)).

The local chemical potential of the isothermal solution is described by

$$\mu_k(\mathbf{x},t) = RT\,ln\left(\gamma_k(\mathbf{x},t)\; c_k(\mathbf{x},t)\right) + \mu_k^0, \quad k = 1,...,n, \tag{4.11}$$

where μ_k^0 is the standard potential and $\gamma_k(\mathbf{x},t)$ is the concentration based activity coefficient of species $k \in S$.

For the prediction of the activity coefficients in an electrolyte solution the eNRTL-model is used which has been proposed by Chen et al. (1982) and has been continuously refined by Chen and Song (2004) and Chen (2006). As the eNRTL model describes activity coefficients for a mole fraction basis in its standard formulation, the correlation derived in Appendix B.2 is used to calculate activity coefficients for the volumetric concentrations basis. For details concerning the eNRTL model it is referred to the original publications (Chen, 2006, Chen et al., 1982, Chen and Song, 2004).

Visser (2001) identified an activity coefficient model for different IEM by generalizing the Bromley model

$$ln\left(\gamma_k(\mathbf{x},t)\right) = \frac{-A\,z_k^2\sqrt{IS(\mathbf{x},t)}}{1+\sqrt{IS(\mathbf{x},t)}} + \sum_{j=1}^{n} \tilde{G}_{kj}\,\frac{c_j(\mathbf{x},t)}{c_w(\mathbf{x},t)\;M_w}, \quad k = 2,...,n, k \neq w. \tag{4.12}$$

Here, the index w refers to water, A is the Debye-Hueckel constant and $IS(\mathbf{x},t) = \sum_{j=1}^{n} z_j^2\,c_j(\mathbf{x},t)$ is the local ionic strength. The matrix $\tilde{G}_{kj}$ is defined as

$$\tilde{G}_{kj} = \begin{cases} \frac{|z_j|+|z_k|}{2}\,\frac{\left(0.006+0.6\,C_{kj}\right)|z_j\,z_k|^3}{|z_j\,z_k|+1.5\,IS(\mathbf{x},t)}, & \text{if} \quad z_k\,z_j < 0, \\ 0, & \text{if} \quad z_k\,z_j \geq 0, \end{cases} \tag{4.13}$$

where C_{kj} are binary interaction parameters defined for all anion-cation pairs in the system.

For notational simplicity in the remainder of this work the activity coefficient and multi-component density models for the activity coefficients $\gamma_k(\mathbf{x},t)$ and the excess volume $V^E(\mathbf{x},t)$ are considered as generic functions

$$\gamma_k(\mathbf{x},t) = f_k^{\gamma}(\mathbf{c}(\mathbf{x},t)), \quad k = 1,...,n \tag{4.14}$$

and

$$V^E(\mathbf{x},t) = f_k^{V}(\mathbf{c}(\mathbf{x},t)) \tag{4.15}$$

in the local concentrations.

Electrostatics

If the magnetic induction of the electrolyte phase can be neglected, which is a reasonable assumption in most electrochemical systems, the electric field $\mathbf{E}(\mathbf{x},t)$ is assumed to be irrotational (Kontturi et al., 2008). This simplifies Faraday's law according to

$$-\frac{\partial \mathbf{B}}{\partial t} = \nabla \times \mathbf{E}(\mathbf{x},t) \approx 0. \tag{4.16}$$

This simplification enables the introduction of the electric potential $\phi(\mathbf{x},t)$, which is defined as the negative gradient of the electric field

$$\mathbf{E}(\mathbf{x},t) = -\nabla\phi(\mathbf{x},t). \tag{4.17}$$

If, in addition, the dielectric permittivity ϵ is assumed to be constant, Gauß's Law, $\nabla\cdot(\epsilon\,\mathbf{E}(\mathbf{x},t)) = F\,\rho^e(\mathbf{x},t)$, can be simplified to the well-known Poisson equation

$$\frac{\epsilon}{F}\nabla\cdot\mathbf{E}(\mathbf{x},t) = \rho^e(\mathbf{x},t), \tag{4.18}$$

where $\rho^e(\mathbf{x},t) = \sum_{k=1}^{n} z_k c_k(\mathbf{x},t)$ is the local charge density. It is important to note that the factor $\frac{\epsilon}{F}$ in Eq. (4.18) in an aqueous electrolyte solution at $25°C$ is of order $\frac{\epsilon}{F} \approx 10^{-14}\frac{equiv.}{V\,m}$ (Newman and Thomas-Alyea, 2004). Hence, a locally non-zero space charge $\rho^e(\mathbf{x},t) > 0$ is associated to tremendously large gradients in the electric field $\mathbf{E}(\mathbf{x},t)$. The resolution of these large gradients in a simulation model demands a very fine resolution of the considered computational domain. This fact strongly limits the size of the physical system that can be described by Eq. (4.18) with a reasonable computational effort. To allow for the description of large physical systems, Eq. (4.18) is commonly simplified by setting $\frac{\epsilon}{F} = 0$, which yields the algebraic constraint

$$0 = \sum_{k=1}^{n} z_k c_k(\mathbf{x},t), \tag{4.19}$$

also known as the electroneutrality condition.

Maxwell-Stefan equations

For the specification of the diffusive flux densities $\mathbf{J}_k(\mathbf{x},t)$, $(n-1)$ constitutive equations have to be specified. A rigorous description of the diffusive and migrative transport processes is found in the Maxwell-Stefan approach (Krishna and Wesselingh, 1997). The fundamental concept of this approach is a local equilibrium of the driving and frictional forces acting on a species k (Bird et al., 2002). This results in

$$\begin{aligned}
&\frac{c_k(\mathbf{x},t)}{RT}\nabla\mu_k(\mathbf{x},t)\\
&+\left(c_k(\mathbf{x},t)\,\tilde{V}_k-\omega_k(\mathbf{x},t)\right)\frac{1}{RT}\nabla p(\mathbf{x},t)\\
&-\frac{F}{RT}\left(z_k c_k(\mathbf{x},t)\;-\omega_k(\mathbf{x},t)\,\rho^e(\mathbf{x},t)\right)\mathbf{E}(\mathbf{x},t)\\
&=\sum_{\substack{j=1\\ j\neq k}}^{n}\frac{c_k(\mathbf{x},t)\,\mathbf{J}_j(\mathbf{x},t)-c_j(\mathbf{x},t)\,\mathbf{J}_k(\mathbf{x},t)}{D_{jk}(\mathbf{x},t)\;c_T(\mathbf{x},t)}\qquad k=2,...,n.
\end{aligned}\tag{4.20}$$

Here, $D_{jk}(\mathbf{x},t)$ are the Maxwell-Stefan diffusion coefficients accounting for the binary interaction of species k and j. The first term on the left-hand side of Eq. (4.20) represents the gradient of the chemical potential; the second term describes the influence of pressure gradients with respect to the difference of the volume fraction $c_k(\mathbf{x},t)\,\tilde{V}_k$ and the mass fraction $\omega_k(\mathbf{x},t)$. The third term expresses the direct and indirect influence of Coulomb forces acting on species $k\in S$.

The first term in the Maxwell-Stefan equations (4.20) is commonly reformulated as

$$\frac{c_k(\mathbf{x},t)}{RT}\nabla\mu_k(\mathbf{x},t)=\sum_{j=2}^{n}\left(\delta_{kj}+c_j(\mathbf{x},t)\left.\frac{\partial ln(\gamma_k)}{\partial c_j}\right|_{T,p,\Sigma}\right)\nabla c_k(\mathbf{x},t),\quad k=2,...,n,\tag{4.21}$$

where δ_{kj} is the Kronecker delta (Taylor and Kooijman, 1991). For notational simplicity the matrix of thermodynamic factors $\Gamma\in R^{(n-1)\times(n-1)}$ is introduced with elements

$$\Gamma_{kj}=\delta_{kj}+c(\mathbf{x},t)\frac{\partial ln(\gamma_k)}{\partial c_j},\quad j,k=2,...,n.\tag{4.22}$$

In general, it is assumed that Γ is invertible, i.e., Γ^{-1} with elements $\Gamma^{-1}_{k,j}$, $k,j\in\{2,...,n\}$ exists (Taylor and Kooijman, 1991).

The general approach (4.20) simplifies for both considered scenarios, as it can be assumed that pressure gradients have a negligible influence on the mass transport (Visser, 2001). Further, in the case of an electroneutral phase the contribution of the space charge $\frac{F}{RT}\omega_k(\mathbf{x},t)\,\rho^e(\mathbf{x},t)$ to the Coulombic forces vanishes. With these assumptions and the introduction of (4.21) and (4.22), Eq. (4.20) is expressed as

$$\begin{aligned}
&\sum_{j=2}^{n}\Gamma_{k,j}\nabla c_j(\mathbf{x},t)-\frac{F}{RT}z_k c_k(\mathbf{x},t)\,\mathbf{E}(\mathbf{x},t)\\
&=\sum_{\substack{j=1\\ j\neq k}}^{n}\frac{c_k(\mathbf{x},t)\,\mathbf{J}_j(\mathbf{x},t)-c_j(\mathbf{x},t)\,\mathbf{J}_k(\mathbf{x},t)}{D_{kj}(\mathbf{x},t)\;c_T(\mathbf{x},t)},\qquad k=2,...,n.
\end{aligned}\tag{4.23}$$

If $\mathbf{J}_1(\mathbf{x},t)$ is eliminated in Eq. (4.23) by introducing Eq. (4.4), the Maxwell-Stefan equations can be expressed in matrix-vector notation as

$$c_T(\mathbf{x},t)\,\Gamma\,\nabla\mathbf{c} - \mathbf{E}\,\mathbf{Z}\,\mathbf{c} = \mathbf{B}\,\mathbf{J}, \tag{4.24}$$

where $\mathbf{c} \in R^{n-1}$ is a vector of the species concentrations $c_k(\mathbf{x},t)$, $k = 2,...,n$. Further, $\mathbf{J} \in R^{(n-1)\times 3}$ is a tensor with elements $\mathbf{J}_k(\mathbf{x},t)$, $k = 2,...,n$, and $\mathbf{Z} \in R^{n-1\times n-1}$ is a matrix defined for $j,k \in \{2,...,n\}$, by

$$Z_{j,k} = \begin{cases} c_T(\mathbf{x},t)\,\frac{F}{RT}\,z_k, & \text{if } j = k, \\ 0, & \text{if } j \neq k. \end{cases} \tag{4.25}$$

The matrix $\mathbf{B} \in R^{(n-1)\times(n-1)}$ is defined for $j,k \in \{2,...,n\}$, by

$$B_{j,k} = \begin{cases} \frac{1}{D_{j,k}(\mathbf{x},t)} - \frac{1}{D_{1,k}(\mathbf{x},t)}\left(\frac{w_j(\mathbf{x},t)}{w_1(\mathbf{x},t)}\right), & \text{if } j \neq k, \\ -\frac{1}{c_k(\mathbf{x},t)}\sum_{\substack{j=1 \\ j\neq k}}^{n}\frac{c_j(\mathbf{x},t)}{D_{j,k}(\mathbf{x},t)} - \frac{1}{D_{1,k}(\mathbf{x},t)}\left(\frac{w_j(\mathbf{x},t)}{w_1(\mathbf{x},t)}\right), & \text{if } j = k, \end{cases} \tag{4.26}$$

(cf. Taylor and Krishna (1993) or Bothe (2011), where a molar-averaged reference velocity with $w_j(\mathbf{x},t) = 1$, $j \in \{1,..n\}$, is considered).

In a concentrated electrolyte solution the Maxwell-Stefan diffusivities $D_{jk}(\mathbf{x},t)$ depend on the local composition. To describe this concentration dependence in the multi-component electrolyte solution and the pseudo-homogenous membrane phase, Visser (2001) proposed the empirical model given in Appendix B.4. For notational simplicity the Maxwell-Stefan diffusivities are considered as generic functions

$$D_{jk}(\mathbf{x},t) = f_{jk}^{D}(\mathbf{c}(\mathbf{x},t)), \quad k,j = 1,...,n, \tag{4.27}$$

in the remainder of this work.

Reaction kinetics and dissociation equilibria

In a system with n_R independent chemical reactions the local volumetric reaction flux density $r_k^V(\mathbf{x},t)$ is given by

$$r_k^V(\mathbf{x},t) = \sum_{j=1}^{n_R}\nu_{j,k}\,r_j^0(\mathbf{x},t), \qquad k = 1,...,n, \tag{4.28}$$

where $\nu_{j,k}$, $j = 1,...,n_R$, $k = 1,...,n$, are the stoichiometric coefficients and $r_j^0(\mathbf{x},t)$, $j \in \{1,...,n\}_R$, are the normalized local reaction rates. In the case of $n_{R,kin}$ non-equilibrium reactions, the normalized reaction rates are commonly modeled using kinetic rate expressions

$$r_j^0(\mathbf{x},t) = k_j(\mathbf{x},t)\prod_{k=1}^{n}c_k(\mathbf{x},t)^{p_{k,j}}, \quad j = 1,...,n_{R,kin}. \tag{4.29}$$

Here, $k_j(\mathbf{x},t)$ are the reaction rate coefficients and $p_{k,j}$ the specific reaction orders. In the case of equilibrium reactions describing the dissociation of an electrolyte, the kinetic approach (4.29)

is not appropriate, as these reactions are characterized by an infinitely fast transition to the equilibrium state. Thus, the kinetic model (4.29) is replaced by equilibrium relations of the form

$$K_j = \prod_{k=1}^{n} c_k^{\nu_{j,k}}(\mathbf{x},t)\,\gamma_k^{\nu_{j,k}}(\mathbf{x},t)\,, \qquad j = 1,...,n_{R,eq}. \tag{4.30}$$

Here, $K_j,\ j = 1,...,n_{R,eq}$ are the equilibrium constants associated to the $n_{R,eq}$ equilibrium reactions.

It is important to note that – as far as heterogeneous electrode reactions are excluded – the charge is conserved in both types of chemical reactions, i.e.

$$0 = \sum_{k=1}^{n} z_k\, r_k^V(\mathbf{x},t)\,. \tag{4.31}$$

4.1.3 Momentum balance equation and hydrodynamics

In the scenario of an electrolyte solution in a flow channel the local fluid velocity $\mathbf{v}(\mathbf{x},t)$ and pressure $p(\mathbf{x},t)$ are rigorously described by a conservation law for the total momentum, e.g., in the form of the Navier-Stokes equations

$$\begin{aligned}&\rho(\mathbf{x},t)\left(\frac{\partial \mathbf{v}^{bar}(\mathbf{x},t)}{\partial t} + \mathbf{v}^{bar}(\mathbf{x},t)\cdot\nabla\mathbf{v}^{bar}(\mathbf{x},t)\right)\\ &= -\nabla p(\mathbf{x},t) + \nu\,\nabla^2\cdot\mathbf{v}^{bar}(\mathbf{x},t) + \rho^e(\mathbf{x},t)\,\mathbf{E}(\mathbf{x},t)\,.\end{aligned} \tag{4.32}$$

Here, ν is the kinematic viscosity of the electrolyte solution. A thorough numerical treatment of the Navier-Stokes equations in combination with a rigorous mass-transfer model requires a large computational effort and tailored numerical methods. As the scope of this work is on models which can be used for the optimization-based design or control with established methods, only scenarios are considered where the local velocities and total pressure can be approximated, e.g., by the film-theory approach introduced in Section 5.1.2.

Thus, for the remainder of this chapter it is assumed that the local velocity with respect to two coordinates are known input functions, i.e.,

$$v_{x_2}^{bar}(\mathbf{x},t) = u_{v_{x_2}}(\mathbf{x},t)\,, \tag{4.33}$$

$$v_{x_3}^{bar}(\mathbf{x},t) = u_{v_{x_3}}(\mathbf{x},t)\,. \tag{4.34}$$

Note that one arbitrary component of $\mathbf{v}^{bar}(\mathbf{x},t)$, e.g., $v_{x_1}^{bar}(\mathbf{x},t)$, is determined by the n species balances and the equation of state (4.10). The local pressure will not be considered as it has nearly no influence on the transport in the incompressible phases considered here (Visser, 2001).

For the scenario of a pseudo-homogenous membrane phase, momentum conservation has to include the external forces required to maintain the membrane material stationary, i.e. to maintain $\mathbf{v}_1 = 0$. As these forces are generally unknown, a common assumption is to neglect the contributions of inertial and viscous forces to the total momentum (Nagy, 2012). With this assumption the momentum balance equation degenerates into a local equilibrium of external forces and pressure gradients. As these are generally not of practical interest, momentum conservation is not considered in the membranes.

4.1.4 Complete mathematical models

Based on the theoretical framework introduced in this section, complete mathematical models are derived for the scenarios of an electrolyte solution and the membrane phase. In both cases it is assumed that the phase is locally electroneutral, which is enforced by the electroneutrality condition (4.19). Further, the description is restricted to a scenario of strong electrolytes which implies $n_R = n_{R,kin}$ and $n_{R,eq} = 0$. The model part which is common for both scenarios is formed by Eqs. (4.9), (4.27), (4.17), (4.19), (4.23), (4.28) and (4.29).

For the scenario of the transport in a liquid electrolyte solution, the model is completed by n species balance equations (4.1), the implicit definition of the volume-averaged velocity (4.6), the equation of state (4.10), the density model (4.15) and the analytical solutions for the velocity profiles (4.33) and (4.34). These equations result in the following PDAE model:

$$\frac{\partial c_k(\mathbf{x},t)}{\partial t} = -\nabla\cdot\mathbf{J}_k(\mathbf{x},t) - \nabla\cdot\left(\mathbf{v}^{va}(\mathbf{x},t)\,c_k(\mathbf{x},t)\right) + r_k^V(\mathbf{x},t), \qquad k=1,...,n, \tag{4.35}$$

$$\begin{aligned}&\sum_{j=2}^{n}\Gamma_{k,j}\nabla c_j(\mathbf{x},t) + \frac{z_k\,c_k(\mathbf{x},t)\;F}{M_k}\mathbf{E}(\mathbf{x},t)\\ &= \sum_{j=1,j\neq k}^{n}\frac{c_k(\mathbf{x},t)\,\mathbf{J}_j(\mathbf{x},t) - \;c_j(\mathbf{x},t)\,\mathbf{J}_k(\mathbf{x},t)}{D_{j,k}(\mathbf{x},t)\;c_T(\mathbf{x},t)}, \qquad k=2,...,n.\end{aligned} \tag{4.36}$$

$$\nabla\phi(\mathbf{x},t) = -\mathbf{E}(\mathbf{x},t), \tag{4.37}$$

$$0 = 1 - \sum_{j=1}^{n} c_j(\mathbf{x},t)\;\tilde{V}_j + V^E(\mathbf{x},t)\;c_T(\mathbf{x},t), \tag{4.38}$$

$$0 = \sum_{j=1}^{n}\left(\tilde{V}_j + V^E(\mathbf{x},t)\right)\mathbf{J}_j(\mathbf{x},t), \tag{4.39}$$

$$0 = c_T(\mathbf{x},t) - \sum_{j=1}^{n} c_j(\mathbf{x},t), \tag{4.40}$$

$$0 = \sum_{k=2}^{n} z_k c_k(\mathbf{x},t), \tag{4.41}$$

$$0 = r_j^0(\mathbf{x},t) - k_j(\mathbf{x},t)\prod_{k=1}^{n} c_k(\mathbf{x},t)^{p_{k,j}}, \quad j=1,...,n_{R,kin}, \tag{4.42}$$

$$0 = \gamma_k(\mathbf{x},t) - f_k^{\gamma}(\mathbf{c}(\mathbf{x},t)), \quad k=1,...,n, \tag{4.43}$$

$$0 = V^E(\mathbf{x},t) - f^V(\mathbf{c}(\mathbf{x},t)), \tag{4.44}$$

$$0 = D_{j,k}(\mathbf{x},t) - f_{jk}^D(\mathbf{c}(\mathbf{x},t)), \quad j,k=1,...,n, \tag{4.45}$$

$$0 = v_{x_2}^{va}(\mathbf{x},t) - f^{v_{x_2}}(\mathbf{x},t), \tag{4.46}$$

$$0 = v_{x_3}^{va}(\mathbf{x},t) - f^{v_{x_3}}(\mathbf{x},t), \tag{4.47}$$

For the scenario of ionic transport in the membrane phase, the model is complemented by $n-1$ species balance equations (4.1) and the implicit definition of the reference velocity (4.8). The model is closed by the specifications $c_1(\mathbf{x},t) = const.$ and $\mathbf{v}(\mathbf{x},t) = 0$. The following model is obtained:

$$\frac{\partial c_k(\mathbf{x},t)}{\partial t} = -\nabla \cdot \mathbf{J}_k(\mathbf{x},t) + r_k^V(\mathbf{x},t), \qquad k = 2,...,n, \tag{4.48}$$

$$\begin{aligned}&\sum_{j=2}^{n} \Gamma_{k,j} \nabla c_j(\mathbf{x},t) + \frac{z_k\, c_k(\mathbf{x},t)\; F}{M_k} \mathbf{E}(\mathbf{x},t) \\ &= \sum_{j=1,j\neq k}^{n} \frac{c_k(\mathbf{x},t)\, \mathbf{J}_j(\mathbf{x},t) - \; c_j(\mathbf{x},t)\, \mathbf{J}_k(\mathbf{x},t)}{D_{j,k}(\mathbf{x},t)\; c_T(\mathbf{x},t)}, \qquad k = 2,...,n.\end{aligned} \tag{4.49}$$

$$\nabla \phi(\mathbf{x},t) = -\mathbf{E}(\mathbf{x},t), \tag{4.50}$$

$$0 = \mathbf{J}_1(\mathbf{x},t), \tag{4.51}$$

$$0 = c_T(\mathbf{x},t) - \sum_{j=1}^{n} c_j(\mathbf{x},t), \tag{4.52}$$

$$0 = z_1\, c_1 + \sum_{k=2}^{n} z_k c_k(\mathbf{x},t), \tag{4.53}$$

$$0 = r_j^0(\mathbf{x},t) - k_j(\mathbf{x},t) \prod_{k=1}^{n} c_k(\mathbf{x},t)^{p_{k,j}}, \quad j = 1,...,n_{R,kin}, \tag{4.54}$$

$$0 = \gamma_k(\mathbf{x},t) - \tilde{f}_k^{\gamma}(\mathbf{c}(\mathbf{x},t)), \quad k = 1,...,n, \tag{4.55}$$

$$0 = D_{j,k}(\mathbf{x},t) - \tilde{f}_k^{D}(\mathbf{c}(\mathbf{x},t)), \quad k = 1,...,n, \tag{4.56}$$

$$c_1 = const. \tag{4.57}$$

Both models are completed by a consistent set of initial and boundary conditions. These conditions will be introduced in Section 4.3.2 after the number of differential degrees of freedom is analyzed in the process of index analysis and reduction.

4.2 Index analysis and reduction

In this section the PDAE models describing ionic-transport in the liquid electrolyte solution and the pseudo-homogenous membrane phase are analyzed in terms of their differential indices. To this end, the method for the index analysis and reduction (IAR) introduced in Chapter 3 is employed.

4.2.1 Index with respect to time

In analogy to the simplified Nernst-Planck formulation introduced in Chapter 3, the index analysis of the models (4.48) - (4.57) and (4.35) - (4.47) with respect to time results in a differential index of two. A first MSSS inducing this high index behavior is formed by the electroneutrality constraint (4.19). Obviously, the constraint couples the molar concentrations of $(n-1)$ species which constitute differential quantities in the species balance equations (4.1). In the index reduction step of the IAR method, in analogy to the example presented in Chapter 3 the corresponding hidden constraint is revealed as

$$0 = -\sum_{j=2}^{n} z_j \nabla \cdot \mathbf{J}_j(\mathbf{x},t) - \underbrace{\sum_{j=2}^{n} z_j \nabla \cdot (\mathbf{v}(x,t)\, c_j(\mathbf{x},t)) + \sum_{j=2}^{n} z_j\, r_j^V(\mathbf{x},t)}_{=0} \tag{4.58}$$

With Eqs. (4.31) and (4.19) the second and third terms on the right hand side of (4.58) are shown to be zero. Thus, by introducing the definition of the local current density

$$\mathbf{i}(\mathbf{x},t) = F \sum_{j=2}^{n} z_j \mathbf{J}_j(\mathbf{x},t)\,, \tag{4.59}$$

the first constraint (4.58) can be interpreted as the stationary local charge balance

$$0 = \nabla \cdot \mathbf{i}(\mathbf{x},t)\,, \tag{4.60}$$

which highlights the charge density $\rho^e(\mathbf{x},t)$ as a dynamic invariant of the system.

For the scenario of an electrolyte solution, a second MSSS is formed by the definition of the total density (4.9) and the equation of state (4.10). With respect to this MSSS the IAR method identifies the hidden constraint

$$\begin{aligned} 0 = &- c_T(\mathbf{x},t)\, \frac{\partial V^E(\mathbf{x},t)}{\partial t} \\ &- \sum_{j=1}^{n} \left(\tilde{V}_j + V^E(\mathbf{x},t)\right) \nabla \cdot \mathbf{J}_j(\mathbf{x},t) \\ &- \sum_{j=1}^{n} \left(\tilde{V}_j + V^E(\mathbf{x},t)\right) \nabla \cdot (\mathbf{v}^{va}(\mathbf{x},t)\, c_j(\mathbf{x},t)) \\ &+ \sum_{j=1}^{n} \left(\tilde{V}_j + V^E(\mathbf{x},t)\right) r_j^V(\mathbf{x},t)\,. \end{aligned} \tag{4.61}$$

This second constraint (4.61) can be simplified by introducing (i) the implicit definition of the volume-averaged reference velocity (4.6), (ii) its derivative with respect to the spatial coordinates,

$$0 = \sum_{j=1}^{n} \left(\tilde{V}_j + V^E(\mathbf{x},t)\right) \nabla \cdot \mathbf{J}_j(\mathbf{x},t) + \sum_{j=1}^{n} \nabla V^E(\mathbf{x},t)\, \mathbf{J}_j(\mathbf{x},t)\,, \tag{4.62}$$

(iii) the equation of state (4.10), and (iv) its derivative with respect to the spatial coordinates,

$$0 = c_T(\mathbf{x},t)\, \nabla V^E(\mathbf{x},t) + \sum_{j=1}^{n} \left(\tilde{V}_j + V^E(\mathbf{x},t)\right) \nabla c_j(\mathbf{x},t)\,. \tag{4.63}$$

These substitutions and subsequent reformulation of Eq. (4.61) yield

$$\begin{aligned} 0 = &- c_T(\mathbf{x},t)\frac{\partial V^E(\mathbf{x},t)}{\partial t} + \nabla V^E(\mathbf{x},t)\left(c_T(\mathbf{x},t)\,\mathbf{v}^{va}(\mathbf{x},t) + \sum_{j=1}^{n}\mathbf{J}_j(\mathbf{x},t)\right) \\ &- \left(1 - V^E(\mathbf{x},t)\,c_T(\mathbf{x},t)\right)\nabla\cdot\mathbf{v}^{va}(\mathbf{x},t) \\ &+ \sum_{j=1}^{n}\left(\tilde{V}_j + V^E(\mathbf{x},t)\right) r_j^V(\mathbf{x},t)\,. \end{aligned} \tag{4.64}$$

Eq. (4.64) can be further simplified if the excess volume is assumed to be constant, i.e. $\frac{\partial V^E(\mathbf{x},t)}{\partial t} = 0$ and $\nabla V^E(\mathbf{x},t) = 0$. In this case Eq. (4.61) simplifies to

$$\begin{aligned} 0 = &- \left(1 - V^E(\mathbf{x},t)\,c_T(\mathbf{x},t)\right)\nabla\cdot\mathbf{v}^{va}(\mathbf{x},t) \\ &+ \sum_{j=1}^{n}\left(\tilde{V}_j + V^E(\mathbf{x},t)\right) r_j^V(\mathbf{x},t)\,. \end{aligned} \tag{4.65}$$

Further, if no reactions take place, i.e. if $r_j^V(\mathbf{x},t) = 0,\ j = 1,...,n$, Eq. (4.65), yields

$$0 = \nabla\cdot\mathbf{v}^{va}(\mathbf{x},t)\,, \tag{4.66}$$

which can be interpreted as the stationary continuity equation for the volume-averaged velocity.

For both scenarios, the electrolyte solution and the pseudo-homogenous membrane, Eq. (4.60) is used to substitute the species balance equation (4.1) for the ionic species n in order to reduce the index. The index reduction for the model of the electrolyte solution further involves the substitution of the species balance equation (4.1) for the charge-neutral species 1 by Eq. (4.64). All substitutions are possible without the loss of physical information as (4.60) and (4.64) represent linear combinations of the species balance equations (4.1).

4.2.2 Index with respect to the spatial coordinates

In the next step, the index with respect to the spatial coordinates is analyzed. For both transport models the analysis determines the differential index with respect to the spatial coordinates as two. This high index behavior arises as again a MSSS is formed by the electroneutrality constraint (4.19). The corresponding hidden constraint is identified by the IAR method as

$$\begin{aligned} 0 = &\sum_{m=2}^{n} z_m \sum_{h=2}^{n} \Gamma^{-1}_{m,h} z_h\, c_h(\mathbf{x},t)\,\frac{F}{RT}\,\mathbf{E}(\mathbf{x},t) \\ &+ \sum_{m=2}^{n} z_m \sum_{h=2}^{n} \Gamma^{-1}_{m,h} \sum_{\substack{j=1 \\ j\neq h}}^{n} \frac{c_h(\mathbf{x},t)\,\mathbf{J}_j(\mathbf{x},t) - c_j(\mathbf{x},t)\,\mathbf{J}_h(\mathbf{x},t)}{D_{j,h}(\mathbf{x},t)\,c_T(\mathbf{x},t)}. \end{aligned} \tag{4.67}$$

The linear combination of the Maxwell-Stefan equations Eq. (4.67) constitutes a purely algebraic equation implicitly describing the propagation of the electric field. In analogy to the additionatal constraint identified for the Nernst-Planck system, it can be interpreted as a generalization of Ohm's Law to a scenario of a concentrated solution with multiple species. To see

this, the scenario of an infinitely diluted solution is considered where Ohm's Law is valid. Here, $\gamma_k(\mathbf{x},t)=1,\ k=1,...,n$, and it is appropriate to replace the binary diffusion coefficients by constant species mobilities $\frac{D_{j,h}(\mathbf{x},t)}{RT}=u_j^m\ j,k=1,...,n,\ k\neq j$ (Newman and Thomas-Alyea, 2004). With these assumptions Eq. (4.67) is reformulated yielding

$$\sum_{h=1}^{n-1} z_h^2\, c_h(\mathbf{x},t)\ F\,\mathbf{E}(\mathbf{x},t) = \underbrace{\sum_{j=1}^{n} \frac{\mathbf{J}_j(\mathbf{x},t)}{c_T(\mathbf{x},t)\ u_j^m} \sum_{h=1}^{n-1} z_h\, c_h(\mathbf{x},t)}_{=0,\,with\ Eq.\ (4.19)} - \sum_{j=1,j\neq h}^{n} \frac{\mathbf{c}_j(\mathbf{x},t)}{c_T(\mathbf{x},t)\ u_j^m} \sum_{h=1}^{n-1} z_h\,\mathbf{J}_h(\mathbf{x},t)\,. \tag{4.68}$$

By introducing Eq. (4.59) and the definition of the conductivity of a diluted solution $\kappa(\mathbf{x},t)=F^2\sum_{j=1}^{n-1} z_j^2\,u_j^m\,c_j(\mathbf{x},t)$ (Newman and Thomas-Alyea, 2004), Eq. (4.68) is further reformulated yielding Ohm's Law

$$\mathbf{i}(\mathbf{x},t) = -\kappa(\mathbf{x},t)\ \mathbf{E}(\mathbf{x},t)\,. \tag{4.69}$$

In both scenarios the index with respect to the spatial coordinates is reduced by using Eq. (4.67) to substitute the Maxwell-Stefan equation (4.23) of the ionic species n. Again, this substitution is not associated with a loss of physical information as Eq. (4.67) is a linear combination of the original Maxwell-Stefan equations (4.23).

4.2.3 Reformulated low index model

The low index models for the distinct scenarios are formed by species balance (4.1) and Maxwell-Stefan equations (4.23) for the species $k=2,...n-1$. Eq. (4.60) is added as tailored balance equation; Eq. (4.67) is added as tailored Maxwell-Stefan equation to both models. For the scenario of the membrane phase this results in the following PDAE model:

$$\frac{\partial c_k(\mathbf{x},t)}{\partial t} = -\nabla\cdot\mathbf{J}_k(\mathbf{x},t) + r_k^V(\mathbf{x},t)\,, \qquad k=2,...,n-1, \tag{4.70}$$

$$0 = \nabla\cdot\mathbf{i}(\mathbf{x},t)\,, \tag{4.71}$$

$$\sum_{j=2}^{n}\Gamma_{k,j}\nabla c_j(\mathbf{x},t) + \frac{z_k\,c_k(\mathbf{x},t)\ F}{M_k}\mathbf{E}(\mathbf{x},t) = \sum_{j=1,j\neq k}^{n} \frac{c_k(\mathbf{x},t)\,\mathbf{J}_j(\mathbf{x},t) - c_j(\mathbf{x},t)\,\mathbf{J}_k(\mathbf{x},t)}{D_{j,k}(\mathbf{x},t)\ c_T(\mathbf{x},t)}, \qquad k=2,...,n-1, \tag{4.72}$$

$$0 = -\sum_{m=2}^{n} z_m \sum_{h=2}^{n}\Gamma_{m,h}^{-1} z_h\, c_h(\mathbf{x},t)\ F\mathbf{E}(\mathbf{x},t) - \sum_{m=2}^{n} z_m \sum_{h=2}^{n}\Gamma_{m,h}^{-1} \sum_{j=1,j\neq h}^{n} \frac{c_h(\mathbf{x},t)\,\mathbf{J}_j(\mathbf{x},t) - c_j(\mathbf{x},t)\,\mathbf{J}_h(\mathbf{x},t)}{D_{j,h}(\mathbf{x},t)\ c_T(\mathbf{x},t)}, \tag{4.73}$$

$$\nabla\phi\left(\mathbf{x},t\right)=-\mathbf{E}\left(\mathbf{x},t\right), \tag{4.74}$$

$$0=\mathbf{J}_1\left(\mathbf{x},t\right), \tag{4.75}$$

$$0=c_T\left(\mathbf{x},t\right)-\sum_{j=1}^{n}c_j\left(\mathbf{x},t\right), \tag{4.76}$$

$$0=z_1\,c_1+\sum_{k=2}^{n}z_k c_k\left(\mathbf{x},t\right), \tag{4.77}$$

$$0=r_j^0\left(\mathbf{x},t\right)-k_j\left(\mathbf{x},t\right)\prod_{k=1}^{n}c_k\left(\mathbf{x},t\right)^{p_{k,j}},\quad j=1,...,n_{R,kin}, \tag{4.78}$$

$$0=\gamma_k\left(\mathbf{x},t\right)-\tilde{f}_k^{\gamma}\left(\mathbf{c}\left(\mathbf{x},t\right)\right),\quad k=1,...,n, \tag{4.79}$$

$$0=D_{j,k}\left(\mathbf{x},t\right)-\tilde{f}_k^{D}\left(\mathbf{c}\left(\mathbf{x},t\right)\right),\quad k=1,...,n, \tag{4.80}$$

$$c_1=const., \tag{4.81}$$

$$0=\mathbf{i}\left(\mathbf{x},t\right)-F\sum_{j=1}^{n-1}z_j\mathbf{J}_j\left(\mathbf{x},t\right). \tag{4.82}$$

The model for the scenario of a liquid electrolyte solution additionally comprises the continuity equation for the volumetric velocity (4.64) to result in the PDAE model:

$$\frac{\partial c_k\left(\mathbf{x},t\right)}{\partial t}=-\nabla\cdot\mathbf{J}_k\left(\mathbf{x},t\right)-\nabla\cdot\left(\mathbf{v}^{va}\left(\mathbf{x},t\right)c_k\left(\mathbf{x},t\right)\right)+r_k^V\left(\mathbf{x},t\right),\qquad k=2,...,n-1, \tag{4.83}$$

$$0=\nabla\cdot\mathbf{i}\left(\mathbf{x},t\right), \tag{4.84}$$

$$0=\nabla\cdot\mathbf{v}^{va}\left(\mathbf{x},t\right), \tag{4.85}$$

$$\begin{aligned}&\sum_{j=2}^{n}\Gamma_{k,j}\nabla c_j\left(\mathbf{x},t\right)+\frac{z_k\,c_k\left(\mathbf{x},t\right)\,F}{M_k}\mathbf{E}\left(\mathbf{x},t\right)\\&=\sum_{j=1,j\neq k}^{n}\frac{c_k\left(\mathbf{x},t\right)\mathbf{J}_j\left(\mathbf{x},t\right)-\,c_j\left(\mathbf{x},t\right)\mathbf{J}_k\left(\mathbf{x},t\right)}{D_{j,k}\left(\mathbf{x},t\right)\,c_T\left(\mathbf{x},t\right)},\qquad k=2,...,n-1,\end{aligned} \tag{4.86}$$

$$\begin{aligned}0=&-\sum_{m=2}^{n}z_m\sum_{h=2}^{n}\Gamma_{m,h}^{-1}z_h\,c_h\left(\mathbf{x},t\right)\,F\mathbf{E}\left(\mathbf{x},t\right)\\&-\sum_{m=2}^{n}z_m\sum_{h=2}^{n}\Gamma_{m,h}^{-1}\sum_{j=1,j\neq h}^{n}\frac{c_h\left(\mathbf{x},t\right)\mathbf{J}_j\left(\mathbf{x},t\right)-\,c_j\left(\mathbf{x},t\right)\mathbf{J}_h\left(\mathbf{x},t\right)}{D_{j,h}\left(\mathbf{x},t\right)\,c_T\left(\mathbf{x},t\right)},\end{aligned} \tag{4.87}$$

$$\nabla\phi\left(\mathbf{x},t\right)=-\mathbf{E}\left(\mathbf{x},t\right), \tag{4.88}$$

$$0=1-\sum_{j=1}^{n}c_j\left(\mathbf{x},t\right)\,\tilde{V}_j+V^E\left(\mathbf{x},t\right)\,c_T\left(\mathbf{x},t\right), \tag{4.89}$$

$$0=\sum_{j=1}^{n}\left(\tilde{V}_j+V^E\left(\mathbf{x},t\right)\right)\,\mathbf{J}_j\left(\mathbf{x},t\right), \tag{4.90}$$

$$0 = c_T(\mathbf{x},t) - \sum_{j=1}^{n} c_j(\mathbf{x},t), \tag{4.91}$$

$$0 = \sum_{k=2}^{n} z_k c_k(\mathbf{x},t), \tag{4.92}$$

$$0 = r_j^0(\mathbf{x},t) - k_j(\mathbf{x},t) \prod_{k=1}^{n} c_k(\mathbf{x},t)^{p_{k,j}}, \quad j = 1,...,n_{R,kin}, \tag{4.93}$$

$$0 = \gamma_k(\mathbf{x},t) - f_k^{\gamma}(\mathbf{c}(\mathbf{x},t)), \quad k = 1,...,n, \tag{4.94}$$

$$0 = V^E(\mathbf{x},t) - f^V(\mathbf{c}(\mathbf{x},t)), \tag{4.95}$$

$$0 = D_{j,k}(\mathbf{x},t) - f_{jk}^D(\mathbf{c}(\mathbf{x},t)), \quad j,k = 1,...,n, \tag{4.96}$$

$$0 = v_{x_2}^{va}(\mathbf{x},t) - f^{v_{x_2}}(\mathbf{c}(\mathbf{x},t)), \tag{4.97}$$

$$0 = v_{x_3}^{va}(\mathbf{x},t) - f^{v_{x_3}}(\mathbf{c}(\mathbf{x},t)), \tag{4.98}$$

$$0 = \mathbf{i}(\mathbf{x},t) - F \sum_{j=1}^{n-1} z_j \mathbf{J}_j(\mathbf{x},t). \tag{4.99}$$

4.3 Reduced system and consistent initial and boundary conditions

The results of the IAR in the previous section illustrate that in both scenarios $(n-2)$ species, rather than the total number of n species, in the system are truly independent. Correspondingly, the reformulated models comprise conservation laws for $(n-2)$ truly independent species, a conservation law for the current density and, in the scenario of an electrolyte solution, a conservation law for the volume-averaged velocity. Uncoupling these conservation laws from the remaining equations strongly simplifies the development of an efficient implementation of the model. Hence, in this section a decoupled system of PDE is derived for which consistent initial and boundary conditions are introduced to obtain a complete problem formulation.

4.3.1 Reformulation into a reduced system of PDE

The reformulation into a reduced system of PDE is obtained in four major steps. For notational simplicity the dependence on the independent variables $(\mathbf{x},t)$ will not be indicated explicitly in the following.

In the first step, an explicit expression for $\mathbf{J}_n$ is derived by introducing Eq. (4.4) into Eq. (4.59) and reformulation yielding

$$\mathbf{J}_n = \mathbf{i}\hat{\beta} + \sum_{j=2}^{n-1} \hat{w}_j \mathbf{J}_j = \mathbf{i}\hat{\beta} + \hat{\mathbf{w}}^T \bar{\mathbf{J}}, \tag{4.100}$$

with

$$\hat{\beta} = \frac{1}{z_n F} \left(1 + \frac{\frac{w_n}{w_1}}{1 - \frac{w_n}{w_1}\frac{z_1}{z_n}} \right) \tag{4.101}$$

and

$$\hat{w}_j = -\frac{z_j}{z_n} - \frac{z_1}{z_n}\frac{\frac{w_n}{w_1}\frac{z_j}{z_n} - \frac{w_j}{w_1}}{1 - \frac{w_n}{w_1}\frac{z_1}{z_n}}, \quad j = 2, ..., n-1. \tag{4.102}$$

To simplify the notation in the following, the vectors $\bar{\mathbf{c}} \in \mathbb{R}^{n-2}$ with elements c_k, the vector $\hat{\mathbf{w}} \in \mathbb{R}^{n-2}$ with elements $\hat{w}_k$ and the tensor $\bar{\mathbf{J}} \in \mathbb{R}^{(n-2)\times 3}$ with elements $\mathbf{J}_k$ for $k = 2, ..., n-1$ are introduced. Further, the matrix $\Theta_1 \in \mathbb{R}^{(n-2)\times(n-2)}$ is introduced with elements $\left(\Gamma^{-1}\,\mathbf{B}\right)_{k,j}$, $k, j \in \{2, ..., n-1\}$, the vector $\Theta_2 \in \mathbb{R}^{n-2}$ is introduced with elements $\left(\Gamma^{-1}\,\mathbf{B}\right)_{k,n}$, $k = 2, ..., n-1$ and the vector $\Theta_3 \in \mathbb{R}^{n-2}$ is introduced with elements $\left(\Gamma^{-1}\,\mathbf{Z}\,\mathbf{c}\right)_k$, $k = 2, ..., n-1$.

In the second step, Eq. (4.100) is used to remove $\mathbf{J}_n$ from Eqs. (4.24) and (4.67). Introducing Eq. (4.100) into the first $(n-2)$ equations of (4.24) yields

$$c_T\,\nabla\bar{\mathbf{c}} - \Theta_3\,\mathbf{E} = \tilde{\mathbf{B}}\,\bar{\mathbf{J}} + \mathbf{a}\,\mathbf{i} \tag{4.103}$$

with

$$\tilde{\mathbf{B}} = \Theta_1 + \Theta_2\,\hat{\mathbf{w}}^T \tag{4.104}$$

and

$$\mathbf{a} = \hat{\beta}\,\Theta_2. \tag{4.105}$$

Further, with the introduction of the charge vector $\mathbf{z} \in \mathbb{R}^{n-1}$ with elements z_k, $k = 2, ..., n$, the vector $\Theta_3 \in \mathbb{R}^{n-2}$ with elements $\left(\mathbf{z}^T\Gamma^{-1}\,\mathbf{B}\right)_k$, $k = 2, ..., n-1$ and $\Theta_4 = \left(\mathbf{z}^T\Gamma^{-1}\,\mathbf{B}\right)_n$, the constraint (4.67) is expressed as

$$-\mathbf{z}^T\Gamma^{-1}\,\mathbf{Z}\,\mathbf{c}\,\mathbf{E} = \Omega_1\,\bar{\mathbf{J}} + \Omega_2\,\mathbf{i}, \tag{4.106}$$

with

$$\Omega_1 = \Theta_3 + \Theta_4\,\hat{\mathbf{w}}^T, \tag{4.107}$$

and

$$\Omega_2 = \hat{\beta}\,\Theta_4. \tag{4.108}$$

In the third step, explicit expressions for $\bar{\mathbf{J}}$ and $\mathbf{i}$ are derived from Eqs. (4.103) and (4.106), respectively. A necessary condition to determine $\bar{\mathbf{J}}$ uniquely from (4.103) is

$$\det\left(\tilde{\mathbf{B}}\right) \neq 0. \tag{4.109}$$

In the following it is assumed that this criterion is fulfilled. From Eq. (4.103) an explicit expression for the diffusive flux densities is obtained as

$$\bar{\mathbf{J}} = c_T\,\tilde{\mathbf{B}}^{-1}\,\nabla\bar{\mathbf{c}} - \Theta_3\mathbf{E} - \mathbf{i}\,\tilde{\mathbf{B}}^{-1}\,\mathbf{a}. \tag{4.110}$$

Introducing Eq. (4.110) into Eq. (4.106) and reformulation yields

$$\mathbf{i} = \Omega_3\,\mathbf{E} + \Omega_4\,\nabla\bar{\mathbf{c}}, \tag{4.111}$$

with

$$\Omega_3 = \frac{\Omega_1\,\tilde{\mathbf{B}}^{-1}\,\Theta_3 - \mathbf{z}^T\Gamma^{-1}\,\mathbf{Z}\mathbf{c}}{\Omega_2 - \Omega_1\,\tilde{\mathbf{B}}^{-1}\,\mathbf{a}} \tag{4.112}$$

and

$$\Omega_4 = -\frac{c_T \Omega_1 \tilde{\mathbf{B}}^{-1}}{\Omega_2 - \Omega_1 \tilde{\mathbf{B}}^{-1} \mathbf{a}}. \tag{4.113}$$

Note that the term $\Omega_2 - \Omega_1 \tilde{\mathbf{B}}^{-1} \mathbf{a}$ in Eqs. (4.112) and (4.113) is a scalar expression. Introducing Eq. (4.111) into Eq. (4.110) yields

$$\bar{\mathbf{J}} = \Omega_5 \nabla \bar{\mathbf{c}} + \Omega_6 \mathbf{E}, \tag{4.114}$$

with

$$\Omega_5 = c_T \tilde{\mathbf{B}}^{-1} \bar{\Gamma} - \tilde{\mathbf{B}}^{-1} \mathbf{a} \Omega_4 \tag{4.115}$$

and

$$\Omega_6 = -\tilde{\mathbf{B}}^{-1} \Theta_3 - \Omega_3 \tilde{\mathbf{B}}^{-1} \mathbf{a}. \tag{4.116}$$

In the last step, Eqs. (4.114) and (4.111) are used to substitute $\bar{\mathbf{J}}$ and $\mathbf{i}$ in the balance equations (4.1), (4.60) and (4.66). By additionally introducing Eq. (4.17), this yields

$$\frac{\partial}{\partial t} \bar{\mathbf{c}} = \nabla \cdot \left(-\Omega_5 \left(\mathbf{c} \right) \nabla \bar{\mathbf{c}} + \Omega_6 \left(\mathbf{c} \right) \nabla \phi \right) - \nabla \cdot \left(\mathbf{v}^{va} \bar{\mathbf{c}} \right), \tag{4.117}$$

$$0 = \nabla \cdot \left(-\Omega_4 \left(\mathbf{c} \right) \nabla \bar{\mathbf{c}} + \Omega_3 \left(\mathbf{c} \right) \nabla \phi \right), \tag{4.118}$$

$$0 = \nabla \cdot \mathbf{v}^{va} \tag{4.119}$$

for the scenario of an electrolyte solution. For the scenario of the pseudo-homogenous membrane the introduction yields

$$\frac{\partial}{\partial t} \bar{\mathbf{c}} = \nabla \cdot \left(-\Omega_5 \left(\mathbf{c} \right) \nabla \bar{\mathbf{c}} + \Omega_6 \left(\mathbf{c} \right) \nabla \phi \right), \tag{4.120}$$

$$0 = \nabla \cdot \left(-\Omega_4 \left(\mathbf{c} \right) \nabla \bar{\mathbf{c}} + \Omega_3 \left(\mathbf{c} \right) \nabla \phi \right). \tag{4.121}$$

In both systems the coefficient matrices $\Omega_k \left(\mathbf{c} \right), k = 3, ..., 6$ still depend on the concentrations c_1 and c_n. By deriving explicit expressions for c_1 and c_n from Eqs. (4.19), (4.10) and (4.9), c_1 and c_n can be eliminated to obtain a completely decoupled system.

4.3.2 Initial and boundary conditions

For both PDAE models, $n-2$ initial conditions

$$c_k \left(\mathbf{x}, 0 \right) = c_{k,0} \left(\mathbf{x} \right), \qquad k = 2, ..., n-1, \tag{4.122}$$

can be specified independently. For the set of parabolic equations (4.117), $n-2$ boundary conditions should be specified at each boundary, e.g., in the form of the surface balance equations

$$J_k \left(\mathbf{x}|_{x_j = x_j^L}, t \right) + v_{x_j^L}^{va} \left(\mathbf{x}|_{x_j = x_j^L}, t \right) c_j \left(\mathbf{x}|_{x_j = x_j^L}, t \right) = \Psi_k^{x_j^L} \left(\mathbf{x}|_{x_i \neq x_j, i = 1..3}, t \right), \tag{4.123}$$

$$J_k \left(\mathbf{x}|_{x_j = x_j^U}, t \right) + v_{x_j^U}^{va} \left(\mathbf{x}|_{x_j = x_j^U}, t \right) c_j \left(\mathbf{x}|_{x_j = x_j^U}, t \right) = \Psi_k^{x_j^U} \left(\mathbf{x}|_{x_i \neq x_j, i = 1..3}, t \right), \tag{4.124}$$

$$j = 1, ..., 3, \quad k = 2, ..., n-1,$$

where $\Psi_k^{x_j^U}\left(\mathbf{x}|_{x_i\neq x_j,\,i=1..3},t\right)$ and $\Psi_k^{x_j^L}\left(\mathbf{x}|_{x_i\neq x_j,\,i=1..3},t\right)$ are total flux densities entering or leaving the domain. For the elliptic equation (4.118) one boundary condition should be specified for each boundary, e.g., in the form of dirichlet boundary conditions for the electric potential:

$$\phi\left(\mathbf{x}|_{x_j=x_j^L},t\right) = \phi^{x_j^L}\left(\mathbf{x}|_{x_i\neq x_j,\,i=1..3},t\right), \quad j=1,...,3, \tag{4.125}$$

$$\phi\left(\mathbf{x}|_{x_j=x_j^U},t\right) = \phi^{x_j^U}\left(\mathbf{x}|_{x_i\neq x_j,\,i=1..3},t\right), \quad j=1,...,3. \tag{4.126}$$

Here, $\phi^{x_j^U}\left(\mathbf{x}|_{x_i\neq x_j,\,i=1..3},t\right)$ are prescribed distributions of the electric potential at the boundaries. For the scenario of ionic transport in an electrolyte solution one additional boundary condition has to be specified for the hyperbolic equation (4.119). Assuming $v_{x^1}^{va}\left(\mathbf{x}|_{x_1=x_1^L},t\right)>0$, a consistent boundary condition is

$$v_{x^1}^{va}\left(\mathbf{x}|_{x_1=x_1^L},t\right) = v_{x^1}^{va,in}\left(\mathbf{x}|_{x_1=x_1^L},t\right). \tag{4.127}$$

4.4 Conclusions

In this chapter rigorous models for the description of ionic mass transport have been derived from widely accepted modeling paradigms. The theoretical basis used for the model development is similar to the one used by Kraaijeveld et al. (1995), Visser (2001) and Hogendoorn et al. (2001). However, this work considers for the first time both dynamic and three-dimensional model formulations. The challenging mathematical characterization and consistent specification of initial and boundary conditions resulting from this generalization has been successfully addressed by the application of the IAR method developed in Chapter 3. In this context the method has proven to be an effective tool to derive low-index PDAE models and strongly supported the thorough interpretation of the model states.

In analogy to the simpler Nernst-Planck system considered in Chapter 3, it has been shown for the first time that the electroneutrality condition induces high-index behavior with respect to both time and spatial coordinates in electrolytic transport models based on the Maxwell-Stefan approach. In the course of the index reduction with respect to time, the systematic procedure reveals the stationary charge balance as an additional constraint implicitly depicted in the model. The index reduction with respect to the spatial coordinates reveals a strictly algebraic constraint, which can be interpreted as a generalization of Ohm's law formulated for of a concentrated non-ideal electrolyte solution. In this way, the identification of the additional constraints allows for the first time a thorough interpretation of the physical principals depicted in models describing electroneutral diffusion in electrolyte systems. Further, with the detection of the high-index behavior, this work identifies a possible cause for the difficulties reported, e.g., by Neubrand (1999) and Newman and Thomas-Alyea (2004), in the context of the numerical treatment of ionic mass transport models.

The low-index models resulting from index reduction have been further reformulated in order to develop a compact representation for an efficient numerical treatment. The general idea for this reformulation is to uncouple the conservation laws in the PDAE systems from the remaining

model equations. This way, it has been possible to derive a novel reduced system of second-order PDE disclosing the structure of a coupled system of parabolic and elliptic equations. To the author's knowledge, this reduced PDE system describing the dynamic transport in an electroneutral electrolyte rigorously has not been reported in prior work. It stands out, as it can be reliably solved numerically in a MOL approach by applying standard discretization schemes and integrators typically available in commercial modeling environments. Next to simulation studies, this allows the use of the models in combination with optimization-based methods, e.g., for parameter estimation or a model-based design of experiments approach, strictly requiring index-one PDAE systems. Thus, the models provide an excellent basis for the development of a dynamic process model of an entire ED plant addressed in Chapter 5.

5 A dynamic process model of an electrodialysis plant

This chapter introduces a dynamic process model allowing the description of ED processes operated in dynamic mode. The rigorous dynamic description of the underlying transport in the membranes and flow channels is based on the generic models systematically derived in Chapter 4. The specification of these models and their integration in the hierarchical structure of the process model is presented in Section 5.1. The developed process model is specified in Section 5.2 to describe the lab-scale ED plant used for the experiments in Chapter 2. Further, this section introduces important details concerning the implementation in a commercial modeling environment. In Section 5.3 it is demonstrated that the developed model can provide first important insight into the dynamic process behavior and the underlying local transport phenomena. The model prediction is compared in Section 5.4 to experimental data from both current-voltage and desalination experiments. The primary objective of this comparison is to analyze whether the model correctly describes important physical principles.

5.1 Hierarchical model structure and model components

The model developed in this chapter is tailored to establish a thorough quantitative relation between the integral process behavior and the underlying local transport phenomena. Hence, as a first objective the model has to describe all process components that are governing the integral behavior of the process. This includes, next to the membrane module, process elements encountered in a typical industrial setting such as storage tanks and pumps. To address the complexity arising from the large number of different process components in the ED process, all model components are organized in a hierarchical model structure. As a second objective the underlying transport phenomena have to be described with high accuracy. Here, it is assumed that the local variation in the transport processes is decisive along the main direction of the electric field and the main flow direction in the flow channels. Hence, a two-dimensional dynamic formulation is used to describe the local transport in both the membranes and flow channels.

The modular set-up of industrial ED plants (cf. Fig. 5.1) motivates the description of the process by means of a hierarchical model structure as depicted in Fig. 5.2. On the highest hierarchical level the models for the storage tanks are connected to one or a series of models for an ED module. The latter is formed by aggregated sub-models for the electrodes, a single CEM and a finite number of electrodialytic cells. Each model of an electrodialytic cell consists

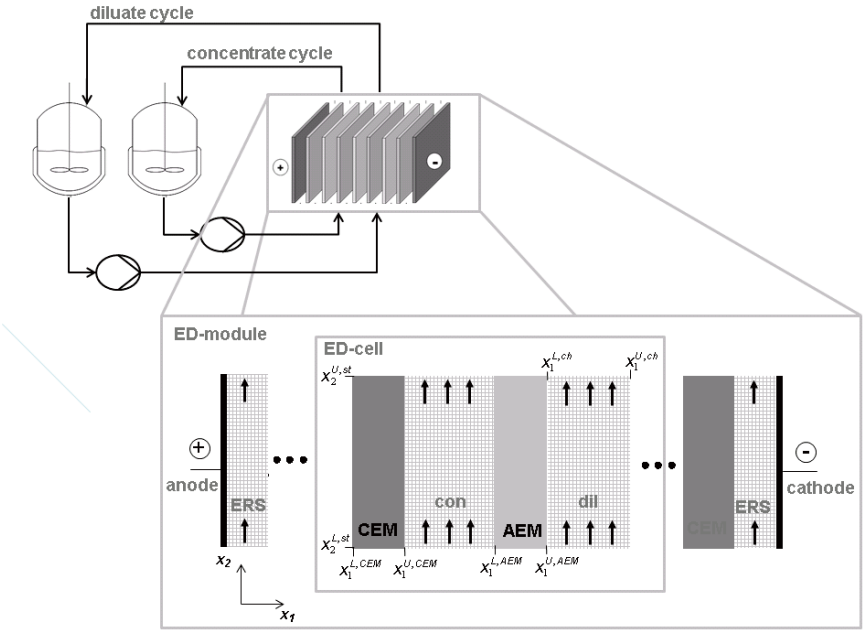

Figure 5.1: Structure of the modeled ED-plant operating in batch mode.

of the models for CEM, concentrate, AEM and diluate. These sub-models will be referred to as elementary model components in the following.

The description of the transport processes in the elementary model components is based on the transport models introduced in Chapter 4. Specifically, the model describing transport in a liquid electrolyte solution is specified in Section 5.1.2 to yield a rigorous description of the transport processes in the spacer-filled channels; the model describing transport in the pseudo-homogenous membrane phase is used as a basis for the development of the models for the CEM and AEM. Before this specification of the elementary models, Section 5.1.1 introduces general modeling assumptions. Section 5.1.3 describes the models for the remaining process elements, i.e., tanks and working electrodes.

5.1.1 General modeling assumptions

To facilitate the simulation of the process model in established modeling environments with a reasonable computational effort, the following simplifying assumptions are introduced:

- In the elementary model components, transport is rigorously described in the direction orthogonal to the planar working electrodes x_1 and the main flow direction in the channels

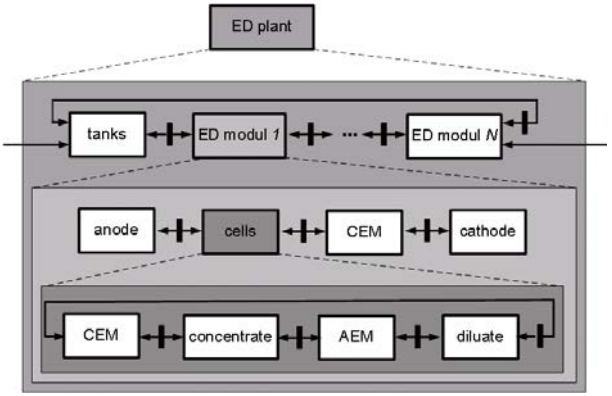

Figure 5.2: Hierachichal structure of the developed process model (Johannink et al., 2010).

x_2 (cf. Fig. 5.1). Transport in x_3-direction, corresponding to the depth of the channel, is neglected.

- Any contributions of the excess volume of the solution V^E to the total concentration are neglected. This implies that the continuity equation for the volume-averaged velocity is expressed as Eq. (4.66).

- The hydrodynamics in the spacer-filled channels are approximated using the film-theory approach (cf. Section 5.1.2).

- The membrane is considered as a pseudo-homogenous polymeric material. Membrane swelling resulting from the sorption of solutes is not considered.

- Due to the congruent set-up of the repeating ED cells, it is assumed that the physico-chemical phenomena in all ED cells are identical. Correspondingly, the model rigorously describes the transport in one cell and extrapolates the results to all cells in the module.

5.1.2 Spacer-filled flow channels and ion exchange membranes

The derivation of a two-dimensional description from the general three-dimensional transport models introduced in Chapter 4 requires dimensional reduction with respect to coordinate x_3. After this reduction, the transport model for the pseudo-homogenous membranes (4.120) and (4.121) is directly applicable in the process model to describe the AEM and CEM membranes. In the transport model for the electrolyte solution (4.117)-(4.119) an appropriate description of the hydrodynamics needs to be specified in addition to the dimensional reduction.

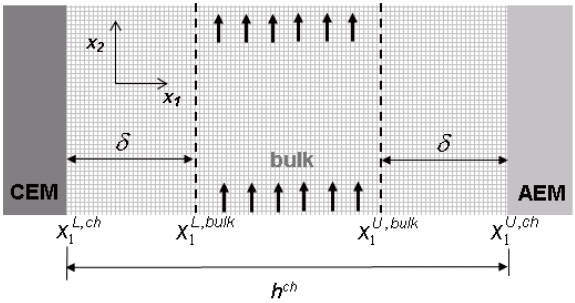

Figure 5.3: Boundary layers with a thickness δ and bulk phase according to the film-theory for the spacer-filled flow channels.

Dimensional reduction

The dimensional reduction with respect to the x_3-coordinate is formally obtained by integration of the models and the introduction of appropriate averaged states. However, this process conserves the original structure without introducing any additional source terms as integrational constants. This is due to the fact that in x_3-direction, corresponding to the depth of the ED stack, the channels and membranes are sealed by impermeable gaskets. Correspondingly, all boundary conditions for the extensive quantities in the model at x_3^L or x_3^U enforce a zero total flux.

Film-theory model

The general model describing transport in a liquid electrolyte solution is tailored to describe the spacer-filled flow channel by specifying an appropriate representation of the hydrodynamics. A rigorous description of the hydrodynamics, e.g., by the Navier-Stokes equations requires a local resolution of the complex spacer geometry and is computationally demanding (cf. Chapter 6). A common simplification to describe the hydrodynamics adjacent to a rigid surface is the introduction of the film-theory model (Taylor and Krishna, 1993, Visser, 2001).

The scenario resulting from the introduction of the film-theory approach for the spacer-filled flow channels is illustrated in Fig. 5.3. Accordingly, two boundary layers with the thickness δ are introduced separating the membrane and the bulk phase. In the bulk phase the hydrodynamics are described using a plug-flow assumption which implies $\frac{\partial v_{x_2}^{va}}{\partial x_1} = 0$. In the adjacent boundary layers, the velocity in the x_2-direction is considered to be negligibly small, i.e., $v_{x_2}^{va} = 0$.

This simplifies the continuity equation for the volume-averaged velocity (4.66) in the left boundary to

$$0 = \frac{\partial v_{x_1}^{va}}{\partial x_1}, \tag{5.1}$$

which is easily integrated yielding $v_{x_1}^{va} = v_{x_1=x_1^{L,ch}}^{va}(x_2)$. Here, $v_{x_1=x_1^{L,ch}}^{va}(x_2)$ is the volume-averaged

velocity entering or leaving the boundary layer at $x_1 = x_1^{L,ch}$. In a similar manner, the volume-averaged velocity in the right boundary layer is $v_{x_1}^{va} = v_{x_1=x_1^{U,ch}}^{va}(x_2)$.

For the bulk phase, Eq. (4.66) is integrated over x_1

$$0 = \int_{x_1^{L,bulk}}^{x_1^{U,bulk}} \frac{\partial v_{x_2}^{va}}{\partial x_2} dx_1 + \int_{x_1^{L,bulk}}^{x_1^{U,bulk}} \frac{\partial v_{x_1}^{va}}{\partial x_1} dx_1 \tag{5.2}$$

yielding

$$0 = \frac{\partial \bar{v}_{x_2}^{va}}{\partial x_2} + \frac{1}{x_1^{U,bulk} - x_1^{L,bulk}} \left[v_{x_1}^{va}\left(x_1^{U,bulk}, x_2\right) - v_{x_1}^{va}\left(x_1^{L,bulk}, x_2\right) \right], \tag{5.3}$$

where $\bar{v}_{x_2}^{va}$ is the x_1-averaged velocity in the x_2-direction.

Summarizing the results of the film-theory model, $\bar{v}_{x_1}^{va}$ is described in the spacer-filled channels by

$$\bar{v}_{x_1}^{va} = \begin{cases} v_{x_1=x_1^{L,ch}}^{va}(x_2), & \text{if } x_1^{L,ch} x_1 < x_1^{L,bulk}, \\ 0, & \text{if } x_1^{L,bulk} x_1 < x_1^{U,bulk}, \\ v_{x_1=x_1^{U,ch}}^{va}(x_2), & \text{if } x_1^{U,bulk} x_1 < x_1^{U,ch}. \end{cases} \tag{5.4}$$

The second component of the volume-averaged velocity $\bar{v}_{x_2}^{va}$ is described by

$$0 = \begin{cases} \bar{v}_{x_2}^{va}, & \text{if } x_1^{L,ch} x_1 < x_1^{L,bulk}, \\ \frac{\partial \bar{v}_{x_2}^{va}}{\partial x_2} + \frac{1}{x_1^{U,bulk} - x_1^{L,bulk}} \Delta v_{x_1}^{va}, & \text{if } x_1^{L,bulk} x_1 < x_1^{U,bulk}, \\ \bar{v}_{x_2}^{va}, & \text{if } x_1^{U,bulk} x_1 < x_1^{U,ch}, \end{cases} \tag{5.5}$$

with

$$\Delta v_{x_1}^{va} = \left[v_{x_1}^{va}\left(x_1^{U,bulk}, x_2\right) - v_{x_1}^{va}\left(x_1^{L,bulk}, x_2\right) \right]. \tag{5.6}$$

Eqs. (5.4) and (5.5) are used to substitute Eqs. (4.119) and (4.33) to tailor the general transport model to the specific scenario of a spacer-filled channel.

The boundary layer thickness δ depends on the mean velocity in the channel. To express this dependence Taylor and Krishna (1993) consider the Sherwood number Sh as a dimensionless boundary thickness which results in

$$Sh = \frac{h^{ch}}{\delta} \tag{5.7}$$

for a spacer-filled channel of thickness h^{ch}. Correlations for the Sherwood number in spacer-filled channels have been identified by Isaacson and Sonin (1976) in the form

$$Sh = \tilde{p}_{1,\delta}\, Sc^{\frac{1}{3}}\, Re^{\tilde{p}_{2,\delta}}. \tag{5.8}$$

Here, $\tilde{p}_{1,\delta}$ and $\tilde{p}_{2,\delta}$ are empirical parameters. The Reynolds number Re and Schmidt number Sc are defined as

$$Re = \frac{v^{ch}\, h^{ch}}{\nu}, \tag{5.9}$$

and

$$Sc = \frac{\nu}{D_s}, \tag{5.10}$$

respectively. Here, v^{ch} is the empty channel velocity and D_s is the Fick diffusion coefficient of a characteristic solute. As the latter corresponds to an additional parameter which is strongly correlated with $\tilde{p}_{1,delta}$, Eq. (5.8) is reformulated as

$$Sh = exp\,(p_{1,\delta} + p_{2,\delta}\,Re)\,. \tag{5.11}$$

With Eq. (5.11) and (5.7), an explicit expression for the boundary layer thickness δ is found as

$$\delta = h^{ch}\,exp\,(-p_{1,\delta} - p_{2,\delta}\,Re)\,. \tag{5.12}$$

The boundary layer thickness is constrained by $\delta < 0.5\,h^{ch}$. Hence, the expression on the right hand side of Eq. (5.12) gives reasonable results for $p_{1,\delta} + p_{2,\delta}\,Re > ln\left(0.5\,h^{ch}\right)$.

5.1.3 Electrodes and plant periphery

The electrode model introduced in this section describes the physico-chemical phenomena associated with the electrode reactions. The model is based on the work of Visser (2001), who successfully applied the model in the context of an ED process.

Electrode rinsing solution and electrode reactions

The working electrodes in the end plates of the ED-stack are continuously rinsed with electrode rinsing solution (ERS). This solution typically corresponds to a concentrated aqueous sodium sulphate solution. In this media, electrodes with an active platinum surface catalyze the reactions at the anode and the cathode, respectively:

$$2\,H_2O \quad \rightarrow \quad 4\,H^+ + O_2 + 4\,e^-, \quad E^0_{anode} = 1.229\,V, \tag{5.13}$$

$$4\,H_2O + 4\,e^- \quad \rightarrow \quad 4\,OH^- + 2\,H_2, \quad E^0_{cathode} = -0.828\,V. \tag{5.14}$$

Here, E^0_{anode} and $E^0_{cathode}$ are the standard electrode potentials related to the electrode reactions at the anode and cathode, respectively (Visser, 2001).

The electric current I is related by

$$I = d_{st} \int_{x_2^L}^{x_2^U} i^m_{x_1}\,dx_2, \qquad m \in \{anode, cathode\} \tag{5.15}$$

to the local electric current density at the electrode $i^m_{x_1}$, $m \in \{anode, cathode\}$. Here, $d_{st} = x_3^U - x_3^L$ is the depth of the rectangular electrode surface. The electric potential difference supplied from the power supply is described by

$$U = R^{circ}\,I + n_{cells}\,U_{cell} + U_{er} \tag{5.16}$$

as the superposition of an ohmic potential loss $R^{circ}\,I$ in the electrical circuit connecting the power supply to the electrodes, a potential drop $n_{cells}\,U_{cell}$ related to the transport in the system

of electrodialytic cells and a potential drop U_{er} related to the electrode reactions. The latter corresponds to

$$U_{er} = E^0_{anode} - E^0_{cathode} + \eta_{anode} - \eta_{cathode} + R^{ERS}\, I, \tag{5.17}$$

where the overpotentials η_{anode} and $\eta_{cathode}$ can be described using the Tafel equation

$$\eta_k = a_m + b_m \ln(I), \quad m \in \{anode, cathode\}, \tag{5.18}$$

with the empirical parameters a_k and b_k. The resistance R^{ERS} accounts for the potential drop resulting from the transport in the electrode rinsing solution and supplementary CEM membrane adjacent to the cathode (cf. Fig. 5.2).

Storage tanks and pumps

The models for the concentrate and diluate tanks are based on n integral balance equations

$$\frac{\partial (V\, c_{out,k})}{\partial t} = Q_{in}\, c_{k,in} + Q_{out}\, c_{out,k}, \qquad k = 1, ..., n. \tag{5.19}$$

Here, V is the volume of the tank; Q_{in} and Q_{out} are the volumetric flow rate of the in- and outflow, respectively.

The mechanical power associated with the pressure drop over the stack Δp^{tot} is

$$P^{pump} = Q_{out}\, \Delta p^{tot}. \tag{5.20}$$

For the prediction of the pressure drop Δp^{tot} for a specific empty channel velocity v^{ch} the model (6.5), (6.25) and (6.26) can be used which is derived in Chapter 6.

5.1.4 Interface models and coupling of model components

The model components introduced in Section 5.1 are coupled by the introduction of appropriate connection models. These models correspond to either simple identities relating extensive quantities or detailed models for the description of the physico-chemical phenomena in interphase layers. The latter case is encountered in the description of the membrane-electrolyte interphases.

Electrolyte-membrane interphase

The membrane-electrolyte interphase is abstracted as an infinitesimally thin phase in which no storage of extensive quantities occurs and no chemical reactions take place. With these assumptions, general surface balance equations

$$\mathbf{n} \cdot (\Psi^e_k - \Psi^m_k) = 0, \qquad k = 1, ..., n, \tag{5.21}$$

describe the conservation of extensive quantities across the interphase. Here, $\mathbf{n}$ is the local normal vector at the membrane surface, $\Psi^e_k = \mathbf{J}^e_k + c^e_k\, \mathbf{v}$ is the total flux in the electrolyte and $\Psi^m_k = \mathbf{J}^m_k$ is the total flux in the membrane phase.

Additional equations are introduced relating the intensive quantities, such as molar concentrations c_k or the electric potential ϕ, at the interphase. Here, the assumption of an electrochemical equilibrium is introduced yielding

$$RT\,ln\,(\gamma_k^m\,c_k^m) + z_k\,F\,\phi^m + \tilde{V}_j\,p^m = RT\,ln\,(\gamma_k^e\,c_k^e) + z_k\,F\,\phi^e + \tilde{V}_j\,p^e, \qquad k = 1, ..., n, \tag{5.22}$$

where the superscripts m and e refer to the membrane and electrolyte phase, respectively (Helfferich, 1995). For strongly cross-linked ion-exchange membranes the swelling pressure $\Pi = p^m - p^e$ negligibly affects the equillibrium distribution (cf. Visser (2001)). Hence, it will be neglected in the following.

Eq. (5.22) describes the distribution of charged and charge-neutral species in an equilibrium state. For given intensive states for the electrolyte phase, Eq. (5.22) and the electroneutrality condition (4.19) completely describe the intensive states in the adjacent membrane phase. The resulting discontinuity in the electric potential $\phi^e - \phi^m$ is referred to as Donnan potential.

Connections between tanks, pumps and flow channels

The tank and the ED module are coupled by the identities

$$0 = Q_{in}^{tank,m} + Q_{out}^{module,m}, \quad m \in \{con,\, dil\}, \tag{5.23}$$

$$0 = Q_{out}^{tank,m} + Q_{in}^{module,m}, \quad m \in \{con,\, dil\}. \tag{5.24}$$

Inside the ED module the processed solutions are equally distributed to the corresponding flow channels as described by

$$Q_{in}^{module,m} = n_{cells}\,Q_{in}^{ch,m}, \quad m \in \{con,\, dil\}, \tag{5.25}$$

$$Q_{out}^{module,m} = n_{cells}\,Q_{out}^{ch,m}, \quad m \in \{con,\, dil\}. \tag{5.26}$$

Here, $Q_{in}^{ch,m}$ is the mean volumetric flow rate in the inflow plane in the channels. The mean volumetric flow rate leaving the flow channel is related to the velocity in the outflow plane by

$$Q_{out}^{ch,m} = \frac{1}{d_{st}} \int_{x_1^L}^{x_1^U} v_{x_2}^{va}\big|_{x_2 = x_2^U}\, dx_1. \tag{5.27}$$

The concentrations in the tanks are coupled to the concentrations in the flow channels by the identities

$$c_{in,k}^{tank,m} = c_{out,k}^{m}, \quad m \in \{con,\, dil\},\, k = 1, ..., n, \tag{5.28}$$

$$c_{out,k}^{tank,m} = c_{in,k}^{m}, \quad m \in \{con,\, dil\},\, k = 1, ..., n. \tag{5.29}$$

Here, $c_{k,in}^m$ is the concentration at the channel inflow. The mean concentration $c_{k,out}^m$ in the channel outflow plane is given by

$$c_{k,out}^{m} = \frac{1}{h_{ch}} \int_{x_1^L}^{x_1^U} c_k|_{x_2 = x_2^U}\, dx_1, \quad m \in \{con,\, dil\},\, k = 1, ..., n. \tag{5.30}$$

Electrodes - ED cell

The electrodes are coupled to the ED cells by the identities for the electric potential

$$\phi^{anode} = \phi|_{x_1=x_1^{L,CEM}}\,, \tag{5.31}$$

$$\phi^{cathode} = \phi|_{x_1=x_1^{U,dil}}\,. \tag{5.32}$$

The electric current densities at the electrodes $i^i_{x_1}$, $i \in \{cathode, anode\}$, are related to the adjacent process components by

$$i^{cathode}_{x_1} = \mathbf{n}_{cathode} \cdot \mathbf{i}|_{x_1=x_1^{L,CEM}} \tag{5.33}$$

and

$$i^{anode}_{x_1} = \mathbf{n}_{anode} \cdot \mathbf{i}|_{x_1=x_1^{U,dil}}\,. \tag{5.34}$$

Here, $\mathbf{n}_m$, $m \in \{anode, cathode\}$ are normal vectors pointing into the corresponding electrode.

In normal operation the potential difference over the cell is prescribed by

$$U_{cell} = \phi|_{x_1=x_1^{L,CEM}} - \phi|_{x_1=x_1^{U,dil}}\,. \tag{5.35}$$

If the power supply is switched off during operation, e.g., in desalination with a pulsed applied current, Eq. (5.35) is substituted by

$$i^{anode}_{x_1} = 0 \tag{5.36}$$

enforcing zero current at the anode. In both scenarios the potential at the cathode is set to a reference value, i.e.,

$$\phi^{cathode} = 0. \tag{5.37}$$

5.2 Problem specification and implementation

This section first presents details concerning the specification of the degrees of freedom and the model parameters (Section 5.2.1) as well as important aspects of the implementation of the model (Section 5.2.2).

5.2.1 Degrees of freedom and model parameters

The process model is adapted to the lab-scale ED plant by specifying the geometrical degrees of freedom to the values given in Tables A.1 and A.2. For a comparison with specific experiments, the flow rate Q^{tank}_{out}, the number of cells n^{cells} and initial concentrations $c_{k,t_0}, k = 2, ..., n-1$ are specified as inputs and initial conditions, respectively, in accordance with the operational degrees of freedom used in the experiment (cf. Chapter 2). In both types of experiments – current-voltage and batch desalination experiment – the applied potential difference U is specified as a model input. For the current-voltage experiments this specification corresponds to the potentiostatic operation in the experiment. For the batch desalination experiments this specification does not

coincide with an amperostatic operation. In this case, the experimentally measured voltage signal is used in the simulation as a piecewise linear input trajectory.

To enable a qualitative comparison with experimental data, the model is parametrized using either parameter values reported in literature or reasonable default values. The concentration-dependent Maxwell-Stefan diffusion coefficients for the aqueous electrolyte solution in the flow channels are described by empirical correlations developed by Visser (2001) as presented in Appendix B.4. The thermodynamic factors are calculated by the eNRTL model given in Chen and Song (2004). The empirical dimensionless parameters in the correlation for the boundary layer thickness are fixed in a first attempt to $p_{1,\delta} = 0.2$ and $p_{2,\delta} = 0.05$. The concentration of the charged functional groups in the membranes is approximated as $c_1 = c_{fix} = 2000\,\frac{mol}{m^3}$. The specific charge number of these groups is specified as $z_1 = 1$ in the CEM and $z_1 = -1$ in the AEM. The parameters for the Tafel equations (5.18) are given in Table B.4.

To the author's knowledge, for the CMX and AMX membranes used in the experiments no Maxwell-Stefan diffusion coefficients and Bromley interaction parameters have been reported (cf. also Hogendoorn et al. (2001)). Hence, in a first attempt, the model is parametrized with parameter values identified by Visser (2001) for Nafion 450 (DuPont Co., USA) and AW-09 (Solvay S.A., Belgium) IEM. For missing parameters default values are pragmatically used. The relevant constant Maxwell-Stefan diffusion coefficients and Bromley interaction parameters are summarized in Tables B.5 and B.3.

A parameter with significant uncertainty is the resistance of the transport in the electrode rinsing solution R^{ERS}. Hence, the parameter is manually adjusted for a first current-voltage experiment with $NaCl$ solution (Exp. 1 in Tab. A.7). For $R^{\mathrm{ERS}} = 0.8\,\Omega$ an acceptable agreement is found between the model prediction and the experimental data (cf. Fig. 5.11 a).

5.2.2 Implementation

The process model is implemented in the modeling environment gPROMS (Process Systems Enterprise, 1997-2009). The model for the flow channels (4.117), (4.121), (5.4) and (5.5) is semi-discretized using central finite differences in the x_1-direction and backward finite differences in the x_2-direction. For the implementation of the membrane model (4.120) and (4.121) central finite differences are used to discretize differential operators with respect to both coordinates. The resulting systems of differential-algebraic equations (DAE) are solved using the implicit integrator *DAsolve* in gPROMS.

The eNRTL and the empirical model for the Maxwell-Stefan diffusivities are based on bulky algebraic models. To simplify the use in a dynamic simulation, these models are implemented in a stand-alone software tool. The coefficient matrices $\Omega_k(\mathbf{c})$, $k = 3, ..., 6$, in the sub-models for the channels and membranes are derived symbolically from its definitions (4.107), (4.108), (4.112) and (4.113). The required symbolic computations are carried out in Maple (Maplesoft, 2005-2014). Here, the resulting explicit symbolic expressions for $\Omega_k(\mathbf{c})$, $k = 3, ..., 6$, are exported as C-code and embedded in the stand-alone software tool for the physico-chemical properties. In a dynamic

simulation this software tool is coupled to gPROMS in the form of a dynamic link library.

5.3 Model-based analysis of dynamic transport effects

In this section it is analyzed to what extent the developed model can support the investigation of the dynamic transport processes in the electrodialysis stack and in particular the open questions which emerged in the course of the experimental analysis in Chapter 2. In a first step, this evaluation of the capabilities of the model is restricted to a conceptual level where it is assumed that the model is parametrized with accurate parameter values. A comparison with experimental data is presented in Section 5.4.

In Section 5.3.1 it is investigated in which way the model can relate the characteristic shape of the current profile after a pulse in the applied potential difference (cf. Section 2.3) to the underlying transport mechanisms. In this context, the predicted dynamic response of a simulated current-voltage experiment is analyzed by investigating the temporal evolution of the predicted local phenomena after the pulse. This allows a first assessment of the contributions of the local phenomena to the characteristic shape of the dynamic current trajectory. On this basis, the distinct contributions of the local phenomena in the membranes and flow channels are investigated in more detail in Section 5.3.2. Here, it is shown in which way the dynamic behavior of effective transport resistances of the different components can be thoroughly discriminated in the model prediction. This analysis is motivated by the substantial uncertainty currently associated with the discussion (cf. (Malek et al., 2013, Mishchuk et al., 2001a) and Section 2.6.3) concerning the effect and the origin of the dynamic process behavior.

Finally, in Section 5.3.3, the model prediction is investigated in order to assess to what extent the model can support the investigation of the effect of a pulsed applied current on the competitive transport of Cl^- and SO_4^{2-} ions in a desalination experiment with multi-salt solutions. Here, the analysis targets at the identification of mechanisms resulting in the significant effect of the pulsed operational mode to the competitive transport. This is of specific relevance, since this effect has been investigated in experimental studies only (cf. Section 2.6.3) and no theoretical explanation is available yet.

5.3.1 Dynamics in pulsed-current electrodialysis

The dynamic response to a pulse in the applied potential difference is investigated in a simulated current-voltage experiment with $NaCl$ solution. Here, the applied potential difference U is instantaneously increased at the beginning of the simulation experiment ($t = 0\,s$) from $U = 0\,V$ to $U = 7\,V$ (cf. Fig. 5.4 a). The predicted current I is shown in Fig. 5.4 b and is characterized by the characteristic peak relaxing to a steady state value. This transition is almost finalized after approx. $10\,s$, which is in good qualitative agreement with the time-scales identified in Section 2.3.

The developed model allows to investigate this dynamic response by visualizing the local transport processes in the ED cells. The predicted local distributions of the concentration of sodium ions c_{Na^+} in the concentrate, AEM, diluate and CEM are shown in Fig. 5.5. In the concentrate

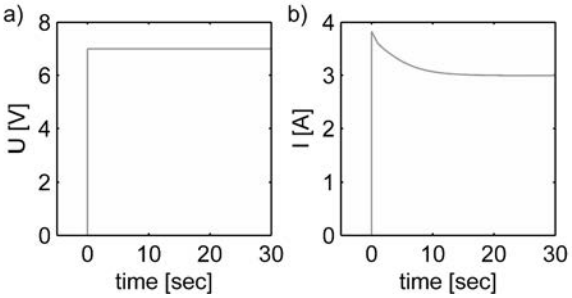

Figure 5.4: Applied pulse in the applied voltage difference U (a) and simulated current profile I (b).

flow channel concentration profiles develop which are characterized in the width of the channel – along the x_1-coordinate – by a significantly increased concentration at the membrane surfaces. Along the length of the channel – the x_2-coordinate – the concentration increases as a result of the net inflow of ions from the IEM. In the diluate channels the concentration profiles illustrate the depletion of ions towards the membrane surfaces as well as along the x_2-coordinate.

In both AEM and CEM curvilinear concentration profiles develop over time at different concentration levels: In the entire CEM the concentration of Na^+ ions exceeds the concentration of negatively charged fixed functional groups $c_{fix} = 2000\,\frac{mol}{m^3}$ in the membrane material. This is an important requirement for the physical plausibility of the model as the negative space charge associated to the fixed functional groups has to be balanced to fulfill the electroneutrality condition. In the AEM the concentration is significantly below the concentration in the adjacent flow channels illustrating the exclusion of Na^+ ions by the positively charged funtional groups in the AEM. In both membranes the concentration gradients across the membrane increase significantly along the x_2-coordinate resulting from the increasing concentration differences between the adjacent diluate and concentrate channels.

Comparing the concentration profiles at $t = 10\,s$ and $t = 30\,s$ only marginal differences are found for both the diluate and concentrate, whereas significant differences are apparent in the profiles for the membranes. This illustrates that diffusive transport in the flow channels is significantly faster in comparison to the transport in the IEM. This is in agreement with the significantly larger diffusivities in the liquid electrolyte phase. Further, this behavior gives rise to a first reasoning concerning the effect of the local phenomena to the integral dynamic process behavior. As the current trajectory is nearly constant after $t = 10\,s$ (cf. Fig. 5.4 b), the pronounced variation of the concentrations in the membranes between $t = 10\,s$ and $t = 30\,s$ is apparently of minor importance for the integral process behavior. Hence, the concentration gradients in the membranes do not significantly affect the behavior of the overall process.

The predicted local distributions of the electric potential ϕ in the concentrate, AEM, diluate and CEM are shown in Fig. 5.6. All profiles at $t = 0\,s$ are characterized by a constant electric potential along the x_2-coordinate and a linear decrease along the x_1-coordinate. The slope of

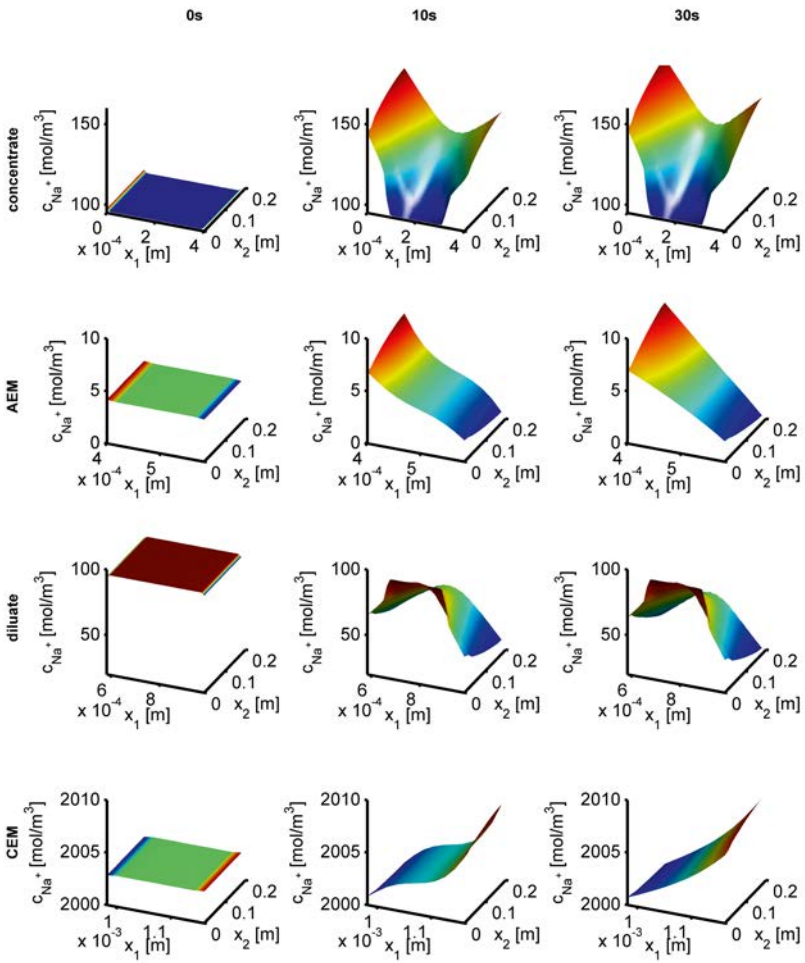

Figure 5.5: Simulated concentration profiles of sodium ions c_{Na+} in the concentrate, AEM, diluate and CEM at $t = 0\,s$, $t = 10\,s$ and $t = 30\,s$ after applying a stepwise increase in the applied potential difference.

this linear decrease is significantly larger in the AEM, diluate and concentrate when compared to the profile in the CEM. These differences are in agreement with the significantly larger diffusion coefficients in the CEM. For $t = 10\,s$ and $t = 30\,s$, the profiles of the concentrate and the CEM show a significant variation along the x_2-coordinate. In the CEM this variation even exceeds the

variation along the x_1-coordinate. The profiles in the diluate and the AEM are still characterized by a nearly linear decrease along the x_1-coordinate while showing only a small variation along the x_2-coordinate.

The nearly identical potential profiles found for $t = 10\,s$ and $t = 30\,s$ indicate an apparently weak interaction of the potential and the concentration profiles in the membranes. This reveals that the transport of the ionic species in the membranes is governed by migration induced by the electric field, rather than diffusion governed by concentration gradients.

5.3.2 Discrimination of transport resistances

The predicted dynamic behavior shown in Fig. 5.4 is analyzed further on, in order to illustrate the individual contributions of the membranes and flow channels to the total energy dissipation in the ED stack. Here, the prediction of the developed model provides valuable information by giving insight into the local profiles of the electric potential loss across the elementary components. From these profiles, the mean electric resistance of the diluate and concentrate flow channels is determined by

$$R_i^m(t) = \frac{1}{I(t)}\frac{1}{l}\int_{x_2^{L,i}}^{x_2^{U,i}} \phi|_{x_1=x_1^{U,i}} - \phi|_{x_1=x_1^{L,i}}\, dx_2, \quad i \in \{concentrate,\, diluate\}. \tag{5.38}$$

The mean electric resistances of the membranes are defined as

$$R_{AEM}^m(t) = \frac{1}{I(t)}\frac{1}{l}\int_{x_2^{L,AEM}}^{x_2^{U,AEM}} \phi|_{x_1=x_1^{L,dil}} - \phi|_{x_1=x_1^{U,con}}\, dx_2 \tag{5.39}$$

and

$$R_{CEM}^m(t) = \frac{1}{I(t)}\frac{1}{l}\int_{x_2^{L,CEM}}^{x_2^{U,CEM}} \phi|_{x_1=x_1^{L,con}} - \phi|_{x_1=x_1^{U,dil}}\, dx_2. \tag{5.40}$$

According to definitions (5.39) and (5.40), the $R_{CEM}^m(t)$ and $R_{AEM}^m(t)$ include the transport resistances associated with both electrolyte-membrane interfaces and the transport inside the membrane material. The mean resistance resulting only from the transport inside the membrane is

$$R_{i,trans}^m(t) = \frac{1}{I(t)}\frac{1}{l}\int_{x_2^{L,i}}^{x_2^{U,i}} \phi|_{x_1=x_1^{U,i}} - \phi|_{x_1=x_1^{L,i}}\, dx_2, \quad i \in \{AEM,\, CEM\}. \tag{5.41}$$

The resistances associated solely with the membrane-electrolyte interfaces then correspond to

$$R_{i,IF}^m(t) = R_i^m(t) - R_{i,trans}^m(t), \quad i \in \{AEM,\, CEM\}. \tag{5.42}$$

The predicted dynamic behavior of the resistances R_i^m, $i \in \{concentrate,\, AEM,\, diluate,\, CEM\}$ are shown in Fig. 5.7 a. The profiles for AEM, CEM and diluate are characterized

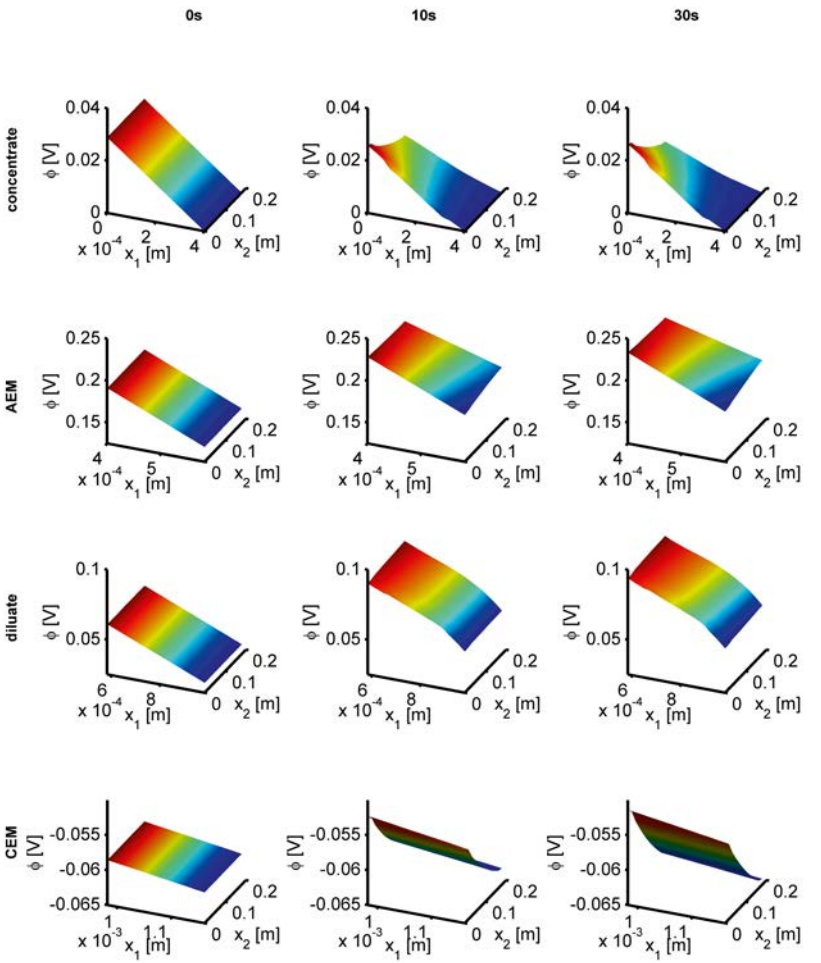

Figure 5.6: Simulated electric potential profile ϕ in the concentrate, AEM, diluate and CEM at $t = 0\,s$, $t = 10\,s$ and $t = 30\,s$ after applying a stepwise increase in the applied potential difference.

by a transient increase before settling after approx. $10\,s$ into a plateau. The resistance of the concentrate decreases slightly to a steady state significantly below the resistances of the remaining process components. The increasing and decreasing resistances found for the diluate and concentrate, respectively, is in good accordance with the temporal depletion or concentration of ionic species shown in Fig. 5.5.

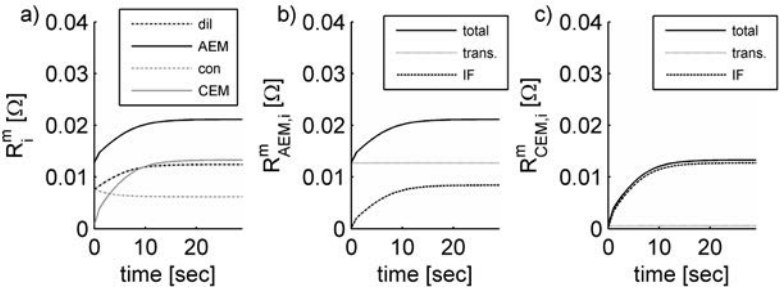

Figure 5.7: Predicted dynamic behavior of the mean electric resistances a) $R_i^m, i \in \{concentrate, AEM, diluate, CEM\}$, b) $R_{AEM,k}^m, k \in \{IF, trans\}$ and c) $R_{CEM,k}^m, k \in \{IF, trans\}$ after the stepwise increase in the potential difference.

When compared to the variation in the profiles of the flow channels, the total variation of the resistances in the IEM is significantly more pronounced. To further analyze this pronounced transient behavior in the membranes, Fig. 5.7 b and c show the profiles of the mean resistances in the membranes R_i^m, the underlying contributions of the interfaces $R_{i,IF}^m$ and the transport inside the membranes $R_{i,trans}^m, \quad i \in \{AEM, CEM\}$. Here the contributions associated with the transport $R_{i,trans}^m$ show a nearly time-invariant profile. This indicates that solely the contributions $R_{i,IF}^m$ influence the transient behavior of the total membrane resistance R_i^m significantly. The fractions of the two contributions to the total resistance differ in AEM and CEM strongly. Whereas in the CEM the contribution of the transport $R_{CEM,trans}^m$ is very small, $R_{AEM,trans}^m$ dominates the total resistance of the AEM. This is in agreement with the profiles of the electric potential ϕ in membranes illustrated in Fig. 5.6 and can be related to the significantly higher diffusivities in the CEM.

The dynamic process model further allows an assessment of the different resistances for the batch desalination experiments conducted in Chapter 2. To this end, a simulation study is conducted with inputs and initial conditions corresponding to Exp. 3 in Table A.9 (cf. Sections 2.4.1 and 5.4.2). Fig. 5.8 a shows the predicted mean resistances R_i^m for the desalination experiment operated with a constant applied current of $I = 1\,A$. The resistances of the AEM and CEM increase with a nearly linear slope in the first $4800\,s$ of the experiment. In this period, the resistances of the diluate and concentrate increase and decrease with a significant smaller slope, respectively. At the end of the experiment the resistances in the AEM, CEM and diluate increase strongly showing a strongly nonlinear profile.

Fig. 5.8 b and c illustrate the contributions of the interface $R_{i,IF}^m$ and the transport inside the membrane $R_{i,trans}^m$ to the total resistances of the membranes $R_i^m, \quad i \in \{AEM, CEM\}$. The contributions of the transport in the membrane $R_{i,trans}^m$ are nearly invariant in the course of the experiment. Hence, the significantly increasing resistances in the membrane at the end of the experiment solely result from the increasing resistances of the membrane-electrolyte interfaces

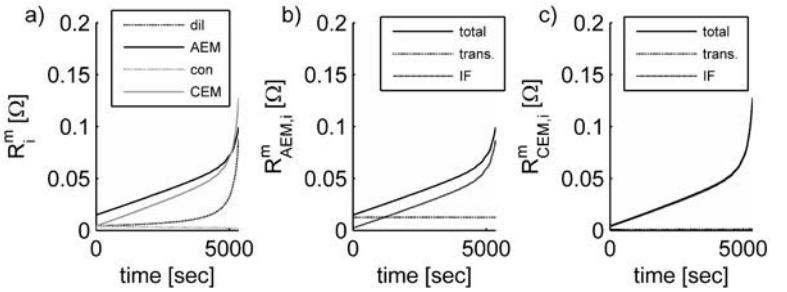

Figure 5.8: Predicted dynamic behavior of the mean electric resistances a) R_i^m, $i \in \{concentrate, AEM, diluate, CEM\}$, b) $R_{AEM,k}^m$, $k \in \{IF, trans\}$ and c) $R_{CEM,k}^m$, $k \in \{IF, trans\}$ in the batch desalination experiment 3 in Table A.9 (cf. Sections 2.4.1 and 5.4.2) with a constant applied current of $I = 1\,A$.

$R_{i,IF}^m$.

5.3.3 Competitive transport in pulsed current experiments

In addition to the information concerning transport resistances, the developed model gives first insight into the mechanisms of the competitive transport of Cl^- and SO_4^{2-} ions in the ED process operated with a pulsed applied current. To illustrate the insight provided by the model, two simulations are carried out with inputs and initial conditions specified in accordance with Exp. 1 and 3 in Table A.8 investigating the batch desalination of $NaCl - Na_2SO_4$ solution operated with either a constant or pulsed applied current of $I = 2\,A$ (cf. Sections 2.6.2 and 5.4.2). As a quantitative measure for the selective transport the predicted mean transference number at the interface between the AEM and diluate channel, i.e., $x_1 = x_1^{U,AEM}$, is introduced as

$$t_k^m(t) = \frac{1}{l} \int_{x_2^{L,AEM}}^{x_2^{U,AEM}} \frac{F\, J_k^{x_1}}{i^{x_1}}\bigg|_{x_1 = x_1^{U,AEM}} dx_2, \quad k \in \{Cl^-, SO_4^{2-}\}. \tag{5.43}$$

Here, $J_k^{x_1}$ is the flux density and i^{x_1} is the current density in the x_1-direction. The transference numbers t_k^m, $k \in \{Cl^-, SO_4^{2-}\}$, indicate the number of moles of ions i transported per mole of transported electrons (Strathmann, 2004).

Fig. 5.9 illustrates the predicted mean transference numbers t_i^m for the two batch desalination experiments. In the experiment operated with the constant applied current t_{Cl-}^m is initially significantly higher than $t_{SO_4^{2-}}^m$ (cf. Fig. 5.9 a) indicating that the charge transport is initially dominated by chloride ions. In the course of the experiment t_{Cl-}^m decreases monotonically while $t_{SO_4^{2-}}^m$ increases until the profiles intersect after approx. $t = 1300\,s$. For the pulsed applied current a similar trend is found, however, superimposed by significant transient effects within the pulse intervals (cf. Fig. 5.9 b). This transient behavior after the stepwise increase in the applied

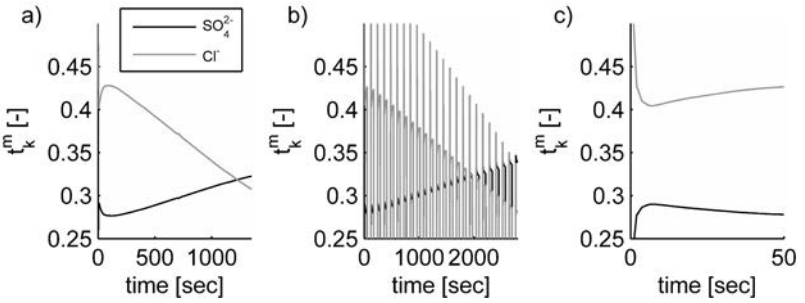

Figure 5.9: Predicted dynamic behavior of the mean transport numbers t_k^m, $k \in \{SO_4^{2-}, Cl^-\}$ in the AEM during the desalination experiments with a) constant and b) pulsed applied current of $I = 2\,A$. c) shows the predicted t_k^m in a single pulse interval.

current is illustrated in more detail in Fig. 5.9 c showing the predicted t_{Cl-}^m and $t_{SO_4^{2-}}^m$ profiles for only one pulse interval. The transient for $t_{SO_4^{2-}}^m$ is characterized by a significant increase at the beginning of the pulse interval before steadily declining after a maximum at approx $t = 7\,s$. The transient for t_{Cl-}^m shows the opposite trend with a minimum at approx. $t = 7\,s$. This predicted dynamic behavior can explain the decreasing selectivity for chloride ions found in the experiments with pulsed applied current (cf. Sections 2.6.2).

5.3.4 Discussion

The results presented in Section 5.3.1 illustrate the significant amount of information available in the fine temporal resolution of the local transport phenomena. The two-dimensional spatial resolution of the phenomena enables a thorough comparison of local variations occurring in the length of the channel and polarization phenomena taking place orthogonally to the membranes. This extends the insight obtained from a one-dimensional description of the transport processes as used by Kraaijeveld et al. (1995) and Visser (2001) significantly. The thorough dynamic description provides for the first time detailed insight into the temporal evolution of the local transport processes.

As shown in the discussion in Section 5.3.2, the prediction of the local transport processes gives rise to a large amount of information concerning the distinct transport resistances in the membranes and flow channels. By this means the model strongly supports a rigorous assessment of the contribution of the distinct elementary components to the overall process performance. The accurate temporal resolution of the developed model can particularly contribute to obtaining pronounced insight into the effect of a transient operation on the individual transport resistances. Such an assessment has not been possible with the previously reported process models (Kraaijeveld et al., 1995, Visser, 2001) because quasi-stationary transport models were used.

In Section 5.3.3 it has been illustrated in which way the model can be used to investigate the

effect of a pulsed applied current on the competitive transport in multi-salt solutions. To this end, particularly the temporal resolution of the fluxes transported across the membranes, which cannot be thoroughly determined from the experiments conducted in Chapter 2 (cf. Section 2.6.3), provides important information.

In summary, in this section it has been shown that the developed model can provide valuable information for the investigation of the dynamic transport in ED processes. As illustrated, the mechanistic model formulation directly allows the investigation of important aspects concerning the qualitative process behavior.

For a thorough quantitative model-based analysis the accurate parametrization of the model is an important prerequisite. The identification of model parameters, particularly the Maxwell-Stefan diffusivities or the parameters in the activity coefficient models in the membranes, requires data from tailored experiments as developed by Visser (2001). The identification of such parameters from integral measurements as available from the experiments in Chapter 2 is not possible. In such an approach the missing information concerning the local phenomena prevents the unique identification of the large number of parameters. However, the data obtained in Chapter 2 provide a good basis for a first experimental evaluation of the integral process behavior predicted by the model.

5.4 Comparison with experimental data

In this section the prediction of the developed model is compared to data from current-voltage (Section 5.4.1) and batch desalination experiments (Section 5.4.2) with aqueous $NaCl$ and $NaCl - Na_2SO_4$ solutions. The primary scope of this comparison is the experimental evaluation of the qualitative process behavior and the physical plausibility of the principles depicted in the model. Further, it allows a first assessment of the quantitative prediction error for the roughly parametrized model.

5.4.1 Current-voltage experiments

$NaCl$ solution

Fig. 5.11 a shows the measured and predicted current trajectory resulting from the manual adjustment of ohmic resistance in the electrode compartments to $R^{ERS} = 0.8\,\Omega$ for Exp. 1 in Tab. A.7 (cf. Section 5.2.1). In this comparison a very good agreement is found in particular for currents $I > 2\,A$. The model prediction is compared against additional current-voltage experiments with varying inlet concentrations and flow rates (Exp. 2-9 in Tab. A.7, cf. Section 2.3) in Fig. 5.11 b-i. Here, a good agreement is found for the experiments with the highest concentration $c_{NaCl} = 192\,\frac{mol}{m^3}$ operated at flow rates of $Q = 1.61 \cdot 10^{-5}\,\frac{m^3}{s}$ and $Q = 0.8 \cdot 10^{-5}\,\frac{m^3}{s}$ (cf. Fig. 5.11 d and g). For the remaining experiments the model generally predicts a current I which is significantly higher than the measured current profile. Despite these deviations, a good qualitative agreement is found with respect to the limiting behavior observed in the current profiles in Figs.

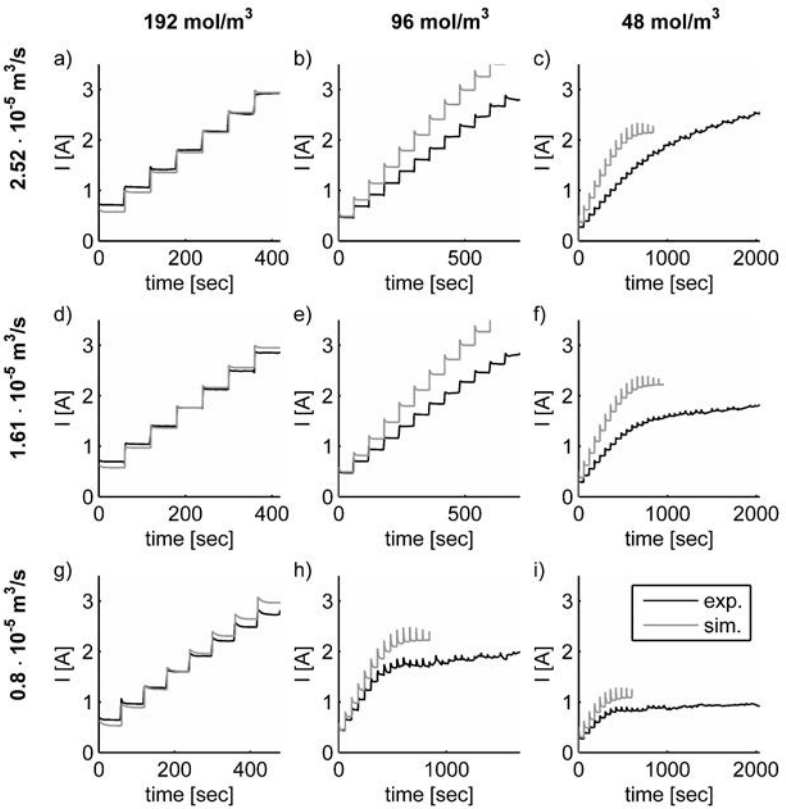

Figure 5.10: Comparison between measured and simulated current profiles for current-voltage experiments with varying concentrations and flow rates.

5.11 c, f, h and i. Here, both the measured and the simulated profile show a curvilinear trend towards a finite limiting current.

Further, a good qualitative agreement is found for nearly all experiments with respect to the dynamic response after the discontinuous increase in the applied potential difference. Here, the predicted and measured current profiles show a characteristic peak, before settling to a steady state plateau. The decreasing size of the peak with increasing concentration and increasing flow rate is seen in good agreement in both the measured and the predicted current profile.

In Fig. 5.11 the model prediction is compared to a series of experiments with a varying number of cells n_{cell} in the stack (Exp. 1, 11 and 12 in Table A.7, cf. Section 2.3). For $n_{cell} = 10$ and

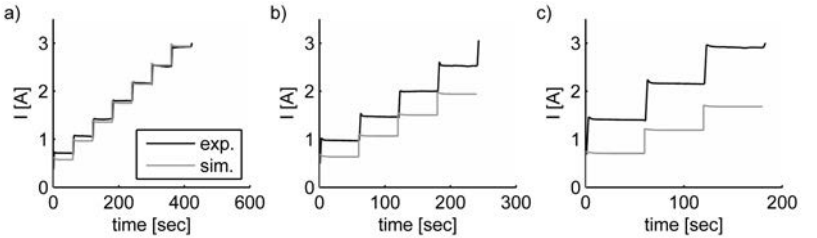

Figure 5.11: Comparison between measured and simulated current profiles for current-voltage experiments with a) $n_{cell} = 14$, b) $n_{cell} = 10$ and c) $n_{cell} = 6$.

$n_{cell} = 6$, the predicted current I is significantly lower when compared to the measurements.

$NaCl$-Na_2SO_4 solution

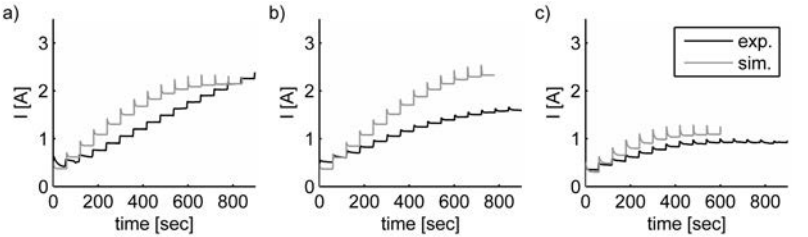

Figure 5.12: Comparison between measured and simulated current profiles for current-voltage experiments with $NaCl - Na_2SO_4$ solution for volumetric flow rates of a) $Q = 2.5 \cdot 10^{-5} \frac{m^3}{s}$, b) $Q = 1.6 \cdot 10^{-5} \frac{m^3}{s}$ and c) $Q = 0.8 \cdot 10^{-5} \frac{m^3}{s}$.

Fig. 5.12 shows a comparison of the model prediction for the current trajectories measured for $NaCl$–Na_2SO_4 solutions for volumetric flow rates of a) $Q = 2.5{\cdot}10^{-5} \frac{m^3}{s}$, b) $Q = 1.6{\cdot}10^{-5} \frac{m^3}{s}$ and c) $Q = 0.8{\cdot}10^{-5} \frac{m^3}{s}$ (Exp. 1-3 in Table A.6, cf. Section 2.3). At the highest volumetric flow rate a significant deviation between prediction and measurement is seen for the qualitative pattern of the current profile (cf. Fig. 5.12 a). Here, the peaks in the predicted dynamic response are significantly more pronounced when compared to the measured data. This qualitative deviation is not seen for the remaining experiments where the limiting behavior is observed in both measurement and prediction. The characteristic current peak in the dynamic response to the stepwise increase in the applied potential difference is significantly larger in the predicted profile.

5.4.2 Batch desalination experiments

$NaCl$ solution

The prediction of the developed process model is compared to data of batch desalination experiments with an applied current of $I = 3\,A$, $I = 2\,A$ and $I = 1\,A$ (Exp. 1-3 in Table A.9) in Fig. 5.13. A good agreement is found in all experiments for the predicted and measured current. Here, a nearly constant current is predicted at the beginning of all experiments. Subsequently the current increases monotonically to values slightly above the constant current values applied in the experiments. The predicted concentration profile in the experiments operated with $I = 3\,A$ and $I = 2\,A$ deviate slightly from the measured profiles. Only a very small deviation is found between the predicted and the measured concentration profiles in the experiment with $I = 1\,A$.

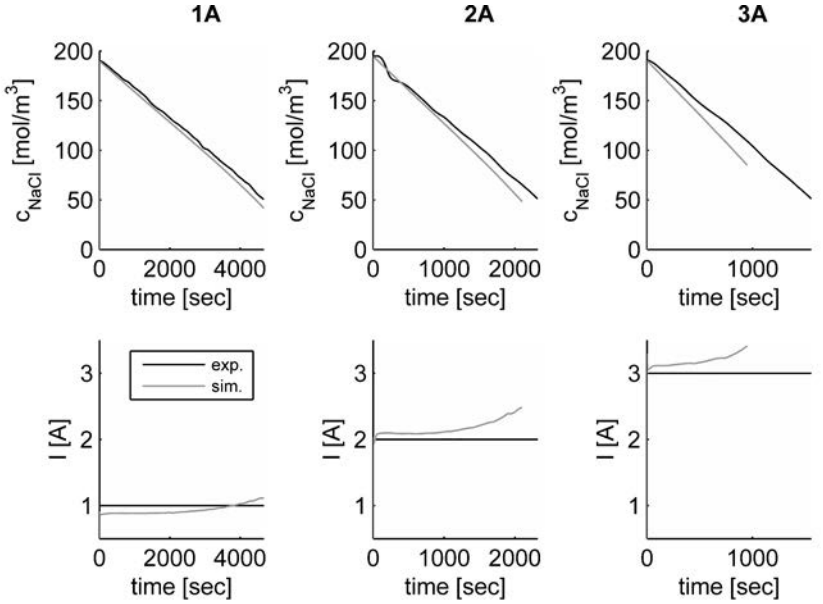

Figure 5.13: Comparison between measured and simulated current and concentration profiles for the desalination of $NaCl$ solution with applied currents of $I = 1\,A$, $I = 2\,A$ and $I = 3\,A$.

A comparison between the model prediction and measured data for experiments with a pulsed applied current of $2\,A$ with pulse rates of $10\,s$, $30\,s$ and $60\,s$ (Exp. 12-14 in Table A.9) is shown in Fig. 5.14. The predicted current significantly exceeds the $2\,A$ applied in the experiments. For the pulse-rates of $30\,s$ and $60\,s$ the predicted current rises in each interval monotonically towards a maximal value. In contrast to this, a slight monotonic decrease is found in the predicted current profiles for the pulse-rate of $10\,s$. The predicted concentration profiles are characterized by distinct plateaus which are not resolved in the measured concentration data. Further, for the

pulse-rates of $30\,s$ and $60\,s$ the predicted decrease in the $NaCl$-concentration is significantly faster than apparent in the measured profiles.

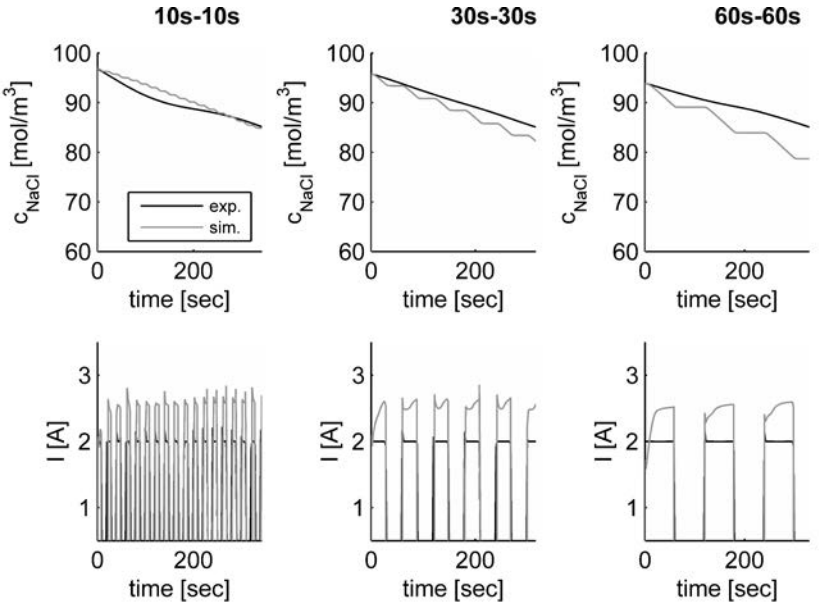

Figure 5.14: Comparison between measured and simulated current and concentration profiles for pulsed applied currents with pulse-rates of $10\,s$, $30\,s$ and $60\,s$.

In Fig. 5.15 the model prediction is compared to the experimental data of the solar ED experiment (Exp. 22 in Table A.9, cf. Section 2.5). Here, a good agreement is found for the measured and predicted concentration profiles. In the entire experiment, the current is predicted significantly higher in comparison to the measured data. Whereas at the end of the experiment the predicted shape of the current profile deviates from the constant values applied in the experiment, a very good agreement is found here in the first $800\,s$ of the desalination run.

$NaCl$-Na_2SO_4 solution

Fig. 5.16 shows a comparison of the model prediction with the desalination experiments of $NaCl - Na_2SO_4$ solutions with a constant applied current of $I = 1\,A$ and $I = 2\,A$ (Exp. 1 and 2 in Table A.8). For the experiment with $I = 1\,A$ a good agreement is found for the predicted concentrations of the ionic species c_{Cl^-}, $c_{SO_4^{2-}}$ and c_{Na^+} and the experimental data. In particular, the predicted competitive transport between the two anions Cl^- and SO_4^{2-} is in good accordance with the measurements. Larger deviations are found for the predicted concentration profiles in the experiment with $I = 2\,A$. Here, the predicted decrease of the ionic species is significantly

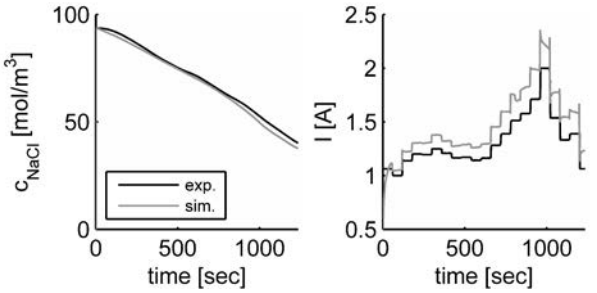

Figure 5.15: Comparison between measured and simulated current and concentration profiles for solar ED experiments.

faster than apparent in the measured data. For both experiments, the predicted current shows a slightly curvilinear trend with a moderate deviation from the constant current applied in the experiment.

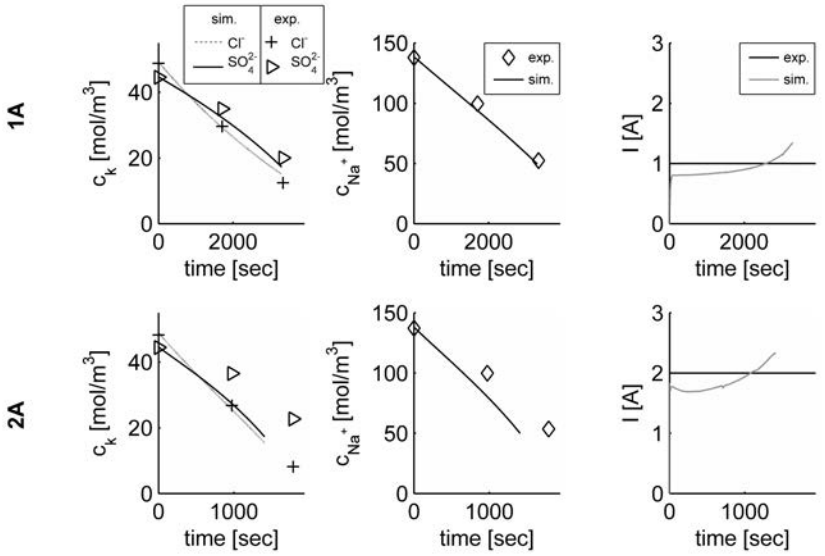

Figure 5.16: Comparison between measured and simulated current and concentration profiles for constant applied currents of $I = 1\,A$ and $I = 2\,A$.

A comparison of the model prediction and data from an experiment for the desalination of $NaCl - Na_2SO_4$ solution with a pulsed applied current (Exp. 3 in Table A.8) is shown in Fig. 5.17. The qualitative trend of the predicted concentrations is in good accordance with the

measured data. The predicted current shows a moderate deviation from the current trajectory prescribed in the experiment by increasing monotonically in the course of the desalination run.

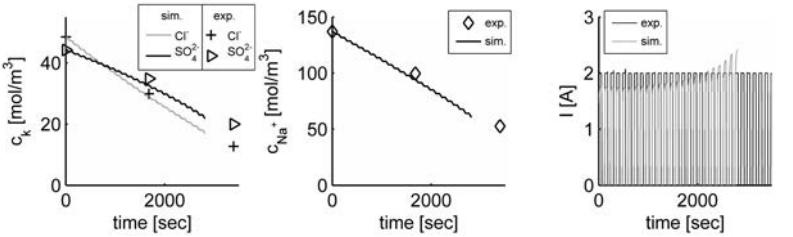

Figure 5.17: Comparison between measured and simulated concentration profiles for the ionic species Cl^-, SO_4^{2-} and Na^+ and the electric current for experiments with pulsed applied current of $I = 2\,A$.

Discussion

In the comparison between the model prediction and data from current-voltage experiments the model is found to describe the qualitative behavior of the ED plant satisfactorily. In particular, the predicted dynamic response to the stepwise increase of the applied potential difference shows a similar shape in comparison with the measured profiles.

Similarly, the comparison with batch desalination experiments results in an appropriate qualitative agreement of the model prediction and experimental data. A moderate systematic deviation is found in all predicted current profiles in the form of a monotonic increase in the course of the experiment. The patterns of the measured concentration profiles are nicely reproduced by the model. In particular, the competitive transport of Cl^- and SO_4^{2-} ions in the desalination of $NaCl - Na_2SO_4$ solutions is satisfactory.

Despite this good qualitative agreement, in a strict quantitative comparison significant deviations are found between the model prediction and experimental data. An attempt to identify the cause of these deviations on the basis of the available integral experimental data is not expedient as multiple factors can have an important effect here. First, the rough parametrization of the membrane and electrode models certainly influences the model accuracy. An additional important aspect is the strongly simplified description of the hydrodynamics by the film-theory approach. Here, no thorough information is available from prior works to approximate the resulting model error in particular for a transient operational mode. Last, the consequences of the missing resolution of secondary transport mechanisms cannot be rigorously assessed.

5.5 Conclusions

In this chapter a dynamic process model of an ED plant has been developed. The model handles the complexity arising from the modular set-up of ED processes by means of a hierarchical model structure. This allows the use of the model for distinct industrially relevant process configurations

with multiple modules operated in either batch or continuous mode. Common limitations of process models developed in prior works (Kraaijeveld et al., 1995, Neubrand, 1999, Visser, 2001) result from the description of the underlying transport by a quasi-stationary one-dimensional transport model. For the first time these limitations are overcome by the process model developed in this work as it describes the ionic mass transport in the flow channels and IEM by means of a dynamic two-dimensional transport model. By this means, the model allows the model-based description of ED processes operated in transient mode for the first time in a rigorous manner.

Further, the model incorporates non-idealities in the form of activity coefficients or thermodynamic factors which have been commonly neglected in privious work. That way, the model is applicable to the description of ED plants processing concentrated multi-salt solutions. The thorough analysis and reformulation of the underlying transport models in Chapter 4 facilitates the implementation of the process model in a commercial modeling environment and does not require tailored numerical methods. By this means, the model can be directly used with established model-based methods, e.g., for the estimation of model parameters, the design of experiments or the optimization of the process design.

In Section 5.3 it is demonstrated that the model can strongly support the investigation of the process dynamics with respect to the underlying principles. In this context it is illustrated how the model can contribute to thoroughly discriminate phenomena occurring either in the membranes, the flow channels or the membrane-electrolyte interfaces. Further, it is shown that the model prediction provides insight into the effect of a pulsed applied current on the competitive transport of Cl^-- and SO_4^{2-}-ions (cf. Gurtler et al. (2008) and Section 2.6.3). This is of specific relevance since no thorough theoretical approach describing the underlying mechanisms is available yet.

The model prediction is compared in Section 5.4 with integral experimental data obtained in Chapter 2. Although the model is roughly parametrized (cf. Section 5.2.1), the comparison for both current-voltage and batch desalination experiments shows good qualitative agreement (cf. Section 5.4.2). In particular, the temporal scales and the characteristic shape found in the experiments are predicted by the model satisfactorily. To the author's knowledge no prior work has reported a mechanistic model capable of describing the dynamic response with a comparable qualitative agreement.

For the reduction of the – in parts – significant deviations between the model prediction and experimental data, two major tasks can be identified. As a first task, the model parameters for the membranes and working electrodes are to be rigorously identified for the specific devices considered in this work. For this purpose, tailored methods, as e.g. used by Visser (2001), can be applied, which are based on distinct steady-state experiments. In addition, for this purpose dynamic experiments can be developed now as the dynamics of the transport process are rigorously considered in the novel transport models developed in this work. It has been shown in different application contexts, e.g., in the identification of reaction kinetics (Brendel et al., 2006) or liquid-phase multi-component diffusion coefficients (Bardow et al., 2003), that the use of dynamically operated experiments increases the information content in the resulting experimental data significantly.

The second task concerns the evaluation of the simplified description of the hydrodynamics in the spacer-filled flow channels by the film-theory model. To the author's knowledge no prior studies have thoroughly investigated the loss of physical information associated with this approximation of the three-dimensional transport phenomena. This is of specific relevance for processes operated in a dynamic mode since it can be expected that the polarization strongly depends on the dynamic input trajectories. Further, the approach does not resolve secondary transport mechanisms which are considered to affect the transport in the membrane-electrolyte interphase significantly (Urtenov et al., 2013, van Pham et al., 2012). Another major drawback of the film-theory approach is the missing resolution of the spacer geometry. This requires the identification of distinct empiric parameters for the description of the models for the polarization film thickness and the pressure drop for distinct spacer geometries. Further, the missing three-dimensional resolution prevents the investigation of the effect of geometric design parameters on the process performance. This second task is addressed in Chapter 6 as a first step of current research activities aiming at the development of a fully three-dimensional model of an ED module.

6 Spacer geometry and process performance

This chapter addresses the development of a three-dimensional model of the flow channels and the effect of the spacer geometry on important performance measures of ED processes. To this end, Section 6.1 summarizes recent activities focusing on the development of a software tool for the coupled simulation of the hydrodynamics and ionic mass transport in spacer-filled channels. A central element of this tool is a hydrodynamic model based on the Lattice-Boltzmann Method (LBM) allowing for the simulation of the complex flow-fields in a reasonable time-frame on high performance computers. This code is used in the remainder of the chapter to investigate the pressure drop in the flow channels as an important design objective for industrial ED processes. In Section 6.3 the prediction of the LBM is evaluated with experimental data. The validated LBM is used in Section 6.4 as a predictive tool to simulate the pressure drop for arbitrary woven and non-woven spacer geometries. The resulting simulated data provide the basis for the identification of semi-empirical models for the prediction of the pressure drop in the entire space spanned by the geometric design parameters. Details concerning the methods used for the experiments, the hydrodynamic simulations and the model identification are introduced in Section 6.2. Elements of this chapter have been published previously in (Johannink et al., 2015)[1]

6.1 Towards an integrated description of hydrodynamics and ionic mass transport

As evident from the results of the experimental study in Chapter 2 and the discussion in Section 1.1.2 the spacer geometry significantly effects important design objectives of industrial ED processes. The quantification of these effects in a model-based analysis requires an adequate resolution of the spacer geometry in the simulation model. The two- or three-dimensional representation of spacer structures has become a standard procedure in the simulation of the hydrodynamics in spacer-filled channels with commercial CFD tools (cf. Section 1.3.1). The integration of the hydrodynamic studies with a rigorous description of the ionic mass transport is significantly less studied.

The isolated analysis of either the hydrodynamics in CFD studies or ionic mass transport in simplified process models constitutes a major limitation for the development of a thorough insight into the transport phenomena in ED processes. This particularly corresponds to an analysis accounting for secondary transport effects since these effects originate from the interaction of

[1] In Johannink et al. (2015) an error occurred in the description of the results published in this chapter. An corrigendum (Johannink et al., 2016a) has been issued correcting the error in the description.

the hydrodynamics and the ionic mass transport. The fact that secondary transport effects can have a significant effect on the transport in the membrane-electrolyte system has been shown by Urtenov et al. (2013) and van Pham et al. (2012) who reported results of a coupled simulation of the hydrodynamics and ionic mass transport in a small empty flow channel.

Recent research activities (Johannink et al., 2011, Masilamani, 2012, Zudrop et al., 2014) focused on the development of mathematical models and appropriate numerical methods for the integrated description of the complex hydrodynamics and ionic mass transport in spacer-filled flow channels. The final objective of this work is the simulation of the transport processes in geometries typically encountered in industrial processes. The resulting high computational effort is addressed by the implementation of the methods in highly scalable software allowing the use of high performance computers with a large number of processors.

The demand for a high scalability is taken into account by expressing the models for the hydrodynamics and diffusive mass transport in the framework of the LBM. Briefly, the LBM corresponds to an efficient numerical scheme for the solution of the Lattice Boltzmann equation which is a discrete representation of the rigorous Boltzmann kinetic equation. Without considering technical details, it has been shown, that in the macroscopic limit the solutions of the Lattice Boltzmann equation for a single molecular species and the Navier-Stokes equations (4.32) coincide (Bernsdorf et al., 2003, Chen and Doolen, 1998). In detailed theoretical and numerical analyses Zudrop et al. (2014) have shown that the solution for a system of Lattice Boltzmann equations of multiple molecular species is in the macroscopic limit identical to the solution of a coupled system formed by the Navier-Stokes (4.32) and Maxwell-Stefan equations (4.20).

Efficient implementations of a single-species LBM approach and the multi-species LBM approach developed by Zudrop et al. (2014) are available in the open source solver MUSUBI (Hasert et al., 2013 // 2014) which is part of the software package APES (Roller et al., 2012). In this framework the multi-species LBM approach has been successfully tested for the description of ionic mass transfer in liquid electrolytes. Here, the approach has been coupled with Poisson's equation (4.18) to describe the propagation of the electric field. The single-species implementation of the LBM has been used by Masilamani (2012) to investigate the hydrodynamics in spacer-filled channels. Here, the solver MUSUBI has proven to be an effective tool for large-scale hydrodynamic simulations in a reasonable time-frame. However, an evaluation of the LBM prediction in a comparison with experimental data is still missing.

With the developed simulation tool it is possible to quantify important design objectives, as the pressure drop in the channel or the local shear stress, for a given spacer geometry in a straight forward manner. By this means it provides a valuable tool in a design process aiming at the identification of a well-performing spacer geometry. However, this task remains challenging as the commonly used spacer geometries can be modified by a large number of design parameters. Hence, to efficiently examine the multi-dimensional space spanned by the design parameters, systematic methods are required. Further, the resulting information concerning the design objectives in the design space needs to be organized in an efficient manner. For this purpose it has shown efficient to represent the simulated design objectives in simple algebraic models (cf. Section 1.3.1).

This work makes two important contributions for the reliable and efficient application of the developed software tool in a spacer-design process: The first contribution is the evaluation of the LBM in a comparison of the predicted pressure drop with experimental data. The second contribution addresses the systematic identification of predictive models for the design objectives in the entire space spanned by the design parameters. To handle the complexity arising from this multi-dimensional design space, a work flow is proposed guiding the execution of specific CFD simulations by means of optimization-based model identification techniques. With this, the approach yields predictive models by a minimal number of simulations. In a first step, the consideration is restricted to the pressure drop constituting one central objective for spacer design.

6.2 Methods

The experimental set-up for the pressure drop experiments is introduced in Section 6.2.1. Subsequently, Section 6.2.5 introduces the systematic work flow for model identification. Section 6.2.4 introduces the algebraic pressure drop models. The methods and concepts related to parameter estimation, parameter identifiability and DOE are introduced in Section 6.2.6.

6.2.1 Pressure drop experiments

Experiments are carried out using the lab-scale electrodialysis plant introduced in Chapter 2. For pressure drop measurements over a single spacer-filled channel, the membrane module is substituted by a tailored test cell. A simplified flow chart of the resulting test stand is shown in Fig. 6.1. Demineralized water is pumped by centrifugal pumps from the storage tank $B1$ through the membrane module and test cell, respectively. The total volumetric flow rate $Q^{FIRC1002}$ is measured by the turbine flow-meter $FIRC1002$. This signal is supplied to a software-based PD-controller which is used to control the volumetric flow rate $Q^{FIRC1002}$ in a bypass configuration by acting on the control valve $V1101$. The construction of the test cell allows to vary the length of the spacer l_{sp} that is included in the channel. This allows the discrimination of the contribution of the spacer and the distribution system of the test cell in a data pretreatment step. Experiments are conducted using *Spacer A* with geometric properties summarized in Table A.2.

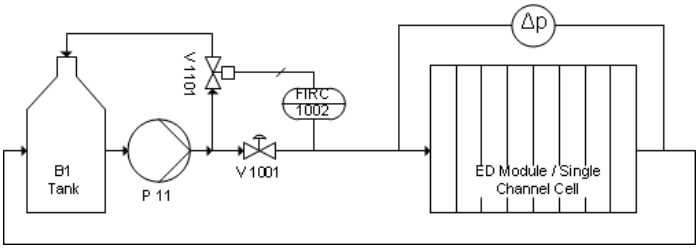

Figure 6.1: Scheme of the experimental set-up for pressure drop measurements.

6.2.2 Geometric modeling of the spacer and simulation scenario

The geometric properties of a non-woven spacer are illustrated in Fig. 6.2. Here, the two layers of parallel filaments that form the spacer are oriented in the $x-z$-plane. Within this plane, two angles characterize the orientation of the filaments: (i) The angle between the parallel filaments in the different layers β and (ii) the angle δ describing the rotation of the symmetry axes relative to the x-coordinate which points into the main flow direction. In technical applications it is required that the symmetry axis of the spacer has to be identical to the mean flow direction (Koutsou et al., 2007). Hence, commonly the flow attack angle is fixed to $\alpha = 90°$ and β is varied in the range $0° < \beta < 180°$.

With these angles, the diameter of the filaments d_f and the orthogonal distance between two parallel spacer filaments l_m, the geometry of the spacer is completely defined. Hence, a three-dimensional design space is spanned by the design parameters $\mathbf{u}^{nw} = [\beta, d_f, l_m]$. For a woven spacer structure principally the same geometric properties β, α, l_m and d_f uniquely specify a given spacer design. However, it is difficult to manufacture a woven mesh with $\beta \neq 90°$ which yields the technically relevant design space $\mathbf{u}^{w} = [d_f, l_m]$.

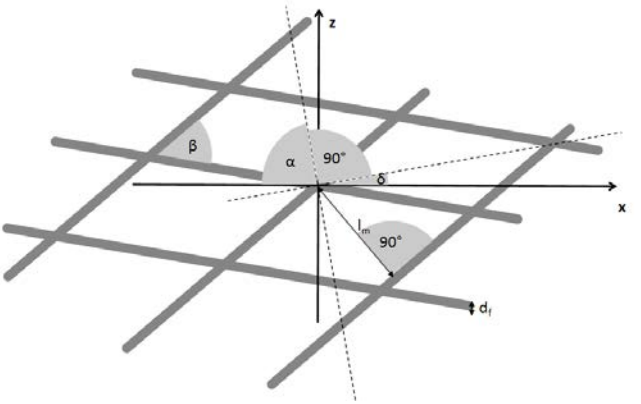

Figure 6.2: Geometry of a non-woven spacer.

For both, woven and non-woven spacer structures the thickness of the channel h_{ch} corresponds to

$$h_{ch} = 2\, d_f\, c_f. \tag{6.1}$$

Here, the factor $c_f = 0.946$ (cf. Fritzmann (2012)) is introduced to account for the fact that the filaments themselves and the bounding membranes are slightly overlapping.

The simulated domain of the spacer-filled flow channel is depicted in Fig. 6.3. The length and width of the domain is chosen to resolve six filament intersections, or unit cells (Koutsou et al., 2007), along the x-coordinate and two filament intersections along the z-coordinate. The

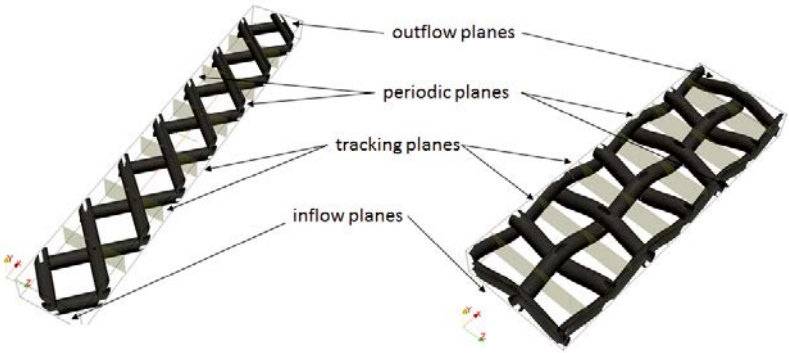

Figure 6.3: Computational domain for a non-woven and woven spacer geometry with tracking planes after every filament intersection.

height of the domain corresponds to the height of the channel h_{ch}. Periodic boundary conditions are specified for the boundary elements in the $x-y-$planes at $z = 0$ and $z = w_{ch}$. For the boundary elements in the $x-z-$planes at $y = 0$ and $y = h_{ch}$ – corresponding to the location of the membranes – no-slip boundary conditions are enforced. In the inlet and outlet planes at $x = 0$ and $x = l_{ch}$ standard in- and outflow conditions are specified. Initial conditions are $\mathbf{v}(\mathbf{x}, t = 0) = 0$ and $p(\mathbf{x}, t = 0) = p_{atm}$, where p_{atm} is the atmospheric pressure. From this initial state, each dynamic simulation is run until it reaches steady state. The total pressure $p_{tp,i}, i = 0, ..., 5$, is tracked in the course of the simulation in six tracking-planes at each filament intersection (cf. Fig. 6.3). In these planes the pressure is averaged to obtain an estimate for the evolution of the pressure in the mean flow direction. The physical properties of the perfusing fluid are specified in accordance with those of demineralized water at $298.15\,K$ (Perry and Green, 2008).

6.2.3 Software and implementation

For the 3D simulations the LBM solver MUSUBI is used with a $D3Q19$ scheme based on 19 discrete lattice velocities and the multiple relaxation (MRT) approach with acoustic scaling. Mesh generation is carried out using SEEDER (Harlacher et al., 2011) to allow for an efficient mesh generation for arbitrary woven or non-woven spacer geometries from elementary geometrical structures. The elementary structures of woven spacers are generated with the WeaveGeo2012 module in the software GeoDict (Math2Market GmbH 2013). For all simulations the domain is discretized with regular cubic elements with a size of $6.25 \cdot 10^{-6} m$. Simulations are performed on Linux cluster of the RWTH Aachen, Germany, and the high performance computing system HERMIT at HLRS Stuttgart, Germany, using 512 to 2048 processors.

6.2.4 Semi-empirical modeling of pressure drop in spacer-filled channels

The pressure drop Δp of an incompressible fluid flowing through a flow channel of arbitrary geometry is typically represented by

$$\Delta p = \zeta^{sp} \frac{l_{ch}}{d_g} \frac{\rho\, v_{ch}^2}{2}, \tag{6.2}$$

where ζ^{sp} is the friction factor, v_{ch} the mean velocity and ρ is the density of the fluid. The quantity l_{ch} is the length and d_g is a characteristic diameter of the channel (Verein Deutscher Ingenieure, 2006).

For the specification of an appropriate characteristic diameter d_g different specifications are employed in literature (Fritzmann, 2012, Koutsou et al., 2009). For non-woven geometries some authors (e.g., Schock and Miquel (1987)) define the characteristic diameter as the hydrodynamic diameter. As alternative specifications the heights of the spacer-filled channel h_{ch} or the filament diameter d_f have been proposed (Isaacson and Sonin, 1976). As these specifications are applicable for conceptually different spacer geometries, the definition $d_g = h_{ch}$ is used for the remainder of this work.

The friction coefficient in spacer-filled channels ζ^{sp} is given by

$$\zeta^{sp} = n^{sp}\, Re^{-m^{sp}} \tag{6.3}$$

with the parameters n^{sp} and m^{sp} (Sonin and Isaacson, 1974). The Reynolds number Re is defined with the characteristic diameter $d_g = h_{ch}$ as

$$Re = \frac{\rho\, v_{ch}\, h_{ch}}{\eta}. \tag{6.4}$$

It is well-known that a unique identification of n^{sp} and m^{sp} in parameter estimation is difficult by drawing similarities to model structures typically arising in reaction kinetics modeling (Buzzi-Ferraris and Manenti, 2010, Himmelblau, 1970). Hence, Eq. (6.3) is reformulated yielding

$$\zeta^{sp} = exp\left(\tilde{n}^{sp} - m^{sp} \frac{ln\,(Re) - ln\,(Re_{min})}{ln\,(Re_{max}) - ln\,(Re_{min})}\right). \tag{6.5}$$

where $\tilde{n}^{sp} = exp\,(n^{sp})$. Re_{min} and Re_{max} are the minimal and maximal Reynolds numbers, respectively, considered in the model identification process.

The parameters $\tilde{n}^{sp}$, m^{sp} in Eq. (6.5) depend on the spacer geometry. In order to identify a model for different spacer geometries Eq. (6.5) needs to be generalized by introducing the parameter functions

$$n^{sp} = g_1\left(\mathbf{u}^k, \hat{\mathbf{p}}^k\right), \tag{6.6}$$

$$m^{sp} = g_2\left(\mathbf{u}^k, \hat{\mathbf{p}}^k\right). \tag{6.7}$$

Eqs. (6.6) and (6.7) depend on the geometric design parameters of non-woven and woven spacers $\mathbf{u}^k$, $k \in \{nw, w\}$, and additional empirical parameters $\hat{\mathbf{p}}^k \in \mathbb{R}^{n_{\hat{p}^k}}$. Appropriate functional relations (6.6) and (6.7) are identified in Section 6.4.

Introducing (6.6) and (6.7) into (6.3) yields an algebraic model

$$\begin{aligned}\zeta^{sp} =& exp\left(g_1\left(\mathbf{u}^k, \hat{\mathbf{p}}^k\right)\right. \\ & \left. -g_2\left(\mathbf{u}^k, \hat{\mathbf{p}}^k\right)\frac{ln\left(Re\right)-ln\left(Re_{min}\right)}{ln\left(Re_{max}\right)-ln\left(Re_{min}\right)}\right).\end{aligned} \tag{6.8}$$

with parameters $\mathbf{p} = \left[\hat{p}_1^k, ..., \hat{p}_{n_{\hat{p}^k}}^k\right]$, inputs $\mathbf{u} = \left[v_{ch}, \mathbf{u}^k\right], k \in \{nw, w\}$, and constants $\mathbf{c} = [\rho, \eta, c_f]$. For an efficient numerical treatment the inputs $\mathbf{u}$ are scaled:

$$\breve{u}_k = \frac{u_k - u_{k,min}}{u_{k,max} - u_{k,min}}, \quad k = 1, ..., n^u. \tag{6.9}$$

The model output is scaled similarly to $\breve{\zeta}^{sp}$ by introducing $\breve{\zeta}^{sp}_{min}$ and $\breve{\zeta}^{sp}_{max}$. The lower and upper bounds that are used for the scaling scheme are summarized in Table 6.1. Note that distinct bounds are used to scale the friction factor in the model for the woven and non-woven spacer according to

$$\breve{\zeta}_k^{sp} = \frac{ln\left(\zeta_k^{sp}\right) - ln\left(\zeta_{k,min}^{sp}\right)}{ln\left(\zeta_{k,max}^{sp}\right) - ln\left(\zeta_{k,min}^{sp}\right)} \quad k \in \{nw, wov\}. \tag{6.10}$$

Table 6.1: Lower and upper bounds used for the scaling of model output and inputs. The subscripts nw and wov refer to the model for the non-woven and woven spacer, respectively.

	v_{ch} $\left[\frac{m}{s}\right]$	$\frac{\beta}{2}$ $[^\circ]$	d_f $[m]$	l_m $[m]$	ζ_{nw}^{sp} $[-]$	ζ_{wov}^{sp} $[-]$
min	0.04	29.00	$0.9{\cdot}10^{-4}$	$0.9{\cdot}10^{-3}$	0.0870	0.1707
max	0.21	61.00	$3.1{\cdot}10^{-4}$	$3.1{\cdot}10^{-3}$	1231.85	1910.19

6.2.5 Work flow for model identification

A major difficulty in the generalization of the algebraic pressure drop models is the identification of an appropriate extended model structure incorporating the design parameters as additional inputs. To this end, the work flow for structure identification is used as depicted in Fig. 6.4 a. Here, simulated data for a basic set of geometries are used to evaluate structurally different model candidates by means of their predictive capabilities.

After the identification of the the best candidate structure, the model is iteratively refined as illustrated in Fig. 6.4 b. The essence of this iterative refinement process is to add experimental pressure drop data for additional spacer geometries to increase the information content of the data set. To maximize the information content added by each new geometry, a model-based design of experiments (DOE) approach is applied. The refinement process is repeated in an iterative process until the augmentation of additional spacer geometries does not improve the reliability in the empirical model parameters.

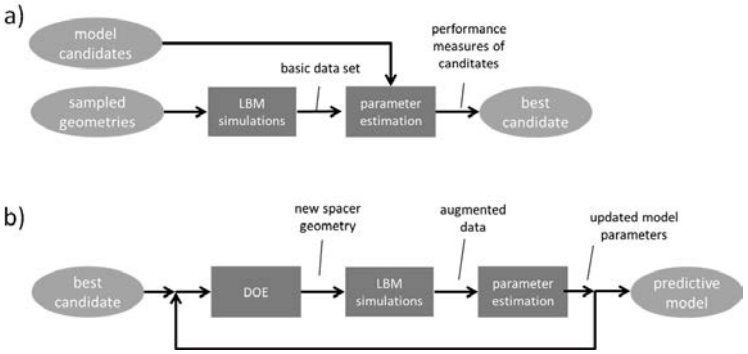

Figure 6.4: Work flow for (a) the discrimination of different model candidates and (b) the iterative model refinement of the best candidate based on DOE and parameter estimation techniques.

6.2.6 Parameter estimation, identifiability analysis and design of experiments

This section briefly introduces the methods applied in the model identification work-flow for the estimation of parameters, the evaluation of parameter reliability and the model-based design of experiments.

Parameter estimation

The parameter estimation problem is formulated as

$$\underset{p\in R^{n_p}}{min}\ \phi = \frac{1}{2}\frac{RSS}{\sigma^2} \tag{6.11}$$

with the residual sum of squares RSS defined as

$$RSS = \sum_{i=1}^{n_{dp}} \left(\check{\zeta}_i^{sp}\left(\mathbf{p},\, \mathbf{u}_i,\, \mathbf{c}\right) - \zeta_i^{MUSUBI}\right)^2. \tag{6.12}$$

n_p and n_{dp} correspond to the number of parameters and data points, respectively; ζ_i^{MUSUBI}, $i = 1, ..., n_{mp}$, represent data points corresponding to the experimental conditions $\mathbf{u}_i$. The uncertainty of the measurements is accounted for by the variance σ^2. For an efficient numerical treatment of the minimization problem first-order derivatives

$$\bar{G}_j = \frac{\partial \phi}{\partial p_j}, \quad j = 1, ..., n_p, \tag{6.13}$$

and second order derivatives

$$\begin{aligned} H_{j,k} = &\sum_{i=1}^{n_{dp}} \frac{\partial \check{\zeta}_i^{sp}\left(\mathbf{p},\, \mathbf{u}_i,\, \mathbf{c}\right)}{\partial p_j}\frac{1}{\sigma^2}\frac{\partial \check{\zeta}_i^{sp}\left(\mathbf{p},\, \mathbf{u}_i,\, \mathbf{c}\right)}{\partial p_k} \\ &+ \left(\frac{\check{\zeta}_i^{sp}\left(\mathbf{p},\, \mathbf{u}_i,\, \mathbf{c}\right) - \zeta_i^{MUSUBI}}{\sigma^2}\right)\frac{\partial^2 \check{\zeta}_i^{sp}\left(\mathbf{p},\, \mathbf{u}_i,\, \mathbf{c}\right)}{\partial p_k \partial p_j}, \end{aligned}$$

$$j,k \in \{1,...,n_p\}, \tag{6.14}$$

are required which are often approximated by

$$F_{j,k} = \sum_{i=1}^{n_{dp}} \frac{\partial \check{\zeta}_i^{sp}(\mathbf{p},\, \mathbf{u}_i,\, \mathbf{c})}{\partial p_j} \frac{1}{\sigma^2} \frac{\partial \check{\zeta}_i^{sp}(\mathbf{p},\, \mathbf{u}_i,\, \mathbf{c})}{\partial p_k}, \tag{6.15}$$
$$j,k \in \{1,...,n_p\}.$$

The Jacobian $\mathbf{G}$, Fischer matrix $\mathbf{F}$ and Hessian $\mathbf{H}$ are calculated using the Symbolic Math Toolbox in Matlab (The Math Works Inc., 2013). The minimization problem (6.11) is solved by using the deterministic optimization routine *fmincon* in Matlab (The Math Works Inc., 2013). This local optimizer is used in a multi-start approach to approximate the globally optimal solution of the parameter estimation problem.

Reliability of parameter estimates

An identifiability analysis can be carried out to check whether the model parameters can be uniquely identified from a given set of data. Technically a model is regarded to be identifiable if for two distinct sets of parameters $\mathbf{p}_1$ and $\mathbf{p}_2$ the identity

$$\check{\zeta}^{sp}(\mathbf{p}_1,\, \mathbf{u},\, \mathbf{c}) = \check{\zeta}^{sp}(\mathbf{p}_2,\, \mathbf{u},\, \mathbf{c}) \tag{6.16}$$

holds if and only if $\mathbf{p}_1 = \mathbf{p}_2$.

Different methods of testing for identifiability have been proposed in literature (Quaiser and Mönnigmann, 2009). This study will employ the eigenvalue method introduced by Vajda et al. (1989) and recently extended by Quaiser and Mönnigmann (2009). The resulting criterion for a parameter p_k to be not uniquely identifiable is that the corresponding eigenvalue λ_j of the Fischer information matrix $\mathbf{F}$ is small or zero.

From a practical point of view, it is important to note that the scaling of the model output $\check{\zeta}^{sp}(\mathbf{u},\, \mathbf{p},\, \mathbf{c})$ strongly determines the absolute values of the eigenvalues λ_j. To eliminate these scaling effects, the identifiability of a parameter p_k is evaluated using the normalized eigenvalue $\frac{\lambda_j}{\lambda_{max}}$ where λ_{max} is the maximal eigenvalue of $\mathbf{F}$. As a measure for the identifiability of the entire model the ratio $\frac{\lambda_{min}}{\lambda_{max}}$ is used, where λ_{min} is the minimal eigenvalue of $\mathbf{F}$.

Another measure for the reliability of the estimates $\mathbf{p}^*$ are the confidence intervals

$$\Delta\theta_k = t_{\frac{\gamma}{2},n^{mp}-(n^p+1)} \sqrt{\frac{RSS}{n^{mp}-(n^p+1)}} \sqrt{G_{k,k}},$$
$$k = 1,...,n^p. \tag{6.17}$$

Here, $\mathbf{G} = \mathbf{F}^{-1}$ and $t_{\frac{\gamma}{2},n^{mp}-(n^p+1)}$ is the upper $\frac{\gamma}{2}$ percentile of the cumulative t-distribution with $n^{mp}-(n^p+1)$ degrees of freedom (Marsili-Libelli et al., 2003). Large confidence intervals indicate significant parameter uncertainty.

A question closely related to identifiability is how many parameters are required to describe the information in the data. This question is of special relevance if $n_m > 1$ different model candidates are available which are characterized by a different number of parameters. A well-established approach to investigate this question is based on Akaike's information criterion (Akaike, 1973, Burnham and Anderson, 2008):

$$AIC_i = n^{mp}\, ln\left(\frac{RSS}{n^{mp} - (n^p + 1)}\right) + 2\,(n^p + 1) + \frac{2\,(n^p + 1)\,(n^p + 2)}{n^{mp} - n^p - 2}, \quad i = 1, ..., n_m. \tag{6.18}$$

On this basis, relative measures are defined as

$$\Delta AIC_{i,c} = AIC_i - AIC_c, \quad i = 1, ..., n_m, \tag{6.19}$$

where candidate i is compared to the *best* candidate c. From the relative measures $\Delta AIC_{i,c}$, $i = 1, ..., n_m$, Akaike weights $w_{i,c}$ are defined as

$$w_{i,c} = \frac{exp\,(-0.5\,\Delta AIC_{i,c})}{\sum_{\substack{j=1 \\ j \neq i}}^{n_m} exp\,(-0.5\,\Delta AIC_{j,c})}, \quad i = 1, ..., n_m. \tag{6.20}$$

The weight $w_{i,c}$ describes the probability of candidate i to be the best model in the set of candidates (Burnham and Anderson, 2008). Here, the *best* candidate is characterized by the minimal Akaike criterion, i.e., $AIC_c = \min_{i \in \{1,...,n_m\}} AIC_i$.

The quality of the model fit is often characterized by the corresponding sum of squares RSS (cf. Eq. 6.12) or more intuitively by the root mean square error $SRSS = \sqrt{RSS}/n_{mp}$. However, these measures give only a limited insight into the predictive capabilities of the model. To assess the model quality the identification procedure is rather supplemented by a cross validation analysis (cf. e.g., Arlot and Celisse (2010)) yielding the averaged root mean square error $SRSSCV$.

Design of experiments

In order to identify the generalized model with a minimum number of CFD simulation, methods for model-based design of experiments (DOE) for parameter precision are applied. For DOE different optimality criteria have been derived exploring different measures of the Fischer information matrix $\mathbf{F}$ at the parameter estimates $\mathbf{p}^*$ (Walter and Pronzato, 1997). In the remainder of this contribution the well-known D-optimality criterion is used which is defined as

$$\max_{\mathbf{u} \in R^{n_u}} D = \det\left(\mathbf{F}\right). \tag{6.21}$$

The optimization problem (6.21) is solved by using the local deterministic optimization routine *fmincon* in Matlab (The Math Works Inc., 2013). The required first-order derivatives are computed by means of the ADiMat software (Bischof et al., 2002) which employs automatic differentiation techniques.

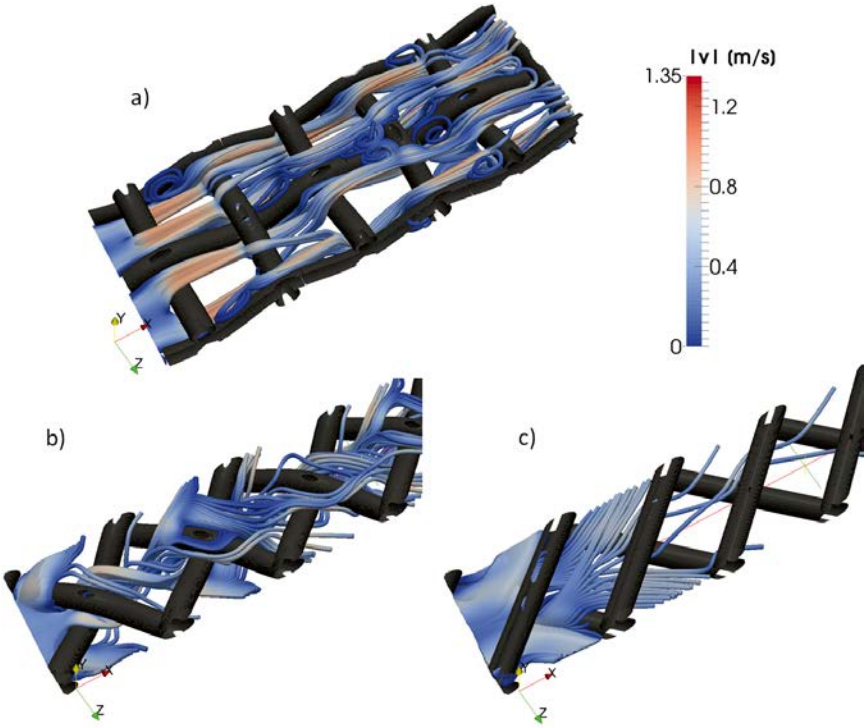

Figure 6.5: Flow pattern for a mean velocity of $v_{ch} = 0.2\,\frac{m}{s}$ (a) for the woven geometry with $\alpha = 0°$ used in the experiments, (b) for a woven geometry with $\alpha = 90°$ and (c) for a non-woven spacer geometry.

6.3 Simulation results and validation

This section presents in Section 6.3.1 the simulated flow-patterns arising in the spacer geometries considered in the comparison with experimental data and in the simulation studies in Section 6.4. This description is necessarily brief, as the qualitative pattern of the flow fields in non-woven geometries have been extensively described elsewhere (cf. e.g., Cao (2001), Fimbres-Weihs and Wiley (2007), Koutsou et al. (2004), Schwinge et al. (2002; 2004)). In Section 6.3.2 the simulated pressure profiles are illustrated, which are compared in Section 6.3.3 to experimental data.

6.3.1 Velocity profiles

Fig. 6.5 a shows the simulated flow pattern for the woven spacer A with design parameters summarized in Tab. A.2 for a mean velocity of $v_{ch} = 0.2\,\frac{m}{s}$. Here, the stream lines illustrate the

flow-path of tracer particles from the inlet plane through the channel. The fluid is strongly accelerated at the spacer filaments orthogonal to the mean flow directions. Stationary vortices arise at the intersections of the filaments in the completely laminar flow field. This laminar character of the hydrodynamics is observed for all simulations in the velocity range $v_{ch} = 0.05, ..., 0.2\,\frac{m}{s}$.

The flow pattern arising in a spacer with identical geometrical properties, but with a flow attack angle $\alpha = 90°$, is shown in Fig. 6.5 b. A significant fraction of the stream lines directly aligns with the orientation of the filaments in the first part of the channel. The acceleration of the fluid at the filament intersections is less significant compared to the woven spacer with $\alpha = 0°$. In all simulations for woven spacers with a flow attack angle $\alpha = 90°$ and design parameter in the range of the considered inputs (cf. Table 6.1) the flow remains completely laminar.

The hydrodynamics are finally simulated for a non-woven spacer with identical geometrical properties and a flow attack angle $\alpha = 90°$. The resulting stream line distribution is shown in Fig. 6.5 c. Here, the mean flow direction immediately aligns with the orientation of the filaments. For nearly all the considered geometries the flow remains completely laminar. Very small periodic oscillations in the velocity and pressure profiles indicating the transition to turbulent flow are found for $v_{ch} = 0.2\,\frac{m}{s}$ and geometries characterized by $d_f = 1 \cdot 10^{-4} m$, $l_m = 3 \cdot 10^{-3} m$ and $\frac{\beta}{2} > 55°$. However, the qualitative time-averaged pattern remains very similar to the laminar flow pattern.

6.3.2 Pressure drop profiles

Fig. 6.6 shows the averaged pressures $p_{tp,i}, i = 0, ..., 5$, at the tracking planes for the non-woven and woven spacers with design parameters summarized in Tab. A.2 and flow attack angles $\alpha = 0°$ and $\alpha = 90°$, respectively. In the mean flow direction the simulation predicts a nearly linear pressure profile. Deviations – caused by inflow and outflow effects – are restricted to the first and last tracking plane. Hence, the friction coefficient is determined by

$$\zeta^{MUSUBI} = \frac{p_{tp,1} - p_{tp,3}}{\Delta z_{1,3}} \frac{2}{\rho\, v_{ch}^2}, \tag{6.22}$$

where $\Delta z_{1,3}$ is the distance between tracking planes 1 and 3.

6.3.3 Comparison with experimental data

The simulated pressure drop is compared to the pressure drop measured over an entire ED module and determined in the single-channel test cell. The comparison is shown in Fig. 6.7. Here, it is seen that the single-channel measurements and the predictions by LBM simulation are in very good agreement for $v_{ch} < 0.1\,\frac{m}{s}$. For $v_{ch} > 0.1\,\frac{m}{s}$ a slight deviation is observed. The measured pressure drop over the ED module is found to be higher in comparison to the LBM prediction. This is reasonable, as the measured data include contributions from the distribution system of the module. Overall, in the range of the measurement error, a good agreement between experiment and model prediction is found. Hence, the LBM based CFD solver is considered as a predictive tool to systematically investigate the hydrodynamics in spacer-filled channels.

6.4 Identification of friction-factor models for varying design parameters

This section presents the model identification results for generalized pressure drop models for non-woven (cf. Sec 6.4.1) and woven (cf. Section 6.4.2) spacers by means of the integrated work flow introduced in Section 6.2.5. The predictive capabilities of the identified models are illustrated in Section 6.4.3.

6.4.1 Non-woven spacers

In a first step, data are generated in simulation experiments for a set of 17 geometries. The design space is systematically covered by Latin hypercube sampling resulting in spacer geometries nos. 1 - 12 in Table C.1. Five additional geometries (nos. 13 - 17) are included to cover the upper and lower bounds of the design parameters. For each geometry in this set, LBM simulations are carried out at four mean velocities $v_{ch} \in \{0.05, 0.1, 0.15, 0.2\}\,\frac{m}{s}$ resulting in 68 simulations. Depending on the specific geometry and the number of processors in the simulations the simulation time for each run varied in between 2 h and 6 h.

The resulting data are used estimate the parameters in the generalized friction coefficient model (6.5). The functional relations (6.6) and (6.7) are represented by 17 empirical candidates summarized in Table C.3 in the Appendix. For each model candidate structure the parameter estimation problem (6.11) is solved with the methods described in Section 6.2.6. The resulting SRSS and SRSSCV are compared in Fig. 6.8. Accordingly, the lowest SRSS is obtained for model 16; slightly

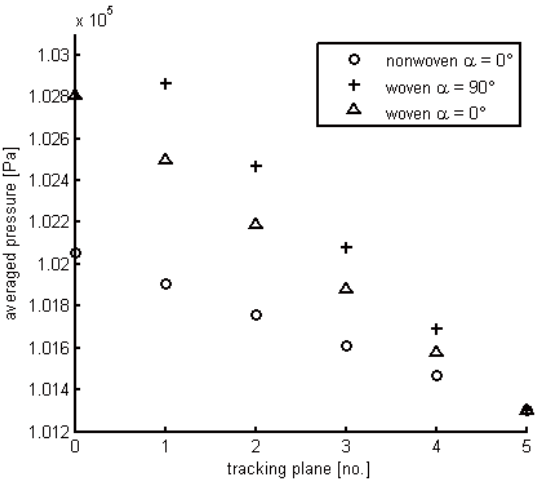

Figure 6.6: Linear trend of the averaged pressure at the tracking planes in the x-coordinate.

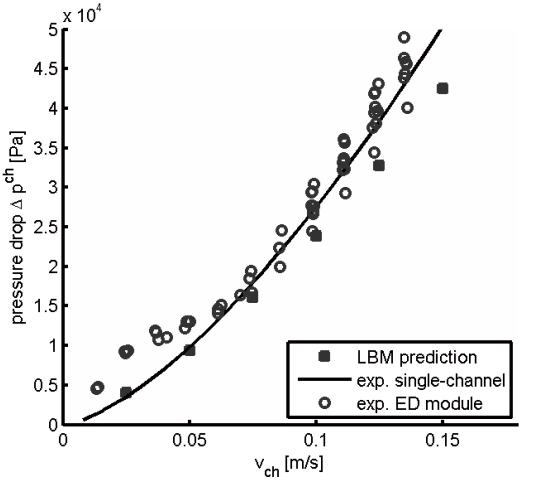

Figure 6.7: Pressure drop in a spacer channel with $l_{sp} = 0.2m$ as predicted by the LBM simulation compared to experimental data from experiments with an ED module and a single-channel test cell.

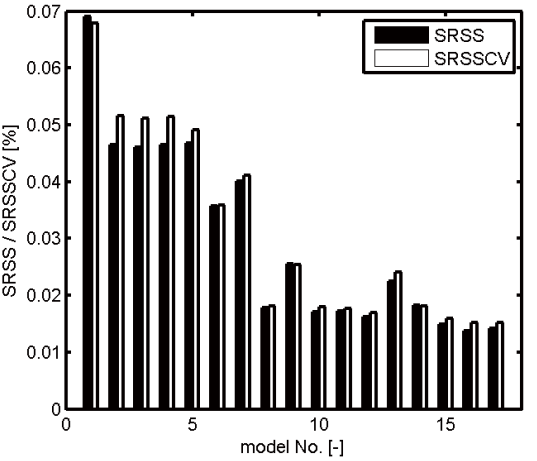

Figure 6.8: Root mean square error (SRSS) of the model fit and mean cross validation error (SRSSCV) for 17 model candidates for the non-woven spacers.

higher SRSS are obtained for the models 8, 10 - 12 and 14 - 17. Significantly higher SRSS are

found for the remaining model candidates.

The resulting eigenvalue ratios of the Fischer information matrix $\frac{\lambda_{min}}{\lambda_{max}}$, the Akaike differences ΔAIC and the Akaike weights $w_{i,8}$ are summarized in Tab. 6.2. For the ratios $\frac{\lambda_{min}}{\lambda_{max}}$ very low values, i.e. $\frac{\lambda_{min}}{\lambda_{max}} < 1{\cdot}10^{-7}$, are observed for the models 10 - 17. Hence, the corresponding estimates are subject to significant parameter uncertainty. Model 8 is the only candidate characterized by both an acceptable eigenvalue ratio of $\frac{\lambda_{min}}{\lambda_{max}} = 1.19{\cdot}10^{-6}$ and a good quality of fit characterized by $SRSS = 1.81\%$. The Akaike information criterion ranks model 8 as the best model candidate in the set resulting in a relative measure $\Delta AIC_8 = 0$. Slightly higher measures are found for models 10 - 12, 15 and 17. For the remaining model candidates, the ΔAIC_i is significantly higher. These results are in agreement with the Akaike weights $w_{i,8}$, $i = 1, ..., 17$. Here, model 8 is ranked as the best model candidate in the set with a probability of $w_{8,8} = 98.3\,\%$.

In summary, model candidate 8 given by

$$\begin{aligned} n^{sp}\left(\mathbf{u}^{nw}\right) = p_1 \frac{\check{\beta}}{2} + p_4 \check{d}_f + p_7 \check{l}_m \\ + p_2 \frac{\check{\beta}}{2}^2 + p_5 \check{d}_f^2 + p_8 \check{l}_m^2 \\ + p_3 \frac{\check{\beta}}{2}^{-1} + p_6 \check{d}_f^{-1} + p_9 \check{l}_m^{-1} + p_{10}, \end{aligned} \tag{6.23}$$

$$m^{sp}\left(\mathbf{u}^{nw}\right) = p_{11} \frac{\check{\beta}}{2} + p_{12} \check{d}_f + p_{13} \check{l}_m + p_{14}, \tag{6.24}$$

stands out by its acceptable identifiability properties while having only a slightly higher SRSS compared to model candidate 16. Further, this model structure is rated as the best in the considered set according to the Akaike's criterion. Hence, the attention is restricted to this candidate in the following.

In the next step the confidence intervals of the parameters in model (6.5), (6.23) and (6.24) are systematically improved by using the work flow introduced in Section 6.2.5 (cf. Fig. 6.4 b). In each iteration the DOE problem (6.21) is solved with the methods described in Section 6.2.6 to derive new experimental conditions $\mathbf{u}^{new} = \left[v_{ch}^{new},\, d_f^{new}\, \beta^{new}\, l_m^{new}\right]$. For any new geometry characterized by d_f^{new}, β^{new} and l_m^{new}, LBM simulations are carried out for the mean inlet velocities $v_{ch} \in \{v_{ch}^{new},\, 0.05,\, 0.1,\, 0.15,\, 0.2\}\frac{m}{s}$. The resulting data are merged with the previous reference data set used before. This augmented data set is used to update the parameter estimates $\mathbf{p}^*$ by solving the parameter estimation problem (6.11) before entering a new refinement cycle.

The results of model refinement are summarized in Table 6.3. In the first five cycles the DOE method yields optimal experiments in which v_{ch}^{new} and d_f^{new} are fixed at the lower bounds while β^{new} and l_m^{new} are varied. In cycles 5 - 13, the DOE approach yields new experimental conditions $\mathbf{u}^{new}$ characterized by the systematic variation of all design parameters. The iterative model refinement is stopped after 13 iterations as the DOE method in cycle 14 derives $\mathbf{u}^{new}$ identical to geometry 15 from the basis set of geometries (cf. Table C.1).

In the course of model refinement, the SRSS slightly increases from 1.78 % to 2.03 %. The eigenvalue ratio $\lambda_{min}/\lambda_{max}$ is increased by 28.1% indicating an improvement in parameter identifiability. Further, a major improvement is found for the confidence intervals $\Delta\theta_k$, $k = 1, ..., n_p$.

Table 6.2: Comparison of different model candidates for non-woven spacers.

no.	n^p	$\frac{\lambda_{min}}{\lambda_{max}}$	$SRSSCV$	ΔAIC	$w_{i,8}$
1	8	1.32E-03	6.19%	159.22	0.00%
2	10	6.81E-04	5.16%	113.19	0.00%
3	10	5.75E-04	5.12%	113.19	0.00%
4	10	8.22E-06	5.14%	114.05	0.00%
5	11	1.53E-04	4.91%	116.19	0.00%
6	11	9.14E-06	3.59%	81.39	0.00%
7	14	4.62E-06	4.11%	110.60	0.00%
8	14	1.19E-06	1.81%	0	98.30%
9	14	1.35E-05	4.68%	49.51	0.00%
10	17	2.41E-08	3.38%	8.79	1.22%
11	17	5.41E-08	3.02%	10.81	0.44%
12	20	2.00E-08	3.29%	18.35	0.01%
13	20	4.16E-07	3.05%	62.66	0.00%
14	20	3.19E-10	1.57%	15.85	0.04%
15	23	2.82E-10	1.57%	27.84	0.00%
16	26	2.55E-09	3.74%	76.97	0.00%
17	29	3.89E-11	2.78%	72.27	0.00%

Here, the maximal $\Delta\theta_{max}$ and the mean $\Delta\theta_{av}$ confidence interval are reduced by 60.7% and 53.4%, respectively.

A residual plot for the final friction factor model model (6.5), (6.23) and (6.24) is shown in Fig. 6.9. The final parameter estimates and confidence intervals are summarized in Table C.3 in the Appendix.

6.4.2 Woven spacer

As for the non-woven spacer geometries, a reference data set of 13 woven geometries is generated (cf. Tab. C.2). LBM simulations are carried out for these geometries and for the four mean velocities $v_{ch} \in \{0.05, 0.1, 0.15, 0.2\}\frac{m}{s}$ resulting in 52 simulations.

For the identification of the unknown structural relations (6.6) and (6.7) 17 empirical candidates are formulated as summarized in Tab. D.3.1. The resulting SRSS and SRSSCV values are illustrated in Fig. 6.10. The SRSS of model candidates 8 - 17 are nearly identical and significantly lower than the SRSS of the model candidates 1 - 7. For model structures 10 - 17 the SRSSCV values significantly exceed the corresponding SRSS values. This indicates, that these candidates can describe the results in the reference data set with high accuracy, however, are less suitable to predict pressure drop in the entire design space.

The resulting measures assessing model performance are shown in Table 6.4. The model candi-

Table 6.3: Optimal experimental conditions for non-woven spacers and performance measures of the resulting model after parameter estimation with augmented data.

cycle	geometry $\left[\frac{m}{s}\right]$	v_{ch}^{new} [°]	$\beta^{new}/2$ $\left[10^{-4}\,m\right]$	d_f^{new} $\left[10^{-3}\,m\right]$	l_m^{new} [%]	SRSS $\left[10^{-6}\right]$	$\lambda_{min}/\lambda_{max}$ $\left[10^{-4}\right]$	$\Delta\theta_{max}$ $\left[10^{-4}\right]$	$\Delta\theta_{av}$
-	-	-	-	-	-	1.78	1.39	2.33	1.12
1	18	0.05	30.96	1	1.9	1.91	1.39	2.43	1.13
2	19	0.05	41.92	1	3	1.91	1.44	2.30	1.06
3	20	0.05	31.06	1	1.2	1.88	1.61	1.88	0.93
4	21	0.05	30	1	2.9	1.95	1.34	1.98	0.97
5	22	0.05	60	1	1.1	2.06	1.65	1.98	0.97
6	23	0.2	60	3	3	2.08	1.59	1.95	0.96
7	24	0.2	31.85	3	1	2.05	1.72	1.75	0.90
8	25	0.05	31.42	1.1	3	2.04	1.73	1.66	0.85
9	26	0.05	45.85	1	1	2.05	1.74	1.62	0.81
10	27	0.2	30	3	3	2.04	1.81	1.58	0.74
11	28	0.05	60	1.03	2.2	2.04	1.86	1.48	0.74
12	29	0.2	30	2.04	1	2.03	1.82	1.46	0.73
13	30	0.05	31.14	1	3	2.03	1.78	1.45	0.73
14	15	0.05	60	1	3	-	-	-	-

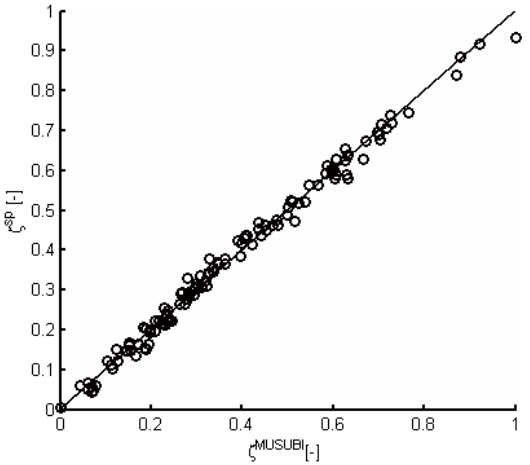

Figure 6.9: Residual plot comparing the prediction of the final friction coefficient model ζ^{sp} and the LBM prediction ζ^{MUSUBI} for non-woven spacers.

dates 10 - 17 are characterized by $\lambda_{min}/\lambda_{max} < 10^{-7}$ clearly indicating that parameter identifiability is problematic, while the ratios are in the range $1.61 \cdot 10^{-3} < \lambda_{min}/\lambda_{max} < 6.10 \cdot 10^{-6}$ for the other candidates. Candidate 8 is characterized with an acceptable eigenvalue ratio $\lambda_{min}/\lambda_{max} = 2.31 \cdot 10^{-6}$. The Akaike information criterion ranks this model as the candidate with a probability of $w_{8,8} = 97.95\,\%$. Hence, model structure 8 given by

$$\begin{aligned} n^{ch}(\mathbf{u}^w) = {} & p_1 \check{d}_f + p_4 \check{l}_m \\ & + p_2 \check{d}_f^2 + p_5 \check{l}_m^2 \\ & + p_3 \check{d}_f^{-1} + p_6 \check{l}_m^{-1} + p_7, \end{aligned} \tag{6.25}$$

$$m^{ch}(\mathbf{u}^w) = p_8 \check{d}_f + p_9 \check{l}_m + p_{10}, \tag{6.26}$$

is considered as the most appropriate model structure to generalize the friction factor model (6.5), (6.25) and (6.26) for woven spacers.

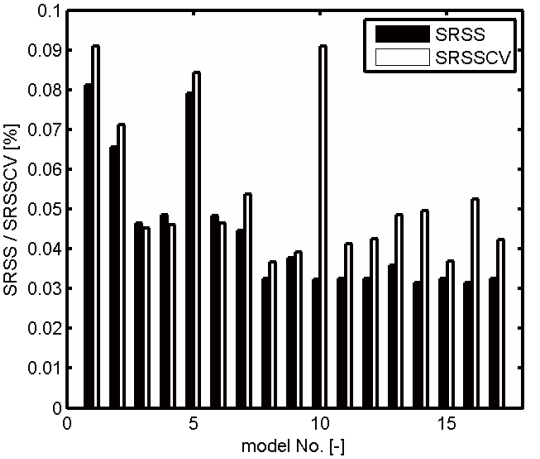

Figure 6.10: Root mean square error (SRSS) of the model fit and mean cross validation error (SRSSCV) for 17 model candidates for the woven spacers

As in case of non-woven spacers, the model (6.5), (6.25) and (6.26) is refined using the model refinement work flow (cf. Fig. 6.4). The results are summarized in Tab. 6.5. In the course of the model refinement, the SRSS slightly increases from 3.24 % to 3.36 %. A major improvement is found with respect to parameter identifiability as indicated by an increase in the eigenvalue ratio $\lambda_{min}/\lambda_{max}$ by 235.5%. Further, the maximal $\Delta\theta_{max}$ and the mean $\Delta\theta_{av}$ confidence intervals are reduced by 60.1% and 64.2%, respectively.

A residual plot for the final model (6.5), (6.25) and (6.26) for woven spacers is shown in Fig. 6.11. The parameter estimates and confidence intervals are summarized in Table C.4 in the

Table 6.4: Comparison of 17 model candidates for woven spacers.

no.	n^p	$\frac{\lambda_{min}}{\lambda_{max}}$	$SRSSCV$	ΔAIC	$w_{i,8}$
1	6	1.61E-03	9.10%	78.30	0.00%
2	8	5.29E-05	7.11%	64.13	0.00%
3	8	8.05E-04	4.53%	28.52	0.00%
4	8	8.44E-04	4.61%	32.79	0.00%
5	8	5.48E-06	8.43%	83.77	0.00%
6	8	1.33E-05	4.64%	32.54	0.00%
7	10	4.35E-05	5.37%	32.96	0.00%
8	10	2.31E-06	3.67%	0	97.95%
9	10	6.10E-06	3.91%	15.40	0.04%
10	12	2.05E-09	9.10%	8.90	1.14%
11	12	5.03E-07	4.12%	9.50	0.85%
12	14	4.09E-08	4.26%	19.86	0.00%
13	14	1.44E-07	4.85%	29.89	0.00%
14	14	2.77E-19	3.70%	19.88	0.00%
15	16	2.45E-19	4.23%	31.34	0.00%
16	18	5.39E-09	4.96%	40.79	0.00%
17	20	2.18E-19	5.24%	54.99	0.00%

Appendix.

Table 6.5: Optimal experimental conditions for the woven geometries and performance measures of the resulting model fit with augmented data.

geometry	v_{ch}^{new} $\left[\frac{m}{s}\right]$	d_f^{new} $\left[10^{-4}\,m\right]$	l_m^{new} $\left[10^{-3}\,m\right]$	SRSS [%]	$\lambda_{min}/\lambda_{max}$ $\left[10^{-6}\right]$	$\Delta\theta_{max}$ $\left[10^{-4}\right]$	$\Delta\bar{\theta}_{av}$ $\left[10^{-4}\right]$
-	-	-	-	3.24	2.31	7.22	3.71
14	0.05	1.17	1.14	3.26	5.56	5.36	2.90
15	0.2	1	1.50	3.24	5.13	5.05	2.75
16	0.2	3	2.50	3.31	5.21	5.12	2.78
17	0.05	2.33	1	3.42	5.11	5.35	2.87
18	0.05	3	1.1	3.42	5.10	5.21	2.73
19	0.05	1.43	1.49	3.39	5.23	4.94	2.60
20	0.05	1.15	1	3.36	5.45	4.51	2.39
7	0.05	3	1	-	-	-	-

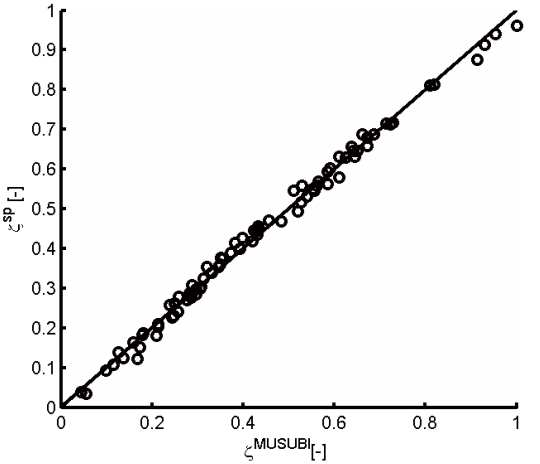

Figure 6.11: Residual plot comparing the predictions of the final friction coefficient model ζ^{sp} with the the LBM prediction ζ^{MUSUBI} for the woven spacer .

6.4.3 Predictive capabilities of the identified pressure drop models

The predicted friction factor $ln\,(\zeta^{sp})$ is shown exemplary in Fig. 6.12 for a non-woven geometry with varying design parameters. In a large part of the design space a significant nonlinear variation is found for the sensitivity of the friction factor with respect to the different design parameters (cf. Figs. 6.12 a and b). Further, it becomes explicit that the sensitivity with respect to v_{ch} is significantly higher compared to the sensitivity with respect to the geometric design parameter $\frac{\beta}{2}$ (cf. Fig. 6.12 c). This dominating influence of v_{ch} is not found in Fig. 6.12 d where the friction factor model is evaluated for varying v_{ch} and d_f.

Fig. 6.14 a shows the influence of d_f and l_m on the predicted friction coefficient for $v_{ch} = 0.2\,\frac{m}{s}$ and $\beta = 45°$. Here it gets explicit that the frequently used assumption of similar hydrodynamic conditions for a constant height to length ratio $\frac{h_{ch}}{l_m}$ is reasonable for $l_m < 1.8{\cdot}10^{-3}$ and $d_f < 2{\cdot}10^{-4}$. However, outside this range the increasing curvature of the isocontour-lines illustrates that this approximation is not appropriate.

Fig. 6.13 illustrates that $ln\,(\zeta^{sp})$ in a woven spacer is comparably affected by v_{ch} and the design parameters. The sensitivity of $ln\,(\zeta^{sp})$ with respect to d_f and l_m at $v_{ch} = 0.2\,\frac{m}{s}$ is illustrated in Fig. 6.14 b. With both an increasing d_f and l_m the friction factor decreases. While for $l_m > 2.2 \cdot 10^{-3} m$ the sensitivity with respect to d_f dominates, for $d_f > 2.4 \cdot 10^{-4} m$ the orthogonal distance of the filaments l_m has a comparably stronger effect on $ln\,(\zeta^{sp})$.

In Fig. 6.14 the predicted $ln\,(\zeta^{sp})$ is shown for varying d_f and l_m at $v_{ch} = 0.2\,\frac{m}{s}$ in (a) a non-woven geometry characterized by $\frac{\beta}{2} = 45°$ and (b) a woven geometry. In the considered range

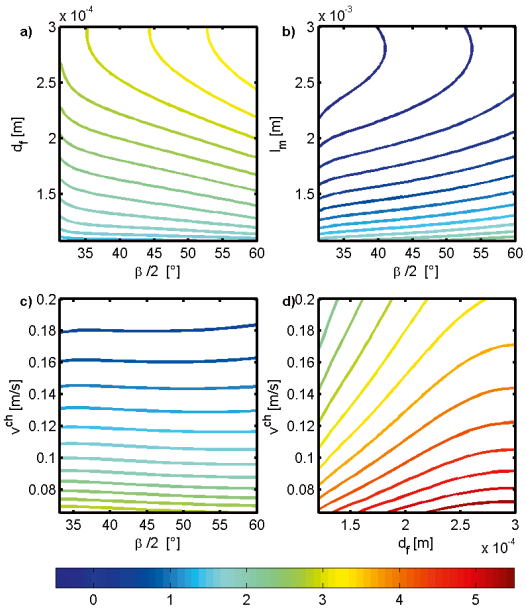

Figure 6.12: Predicted $ln\,(\zeta^{sp})$ for non-woven geometries with varying design parameters: (a) varying d_f and $\frac{\beta}{2}$ for $l_m = 1{\cdot}10^{-3}m$ and $v_{ch} = 0.2\,\frac{m}{s}$; (b) varying l_m and $\frac{\beta}{2}$ for $d_f = 1{\cdot}10^{-4}m$ and $v_{ch} = 0.2\,\frac{m}{s}$; (c) varying v_{ch} and $\frac{\beta}{2}$ for $d_f = 1 \cdot 10^{-4}m$ and $l_m = 1 \cdot 10^{-3}m$ and (d) varying v_{ch} and d_f for $\frac{\beta}{2} = 45°$ and $l_m = 1 \cdot 10^{-3}m$.

of design parameters, the pressure drop in non-woven geometries is significantly lower compared to the corresponding woven geometries. A common characteristic is found in the decreasing sensitivity of $ln\,(\zeta^{sp})$ with respect to both design parameters with increasing d_f and l_m. However, the total variation of $ln\,(\zeta^{sp})$ is significantly higher for the non-woven spacer configuration.

6.5 Summary and Discussion

In this chapter a new LBM-based simulation tool has been used to systematically study the pressure drop in woven and non-woven spacer structures. The LBM prediction has been evaluated using data from experiments with both an ED membrane module and a tailored test-cell. In this comparison a good agreement was found between the experiments and the LBM prediction. The validated LBM has been successfully used as a predictive tool to investigate the hydrodynamics in a large number of simulations in a reasonable time-frame.

Predictive models for the friction coefficient of the spacer have been identified by generalizing

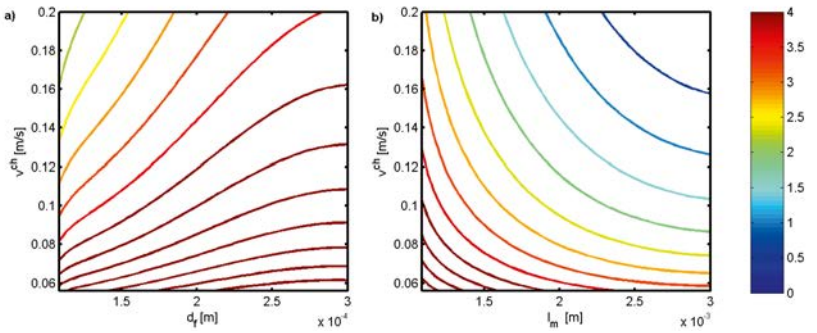

Figure 6.13: Predicted $ln\,(\zeta^{sp})$ for a woven geometry with (a) varying d_f and v_{ch} for $l_m = 1 \cdot 10^{-3} m$ and (b) with varying l_m and v_{ch} for $l_m = 3 \cdot 10^{-4} m$.

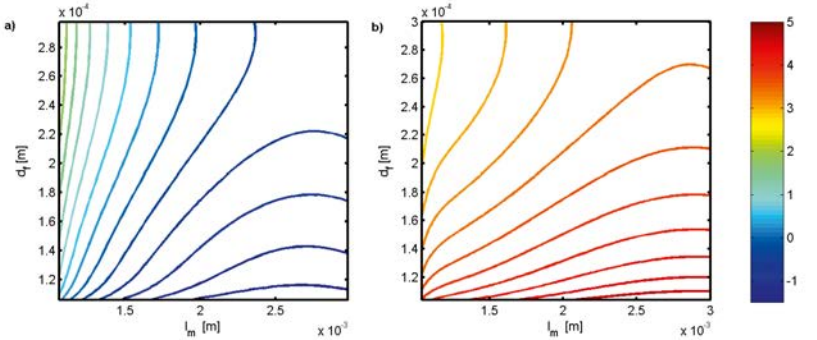

Figure 6.14: Predicted $ln\,(\zeta^{sp})$ for varying d_f and l_m in a (a) non-woven and (b) woven spacer with $\frac{\beta}{2} = 45°$ for $v_{ch} = 0.2\,\frac{m}{s}$.

the commonly used model structures to include the dependence on the design parameters by additional functional relations. Here, a systematic work flow has been used for the identification of an adequate generalized model structure and the iterative model refinement on the basis of DOE techniques. The developed work flow has proven as an effective tool to handle the complexity arising from the multi-dimensional design space.

The identified models allow for the first time a thorough quantitative investigation of the pressure drop in the entire design space of the spacer geometries. Here, it gets explicit, that the dependence of the pressure drop on the design parameters partially shows strongly nonlinear patterns. Hence, the generalization of trends from a small number of CFD simulations has to be considered as problematic for a certain range of the design space. For both the non-woven

and woven geometries, the sensitivity of the friction factor with respect to the mean velocity in the channel v_{ch} and the filament thickness d_f is comparable for a wide range of the considered parameters. Compared to these factors, the sensitivity with respect to the design parameters β and l_m is significantly lower. As a general result of a comparison between non-woven and woven structures it is found that the pressure drop is significantly higher in the woven geometries.

The presented work flow effectively integrates detailed simulations and the identification of simplified models for the thorough quantitative exploitation of the design space. In future studies, the work flow can be applied to other design objectives in a straight forward manner. Such studies should include appropriate measures for the mean mass transport intensity, fouling potential and axial dispersion in the channel.

7 Concluding remarks

7.1 Summary

The electrodialysis process has been established in industry for several decades for the desalination or concentration of liquid electrolytes. The development of more cost- and energy-efficient process designs is hampered by the limited insight into the underlying transport phenomena. This limited insight is specifically pronounced for innovative process concepts operated in a transient mode and comes along with a severe lack of reliable dynamic process models. The development of novel dynamic models in a systematic model development process is the focus of this work. By this means, the work makes important contributions towards both the model-based analysis of the underlying transport mechanisms and the model-based optimization of process designs in industrial applications.

As a basis for the model development, Chapter 2 presents results of an experimental study aiming at a first characterization of the process behavior. This includes the assessment of the sensitivities with respect to operational and design parameters. In contrast to prior work, the experimental sensitivity analysis provides coherent sensitivity information with respect to all degrees of freedom and includes the sensitivities of the process dynamics. The dynamic process behavior was further analyzed in additional experiments operated with either a transient or pulsed applied current. These experiments aimed at the identification of the temporal scales and the characteristic shape of the dynamic response to a stepwise increase of the applied current. These results significantly extend the current knowledge concerning the current-voltage behavior of entire ED systems, which at present relies on a considerable amount of experiments single-membrane test cells only.

Based on the experimental findings, it is possible to identify a set of specific requirements for an accurate model-based description of the process. One important requirement emerged in the form of a detailed mechanistic description of the coupled charge and mass transport in the membrane-electrolyte system. The detailed description is important to accurately describe the substantial sensitivity of the current-voltage behavior with respect to the concentrations of the ionic species. By this means, the model development focused on the derivation of a transport model on the basis of the mechanistic Maxwell-Stefan approach coupled with the well-known electroneutrality condition. This system was successfully applied in an ED process model by Kraaijeveld et al. (1995) and Visser (2001). However, their model was strongly simplified by restricting the description of the transport to one spatial coordinate and a pseudo-stationary scenario. Both aspects prevent the application of the model for the description of ED processes

operated in a transient mode.

In this context, a specific focus of this work is on the development of a generalized dynamic three-dimensional transport model. This transport model constitutes a PDAE system of which it is well-known that the mathematical characterization and the identification of consistent initial and boundary conditions is challenging and sparsely investigated. Hence, as a second important prerequisite for the development of a process model, Chapter 3 is devoted to the analysis and characterization of general detailed transport models in the form of PDAE systems. Here, it was possible to develop a new systematic procedure for the index analysis and reduction of PDAE systems. For the first time, it generalizes effective methods for the index reduction of DAE (Asbjørnsen and Fjeld, 1970, Moe, 1995) to the case of distributed PDAE systems. During the derivation of the method it was demonstrated that for the development of a well-posed ionic transport model, even for the simplified scenario of an infinitely diluted electrolyte, the analysis and reformulation are essential.

The procedure for the index analysis and reduction was successfully applied in Chapter 4 to derive the generalized transport model on the basis of the Maxwell-Stefan approach and the well-known electroneutrality condition. In this process it is found that the electroneutrality condition induces high index behavior with respect to time and the spatial coordinates. This finding was not observed in prior works and can help to explain numerous difficulties observed in the context of the numerical solution of ionic mass transfer models for the first time. The corresponding index reduction reveals hidden constraints, which can be interpreted as the stationary charge balance and a purely algebraic relation corresponding to a generalization of Ohm's law. The derivation of these relations contributes significantly to a better understanding of the mechanisms of the electro-neutral transport of ions. The final PDAE model is characterized by differential indices of one and allows for both the identification of consistent initial and boundary conditions and an efficient numerical treatment with standard methods.

The detailed transport models developed in Chapter 5 provide the basis for the development of a dynamic ED process model. The process model describes the local phenomena in the membranes and flow channels in two spatial coordinates in a thoroughly dynamic manner. By this means, it overcomes the limitations of the transport models developed by Kraaijeveld et al. (1995) and Visser (2001) and allows the mechanistic simulation of ED processes operated in a dynamic model for the first time. In this context it was demonstrated that the model can provide important insight into the underlying transport phenomena. The model prediction yields in particular information concerning the temporal evolution of transport resistances in the distinct process components and the underlying mechanisms of multi-salt transport in a pulsed applied field. The latter is of specific relevance since these mechanisms are not entirely understood and were not assessable in prior purely experimental studies.

In a comparison with data from the experiments presented in Chapter 2 the model prediction shows a good qualitative agreement. In particular, the sensitivities with respect to operational parameters, the temporal scales and the characteristic shape of the dynamic response to a pulse in the applied current or voltage are reproduced nicely. Hence, the mechanisms depicted in the model

are apparently in accordance with the most important mechanism governing the dynamic process behavior. In a strictly quantitative sense the model shows in parts significant deviations from the experimental data, which is likely to result from the rough parametrization of the membrane and electrode models with parameter values from literature. However, a potential additional cause of the deviations might be found in the application of the commonly used strongly simplified film-theory model for the approximation of the complex hydrodynamics in the flow channels.

The uncertainty resulting from the use of the film-theory model and the associated missing resolution of the spacer geometry motivated the further extension of the considered transport models in Chapter 6. Here, recent research activities are summarized aiming at the development of a novel software tool allowing the integrated simulation of the complex hydrodynamics and ionic mass transport in large-scale systems on high performance compute clusters. In this work it is shown that the hydrodynamic conditions predicted with a novel single species LBM approach is in good accordance with experimental results from both a single spacer test cell and an entire module.

Further, it is demonstrated that the validated LBM solver can be successfully applied to simulate the hydrodynamics in the spacer-filled flow channels by exploiting the massive parallel structure of high performance computers. These simulations result in a large amount of information concerning the local hydrodynamics in arbitrary complex spacer geometries in a straightforward manner. For the efficient implementation of this local information in an industrial design process, a systematic work-flow is presented yielding predictive algebraic models for important performance measures in the entire space spanned by the design parameter of a spacer structure. The novel work flow is based on optimization-based methods for model identification and the design of experiments. With these methods it was possible to identify predictive pressure drop models for arbitrary non-woven or woven spacer geometries for the first time in a wide range of design parameters.

7.2 Outlook

The experimental analysis in Chapter 2 provided important information for a first assessment of the dynamic process behavior and the systematic model development. In future work, the experiments should be more closely integrated with the refinement of the developed models. The systematic evaluation of the entire space spanned by the large number of operational parameters remains as a major challenge. As demonstrated in Chapter 6, this task can be effectively supported by model-based methods for the optimal design of experiments. The experimental investigation of ED processes operated in a dynamic mode should be expanded to widen the range of considered pulse-rates and dynamic input trajectories.

It has been demonstrated that the method for the procedural index analysis and reduction developed in this work constitutes a good basis for the systematic derivation of large and strongly coupled PDAE models. However, it only provides limited information concerning the consistent specification of boundary conditions. Additional information has been generated in this work by the derivation of a reduced system of second order PDE. However, this has been time-consuming

and the resulting information is specific for the considered transport models. Future work should address the development of methods supporting the consistent specification of boundary conditions for general PDAE.

A major limitation for the application of the developed process model results from its rough parametrization and the corresponding uncertainty in the model prediction. Hence, the focus of future work should be directed at the identification of reliable model parameters and the evaluation of the used model structures. For this purpose generic optimization-based methods are applicable as the developed model, after discretization of the spatial coordinates, reduces to an index-one DAE system. However, certain effort should be directed in the derivation of analytical derivatives of the model states to improve the convergence in the optimization.

Of particular importance for the parameter estimation is the question in which way the integral measurement data from the experiments at the lab-scale ED plant can be supplemented by significantly more detailed experimental data from tailored experiments or improved measurement devices allowing a high spatio-temporal resolution of the transport phenomena. This is an important prerequisite to provide sufficient information for a unique identification of all model parameters and a thorough evaluation of the model structure. Certainly, the use of dynamically operated experiments will enrich the information content of the data. In this context it may be interesting to derive dynamic input trajectories with model-based DOE methods maximizing the information content of the resulting data. Further, it should be evaluated to what extent the model can be used to support the evaluation of experimental data from impedance spectroscopic (Dlugolecki, 2009) and chronopotentiometric (Krol, 1999) or chronoamperometric (Moya and Sistat, 2013) experiments.

The evaluation of certain modeling assumptions, e.g., resulting from the film-theory approach, can also be supported by the generalized transport models introduced in Chapter 6. In this context, future work should include a thorough comparison between the model predictions of the simplified transport model used in the process model and the generalized transport model based on the LBM. The work flow for the identification of simple algebraic models from detailed simulation results can be used for the investigation of additional design objectives. Of major importance are here, next to the pressure drop considered in this work, the shear stress rate at the membrane surface and the mass transfer rates. A model-based description of all these design objectives in the entire design space would allow the design of a tailored spacer geometry for a specific application in an industrial engineering process.

A major task remains in the further development and the thorough analysis of the integrated model for the description of the ionic mass transport and the hydrodynamics. The efficient use of extensive computational resources in the developed software tool APES (Masilamani, 2012, Roller et al., 2012) provides the possibility to thoroughly investigate the phenomena in large-scale systems or with a very high local resolution. This will constitute a further important step towards a rigorous ED process model including all mayor transport mechanisms introduced in Chapter 1. Certain aspects of these works will be addressed in the further development of the software tool by Roller et al. (2012) and Masilamani (2012).

The application in model-based design and control studies should be considered as the final objective for the further refinement of the models. Of particular interest for the improvement of the economic performance of industrial ED processes would be the integration of the experiments with the model-based optimization of the used control trajectories. The control system of the lab-scale ED plant developed in the context of this work can be easily extended for this purpose. Further, thanks to the representation of the models in index-one PDAE systems, established methods for the generation of the optimized control trajectories should be readily applicable. A specific potential for model-based design studies can be seen for ED systems processing complex electrolyte solutions. Here, the general formulation of the developed process model supports the investigation of innovative processes in new application areas. One example may be the selective removal of specific ionic species with ED operated with a pulsed applied current.

Appendices

A Geometrical properties and reproducibility of the experiments

This chapter provides additional information concerning the geometrical properties of the lab-scale ED plant and the measurement error in the experiments. Section A.1 provides the geometric properties of the lab-scale ED plant used in the experiments in Chaper 2. The repeatability of the experiments is discussed in Section A.2. Sections A.3 and A.4 give an overview of the conducted current-voltage and batch desalination experiments and summarize the specific experimental conditions.

A.1 Geometric properties of the lab-scale ED plant

Table A.1 summarizes the geometric properties of the ED stack $ED-200$ (PCCell GmbH, Germany) and the Neosepta CMX and AMX membranes (Tokuyama Co., Japan) used in the experiments in Chapter 2. The geometric properties of the used woven spacers A and B both from PCCELL GmbH (Germany) are given in Table A.2. The geometrical properties are further used in Chapter 5 to parametrize the ED process model for the comparison with the experimental data.

Table A.1: Geometric properties of the ED stack and ion-exchange membranes.

$l_{st}[m]$	$d_{st}[m]$	$l_{ch}[m]$	$d_{ch}[m]$	$h_{CEM}[m]$	$h_{AEM}[m]$
0.2	0.1	0.18	0.09	$1.9 \cdot 10^{-4}$	$1.8 \cdot 10^{-4}$

Table A.2: Geometric properties of spacers used in the experiments.

	$d_f[m]$	l_m [m]	β [°]	α[°]	ϵ_{sp} [-]
spacer A	$2 \cdot 10^{-4}$	$6.5 \cdot 10^{-4}$	90	0	0.61
spacer B	$2.5 \cdot 10^{-4}$	$9 \cdot 10^{-4}$	90	0	0.55

A.2 Repeatability and measurement error

The repeatability of the experiments has been evaluated in a series of experiments. The results of this analysis are presented in Section A.2.1 for desalination experiments of $NaCl$ solution

operated with pulsed currents. Section A.2.2 presents the results for desalination experiments of $NaCl - Na_2SO_4$ solution operated in constant current mode. The repeatability of the current voltage experiments is discussed in Section A.2.3.

As a measure for the repeatability in dynamic experiments with with n_{mp} measurement points in time, the relative standard deviation, or coefficient of variation, CV is used given by

$$CV\left(t_i\right) = \frac{\sigma\left(t_i\right)}{\mu\left(t_i\right)}, \quad i = 1, ..., n_{mp} \tag{A.1}$$

with $\sigma\left(t_i\right)$ as the standard deviation which is defined for the measurements $\tilde{x}_j(t_i)$ in n_{exp} distinct experiments as:

$$\sigma\left(t_i\right) = \sqrt{\frac{1}{n_{exp}} \sum_{j=1}^{n_{exp}} \left(\tilde{x}_j(t_i) - \mu_i(t_i)\right)}, \quad i = 1, ..., n_{mp}, \tag{A.2}$$

and with $\mu\left(t_i\right)$ as the arithmetic mean given by

$$\mu\left(t_i\right) = \frac{1}{n_{exp}} \sum_{j=1}^{n_{exp}} \tilde{x}_j(t_i), \quad i = 1, ..., n_{mp}. \tag{A.3}$$

A.2.1 Pulsed current

Fig. A.1 shows the profiles of the salt concentration c_{NaCl} (a), the voltage difference U (b) and the voltage difference U in the interval $t = 1000...1100s$ for the experiments 1 - 3 in Table A.3 operated with pulsed current and identical degrees of freedom. The corresponding CV profiles are shown in Figs. A.1 b, d and f. The c_{NaCl} profiles show a very good repeatability with maximal and mean CV of $CV_{max} = 0.04$ and $CV_{mean} = 0.01$, respectively. The measured U profiles show mostly an adequate repeatability characterized by $CV_{mean} = 0.02$. However, it is found that the profiles in parts significantly deviate resulting in a maximal value of $CV_{max} = 0.54$. The regions with a strongly increasing deviation are located in the beginning and the end of the applied current pulse (cf. Fig. A.1 e and f) and are restricted to a duration of $1 - 2\,s$.

Table A.3: Experimental conditions of $NaCl$ desalination experiments for the evaluation of the repeatability.

no.	n_{cells}	spacer	$c_{NaCl}\left(t_0\right)$ $\left[\frac{mol}{m^3}\right]$	$c_{NaCl}\left(t_f\right)$ $\left[\frac{mol}{m^3}\right]$	Q_{1002} $10^{-6}\left[\frac{m^3}{s}\right]$	Q_{2002} $10^{-6}\left[\frac{m^3}{s}\right]$	Δp $10^4\ [Pa]$
1	14	A	97.57	26.52	24.87	24.96	2.146
2	14	A	95.39	26.52	24.87	24.96	2.209
3	14	A	95.36	26.53	24.87	24.93	2.257

Fig. A.4 shows the coefficient of variation CV for the desalination time, total energy demand, energy demand of the electrodes and the energy demand of the pumps for the three experiments 1-3. A good repeatability is found characterized by CV in the range 0.02 and 0.04.

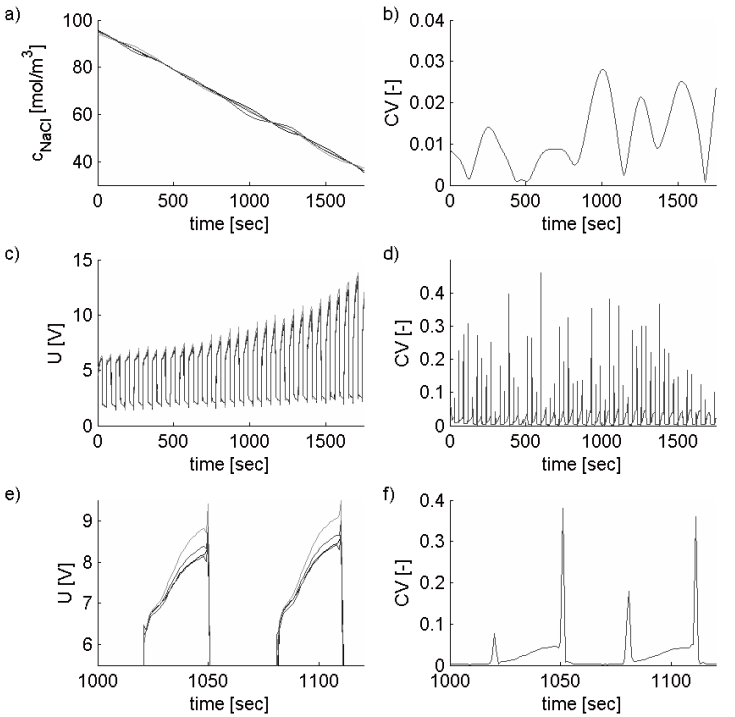

Figure A.1: Profiles of measured a) c_{NaCl}, b) U and c) U in the interval $t \in [1000, 1100]$ s with corresponding CV (b, d and f) for three pulsed current experiments.

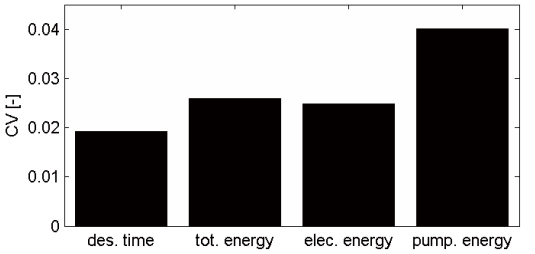

Figure A.2: CV for the desalination time, total energy demand, energy demand of the electrodes and the energy demand of the pumps for three pulsed current experiments.

A.2.2 Mixture experiments

The profiles of the conductivity κ, voltage difference U, species concentrations of Na^+, Cl^- and SO_4^{2-} ions of experiments 1 and 2 in Table A.4 are shown in Fig. A.3 a, c and e. Fig. A.3 g shows the concentration ratio $\frac{c_{Cl^-}}{c_{SO_4^{2-}}}$ measured in the two experiments. The corresponding CV are shown in Fig. A.3 b, d ,f and h. A very small deviation is found for the measured conductivity profiles resulting in $CV_{max} = 0.04$. Similarly the measured U is in good agreement characterized by $CV_{max} = 0.06$. Here, the CV profile shows three distinct peaks which can be related to the points in time where the $5\,ml$ samples have been drawn for the ex-situ analysis of the species concentrations. The minimal and maximal CV for the ratio of Cl^- and SO_4^{2-} is characterized by $CV_{max} = 0.003$ and $CV_{max} = 0.03$.

Table A.4: Experimental conditions of $NaCl - Na_2SO_4$ desalination experiments for the evaluation of the reproducability of the experiments.

no.	n_{cells}	spacer	$\kappa\,(t_0)$ $\left[\frac{mS}{cm}\right]$	$\kappa\,(t_f)$ $\left[\frac{mS}{cm}\right]$	Q_{1002} $10^{-6}\left[\frac{m^3}{s}\right]$	Q_{2002} $10^{-6}\left[\frac{m^3}{s}\right]$	Δp $10^4\,[Pa]$
1	14	A	14.86	1.044	24.16	24.16	2.111
2	14	A	14.83	1.045	24.05	24.06	2.136

Fig. A.4 shows the coefficient of variation CV for the desalination time, total energy demand, energy demand of the electrodes and the energy demand of the pumps for the two multi-salt desalination experiments. A good repeatability is found characterized by CV in between 0.005 and 0.03.

A.2.3 Current-voltage experiments

Fig. A.5 a shows the measured current profiles I for the experiments 1 and 2 in Table A.5 operated with $Q = 2.5 \cdot 10^{-5}\frac{m^3}{s}$. The profiles of measured current I for experiments 3 and 4 in Table A.5 operated with $Q = 1.6 \cdot 10^{-5}\frac{m^3}{s}$ are shown in Fig. A.5 c. The corresponding CV profiles are shown in Fig. A.5 b and d. The repeatability of the experiment is characterized by $CV < 0.09$ except for distinct peaks ranging up to $CV_{max} = 0.2$. These peaks are located at the discontinuous increase of the applied current and are restricted to 1 - 2 s. Hence, an adequate repeatability of the current voltage experiments is found.

A.3 Overview current-voltage experiments

Tables A.6 and A.7 provide an overview of the experimental conditions in the conducted current-voltage experiments with $NaCl{-}Na_2SO_4$ and $NaCl$ solution presented in Chapter 2, respectively.

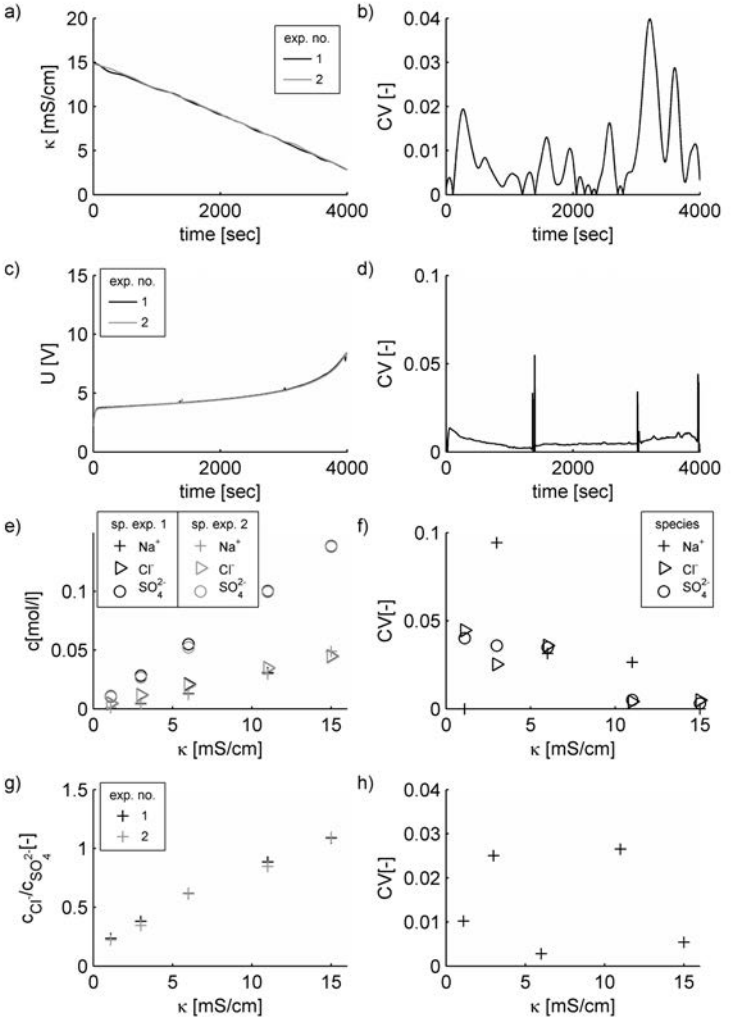

Figure A.3: Profiles of a) conductivity κ, b) potential difference U, e) concentrations of Na^+, Cl^- and SO_4^{2-} ions and g) the concentration ratio of Cl^- and SO_4^{2-} for two identical desalination experiments with $NaCl - Na_2SO_4$ solution. The corresponding CV are shown in b), d), f) and h).

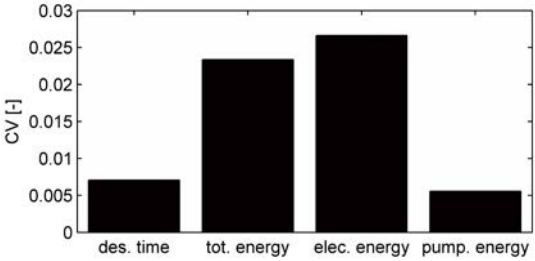

Figure A.4: CV for the desalination time, total energy demand, energy demand of the electrodes and the energy demand of the pumps for two desalination experiments with $NaCl - Na_2SO_4$ solution.

Table A.5: Experimental conditions of current-voltage experiments with $NaCl$ solution used for the reproducability analysis.

no.	n_{cells}	spacer	c_{NaCl} $\left[\frac{mol}{m^3}\right]$	Q_{2002} 10^{-6} $\left[\frac{m^3}{s}\right]$	Δp 10^4 $[Pa]$
1	14	A	22.16	25.06	1.34
2	14	A	20.29	25.35	1.858
3	14	A	20.64	16.77	1.453
4	14	A	19.88	16.68	1.376

Table A.6: Experimental conditions of current-voltage experiments with $NaCl - Na_2SO_4$ solution.

no.	n_{cells}	spacer	c_{Na+} $\left[\frac{mol}{m^3}\right]$	c_{Cl-} $\left[\frac{mol}{m^3}\right]$	$c_{SO_4^{2-}}$ $\left[\frac{mol}{m^3}\right]$	Q_{2002} 10^{-6} $\left[\frac{m^3}{s}\right]$	Δp 10^4 $[Pa]$
1	14	A	42.53	20.87	10.82	25.11	1.503
1	14	A	42.53	20.87	10.82	16.36	1.079
1	14	A	42.53	20.87	10.82	8.288	0.7128

A.4 Desalination experiments

Tables A.8 and A.9 provide an overview of the experimental conditions in the conducted current-voltage experiments with $NaCl-Na_2SO_4$ and $NaCl$ solution presented in Chapter 2, respectively.

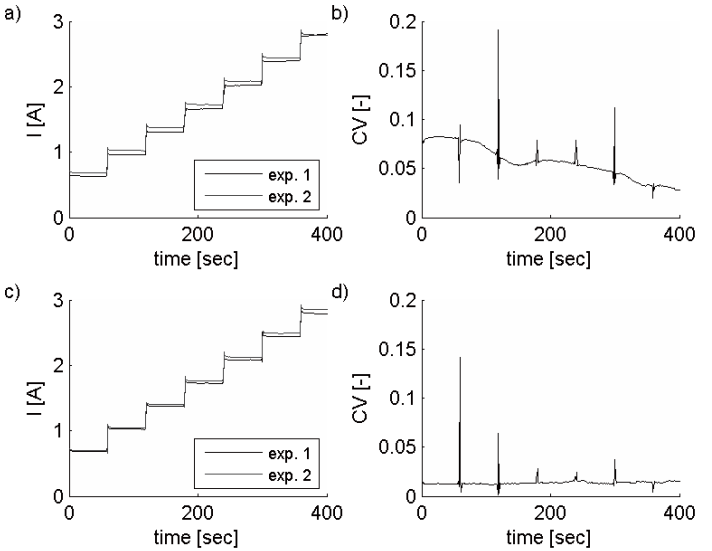

Figure A.5: Profiles of measured current I (a and c) and corresponding CV (b and c) for current voltage experiments with $Q = 2.5 \cdot 10^{-5} \frac{m^3}{s}$ and $Q = 1.6 \cdot 10^{-5} \frac{m^3}{s}$.

Table A.7: Experimental conditions of current-voltage experiments with $NaCl$ solution.

no.	n_{cells}	spacer	c_{NaCl} $\left[\frac{mol}{m^3}\right]$	Q_{2002} 10^{-6} $\left[\frac{m^3}{s}\right]$	Δp 10^4 $[Pa]$
1	14	A	192	25.35	1.858
2	14	A	96	25.13	1.269
3	14	A	48	25.03	1.302
4	14	A	192	8.227	0.8015
5	14	A	96	8.371	0.7339
6	14	A	48	8.274	0.7666
7	14	A	192	16.68	1.376
8	14	A	96	16.98	1.1
9	14	A	48	16.72	1.161
10	10	A	192	17.97	1.565
11	6	A	192	10.64	1.443

Table A.8: Experimental conditions of $NaCl - Na_2SO_4$ desalination experiments

no.	n_{cells}	spacer	$\kappa\,(t_0)$ $\left[\frac{mS}{cm}\right]$	$\kappa\,(t_f)$ $\left[\frac{mS}{cm}\right]$	Q_{1002} $10^{-6}\left[\frac{m^3}{s}\right]$	Q_{2002} $10^{-6}\left[\frac{m^3}{s}\right]$	Δp $10^4\,[Pa]$
1	14	A	14.83	2.81	24.05	24.06	2.135
2	14	A	15.08	2.82	24.24	24.26	2.129
3	14	A	15.01	2.81	24.1	24.03	2.082

Table A.9: Experimental conditions of $NaCl$ desalination experiments

no.	n_{cells}	spacer	$c_{NaCl}\,(t_0)$ $\left[\frac{mol}{m^3}\right]$	$c_{NaCl}\,(t_f)$ $\left[\frac{mol}{m^3}\right]$	Q_{1002} $10^{-6}\left[\frac{m^3}{s}\right]$	Q_{2002} $10^{-6}\left[\frac{m^3}{s}\right]$	Δp $10^4\,[Pa]$
1	14	A	192	35.01	24.87	25.09	2.124
2	14	A	192	34.96	24.95	25.07	1.41
3	14	A	192	35	25.12	25.03	2.154
4	14	B	96	34.93	25.17	25.12	2.232
5	14	B	96	35	8.289	8.29	0.7562
6	14	B	96	26.55	25.17	25.13	2.23
7	14	B	96	26.54	25.03	25.16	2.306
8	14	A	96	29.97	8.28	8.266	0.9257
9	14	B	96	30	8.29	8.297	0.9191
10	14	B	96	34.5	8.309	8.308	0.7573
11	14	B	96	36.33	8.289	8.29	0.7562
12	14	A	96	35.03	24.9	24.9	2.17
13	14	A	96	35.01	24.88	24.88	2.146
14	14	A	96	35.01	24.91	24.91	2.187
15	14	A	96	40.02	24.85	24.85	2.252
16	14	A	96	40.03	24.87	24.87	2.196
17	14	A	96	40.02	25.14	25.14	2.296
18	14	A	96	35.47	24.87	24.87	2.257
19	14	A	96	34.1	8.27	8.27	0.9026
20	14	A	96	34.56	24.91	24.91	2.187
21	14	B	96	33.91	25.04	25.04	2.084
22	14	A	96	20.99	8.257	8.313	0.9115

B Physico-chemical property models for electrolytes

This chapter provides additional information concerning the physico-chemical property models used for the development of rigorous transport models in Chapter 4. Sections B.1 and B.2 summarize the relations between the velocities and activity coefficients defined for different reference frames, respectively. The model for the density and the Maxwell-Stefan diffusivities in a multi-species electrolyte solution is presented in Sections B.3 and B.4. Section B.5 provides a summary of the model parameters for the Bromley model, the Tafel equations and the Maxwell-Stefan diffusion coefficients in the membranes used in Chapter 5 to parametrize the ED process model.

B.1 Conversion of different reference velocities

The total mass flux density of species k comprising a diffusive and convective component is expressed by

$$\mathbf{J}_k^t(\mathbf{x},t) = c_k(\mathbf{x},t)\; M_k\, \mathbf{v}^{\alpha}(\mathbf{x},t) + \mathbf{J}_k^{\alpha}(\mathbf{x},t)\; M_k, \qquad k = 1,...,n, \tag{B.1}$$

for a reference velocity $\mathbf{v}^{\alpha}(\mathbf{x},t)$. The total mass flux density is independent of the specified reference velocity. Thus, equating Eq. (B.1) for the barycentric and volume-averaged reference frame yields

$$c_k(\mathbf{x},t)\; M_k\, \mathbf{v}^{bar}(\mathbf{x},t) + M_k\, \mathbf{J}_k^{bar}(\mathbf{x},t) = c_k(\mathbf{x},t)\; M_k\, \mathbf{v}^{va}(\mathbf{x},t) + M_k\, \mathbf{J}_k(\mathbf{x},t), \quad k = 1,...,n. \tag{B.2}$$

Here, $\mathbf{J}_k^{bar}(\mathbf{x},t)$ is the molar diffusive flux density relative to convective flow with the barycentric reference velocity $\mathbf{v}^{bar}(\mathbf{x},t)$. By summing up Eq. (B.2) for all $k \in S$ and using

$$0 = \sum_{j=1}^{n} M_k\, \mathbf{J}_k^{bar}(\mathbf{x},t) \tag{B.3}$$

the baricentric velocity $\mathbf{v}^{bar}(\mathbf{x},t)$ is expressed as

$$\mathbf{v}^{bar}(\mathbf{x},t) = \mathbf{v}^{va}(\mathbf{x},t) + \frac{\sum_{j=1}^{n} \mathbf{J}_j(\mathbf{x},t)\; M_j}{\sum_{j=1}^{n} c_j(\mathbf{x},t)\; M_j}. \tag{B.4}$$

B.2 Conversion of activity coefficients

The activity coefficients $\tilde{\gamma}_k(\mathbf{x},t)$ predicted by the eNRTL model (Chen et al., 1982) for mole fraction based reference frame are converted into molar concentration-based activity coefficients

$\gamma_k(\mathbf{x},t)$. A correlation between these quantities can be derived by considering that the chemical potential of any species k is independent of the composition measure (Robinson and Stokes, 2002), i.e.,

$$\mu_k^{0,c} + RT\,ln\left(\gamma_k(\mathbf{x},t)\; c_k(\mathbf{x},t)\right) = \mu_k^{0,\chi} + RT\,ln\left(\tilde{\gamma}_k(\mathbf{x},t)\; \chi_k(\mathbf{x},t)\right), \qquad k = 1,...,n. \tag{B.5}$$

Here, $\mu_k^{0,c}$ and $\mu_k^{0,\chi}$ are the standard chemical potentials in the concentration- and mole fraction-based description, respectively. The introduction of the definition of the mole fractions $\chi_k(\mathbf{x},t) = \frac{c_k(\mathbf{x},t)}{c_T(\mathbf{x},t)}$, $k = 1,...,n$, into (B.5) and reformulation yields

$$ln\left(\gamma_k(\mathbf{x},t)\right) = ln\left(\frac{1}{c_T(\mathbf{x},t)}\right) + ln\left(\tilde{\gamma}_k(\mathbf{x},t)\right) + \frac{\mu_k^{0,\chi} - \mu_k^{0,c}}{RT}, \qquad k = 1,...,n. \tag{B.6}$$

To reformulate the last term on the right hand side of (B.6), the fact is used that the definition of the reference frame for the mole fraction-based activity coefficients implies for $\chi_k(\mathbf{x},t) \to 0$ that $\tilde{\gamma}_k(\mathbf{x},t) \to 1$. Analogously for the concentration-based activity coefficients $c_k(\mathbf{x},t) \to 0$ implies $\gamma_k(\mathbf{x},t) \to 1$. Thus, in the limit of infinite dilution (B.6) defines

$$\frac{\mu_k^{0,\chi} - \mu_k^{0,c}}{RT} = -ln\left(\frac{1}{c_T(\mathbf{x},t)|_{c_k(\mathbf{x},t)=0}}\right), \qquad k = 1,...,n. \tag{B.7}$$

Eq. (B.7) is introduced into (B.6) yielding the correlation

$$ln\left(\gamma_k(\mathbf{x},t)\right) = ln\left(\frac{c_T(\mathbf{x},t)|_{c_k(\mathbf{x},t)=0}}{c_T(\mathbf{x},t)}\right) + ln\left(\tilde{\gamma}_k(\mathbf{x},t)\right), \qquad k = 1,...,n. \tag{B.8}$$

B.3 Multi-component density model

For the description of the total molar density in an aqueous electrolyte solution, Mathias (2004) proposed the correlation

$$\frac{1}{c_T(\mathbf{x},t)} = \chi_w(\mathbf{x},t)\,\tilde{V}_w(\mathbf{x},t) + \chi_e(\mathbf{x},t)\,V_e(\mathbf{x},t) \tag{B.9}$$

where, $\chi_w(\mathbf{x},t) = \frac{c_w(\mathbf{x},t)}{c_T(\mathbf{x},t)}$ and $\chi_e(\mathbf{x},t) = 1 - \chi_w(\mathbf{x},t)$ are the mole fractions of water and total electrolyte in the solution. The quantities $\tilde{V}_w(\mathbf{x},t)$ and $V_e(\mathbf{x},t)$ correspond to the molar volumes of water and total electrolyte in the solution, respectively. $\tilde{V}_w(\mathbf{x},t)$ is approximated by the partial molar volume of pure water and thus only a function of temperature and pressure. The molar volume of electrolyte is expressed as (Mathias, 2004)

$$V_e(\mathbf{x},t) = V_e^{\infty}(\mathbf{x},t) + \left(V_e^0(\mathbf{x},t) - V_e^{\infty}(\mathbf{x},t)\right)\,\chi_e(\mathbf{x},t), \tag{B.10}$$

with

$$V_e^{\infty}(\mathbf{x},t) = \sum_{\substack{j=1\\ j\neq w}}^{n} \chi_j(\mathbf{x},t)\;\tilde{V}_j + \sum_{\substack{j=1\\ j\neq w}}^{n}\sum_{\substack{k=1\\ k\neq w}}^{n} \chi_j(\mathbf{x},t)\;\chi_k(\mathbf{x},t)\;B_{j,k}(\mathbf{x},t), \tag{B.11}$$

$$B_{j,j} = 0, \qquad j = 1,...,n,\; j \neq w, \tag{B.12}$$

$$B_{j,k}(\mathbf{x},t) = B^0_{j,k} + \left(\frac{T-T_0}{t_0}\right) B^1_{j,k}, \qquad j,k = 1,...,n,\ j \neq k,\ j \neq w, \tag{B.13}$$

$$V^0_e(\mathbf{x},t) = \sum_{\substack{j=1 \\ j\neq w}}^{n} \chi_j(\mathbf{x},t)\ V^0_j + \sum_{\substack{j=1 \\ j\neq w}}^{n} \sum_{\substack{k=1 \\ k\neq w}}^{n} \chi_j(\mathbf{x},t)\ \chi_k(\mathbf{x},t)\ C_{j,k}(\mathbf{x},t), \tag{B.14}$$

$$C_{j,j} = 0, \qquad j = 1,...,n,\ j \neq w, \tag{B.15}$$

$$C_{j,k}(\mathbf{x},t) = C^0_{j,k} + \left(\frac{T-T_0}{t_0}\right) C^1_{j,k}, \qquad j,k = 1,...,n,\ j \neq k,\ j \neq w. \tag{B.16}$$

Here, $\chi_j(\mathbf{x},t),\ j = 1,...,n$, are the mole fractions, $\tilde{V}_j,\ j = 1,...,n,\ j \neq w$ is the infinite dilution partial molar volume and $V^0_j,\ j = 1,...,n,\ j \neq w$ is the pure molar volume of the ionic species at the reference temperature of $T_0 = 25°C$. The parameters $B^0_{j,k}$, $B^1_{j,k}$ and $C^0_{j,k}$, $C^1_{j,k}$ are symmetric binary coefficients accounting for the interactions of an ion pair jk (Mathias, 2004).

To decouple the ideal behavior, corresponding to the state of infinite dilution, from the concentration-dependent non-ideal excess contribution, the excess volume of the solution is introduced as (Djordjević et al., 1994, Rouquerol and Sabbah, 1977)

$$V^E(\mathbf{x},t) = \chi_e(\mathbf{x},t)\, V_e(\mathbf{x},t) - \sum_{\substack{j=1 \\ j\neq w}}^{n} \chi_j(\mathbf{x},t)\ \tilde{V}_j. \tag{B.17}$$

With this definition, Eq. (B.9) can be rewritten as

$$1 = \sum_{j=1}^{n} c_j(\mathbf{x},t)\ \tilde{V}_j + V^E(\mathbf{x},t)\ c_T(\mathbf{x},t). \tag{B.18}$$

B.4 Maxwell-Stefan diffusion coefficients for aqueous electrolyte solutions

On the basis of experimental data reported by Chapman (1968), Visser (2001) identified an empirical model for concentration-dependent Maxwell-Stefan diffusion coefficients of ionic species in an aqueous solution. The model is based on the relation

$$D_{ij} = p_1 + p_2 c_S + p_3 c_S^{1.5} + p_4 c_S^2 + p_5 \sqrt{c_S} \tag{B.19}$$

to express binary diffusion coefficients in a single-salt electrolyte with the concentration c_S. Parameter values for p_i, $i = 1,...,5$, are summarized in Table B.1 and B.2 for the salts $NaCl$ and Na_2SO_4, respectively. Eq. (B.19) is applicable at $T = 295.13\,K$ in a concentration range of $c_{NaCl} \in \left[0,\ 5000\ \frac{mol}{m^3}\right]$ and $c_{Na_2SO_4} \in \left[0,\ 1500\ \frac{mol}{m^3}\right]$.

The predicted single-salt diffusivities are also used to predict the Maxwell-Stefan diffusion coefficients in multi-salt electrolytes. In this generalization, major difficulties arise from the facts that (i) the concentration measure c_S is not unambiguously defined and (ii) multiple diffusivities are to be averaged by appropriate mixing rules. To overcome these problems, Visser (2001) proposes the following empirical relations for the diffusion coefficients of ion-ion and ion-water pairs.

Table B.1: Parameter values for p_i, $i = 1, ..., 5$, identified by Visser (2001) for aqueous $NaCl$ solution.

	p_1	p_2	p_3	p_4	p_5
D_{Na^+,Cl^-}	0	$8.02 \cdot 10^{-14}$	$-2.09 \cdot 10^{-16}$	$-7.03 \cdot 10^{-18}$	$2.18 \cdot 10^{-12}$
D_{Na^+,H_2O}	$1.34 \cdot 10^{-9}$	$-3.06 \cdot 10^{-14}$	$-3.91 \cdot 10^{-15}$	$3.77 \cdot 10^{-17}$	$-1.77 \cdot 10^{-12}$
D_{Cl^-,H_2O}	$2.04 \cdot 10^{-9}$	$-2.24 \cdot 10^{-13}$	$-3.79 \cdot 10^{-15}$	$3.78 \cdot 10^{-17}$	$8.32 \cdot 10^{-12}$

Table B.2: Parameter values for p_i, $i = 1, ..., 5$, identified by Visser (2001) for aqueous Na_2SO_4 solution.

	p_1	p_2	p_3	p_4	p_5
$D_{Na^+,SO_4^{2-}}$	0	$2.943 \cdot 10^{-14}$	$-5.839 \cdot 10^{-16}$	$-1.592 \cdot 10^{-19}$	$6.08 \cdot 10^{-13}$
D_{Na^+,H_2O}	$1.367 \cdot 10^{-9}$	$1.724 \cdot 10^{-12}$	$-6.571 \cdot 10^{-14}$	$6.18 \cdot 10^{-16}$	$2.698 \cdot 10^{-12}$
$D_{SO_4^{2-},H_2O}$	$1.079 \cdot 10^{-9}$	$1.125 \cdot 10^{-12}$	$-4.653 \cdot 10^{-14}$	$4.435 \cdot 10^{-16}$	$6.83 \cdot 10^{-12}$

B.4.1 MS coefficients of ion-ion pairs

In a mixture of two salts with a common anion A the interaction coefficient D_{C_1,C_2} for the two cationic species C_1 and C_2 is determined as

$$D_{C_1,C_2} = -\left(D_{C_1,A} D_{C_2,A}\right)^{\frac{1}{2}}, \tag{B.20}$$

where $D_{C_1,A}$ and $D_{C_2,A}$ are the binary coefficients of the corresponding single-salt electrolyte. It is important to note that the cation-cation diffusion coefficients predicted by Eq. (B.20) are negative, which is physically reasonable (cf. Kraaijeveld and Wesselingh (1993)).

Whereas Eq. (B.20) has been successfully applied to different systems with common cations (Miller, 1967, Visser, 2001), no reliable approach is available for mixtures of two salts with a common cation C and two distinct anions A_1 and A_2. To allow for the analysis of these systems with the models developed in this work, Eq. (B.20) is generalized in a straight-forward manner yielding

$$D_{A_1,A_2} = -\left(D_{A_1,C} D_{A_2,C}\right)^{\frac{1}{2}}. \tag{B.21}$$

For the calculation of the interaction coefficient for a cation C and an anion A in a multi-salt solution Visser (2001) directly evaluates Eq. (B.19) with parameters for the corresponding single-salt solution. In this evaluation the concentration measure is chosen as

$$c_S = \begin{cases} c_K, & \text{if } c_C > c_A, \\ c_A, & \text{if } c_A > c_C. \end{cases} \tag{B.22}$$

B.4.2 MS coefficients of ion-water pairs

For the calculation of the diffusion coefficients for cation-water pairs Visser (2001) proposes the relation

$$D_{C,H_2O} = \sum_{i=1}^{n_a} \frac{c_i}{\sum_{j=1}^{n_a} c_j} D^i_{C,H_2O}\left(IS\right). \tag{B.23}$$

Here, the sum accounts for a set of n_a anionic species in the system and the resulting n_a distinct binary diffusion coefficients $D^i_{C,H_2O}\left(IS\right)$, $i = 1, ..., n_a$. The binary coefficients are calculated from Eq. (B.19) by using the ionic strength

$$IS = \sum_{i=1}^{n} z_i^2 \, c_i. \tag{B.24}$$

as concentration measure. The coefficients for anion-water pairs are calculated with the analogous relation

$$D_{A,H_2O} = \sum_{i=1}^{n_c} \frac{c_i}{\sum_{j=1}^{n_c} c_j} D^i_{A,H_2O}\left(IS\right), \tag{B.25}$$

where n_c is the number of cationic species in the system and $D^i_{A,H_2O}\left(IS\right)$ are the distinct binary diffusion coefficients evaluated with $c_S = IS$.

B.5 Model parameters

Tables B.3 and B.5 summarize the Bromley interaction parameters and Maxwell-Stefan diffusion coefficients used to parametrize the IEM models. The parameters for the Tafel equations in the electrode models are given in Table B.4.

Table B.3: Bromley interaction parameters for the ion-exchange membranes as identified by (Visser, 2001). The parameters labeled by asterisks correspond to default values as no values have been reported.

parameter	unit	ref. Value
$C^{CEM}_{Na^+,Cl^-}$	$\left[\frac{mol}{kg}\right]$	-0.0271
$C^{CEM}_{Na^+,SO_4^{2-}}$	$\left[\frac{mol}{kg}\right]$	-0.0922
$C^{CEM}_{Na^+,m^-}$	$\left[\frac{mol}{kg}\right]$	0.2214
$C^{AEM}_{Na^+,Cl^-}$	$\left[\frac{mol}{kg}\right]$	*0.04
$C^{AEM}_{Na^+,SO_4^{2-}}$	$\left[\frac{mol}{kg}\right]$	*0.01
$C^{AEM}_{Cl^-,m^+}$	$\left[\frac{mol}{kg}\right]$	0.0636
$C^{AEM}_{SO_4^{2-},m^+}$	$\left[\frac{mol}{kg}\right]$	0.1631

Table B.4: Empirical parameters for the Tafel equations.

parameter	unit	reference	value
a^{anode}	$[V]$	Visser (2001)	0.5962
b^{anode}	$[V]$	Visser (2001)	0.0616
$a^{cathode}$	$[V]$	Hine (1985)	0.04
$b^{cathode}$	$[V]$	Hine (1985)	-0.03

Table B.5: Maxwell-Stefan diffusivities identified by Visser (2001) for Nafion 450 (DuPont, USA) cation exchange and ARA (Solvay, France) anion exchange membranes. The coefficients labeled by asterisks correspond to default values as no values have been reported.

parameter	unit	value
$D^{AEM}_{Na^+,Cl^-}$	$\left[\frac{m^2}{s}\right]$	$^*5.80 \cdot 10^{-11}$
$D^{AEM}_{Na^+,SO_4^{2-}}$	$\left[\frac{m^2}{s}\right]$	$^*2.87 \cdot 10^{-9}$
$D^{AEM}_{Na^+,m^-}$	$\left[\frac{m^2}{s}\right]$	$^*2.26 \cdot 10^{-11}$
$D^{AEM}_{Cl^-,m^-}$	$\left[\frac{m^2}{s}\right]$	$2.28 \cdot 10^{-11}$
$D^{AEM}_{SO_4^{2-},m^-}$	$\left[\frac{m^2}{s}\right]$	$3.13 \cdot 10^{-12}$
$D^{AEM}_{H_2O,m^-}$	$\left[\frac{m^2}{s}\right]$	$1.44 \cdot 10^{-10}$
$D^{AEM}_{Na^+,H_2O}$	$\left[\frac{m^2}{s}\right]$	$7.98 \cdot 10^{-11}$
$D^{AEM}_{Cl^-,H_2O}$	$\left[\frac{m^2}{s}\right]$	$2.39 \cdot 10^{-10}$
$D^{AEM}_{SO_4^{2-},H_2O}$	$\left[\frac{m^2}{s}\right]$	$4.33 \cdot 10^{-11}$
$D^{AEM}_{SO_4^{2-},Cl^-}$	$\left[\frac{m^2}{s}\right]$	$^*2.87 \cdot 10^{-9}$
$D^{CEM}_{Na^+,Cl^-}$	$\left[\frac{m^2}{s}\right]$	$5.80 \cdot 10^{-11}$
$D^{CEM}_{Na^+,SO_4^{2-}}$	$\left[\frac{m^2}{s}\right]$	$2.87 \cdot 10^{-9}$
$D^{CEM}_{Na^+,m^-}$	$\left[\frac{m^2}{s}\right]$	$2.26 \cdot 10^{-10}$
$D^{CEM}_{Cl^-,m^-}$	$\left[\frac{m^2}{s}\right]$	$1.69 \cdot 10^{-11}$
$D^{CEM}_{SO_4^{2-},m^-}$	$\left[\frac{m^2}{s}\right]$	$7.41 \cdot 10^{-12}$
$D^{CEM}_{H_2O,m^-}$	$\left[\frac{m^2}{s}\right]$	$7.92 \cdot 10^{-10}$
$D^{CEM}_{Na^+,H_2O}$	$\left[\frac{m^2}{s}\right]$	$5.14 \cdot 10^{-10}$
$D^{CEM}_{Cl^-,H_2O}$	$\left[\frac{m^2}{s}\right]$	$6.23 \cdot 10^{-10}$
$D^{CEM}_{SO_4^{2-},H_2O}$	$\left[\frac{m^2}{s}\right]$	$1.62 \cdot 10^{-10}$
$D^{CEM}_{SO_4^{2-},Cl^-}$	$\left[\frac{m^2}{s}\right]$	$^*2.87 \cdot 10^{-9}$

C Results of pressure drop model identification

This chapter provides additional information for the identification of the predictive pressure drop models in Chapter 6. Section C.1 summarizes the geometrical parameters of the spacer geometries used for the generation of the initial data set. The parameter estimates of the final models for woven and non-woven geometries are given in Section C.2. The distinct model structures used as a basis for the identification of a generalized pressure drop model are provided in Section C.3.

C.1 Geometric parameters of the spacer geometries in the basis data set

Table C.1: Geometric properties of non-woven spacers for the generation of the basis set of simulated pressure drop data.

geometry	$\frac{\beta}{2}$ [deg]	d_f $\left[10^{-4}\,m\right]$	l_m $\left[10^{-3}\,m\right]$
1	38.75	1.75	1.25
2	41.25	2.75	2.25
3	58.75	1.25	2.75
4	53.75	2.25	1.75
5	43.75	1.08	1.58
6	48.75	2.92	2.42
7	56.25	2.42	1.08
8	31.25	1.92	2.92
9	51.25	2.08	2.58
10	46.25	1.58	2.08
11	33.75	2.58	1.42
12	36.25	1.42	1.92
13	30	1	1
14	30	3	1.3
15	60	1	3
16	60	3	1
17	60	1	1

Table C.2: Geometric properties of woven spacers for the generation of the basis set of simulated pressure-drop data.

geometry	$d_f\ [10^{-4}\,m]$	$l_m\ [10^{-3}\,m]$
1	1.13	1.94
2	2.34	1.21
3	2.70	2.06
4	1.61	2.66
5	1	1
6	3	3
7	3	1
8	1	3
9	2	1
10	2	3
11	1	2
12	3	2
13	2	2

C.2 Parameter estimates for the final friction coefficient model for the non-woven and woven spacer

Table C.3: Parameter estimates $\mathbf{p}^*$ and confidence intervals θ of the final friction coefficient model for non-woven spacer geometries.

parameter no.	1	2	3	4	5	6	7
p_k^*	-0.14196	0.07487	-0.00078	0.82367	-0.41847	-0.01312	-0.36281
$\Delta\theta_k$	$9.43{\cdot}10^{-5}$	$1.16{\cdot}10^{-4}$	$9.94{\cdot}10^{-7}$	$1.16{\cdot}10^{-4}$	$1.45{\cdot}10^{-4}$	$1.84{\cdot}10^{-6}$	$1.12{\cdot}10^{-4}$

	8	9	10	11	12	13	14
	0.22844	0.00669	0.86565	-0.13454	-0.04451	0.08643	0.90875
	$1.39{\cdot}10^{-4}$	$1.69{\cdot}10^{-6}$	$6.67{\cdot}10^{-5}$	$4.71{\cdot}10^{-5}$	$7.66{\cdot}10^{-5}$	$4.91{\cdot}10^{-5}$	$5.10{\cdot}10^{-35}$

Table C.4: Parameter estimates $\mathbf{p}^*$ and confidence intervals θ of the final friction factor model for woven spacer geometries.

k	1	2	3	4	5
p_k^*	0.79880	-0.38254	-0.01358	-0.42319	0.24944
$\Delta\theta_k$	1.19E-04	9.28E-05	1.63E-06	1.23E-04	9.19E-05

	6	7	8	9	10
	0.00584	0.87022	-0.07353	0.10586	0.86482
	1.52E-06	5.13E-05	7.27E-05	5.45E-05	4.74E-05

C.3 Model candidates for the identification of a generalized pressure drop model

Table C.5: Model candidates for the generalized friction coefficient model.

no.	a) non-woven	b) woven
1	$n^{sp}(\mathbf{u}^{nw}) = p_1 \frac{\check{\beta}}{2} + p_2 \check{d}_f + p_3 \check{l}_m + p_4$ $m^{sp}(\mathbf{u}^{nw}) = p_5 \frac{\check{\beta}}{2} + p_6 \check{d}_f + p_7 \check{l}_m + p_8$	$n^{ch}(\mathbf{u}^{w}) = p_1 \check{d}_f + p_2 \check{l}_m + p_3$ $m^{ch}(\mathbf{u}^{w}) = p_4 \check{d}_f + p_5 \check{l}_m + p_6$
2	$n^{sp}(\mathbf{u}^{nw}) = p_1 \frac{\check{\beta}}{2} + p_3 \check{d}_f + p_5 \check{l}_m + p_2 \check{d}_f^2 + p_4 \check{l}_m^2 + p_6$ $m^{sp}(\mathbf{u}^{nw}) = p_7 \frac{\check{\beta}}{2} + p_8 \check{d}_f + p_9 \check{l}_m + p_{10}$	$n^{ch}(\mathbf{u}^{w}) = p_1 \check{d}_f + p_3 \check{l}_m + p_2 \check{d}_f \check{l}_m + p_4 \frac{\check{d}_f}{\check{l}_m} + p_5$ $m^{ch}(\mathbf{u}^{w}) = p_6 \check{d}_f + p_7 \check{l}_m + p_8$
3	$n^{sp}(\mathbf{u}^{nw}) = p_1 \frac{\check{\beta}}{2} + p_3 \check{d}_f + p_5 \check{l}_m + p_2 \check{d}_f^2 + p_4 \check{l}_m^2 + p_6$ $m^{sp}(\mathbf{u}^{nw}) = p_7 \frac{\check{\beta}}{2} + p_8 \check{d}_f + p_9 \check{l}_m + p_{10}$	$n^{ch}(\mathbf{u}^{w}) = p_1 \check{d}_f + p_3 \check{l}_m + p_2 \check{d}_f^2 + p_4 \check{l}_m^2 + p_5$ $m^{ch}(\mathbf{u}^{w}) = p_6 \check{d}_f + p_7 \check{l}_m + p_8$
4	$n^{sp}(\mathbf{u}^{nw}) = p_1 \frac{\check{\beta}}{2} + p_3 \check{d}_f + p_5 \check{l}_m + p_2 \check{d}_f^2 + p_4 \check{d}_f^{-1} + p_6$ $m^{sp}(\mathbf{u}^{nw}) = p_7 \frac{\check{\beta}}{2} + p_8 \check{d}_f + p_9 \check{l}_m + p_{10}$	$n^{ch}(\mathbf{u}^{w}) = p_1 \check{d}_f + p_3 \check{l}_m + p_2 \check{d}_f \check{l}_m + p_4 \left(\check{l}_m \check{d}_f\right)^2 + p_5$ $m^{ch}(\mathbf{u}^{w}) = p_6 \check{d}_f + p_7 \check{l}_m + p_8$
5	$n^{sp}(\mathbf{u}^{nw}) = p_1 \frac{\check{\beta}}{2} + p_3 \check{d}_f + p_5 \check{l}_m + p_2 \frac{\check{\beta}}{2}^{-1} + p_4 \check{d}_f^{-1} + p_6 \check{l}_m^{-1} + p_7$ $m^{sp}(\mathbf{u}^{nw}) = p_8 \frac{\check{\beta}}{2} + p_9 \check{d}_f + p_{10} \check{l}_m + p_{11}$	$n^{ch}(\mathbf{u}^{w}) = p_1 \check{d}_f + p_3 \check{l}_m + p_2 \check{d}_f^{-1} + p_4 \check{l}_m^{-1} + p_5$ $m^{ch}(\mathbf{u}^{w}) = p_6 \check{d}_f + p_7 \check{l}_m + p_8$

6	$n^{sp}(\mathbf{u}^{nw}) = p_1 \frac{\check{\beta}}{2} + p_3 \check{d}_f + p_5 \check{l}_m + p_2 \left(\frac{\check{\beta}}{2}\right)^2 + p_4 \check{d}_f^2 + p_6 \check{l}_m^2 + p_7$ $m^{sp}(\mathbf{u}^{nw}) = p_8 \frac{\check{\beta}}{2} + p_9 \check{d}_f + p_{10} \check{l}_m + p_{11}$	$n^{ch}(\mathbf{u}^{w}) = p_1 \check{d}_f + p_3 \check{l}_m + p_2 \check{d}_f^{-1} + p_4 \check{l}_m^{-1} + p_5$ $m^{ch}(\mathbf{u}^{w}) = p_6 \check{d}_f + p_7 \check{l}_m + p_8$
7	$n^{sp}(\mathbf{u}^{nw}) = p_1 \frac{\check{\beta}}{2} + p_3 \check{d}_f + p_5 \check{l}_m + p_2 \frac{\check{\beta}}{2}^2 + p_4 \check{d}_f^2 + p_6 \check{l}_m^2 + p_7$ $m^{sp}(\mathbf{u}^{nw}) = p_8 \frac{\check{\beta}}{2} + p_{10} \check{d}_f + p_{12} \check{l}_m + p_9 \frac{\check{\beta}}{2}^2 + p_{11} \check{d}_f^2 + p_{13} \check{l}_m^2 + p_{14}$	$n^{ch}(\mathbf{u}^{w}) = p_1 \check{d}_f + p_3 \check{l}_m + p_2 \check{d}_f^2 + p_4 \check{l}_m^2 + p_5$ $m^{ch}(\mathbf{u}^{w}) = p_6 \check{d}_f + p_8 \check{l}_m + p_7 \check{d}_f^2 + p_9 \check{l}_m^2 + p_{10}$
8	$n^{sp}(\mathbf{u}^{nw}) = p_1 \frac{\check{\beta}}{2} + p_4 \check{d}_f + p_7 \check{l}_m + p_2 \frac{\check{\beta}}{2}^2 + p_5 \check{d}_f^2 + p_8 \check{l}_m^2 + p_3 \frac{\check{\beta}}{2}^{-1} + p_6 \check{d}_f^{-1} + p_9 \check{l}_m^{-1} + p_{10}$ $m^{sp}(\mathbf{u}^{nw}) = p_{11} \frac{\check{\beta}}{2} + p_{12} \check{d}_f + p_{13} \check{l}_m + p_{14}$	$n^{ch}(\mathbf{u}^{w}) = p_1 \check{d}_f + p_4 \check{l}_m + p_2 \check{d}_f^2 + p_5 \check{l}_m^2 + p_3 \check{d}_f^{-1} + p_6 \check{l}_m^{-1} + p_7$ $m^{ch}(\mathbf{u}^{w}) = p_8 \check{d}_f + p_9 \check{l}_m + p_{10}$
9	$n^{sp}(\mathbf{u}^{nw}) = p_1 \frac{\check{\beta}}{2} + p_4 \check{d}_f + p_7 \check{l}_m + p_2 \frac{\check{\beta}}{2}^2 + p_5 \check{d}_f^2 + p_8 \check{l}_m^2 + p_3 \frac{\check{\beta}}{2}^3 + p_6 \check{d}_f^3 + p_9 \check{l}_m^3 + p_{10}$ $m^{sp}(\mathbf{u}^{nw}) = p_{11} \frac{\check{\beta}}{2} + p_{12} \check{d}_f + p_{13} \check{l}_m + p_{14}$	$n^{ch}(\mathbf{u}^{w}) = p_1 \check{d}_f + p_4 \check{l}_m + p_2 \check{d}_f^2 + p_5 \check{l}_m^2 + p_3 \check{d}_f^3 + p_6 \check{l}_m^3 + p_7$ $m^{ch}(\mathbf{u}^{w}) = p_8 \check{d}_f + p_9 \check{l}_m + p_{10}$
10	$n^{sp}(\mathbf{u}^{nw}) = p_1 \frac{\check{\beta}}{2} + p_5 \check{d}_f + p_9 \check{l}_m + p_2 \frac{\check{\beta}}{2}^2 + p_6 \check{d}_f^2 + p_{10} \check{l}_m^2 + p_3 \frac{\check{\beta}}{2}^3 + p_7 \check{d}_f^3 + p_{11} \check{l}_m^3 + p_4 \frac{\check{\beta}}{2}^{-1} + p_8 \check{d}_f^{-1} + p_{12} \check{l}_m^{-1} + p_{13}$ $m^{sp}(\mathbf{u}^{nw}) = p_{14} \frac{\check{\beta}}{2} + p_{15} \check{d}_f + p_{16} \check{l}_m + p_{17}$	$n^{ch}(\mathbf{u}^{w}) = p_1 \check{d}_f + p_5 \check{l}_m + p_2 \check{d}_f^2 + p_6 \check{l}_m^2 + p_3 \check{d}_f^3 + p_7 \check{l}_m^3 + p_4 \check{d}_f^{-1} + p_8 \check{l}_m^{-1} + p_9$ $m^{ch}(\mathbf{u}^{w}) = p_{10} \check{d}_f + p_{11} \check{l}_m + p_{12}$

11	$n^{sp}(\mathbf{u}^{nw}) = p_1 \frac{\check{\beta}}{2} + p_4 \check{d}_f + p_7 \check{l}_m + p_2 \frac{\check{\beta}}{2}^2 + p_5 \check{d}_f^2 + p_8 \check{l}_m^2 + p_3 \frac{\check{\beta}}{2}^{-1} + p_6 \check{d}_f^{-1} + p_9 \check{l}_m^{-1} + p_{10}$ $m^{sp}(\mathbf{u}^{nw}) = p_{11} \frac{\check{\beta}}{2} + p_{13} \check{d}_f + p_{15} \check{l}_m + p_{12} \frac{\check{\beta}}{2}^2 + p_{14} \check{d}_f^2 + p_{16} \check{l}_m^2 + p_{17}$	$n^{ch}(\mathbf{u}^{w}) = p_1 \check{d}_f + p_4 \check{l}_m + p_2 \check{d}_f^2 + p_5 \check{l}_m^2 + p_3 \check{d}_f^{-1} + p_6 \check{l}_m^{-1} + p_7$ $m^{ch}(\mathbf{u}^{w}) = p_8 \check{d}_f + p_{10} \check{l}_m + p_9 \check{d}_f^2 + p_{11} \check{l}_m^2 + p_{12}$
12	$n^{sp}(\mathbf{u}^{nw}) = p_1 \frac{\check{\beta}}{2} + p_5 \check{d}_f + p_9 \check{l}_m + p_2 \frac{\check{\beta}}{2}^2 + p_6 \check{d}_f^2 + p_{10} \check{l}_m^2 + p_3 \frac{\check{\beta}}{2}^3 + p_7 \check{d}_f^3 + p_{11} \check{l}_m^3 + p_4 \frac{\check{\beta}}{2}^{-1} + p_8 \check{d}_f^{-1} + p_{12} \check{l}_m^{-1} + p_{13}$ $m^{sp}(\mathbf{u}^{nw}) = p_{14} \frac{\check{\beta}}{2} + p_{16} \check{d}_f + p_{18} \check{l}_m + p_{15} \frac{\check{\beta}}{2}^2 + p_{17} \check{d}_f^2 + p_{19} \check{l}_m^2 + p_{20}$	$n^{ch}(\mathbf{u}^{w}) = p_1 \check{d}_f + p_5 \check{l}_m + p_2 \check{d}_f^2 + p_6 \check{l}_m^2 + p_3 \check{d}_f^3 + p_7 \check{l}_m^3 + p_4 \check{d}_f^{-1} + p_8 \check{l}_m^{-1} + p_9$ $m^{ch}(\mathbf{u}^{w}) = p_{10} \check{d}_f + p_{12} \check{l}_m + p_{11} \check{d}_f^2 + p_{13} \check{l}_m^2 + p_{14}$
13	$n^{sp}(\mathbf{u}^{nw}) = p_1 \frac{\check{\beta}}{2} + p_4 \check{d}_f + p_7 \check{l}_m + p_2 \frac{\check{\beta}}{2}^2 + p_5 \check{d}_f^2 + p_8 \check{l}_m^2 + p_3 \frac{\check{\beta}}{2}^3 + p_6 \check{d}_f^3 + p_9 \check{l}_m^3 + p_{10}$ $m^{sp}(\mathbf{u}^{nw}) = p_{11} \frac{\check{\beta}}{2} + p_{14} \check{d}_f + p_{17} \check{l}_m + p_{12} \frac{\check{\beta}}{2}^2 + p_{15} \check{d}_f^2 + p_{18} \check{l}_m^2 + p_{13} \frac{\check{\beta}}{2}^3 + p_{16} \check{d}_f^3 + p_{19} \check{l}_m^3 + p_{20}$	$n^{ch}(\mathbf{u}^{w}) = p_1 \check{d}_f + p_4 \check{l}_m + p_2 \check{d}_f^2 + p_5 \check{l}_m^2 + p_3 \check{d}_f^3 + p_6 \check{l}_m^3 + p_7$ $m^{ch}(\mathbf{u}^{w}) = p_8 \check{d}_f + p_{11} \check{l}_m + p_9 \check{d}_f^2 + p_{12} \check{l}_m^2 + p_{10} \check{d}_f^3 + p_{13} \check{l}_m^3 + p_{14}$
14	$n^{sp}(\mathbf{u}^{nw}) = p_1 \frac{\check{\beta}}{2} + p_6 \check{d}_f + p_{11} \check{l}_m + p_2 \frac{\check{\beta}}{2}^2 + p_7 \check{d}_f^2 + p_{12} \check{l}_m^2 + p_3 \frac{\check{\beta}}{2}^3 + p_8 \check{d}_f^3 + p_{13} \check{l}_m^3 + p_4 \frac{\check{\beta}}{2}^4 + p_9 \check{d}_f^4 + p_{14} \check{l}_m^4 + p_5 \frac{\check{\beta}}{2}^{-1} + p_{10} \check{d}_f^{-1} + p_{15} \check{l}_m^{-1} + p_{16}$ $m^{sp}(\mathbf{u}^{nw}) = p_{17} \frac{\check{\beta}}{2} + p_{18} \check{d}_f + p_{19} \check{l}_m + p_{20}$	$n^{ch}(\mathbf{u}^{w}) = p_1 \check{d}_f + p_6 \check{l}_m + p_2 \check{d}_f^2 + p_7 \check{l}_m^2 + p_3 \check{d}_f^3 + p_8 \check{l}_m^3 + p_4 \check{d}_f^4 + p_9 \check{l}_m^4 + p_5 \check{d}_f^{-1} + p_{10} \check{l}_m^{-1} + p_{11}$ $m^{ch}(\mathbf{u}^{w}) = p_{12} \check{d}_f + p_{13} \check{l}_m + p_{14}$

15	$n^{sp}(\mathbf{u}^{nw}) = p_1 \frac{\check{\beta}}{2} + p_9 \check{d}_f + p_3 \check{l}_m + p_2 \frac{\check{\beta}}{2}^2 + p_6 \check{d}_f^2 + p_{10} \check{l}_m^2 + p_3 \frac{\check{\beta}}{2}^3 + p_7 \check{d}_f^3 + p_{11} \check{l}_m^3 + p_4 \frac{\check{\beta}}{2}^4 + p_8 \check{d}_f^4 + p_{12} \check{l}_m^4 + p_{13}$ $m^{sp}(\mathbf{u}^{nw}) = p_{14} \frac{\check{\beta}}{2} + p_{18} \check{d}_f + p_{22} \check{l}_m + p_{15} \frac{\check{\beta}}{2}^2 + p_{19} \check{d}_f^2 + p_{23} \check{l}_m^2 + p_{16} \frac{\check{\beta}}{2}^3 + p_{20} \check{d}_f^3 + p_{24} \check{l}_m^3 + p_{17} \frac{\check{\beta}}{2}^4 + p_{21} \check{d}_f^4 + p_{25} \check{l}_m^4 + p_{26}$	$n^{ch}(\mathbf{u}^{w}) = p_1 \check{d}_f + p_5 \check{l}_m + p_2 \check{d}_f^2 + p_6 \check{l}_m^2 + p_3 \check{d}_f^3 + p_7 \check{l}_m^3 + p_4 \check{d}_f^4 + p_8 \check{l}_m^4 + p_9$ $m^{ch}(\mathbf{u}^{w}) = p_{10} \check{d}_f + p_{14} \check{l}_m + p_{11} \check{d}_f^2 + p_{15} \check{l}_m^2 + p_{12} \check{d}_f^3 + p_{16} \check{l}_m^3 + p_{13} \check{d}_f^4 + p_{17} \check{l}_m^4 + p_{18}$
16	$n^{sp}(\mathbf{u}^{nw}) = p_1 \frac{\check{\beta}}{2} + p_7 \check{d}_f + p_{13} \check{l}_m + p_2 \frac{\check{\beta}}{2}^2 + p_8 \check{d}_f^2 + p_{14} \check{l}_m^2 + p_3 \frac{\check{\beta}}{2}^3 + p_9 \check{d}_f^3 + p_{15} \check{l}_m^3 + p_4 \frac{\check{\beta}}{2}^4 + p_{10} \check{d}_f^4 + p_{16} \check{l}_m^4 + p_5 \frac{\check{\beta}}{2}^5 + p_{11} \check{d}_f^5 + p_{17} \check{l}_m^5 + p_6 \frac{\check{\beta}}{2}^{-1} + p_{12} \check{d}_f^{-1} + p_{18} \check{l}_m^{-1} + p_{19}$ $m^{sp}(\mathbf{u}^{nw}) = p_{20} \frac{\check{\beta}}{2} + p_{22} \check{d}_f + p_{24} \check{l}_m + p_{21} \frac{\check{\beta}}{2}^2 + p_{23} \check{d}_f^2 + p_{25} \check{l}_m^2 + p_{26}$	$n^{ch}(\mathbf{u}^{w}) = p_1 \check{d}_f + p_7 \check{l}_m + p_2 \check{d}_f^2 + p_8 \check{l}_m^2 + p_3 \check{d}_f^3 + p_9 \check{l}_m^3 + p_4 \check{d}_f^4 + p_{10} \check{l}_m^4 + p_5 \check{d}_f^5 + p_{11} \check{l}_m^5 + p_6 \check{d}_f^{-1} + p_{12} \check{l}_m^{-1} + p_{13}$ $m^{ch}(\mathbf{u}^{w}) = p_{14} \check{d}_f + p_{16} \check{l}_m + p_{15} \check{d}_f^2 + p_{17} \check{l}_m^2 + p_{18}$

17	$n^{sp}(\mathbf{u}^{nw}) = p_1 \frac{\check{\beta}}{2} + p_6 \check{d}_f + p_{11} \check{l}_m + p_2 \frac{\check{\beta}}{2}^2 + p_7 \check{d}_f^2 + p_{12} \check{l}_m^2 + p_3 \frac{\check{\beta}}{2}^3 + p_8 \check{d}_f^3 + p_{13} \check{l}_m^3 + p_4 \frac{\check{\beta}}{2}^4 + p_9 \check{d}_f^4 + p_{14} \check{l}_m^4 + p_5 \frac{\check{\beta}}{2}^{-1} + p_{10} \check{d}_f^{-1} + p_{15} \check{l}_m^{-1} + p_{16}$ $m^{sp}(\mathbf{u}^{nw}) = p_{17} \frac{\check{\beta}}{2} + p_{21} \check{d}_f + p_{25} \check{l}_m + p_{18} \frac{\check{\beta}}{2}^2 + p_{22} \check{d}_f^2 + p_{26} \check{l}_m^2 + p_{19} \frac{\check{\beta}}{2}^3 + p_{23} \check{d}_f^3 + p_{27} \check{l}_m^3 + p_{20} \frac{\check{\beta}}{2}^4 + p_{24} \check{d}_f^4 + p_{28} \check{l}_m^4 + p_{29}$	$n^{ch}(\mathbf{u}^{w}) = p_1 \check{d}_f + p_6 \check{l}_m + p_2 \check{d}_f^2 + p_7 \check{l}_m^2 + p_3 \check{d}_f^3 + p_8 \check{l}_m^3 + p_4 \check{d}_f^4 + p_9 \check{l}_m^4 + p_5 \check{d}_f^{-1} + p_{10} \check{l}_m^{-1} + p_{11}$ $m^{ch}(\mathbf{u}^{w}) = p_{12} \check{d}_f + p_{16} \check{l}_m + p_{13} \check{d}_f^2 + p_{17} \check{l}_m^2 + p_{14} \check{d}_f^3 + p_{18} \check{l}_m^3 + p_{15} \check{d}_f^4 + p_{19} \check{l}_m^4 + p_{20}$

Bibliography

H. Akaike. Information theory and an extension of the maximum likelihood principle. In B. N. Petrov and F. Csaki, editors, *Second International Symposium on Information Theory*, pages 267–281. Budapest, 1973.

H. AlMadani. Water desalination by solar powered electrodialysis process. *Renewable Energy*, 28 (12):1915–1924, 2003.

L. Angermann and J. Rang. Perturbation index of linear partial differential-algebraic equations with a hyperbolic part. *Central European Journal of Mathematics*, 5(1):19–49, 2007.

S. Arlot and A. Celisse. A survey of cross-validation procedures for model selection. *Statistics Surveys*, 4(0):40–79, 2010.

O. A. Asbjørnsen and M. Fjeld. Response modes of continuous stirred tank reactors. *Chemical Engineering Science*, 25(11):1627–1636, 1970.

Aspentech. Aspen Custom Modeler, http://www.aspentech.com/products/aspen-custom-modeler.aspx, rev. 12.06.2014, 1994-2013.

R. Bachmann, L. Brüll, T. Mrziglod, and U. Pallaske. On methods for reducing the index of differential algebraic equations. *Computers & Chemical Engineering*, 14(11):1271–1273, 1990.

J. Balster, M. H. Yildirim, D. F. Stamatialis, R. Ibanez, R. G. H. Lammertink, V. Jordan, and M. Wessling. Morphology and microtopology of cation-exchange polymers and the origin of the overlimiting current. *The Journal of Physical Chemistry B*, 111(9):2152–2165, 2007.

V. Baltazar, G. Harris, and C. White. The selective recovery and concentration of sulphuric acid by electrodialysis. *Hydrometallurgy*, 30(1-3):463–481, 1992.

A. Bardow, W. Marquardt, V. Göke, H.-J. Koss, and K. Lucas. Model-based measurement of diffusion using Raman spectroscopy. *AIChE Journal*, 49(2):323–334, 2003.

J. W. Bartlett and C. Frost. Reliability, repeatability and reproducibility: analysis of measurement errors in continuous variables. *Ultrasound in Obstetrics & Gynecology*, 31(4):466–475, 2008.

J. Bausa and W. Marquardt. Detailed modeling of stationary and transient mass transfer across pervaporation membranes. *AIChE Journal*, 47(6):1318–1332, 2001.

J. Bernsdorf, U. Jaekel, T. Zeiser, T. Takei, H. Matsumoto, and K. Nishizawa. Lattice Boltzmann simulation and visualisation of adsorption processes in complex geometries. In P. Sloot, D. Abramson, A. Bogdanov, J. Dongarra, A. Zomaya, and Y. Gorbachev, editors, *Computational Science — ICCS 2003*, volume 2657 of *Lecture Notes in Computer Science*, pages 1054–1061. Springer Berlin Heidelberg, 2003.

R. B. Bird, W. E. Stewart, and E. N. Lightfoot. *Transport Phenomena*. Wiley, New York, 2002.

C. Bischof, H. Bucker, B. Lang, A. Rasch, and A. Vehreschild. Combining source transformation and operator overloading techniques to compute derivatives for MATLAB programs. *Proceedings of the Second IEEE International Workshop on Source Code Analysis and Manipulation (SCAM 2002)*, pages 65–72, 2002.

F. J. Borges, H. R.-d. Balmann, and R. Guardani. Modeling electrodialysis and photochemical process for their integration in saline wastewater treatment. In *10th International Symposium on Process Systems Engineering: Part A*, volume 27 of *Computer Aided Chemical Engineering*, pages 741–746. Elsevier, 2009.

D. Bothe. On the Maxwell-Stefan approach to multicomponent diffusion: Parabolic problems. *Progress in Nonlinear Differential Equations and Their Applications*, (80):81–93, 2011.

D. Brandell, J. Karo, A. Liivat, and J. O. Thomas. Molecular dynamics studies of the nafion, dow and aciplex fuel-cell polymer membrane systems. *Journal of Molecular Modeling*, 13(10): 1039–1046, 2007.

K. E. Brenan, S. L. Campbell, and L. R. Petzold. *Numerical Solution of Initial-Value Problems in Differential-Algebraic Equations*. Society for Industrial and Applied Mathematics, Philadelphia, 1996.

M. Brendel, D. Bonvin, and W. Marquardt. Incremental identification of kinetic models for homogeneous reaction systems. *Chemical Engineering Science*, 61(16):5404–5420, 2006.

K. P. Burnham and D. R. Anderson. *Model Selection and Multimodel Inference: A Practical Imformation-Theoretic Approach*. Springer, New York, NY, 2008.

G. Buzzi-Ferraris and F. Manenti. Better reformulation of kinetic models. *Computers & Chemical Engineering*, 34(11):1904–1906, 2010.

S. L. Campbell and W. Marszalek. ODE / DAE integrators and MOL problems. *ZAMM - Journal of Applied Mathematics and Mechanics / Zeitschrift für Angewandte Mathematik und Mechanik*, 76(S1):251–254, 1996.

S. Campbell and W. Marszalek. The index of an infinite-dimensional implicit system. *Mathematical and Computer Modelling of Dynamical Systems*, 5(1):18–42, 1999.

Z. Cao. CFD simulations of net-type turbulence promoters in a narrow channel. *Journal of Membrane Science*, 185(2):157–176, 2001.

C. Casademont, P. Sistat, B. Ruiz, G. Pourcelly, and L. Bazinet. Electrodialysis of model salt solution containing whey proteins: Enhancement by pulsed electric field and modified cell configuration. *Journal of Membrane Science*, 328(1-2):238–245, 2009.

T. Chapman. *The Transport Properties of Concentrated Electrolytic Solutions*. PhD thesis, University of California, Berkeley, 1968.

F. Chaumeil and M. Crapper. DEM simulations of initial deposition of colloidal particles around non-woven membrane spacers. *Journal of Membrane Science*, 442:254–263, 2013.

C.-C. Chen. Toward development of activity coefficient models for process and product design of complex chemical systems. *Fluid Phase Equilibria*, 241(1-2):103–112, 2006.

C.-C. Chen, H. I. Britt, J. F. Boston, and L. B. Evans. Local composition model for excess gibbs energy of electrolyte systems. Part i: Single solvent, single completely dissociated electrolyte systems. *AIChE Journal*, 28(4):588–596, 1982.

C.-C. Chen and Y. Song. Generalized electrolyte-NRTL model for mixed-solvent electrolyte systems. *AIChE Journal*, 50(8):1928–1941, 2004.

S. Chen and G. D. Doolen. Lattice Boltzmann method for fluid flows. *Annual Review of Fluid Mechanics*, 30(1):329–364, 1998.

K. Chudej, P. Heidebrecht, V. Petzet, S. Scherdel, K. Schittkowski, H. Pesch, and K. Sundmacher. Index analysis and numerical solution of a large scale nonlinear pdae system describing the dynamical behaviour of molten carbonate fuel cells. *ZAMM*, 85(2):132–140, 2005.

C. F. Curtiss and R. B. Bird. Multicomponent diffusion. *Industrial & Engineering Chemistry Research*, 38(7):2515–2522, 1999.

A. Da Costa, A. Fane, and D. Wiley. Spacer characterization and pressure drop modelling in spacer-filled channels for ultrafiltration. *Journal of Membrane Science*, 87(1-2):79–98, 1994.

P. Deuflhard, E. Hairer, and J. Zugck. One-step and extrapolation methods for differential-algebraic systems. *Numerische Mathematik*, 51(5):501–516, 1987.

B. D. Djordjević, S. P. Šerbanovlć, and D. K. Grozdanić. Calculation of excess molar volumes with different cubic equations of state and different mixing rules. *The Canadian Journal of Chemical Engineering*, 72(1):171–176, 1994.

P. Dlugolecki. *Mass transport in reverse electrodialysis for sustainable energy generation*. PhD thesis, University of Twente, Enschede, 2009.

P. Długołęcki, P. Ogonowski, S. J. Metz, M. Saakes, K. Nijmeijer, and M. Wessling. On the resistances of membrane, diffusion boundary layer and double layer in ion exchange membrane transport. *Journal of Membrane Science*, 349(1-2):369–379, 2010.

C. Eichler-Liebenow. *Zur numerischen Behandlung räumlich mehrdimensionaler parabolischer Differentialgleichungen mit linear-impliziten Splitting-Methoden und linearer partieller differentiell-algebraischer Systeme*. PhD thesis, Martin-Luther-Universität Halle-Wittenberg, Halle (Saale), 1999.

J. A. Elliott, D. Wu, S. J. Paddison, and R. B. Moore. A unified morphological description of nafion membranes from saxs and mesoscale simulations. *Soft Matter*, 7(15):6820, 2011.

J. Fárková. The pressure drop in membrane module with spacers. *Journal of Membrane Science*, 64(1–2):103–111, 1991.

S. Feldberg. On the dilemma of the use of the electroneutrality constraint in electrochemical calculations. *Electrochemistry Communications*, 2(7):453–456, 2000.

M. Fidaleo and M. Moresi. Optimal strategy to model the electrodialytic recovery of a strong electrolyte. *Journal of Membrane Science*, 260(1-2):90–111, 2005.

M. Fidaleo and M. Moresi. Application of the nernst–planck approach to model the electrodialytic recovery of disodium itaconate. *Journal of Membrane Science*, 349(1-2):393–404, 2010.

G. A. Fimbres-Weihs. *Numerical Simulation Studies of Mass Transfer under Steady and Unsteady Fluid Flow in Two- and Three-Dimensional Spacer-Filled Channels*. PhD thesis, The University of New South Wales, Sydney Australia, 2008.

G. A. Fimbres-Weihs and D. Wiley. Numerical study of mass transfer in three-dimensional spacer-filled narrow channels with steady flow. *Journal of Membrane Science*, 306(1-2):228–243, 2007.

V. Freger and S. Bason. Characterization of ion transport in thin films using electrochemical impedance spectroscopyi. principles and theory. *Journal of Membrane Science*, 302(1-2):1–9, 2007.

V. Freger, E. Korin, J. Wisniak, E. Korngold, M. Ise, and K. D. Kreuer. Diffusion of water and ethanol in ion-exchange membranes: limits of the geometric approach. *Journal of Membrane Science*, 160(2):213–224, 1999.

C. Fritzmann. *Micro Structured Spacers for Intensified Membrane Process Performance*. PhD thesis, RWTH Aachen University, Aachen, 2012.

A. H. Galama, D. A. Vermaas, J. Veerman, M. Saakes, H. Rijnaarts, J. W. Post, and K. Nijmeijer. Membrane resistance: The effect of salinity gradients over a cation exchange membrane. *Journal of Membrane Science*, 467:279–291, 2014.

C. W. Gear. Differential-algebraic equations, indices, and integral algebraic equations. *SIAM Journal on Numerical Analysis*, 27(6):1527–1534, 1990.

C. W. Gear and L. R. Petzold. ODE methods for the solution of differential/algebraic systems. *SIAM Journal on Numerical Analysis*, (21(4)):716–728, 1984.

R. Goering, C. Bowman, C. Koval, R. Noble, and D. Williamson. Role of ion-exchange membrane morphology and sorption properties in facilitated transport di-olefin/mono-olefin separations. *Journal of Membrane Science*, 144(1-2):133–143, 1998.

B. K. Gurtler, T. A. Vetter, E. M. Perdue, E. Ingall, J.-F. Koprivnjak, and P. H. Pfromm. Combining reverse osmosis and pulsed electrical current electrodialysis for improved recovery of dissolved organic matter from seawater. *Journal of Membrane Science*, 323(2):328–336, 2008.

J. Hadamard. Sur les problèmes aux dérivés partielles et leur signification physique. *Princeton University Bulletin*, 13:49–52, 1902.

E. Hairer, C. Lubich, and M. Roche. *The Numerical Solution of Differential-Algebraic Systems by Runge-Kutta Methods*, volume 1409 of *Lecture Notes in Mathematics*. Springer-Verlag, Berlin, New York, 1989.

E. Hairer, S. P. Nørsett, and G. Wanner. *Solving Ordinary Differential Equations*, volume 8, 14 of *Springer Series in Computational Mathematics*. Springer-Verlag, New York, 1993.

R. Hanke-Rauschenbach. *Strukturierte Modellierung und nichtlineare Analyse von PEM-Brennstoffzellen*. PhD thesis, Magdeburg, 2007.

D. F. Harlacher, M. Hasert, H. Klimach, S. Zimny, and S. Roller. Tree based voxelization of STL data. *High Performance Computing on Vector Systems 2011*, pages 81–92, 2011.

M. Hasert, K. Masilamani, S. Zimny, H. Klimach, J. Qi, J. Bernsdorf, and S. Roller. Complex fluid simulations with the parallel tree-based Lattice Boltzmann solver Musubi. *Journal of Computational Science*, 5(5):784–794, 2013 // 2014.

F. G. Helfferich. *Ion Exchange*. Dover Science Books. Dover Publications, New York, 1995.

D. M. Himmelblau. *Process Analysis by Statistical Methods*. Wiley, New York, 1970.

F. Hine. *Electrode Processes and Electrochemical Engineering*. Springer Verlag and Springer US, Boston, MA, 1985.

J. Hogendoorn, van der Veen, A..J, van der Stegen, J. H. G., J. Kuipers, and G. Versteeg. Application of the maxwell–stefan theory to the membrane electrolysis process: Model development and simulations. *Computers & Chemical Engineering*, 25(9-10):1251–1265, 2001.

C. Huang, T. Xu, Y. Zhang, Y. Xue, and G. Chen. Application of electrodialysis to the production of organic acids: State-of-the-art and recent developments. *Journal of Membrane Science*, 288 (1-2):1–12, 2007.

M. S. Isaacson and A. A. Sonin. Sherwood number and friction factor correlations for electrodialysis systems, with application to process optimization. *Industrial & Engineering Chemistry Process Design and Development*, 15(2):313–321, 1976.

G. Jing, W. Du, and Y. Guo. Studies on prediction of separation percent in electrodialysis process via bp neural networks and improved bp algorithms. *Desalination*, 291:78–93, 2012.

M. Johannink, A. Mhamdi, and W. Marquardt. Rigorous modeling of electrodialysis processes. In T. Melin, editor, *13th Aachener Membran Kolloquium Proceedings*, pages 473–480, 2010.

M. Johannink, K. Masilamani, A. Mhamdi, S. Roller, and W. Marquardt. Predictive pressure drop models for membrane channels with non-woven and woven spacers. *Desalination*, 376: 41–54, 2015.

M. Johannink, K. Masilamani, A. Mhamdi, S. Roller, and W. Marquardt. Corrigendum to 'predictive pressure drop models for membrane channels with non-woven and woven spacers'. *Desalination*, 397:213–214, 2016a.

M. Johannink, A. Mhamdi, and W. Marquardt. Towards a rigorous model of electrodialysis processes. *Proceedings of ESCAPE 21, European Symposium on Computer Aided Process Engineering*, 29:116–120, 2011.

M. Johannink, A. Mhamdi, and W. Marquardt. Index analysis and reduction of systems of quasi-linear partial-differential and algebraic equations. *Computers & Chemical Engineering*, 89:41–52, 2016b.

M. Johannink, A. Mhamdi, and W. Marquardt. A mechanistic model for transient electrodialysis processes. in preparation. 2016c.

A. I. Kakhu and C. C. Pantelides. Dynamic modelling of aqueous electrolyte systems. *Computers & Chemical Engineering*, 27(6):869–882, 2003.

J. Kaláb and Z. Palatý. Electrodialysis of oxalic acid: batch process modeling. *Chemical Papers*, 66(12):1118–1123, 2012.

Y. V. Karlin and V. N. Kropotov. Electrodialysis separation of Na^+ and Ca^{2+} in a pulsed current mode. *Russian Journal of Electrochemistry*, 31(5):472, 1995.

J. Karo, A. Aabloo, J. O. Thomas, and D. Brandell. Molecular dynamics modeling of proton transport in nafion and hyflon nanostructures. *The Journal of Physical Chemistry B*, 114(18): 6056–6064, 2010.

Y. Kim, W. S. Walker, and D. F. Lawler. Competitive separation of di- vs. mono-valent cations in electrodialysis: effects of the boundary layer properties. *Water Research*, 46(7):2042–2056, 2012.

K. Kontturi, L. Murtomäki, and J. A. Manzanares. *Ionic Transport Processes*. Oxford University Press, Oxford, England, 2008.

M. J. Kotelyanskii, N. J. Wagner, and M. E. Paulaitis. Molecular dynamics simulation study of the mechanisms of water diffusion in a hydrated, amorphous polyamide. *Computational and Theoretical Polymer Science*, 9(3-4):301–306, 1999.

C. P. Koutsou, S. G. Yiantsios, and A. J. Karabelas. Numerical simulation of the flow in a plane-channel containing a periodic array of cylindrical turbulence promoters. *Journal of Membrane Science*, 231:81–90, 2004.

C. P. Koutsou, S. G. Yiantsios, and A. J. Karabelas. Direct numerical simulation of flow in spacer-filled channels: Effect of spacer geometrical characteristics. *Journal of Membrane Science*, 291: 53–69, 2007.

C. Koutsou, S. Yiantsios, and A. Karabelas. A numerical and experimental study of mass transfer in spacer-filled channels: Effects of spacer geometrical characteristics and Schmidt number. *Journal of Membrane Science*, 326(1):234–251, 2009.

G. Kraaijeveld, V. Sumberova, S. Kuindersma, and H. Wesselingh. Modelling electrodialysis using the Maxwell-Stefan description. *The Chemical Engineering Journal*, (57):163–176, 1995.

G. Kraaijeveld and J. A. Wesselingh. Negative Maxwell-Stefan diffusion coefficients. *Industrial & Engineering Chemistry Research*, 32(4):738–742, 1993.

R. Krishna and J. A. Wesselingh. The Maxwell-Stefan approach to mass transfer. *Chemical Engineering Science*, 52(6):861–911, 1997.

J. Krol. *Monopolar and Bipolar Ion Exchange Membranes: Mass Transport Limitations*. PhD thesis, University of Twente, Enschede, 1997.

J. Krol. Chronopotentiometry and overlimiting ion transport through monopolar ion exchange membranes. *Journal of Membrane Science*, 162(1-2):155–164, 1999.

F.-F. Kuppinger. *Experimentelle Untersuchung und mathematische Modellierung von Elektrodialyseverfahren*. PhD thesis, Universität Stuttgart, Stuttgart, 1997.

F.-F. Kuppinger, Neubrand, Wolfgang, H.-J. Rapp, and G. Eigenberger. Elektromembranverfahren teil 1: Grundlagen und Modellbildung. *Chemie-Ingenieur-Technik*, (67):441–448, 1995.

H.-J. Lee, F. Sarfert, H. Strathmann, and S.-H. Moon. Designing of an electrodialysis desalination plant. *Desalination*, 142(3):267–286, 2002.

F. Li, W. Meindersma, A. d. Haan, and T. Reith. Optimization of commercial net spacers in spiral wound membrane modules. *Journal of Membrane Science*, 208(1-2):289–302, 2002.

X.-W. Li and X.-S. Zhang. Photovoltaic–electrodialysis regeneration method for liquid desiccant cooling system. *Solar Energy*, 83(12):2195–2204, 2009.

Y.-L. Li, K.-L. Tung, Y.-S. Chen, and K.-J. Hwang. CFD analysis of the initial stages of particle deposition in spiral-wound membrane modules. *Desalination*, 287:200–208, 2012.

W. Lucht, K. Strehmel, and C. Eichler-Liebenow. Indexes and special discretization methods for linear partial differential algebraic equations. *BIT Numerical Mathematics*, 39(3):484–512, 1999.

P. Malek, J. M. Ortiz, B. S. Richards, and A. I. Schäfer. Electrodialytic removal of nacl from water: Impacts of using pulsed electric potential on ion transport and water dissociation phenomena. *Journal of Membrane Science*, 435:99–109, 2013.

Maplesoft. Maple 14, http://www.maplesoft.com/products/maple/, rev. 12.06.2014, 2005-2014.

W. Marquardt. Computer-aided generation of chemical engineering process models. *International Journal of Chemical Engineering*, 34:28–46, 1994.

S. Marsili-Libelli, S. Guerrizio, and N. Checchi. Confidence regions of estimated parameters for ecological systems. *Ecological Modelling*, 165(2-3):127–146, 2003.

W. Marszalek and Z. W. Trzaska. Analysis of implicit hyperbolic multivariable systems. *Applied Mathematical Modelling*, 19(7):400–410, 1995.

M. C. Martí-Calatayud, D. C. Buzzi, M. García-Gabaldón, A. M. Bernardes, J. Tenório, and V. Pérez-Herranz. Ion transport through homogeneous and heterogeneous ion-exchange membranes in single salt and multicomponent electrolyte solutions. *Journal of Membrane Science*, 466:45–57, 2014.

W. S. Martinson. *Index and Characteristic Analysis of Partial Differential Equations*. PhD thesis, Massachusetts Institute of Technology, Cambridge, 2000.

W. S. Martinson and P. I. Barton. A differentiation index for partial differential-algebraic equations. *SIAM Journal on Scientific Computing*, 21(6):2295, 2000.

W. S. Martinson and P. I. Barton. Distributed models in plantwide dynamic simulators. *AIChE Journal*, (47(6)):1372ff., 2001a.

W. S. Martinson and P. I. Barton. Distributed models in plantwide dynamic simulators. *AIChE Journal*, 47(6):1372–1386, 2001b.

W. S. Martinson and P. I. Barton. Index and characteristic analysis of linear PDAE systems. *SIAM Journal on Scientific Computing*, 24(3):905, 2003.

K. Masilamani. Large scale flow simulation with complex spacer geometry in electrodialysis for sea water desalination. In J. Eberhardsteiner, editor, *European Congress on Computational Methods in Applied Sciences and Engineering (ECCOMAS 2012)*. Vienna and Austria, 2012.

Math2Market GmbH. GeoDict 2013, http://www.geodict.com/, rev. 03.05.2014.

P. M. Mathias. Correlation for the density of multicomponent aqueous electrolytes. *Industrial & Engineering Chemistry Research*, 43(19):6247–6252, 2004.

M. Matthes. *Numerical Analysis of Nonlinear Partial Differential-Algebraic Equations: A Coupled and an Abstract Systems Approach.* PhD thesis, Universität zu Köln, Köln, 2012.

S. E. Mattsson and G. Soderlind. Index reduction in differential-algebraic equations using dummy derivatives. *SIAM Journal on Scientific Computing*, 14(3):677, 1993.

T. Melin and R. Rautenbach. *Membranverfahren: Grundlagen der Modul- und Anlagenauslegung.* Verfahrenstechnik. Springer, Berlin, 2004.

S. Mikhaylin, V. V. Nikonenko, G. Pourcelly, and L. Bazinet. Intensification of demineralization process and decrease in scaling by application of pulsed electric field with short pulse/pause conditions. *Journal of Membrane Science*, 468:389–399, 2014.

D. G. Miller. Application of irreversible thermodynamics to electiolyte solutions. ii. Ionic coefficients for isothermal vector transport processes in ternary systems. *The Journal of Physical Chemistry*, 71(3):616–632, 1967.

N. A. Mishchuk, L. K. Koopal, and F. Gonzalez-Caballero. Intensification of electrodialysis by applying a non-stationary electric field. *Colloids and Surfaces A: Physicochemical and Engineering Aspects*, 176(2-3):195–212, 2001a.

N. A. Mishchuk, S. V. Verbich, and F. Gonzales-Caballero. Concentration polarization and specific selectivity of membranes in pulse mode. *Colloid Journal*, 63(5):586–595, 2001b.

H. I. Moe. *Dynamic Process Simulation. Studies on Modeling and Index Reduction.* PhD thesis, NTH, Trondheim, 1995.

P. J. Moon, S. J. Parulekar, and S.-P. Tsai. Competitive anion transport in desalting of mixtures of organic acids by batch electrodialysis. *Journal of Membrane Science*, 141(1):75–89, 1998.

A. A. Moya and J. Horno. Application of the network simulation method to ionic transport in ion-exchange membranes including diffuse double-layer effects. *The Journal of Physical Chemistry B*, 103(49):10791–10799, 1999.

A. A. Moya and P. Sistat. Chronoamperometric response of ion-exchange membrane systems. *Journal of Membrane Science*, 444:412–419, 2013.

E. Nagy. *Basic Equations of the Mass Transport Through a Membrane Layer.* Elsevier, London, 2012.

National Renewable Energy Laboratory. Oahu solar measurement grid: Solar Measurement Grid (2011) , Oahu, Hawaii, `www.nrel.gov/midc/oahu_archive/`, rev. 08.12.2014.

W. Neubrand. *ModeIlbildung und Simulation von Elektromembranverfahren*. PhD thesis, Universität Stuttgart, Stuttgart, 1999.

J. Neumann. *Consisteney Analysis of Systems of Partial and Ordinary Differential and Algebraic Equations*. PhD thesis, Imperial College London, London, 2004.

J. Neumann and C. C. Pantelides. Consistency of general point conditions for DAE systems. *Computers & Chemical Engineering*, 30(1):125–136, 2005.

J. Neumann and C. C. Pantelides. Consistency on domain boundaries for linear PDAE systems. *SIAM Journal on Scientific Computing*, 30(2):916–936, 2008.

J. S. Newman and K. E. Thomas-Alyea. *Electrochemical Systems*. Electrochemical Society Series. Wiley-Interscience, Hoboken, NJ, 3rd edition, 2004.

V. V. Nikonenko, K. A. Lebedev, and S. S. Suleimanov. Influence of the convective term in the nernst-planck equation on properties of ion transport through a layer of solution or membrane. *Russian Journal of Electrochemistry*, 45(2):160–169, 2009.

V. V. Nikonenko, N. D. Pismenskaya, E. I. Belova, P. Sistat, P. Huguet, G. Pourcelly, and C. Larchet. Intensive current transfer in membrane systems: Modelling, mechanisms and application in electrodialysis. *Advances in Colloid and Interface Science*, 160(1-2):101–123, 2010.

O. Okeowo and J. R. Dorgan. Multicomponent swelling of polymer networks. *Macromolecules*, 39(23):8193–8202, 2006.

J. M. Ortiz, J. Sotoca, E. Exposito, F. Gallud, V. Garciagarcia, V. Montiel, and A. Aldaz. Brackish water desalination by electrodialysis: batch recirculation operation modeling. *Journal of Membrane Science*, 252(1-2):65–75, 2005.

M. Otter. A constructive definition of the perturbation index. *COSY Workshop on Mathematical Modeling of Complex Systems, Lund (Sweden), http://elib.dlr.de/28464/, rev. 12.06.2014*, 1996.

C. C. Pantelides. The consistent initialization of differential-algebraic systems. *SIAM Journal on Scientific and Statistical Computing*, 9(2):213, 1988.

S. J. Parulekar. Optimal current and voltage trajectories for minimum energy consumption in batch electrodialysis. *Journal of Membrane Science*, 148(1):91–103, 1998.

S. Pawlowski, J. G. Crespo, and S. Velizarov. Pressure drop in reverse electrodialysis: Experimental and modeling studies for stacks with variable number of cell pairs. *Journal of Membrane Science*, 462:96–111, 2014.

R. H. Perry and D. W. Green. *Perrys Chemical Engineers Handbook*. McGraw-Hill, New York, 2008.

L. Petzold. A description of DASSL: A differential/algebraic system solver. *Proc. IMACS World Congress*, pages 3–7, 1982a.

L. Petzold. Differential/algebraic equations are not ODE' s. *SIAM Journal on Scientific and Statistical Computing*, 3(3):367–384, 1982b.

C. Picioreanu, J. Vrouwenvelder, and M. van Loosdrecht. Three-dimensional modeling of biofouling and fluid dynamics in feed spacer channels of membrane devices. *Journal of Membrane Science*, 345(1-2):340–354, 2009.

J. W. Post, H. V. Hamelers, and C. J. Buisman. Influence of multivalent ions on power production from mixing salt and fresh water with a reverse electrodialysis system. *Journal of Membrane Science*, 330(1-2):65–72, 2009.

O. A. Prado-Rubio. *Integration of Bioreactor and Membrane Separation Processes: A model based approach: Reverse Electro-Enhanced Dialysis process for lactic acid fermentation.* PhD thesis, Technical University of Denmark, Copenhagen, Denmark, 2010.

Process Systems Enterprise. gPROMS, www.psenterprise.com/gproms, rev. 12.06.2014, 1997-2009.

S. T. P. Psaltis and T. W. Farrell. Comparing charge transport predictions for a ternary electrolyte using the maxwell–stefan and nernst–planck equations. *Journal of The Electrochemical Society*, 158(1):A33, 2011.

T. Quaiser and M. Mönnigmann. Systematic identifiability testing for unambiguous mechanistic modeling – application to JAK-STAT, MAP kinase, and NF-κ B signaling pathway models. *BMC Systems Biology*, 3(1):50, 2009.

A. Radu, J. Vrouwenvelder, M. van Loosdrecht, and C. Picioreanu. Modeling the effect of biofilm formation on reverse osmosis performance: Flux, feed channel pressure drop and solute passage. *Journal of Membrane Science*, 365(1-2):1–15, 2010.

P. Ramírez. Modeling of amino acid electrodiffusion through fixed charge membranes. *Journal of Colloid and Interface Science*, 242(1):164–173, 2001.

J. Rang and L. Angermann. Perturbation index of linear partial differential-algebraic equations. *Applied Numerical Mathematics*, 53(2-4):437–456, 2005.

G. Reissig, W. S. Martinson, and P. I. Barton. Differential–algebraic equations of index 1 may have an arbitrarily high structural index. *SIAM Journal on Scientific Computing*, 21(6):1987–1990, 2000.

W. C. Rheinboldt. Differential-algebraic systems as differential equations on manifolds. *Mathematics of Computation*, 43(168):473–482, 1984.

R. A. Robinson and R. H. Stokes. *Electrolyte Solutions*. Dover Publications, Mineola, NY, 2002.

S. Roller, J. Bernsdorf, H. Klimach, M. Hasert, D. Harlacher, M. Cakircali, S. Zimny, K. Masilamani, L. Didinger, and J. Zudrop. An adaptable simulation framework based on a linearized octree. In M. Resch, X. Wang, W. Bez, E. Focht, H. Kobayashi, and S. Roller, editors, *High Performance Computing on Vector Systems 2011*, pages 93–105. Springer Berlin Heidelberg, 2012.

J. Rouquerol and R. Sabbah. *Chemical Thermodynamics, 4: Plenary Lectures*. Pergamon Press, Oxford, England, 1977.

I. Rubinstein and B. Zaltzman. Electro-osmotically induced convection at a permselective membrane. *Physical Review E*, 62(2):2238–2251, 2000.

I. Rubinstein. *Electro-diffusion of ions*, volume 11 of *SIAM Studies in Applied Mathematics*. Society for Industrial and Applied Mathematics, Philadelphia, 1990.

B. Ruiz, P. Sistat, P. Huguet, G. Pourcelly, M. Arayafarias, and L. Bazinet. Application of relaxation periods during electrodialysis of a casein solution: Impact on anion-exchange membrane fouling. *Journal of Membrane Science*, 287(1):41–50, 2007.

J.-U. Rype. *Modeling of Electrically Driven Membrane Processes*. PhD thesis, Technical University of Denmark, Copenhagen, Denmark, 2002.

V. Saarinen, K. D. Kreuer, M. Schuster, R. Merkle, and J. Maier. On the swelling properties of proton conducting membranes for direct methanol fuel cells. *Solid State Ionics*, 178(7-10): 533–537, 2007.

M. Sadrzadeh, T. Mohammadi, J. Ivakpour, and N. Kasiri. Neural network modeling of Pb^{2+} removal from wastewater using electrodialysis. *Chemical Engineering and Processing: Process Intensification*, 48(8):1371–1381, 2009.

T. Sata. *Ion Exchange Membranes: Preparation, Characterization, Modification and Application*. Royal Society of Chemistry, Cambridge, 2004.

M. Schlegel, W. Marquardt, R. Ehrig, and U. Nowak. Sensitivity analysis of linearly-implicit differential–algebraic systems by one-step extrapolation. *Applied Numerical Mathematics*, 48 (1):83–102, 2004.

G. Schock and A. Miquel. Mass transfer and pressure loss in spiral wound modules. *Desalination*, 64(0):339–352, 1987.

J. Schwinge, Wiley, and D. F. Fletcher. A CFD study of unsteady flow in narrow spacer-filled channels for spiral-wound membrane modules. *Desalination*, 146:195–201, 2002.

J. Schwinge, D. Wiley, and A. Fane. Novel spacer design improves observed flux. *Journal of Membrane Science*, 229(1-2):53–61, 2004.

M. Shakaib, S. M. F. Hasani, and M. Mahmood. CFD modeling for flow and mass transfer in spacer-obstructed membrane feed channels. *Journal of Membrane Science*, 326:270–284, 2009.

I. M. Shiryaeva and A. I. Victorov. Equilibrium of ion-exchange polymeric membrane with aqueous salt solution and its thermodynamic modeling. *Fluid Phase Equilibria*, 180(1-2):115–138, 2001.

A. A. Sonin and M. S. Isaacson. Optimization of flow design in forced flow electrochemical systems, with special application to electrodialysis. *Industrial & Engineering Chemistry Process Design and Development*, 13(3):241–248, 1974.

K. Sternberg. *Simulation, Optimale Steuerung und Sensitivitätsanalyse einer Schmelzkarbonat-Brennstoffzelle mithilfe eines partiellen differential-algebraischen dynamischen Gleichungssystems*. PhD thesis, Universität Bayreuth, Bayreuth, 2006.

H. Strathmann. Electrodialysis, a mature technology with a multitude of new applications. *Desalination*, 264(3):268–288, 2010.

H. Strathmann. *Ion-exchange Membrane Separation Processes*. Membrane Science and Technology Series. Elsevier, Amsterdam, 2004.

K. Strehmel. *Linear-implizite Runge-Kutta-Methoden und ihre Anwendung*. Teubner-Texte zur Mathematik. B.G. Teubner, Stuttgart, 1992.

J. C. Strikwerda. *Finite Difference Schemes and Partial Differential Equations*. Society for Industrial and Applied Mathematics, Philadelphia, 2004.

Y. Tanaka. Mass transport and energy consumption in ion-exchange membrane electrodialysis of seawater. *Journal of Membrane Science*, 215(1-2):265–279, 2003.

Y. Tanaka, H. Uchino, and M. Murakami. Continuous ion-exchange membrane electrodialysis of mother liquid discharged from a salt-manufacturing plant and transport of cl^- ions and so_4^{2-} ions. *Membrane Water Treatment*, 3(1):63–76, 2012.

R. Taylor and H. A. Kooijman. Composition derivatives of activity coefficient models (for the estimation of thermodynamic factors in diffusion): Chemical engineering communications. *Chemical Engineering Communications*, 102(1):87–106, 1991.

R. Taylor and R. Krishna. *Multicomponent Mass Transfer*. Wiley, New York, 1993.

The Math Works Inc., 2013. Matlab, Version 2013a, Natick, Massachusetts.

J. Unger, A. Kröner, and W. Marquardt. Structural analysis of differential-algebraic equation systems - theory and applications. *Computers & Chemical Engineering*, (19):867–882, 1995.

M. K. Urtenov, A. M. Uzdenova, A. V. Kovalenko, V. V. Nikonenko, N. D. Pismenskaya, V. I. Vasil'eva, P. Sistat, and G. Pourcelly. Basic mathematical model of overlimiting transfer enhanced by electroconvection in flow-through electrodialysis membrane cells. *Journal of Membrane Science*, 447:190–202, 2013.

S. Vajda, H. Rabitz, E. Walter, and Y. Lecourtier. Qualitative and quantitative identifiability analysis of nonlinear chemical kinetic models. *Chemical Engineering Communications*, 83(1): 191–219, 1989.

R. Valerdi-Pérez, M. López-Rodríguez, and J. A. Ibáñez-Mengual. Characterizing an electrodialysis reversal pilot plant. *Desalination*, 137(1-3):199–206, 2001.

R. Valerdi-Pérez and J. Ibáñez-Mengual. Current—voltage curves for an electrodialysis reversal pilot plant: determination of limiting currents. *Desalination*, 141(1):23–37, 2001.

F. Valero and R. Arbós. Desalination of brackish river water using electrodialysis reversal (EDR): Control of the thms formation in the barcelona (ne spain) area. *Desalination*, 253(1-3):170–174, 2010.

van der Stegen, J.H.G., H. H. Weerdenburg, A. J. Veen, J. A. Hogendoorn, G. F. Versteeg, H. Weerdenburg, and van der Veen, A.J. Application of the pitzer model for the estimation of activity coefficients of electrolytes in ion selective membranes. *Fluid Phase Equilibria*, 157(2): 181–196, 1999.

S. van Pham, Z. Li, K. M. Lim, J. K. White, and J. Han. Direct numerical simulation of electroconvective instability and hysteretic current-voltage response of a permselective membrane. *Physical Review E*, 86(4), 2012.

Verein Deutscher Ingenieure, editor. *VDI-Wärmeatlas*. Springer, Berlin, 10 edition, 2006. ISBN 978-3-540-29646-1.

C. R. Visser. *Electrodialytic Recovery of Acids and Bases: Multicomponent Mass Transfer Description*. PhD thesis, Rijksuniversiteit Groningen, Groningen, 2001.

E. Vitillaro and A. Fiscella. Local Hadamard well–posedness and blow–up for reaction–diffusion equations with non–linear dynamical boundary conditions. *Discrete and Continuous Dynamical Systems*, 33(11/12):5015–5047, 2013.

E. Walter and L. Pronzato. *Identification of parametric models from experimental data*. Communications and Control engineering. Springer and Masson, Berlin, 1997.

Y. Wang, C. Huang, and T. Xu. Optimization of electrodialysis with bipolar membranes by using response surface methodology. *Journal of Membrane Science*, 362(1-2):249–254, 2010.

A. Z. Weber and C. Delacourt. Mathematical modelling of cation contamination in a proton-exchange membrane. *Fuel Cells*, 8(6):459–465, 2008.

A. Z. Weber and J. Newman. Transport in polymer-electrolyte membranes: I. physical model. *Journal of The Electrochemical Society*, 150(7):A1008, 2003.

A. Z. Weber and J. S. Newman. A theoretical study of membrane constraint in polymer-electrolyte fuel cells. *AIChE Journal*, 50(12):3215–3226, 2004.

Online-Buchshop für Ingenieure

VDI nachrichten **BUCHSHOP**

Online-Shops

Fachliteratur und mehr - jetzt bequem online recherchieren & bestellen unter: www.vdi-nachrichten.com/Der-Shop-im-Ueberblick

Täglich aktualisiert: Neuerscheinungen VDI-Schriftenreihen

Im Buchshop von vdi-nachrichten.com finden Ingenieure und Techniker ein speziell auf sie zugeschnittenes, umfassendes Literaturangebot.

Mit der komfortablen Schnellsuche werden Sie in den VDI-Schriftenreihen und im Verzeichnis lieferbarer Bücher unter 1.000.000 Titeln garantiert fündig.

Im Buchshop stehen für Sie bereit:

VDI-Berichte und die Reihe **Kunststofftechnik:**

Berichte nationaler und internationaler technischer Fachtagungen der VDI-Fachgliederungen

Fortschritt-Berichte VDI:

Dissertationen, Habilitationen und Forschungsberichte aus sämtlichen ingenieurwissenschaftlichen Fachrichtungen

Newsletter „Neuerscheinungen":

Kostenfreie Infos zu aktuellen Titeln der VDI-Schriftenreihen bequem per E-Mail

Autoren-Service:

Umfassende Betreuung bei der Veröffentlichung Ihrer Arbeit in der Reihe Fortschritt-Berichte VDI

Buch- und Medien-Service:

Beschaffung aller am Markt verfügbaren Zeitschriften, Zeitungen, Fortsetzungsreihen, Handbücher, Technische Regelwerke, elektronische Medien und vieles mehr – einzeln oder im Abo und mit weltweitem Lieferservice

Die Reihen der Fortschritt-Berichte VDI:

1 Konstruktionstechnik/Maschinenelemente
2 Fertigungstechnik
3 Verfahrenstechnik
4 Bauingenieurwesen
5 Grund- und Werkstoffe/Kunststoffe
6 Energietechnik
7 Strömungstechnik
8 Mess-, Steuerungs- und Regelungstechnik
9 Elektronik/Mikro- und Nanotechnik
10 Informatik/Kommunikation
11 Schwingungstechnik
12 Verkehrstechnik/Fahrzeugtechnik
13 Fördertechnik/Logistik
14 Landtechnik/Lebensmitteltechnik
15 Umwelttechnik
16 Technik und Wirtschaft
17 Biotechnik/Medizintechnik
18 Mechanik/Bruchmechanik
19 Wärmetechnik/Kältetechnik
20 Rechnerunterstützte Verfahren (CAD, CAM, CAE CAQ, CIM ...)
21 Elektrotechnik
22 Mensch-Maschine-Systeme
23 Technische Gebäudeausrüstung

ISBN 978-3-18-394903-8